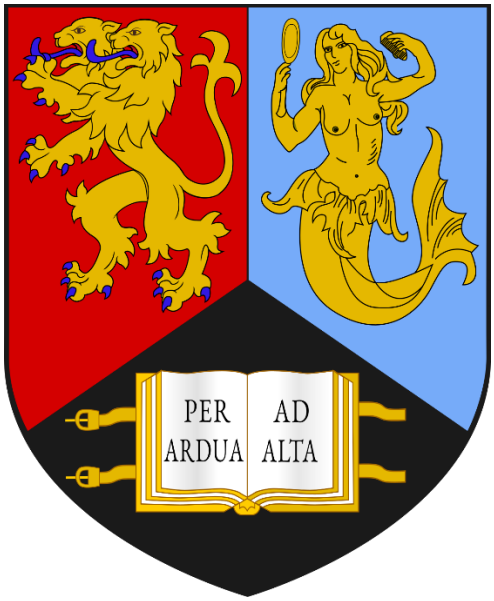

BATTERY THERMAL MANAGEMENT USING COMPOSITE PHASE CHANGE MATERIALS

By

Yanqi Zhao

A thesis submitted to the

University of Birmingham for the

Degree of Doctor of Philosophy

School of Chemical Engineering

College of Engineering and physical Sciences

The University of Birmingham

November 2020

Abstract

This PhD study reports the research on an active cooling-based battery thermal management system (BTMS) using composite phase change materials (CPCMs). The hybrid BTMS has a great potential to replace current commercial BTMS as it could control not only the maximum battery pack temperature but also temperature uniformity. However, there are insufficient studies on the area and hence research gaps, particularly the following aspects needs to be overcome. Firstly, there has been inadequate studies of particle size effect on the thermal property of CPCMs. Secondly, many published papers did not include accurate descriptions of the battery thermal behaviour in their study. However, the heat generation rate can fluctuate wildly in the charge/discharge process. Thirdly, there have been very few studies compared the performance of different CPCMs in the BTMS. In this PhD study, three types of CPCMs, expanded graphite (EG)/paraffin, copper foam/paraffin and colloidal graphite/paraffin composites were investigated. Their surface morphologies, structures, phase change behaviour, thermal stability, and thermal conductivity were studied experimentally. Thermal behaviour and energy efficiency of the lithium-ion battery (LIB) was investigated experimentally, under different charge/discharge rates, and at different temperatures. An experimental set up and computational fluid dynamics (CFD) modelling using Ansys® fluent were carried out to examine the performance of the active cooling based BTMS using CPCM.

In the study of EG/paraffin composite, porous structure and the particle size of the EG are found to be the determining factors of the properties of EG/paraffin composites. The surface morphology, phase change temperature, thermal degradation temperature, cycling stability and thermal conductivity are affected by the porous structure and the particle size. In the investigation of copper foam/paraffin composites, the porosity of the copper foam can efficiently affect the thermal property of the CPCMs, with the latent heat inversely proportional to the thermal conductivity. In the study of colloidal graphite/paraffin composites, it was found that melamine is the excellent fire-retardant material for colloidal graphite/paraffin composite, which could vastly improve the thermal degradation temperature with a reasonable amount.

In the characterization of single cells, the temperature increase of the LIB under charge and discharge was accurately measured under an adiabatic condition. The heat generation rate was retrieved from temperature increase, and its variation was studied. It was also found that low current rates and high operation temperatures lead to higher specific energy, high specific power, and high round trip efficiency. Battery polarization has been identified as the main

factor which caused the variation on the battery thermal behaviour and energy performance under different operating conditions.

In the BTMS study, two models with both active liquid cooling and passive CPCM cooling were then developed to examine the performance of BTMS. The first numerical model used a round tube with a relatively small volume occupancy and a small heat transfer area. An experimental investigation on the same device setup has successfully validated the accuracy of the model. Effect of inlet velocity of the heat transfer fluid (HTF) and the battery current rate has been investigated. High inlet velocity of HTF can reduce the maximum battery temperature, and CPCM can provide temperature uniformity to the battery pack. The second model used a tabular tube with a relatively large volume and a large heat transfer area. The simulation serves the objective to study the impacts of CPCM types and inlet velocity of HTF on both the maximum battery temperature and temperature distribution under different current rates. The results showed that liquid cooling is efficient in controlling battery temperature under continuous battery charging/discharging cycles. The EG/paraffin composite is better than the copper foam/paraffin composite in both reducing the maximum battery temperature and providing temperature uniformity to the battery pack. In a search for generalized results, dimensional analysis of the results is performed and presented as the Nusselt numbers and dimensionless temperature against the Fourier and Stefan numbers.

Acknowledgements

My deep gratitude goes first to my supervisor Professor Yulong Ding, who continuously guided and supported me throughout my PhD study. His enthusiasm for thermal energy storage kept me constantly engaged with my research, and his generosity helped make my time at Birmingham Centre for Energy Storage enjoyable.

My appreciation extends to my co-supervisor Dr Yongliang Li, who's mentoring and encouragement has been incredibly valuable. Thanks also go to my colleague, Dr Boyang Zou, who helped me with my experiments and reviewed the thesis. I wish to acknowledge the help provided by all the other members in Birmingham Centre for Energy Storage.

I also greatly appreciate the China Scholarship Council for the partial financial support of my PhD study.

Finally, I wish to acknowledge the support and great love of my parents, my mother and father-in-law, my wife Yao, and my new-born daughter Charlotte, who accompanied with me in the lockdown life in 2020. They kept me going on, and this work would not have been possible without their input.

Table of Contents

List of Tables

List of Figures

Abbreviations

ARC:	Accelerating rate calorimeters
BTMS:	Battery thermal management system
BMS:	Battery management system
BEV:	Pure battery electric vehicle
BNNS:	Boron nitride nanosheet
CPCM:	Composite phase change material
CNT:	Carbon nanotubes
CE:	Coulombic efficiency
CM:	Copper mesh
DSC:	Differential scanning calorimetry
DOD:	Depth of discharge
DTG:	Derivative thermogravimetry
EG:	Expended graphite
EV:	Electric vehicle
EE:	Energy efficiency
GNP:	Graphite nanoplate
HDPE:	High-density polyethene
HTF:	Heat transfer fluid
ICE:	Internal combustion engine
LIB:	Lithium-ion battery
LHS:	Latent heat storage
LDPE:	Low-density polyethene
LFA:	Laser Flash Apparatus
LTO:	$LiCoO_2$ cathode
LMO:	$LiMn_2O_4$ cathode
LFP:	$LiFePO_4$ cathode
LTO:	$Li_4Ti_5O_{12}$ anode
MWCNT:	Multi-walled carbon nanotubes
NCM:	$LiNiMnCoO_2$ cathode
NCA:	$LiNiCoAlO_2$ cathode
NS:	Nano-silica
OCV:	Open circuit voltage

ODH:	Oxygen Dumbbell Hop
OSSE:	Octahedral-site stabilization energy
OBC:	Olefin block copolymer
PLIB:	Post lithium-ion battery
PCM:	Phase change material
PEG:	Polyethene glycol
PE:	Polyethylene
PRT:	Platinum resistance thermometer
PPI:	Pore number per inch
PHEV:	plug-in electric vehicle
RTE:	Round trip efficiency
SSB:	Solid-state battery
SHS:	Sensible heat storage
SoC:	State of charge
SEM-EDS:	Scanning Electron Microscopy with Energy Dispersive X-ray Spectrometry
STA:	Simultaneous thermal analyser
SEI:	Solid electrolyte interface
TES:	Thermal energy storage
TCES:	Thermochemical energy storage
THB:	Thermal hot bridge
TSH:	Tetrahedral Site Hop
VE:	Voltage efficiency
XRT:	Nano-CT system

Nomenclature

a	surface area, m^2
A	permeability
A_{sf}	interfacial surface area, m^{-1}
C	current rate
C_p	specific heat at constant pressure, J/(kg·K)
c_i	inertia coefficient
d_f	ligament diameter, m
d_p	average diameter, m
h	sensible enthalpy, J
h_{sf}	heat transfer coefficient, W/m^2K
H	enthalpy, J
k	thermal conductivity, W/(m·K)
l	length through heat conduction, m
I	current, A
L	latent heat, J/kg
m	mass, g
Nu	Nusselt number
P	pressure, Pa
Pr	Prandtl number
q	energy, J
$\dot{q}$	heat flow, W
$\vec{q}$	heat flux, W/m^2
R	internal resistance, Ω
S	source term
t	time, s
T	temperature, K
ΔT	temperature difference, K
U	Open circuit voltgae, V
u, v, w	velocity in x, y, z direction, m/s
x, y	Cartesian coordinates

Greek symbols	
α	thermal diffusivity, m^2/s
ρ	density, kg/m^3
β	liquid fraction, %
η	efficiency, %
γ	Constant
μ	viscosity, kg/(m·s)
ω	pore density, PPI
ε	Porosity, %
ε_{em}	emissivity coefficient
τ	dimensionless time
θ	dimensionless temperature
Subscripts	
a	ambient
ave	average
c	composite
e, eff	effective value
f	heat transfer fluid
i	initial
in	inlet
l	liquid
max	maximum
m	melting
me	metal foam
ref	reference value
s	solid
pcm	phase change material

Chapter 1 Introduction

1.1. Background

The plug-in electric vehicle (PHEV) sale is growing dramatically year by year, and it has reached 2.2 million in 2019, which accounts for 2.5% market share [1]. However, as one of the key components of the electric vehicle (EV), tractions batteries remain as one of the major challenges. The energy density, charging and discharge performance and safety issues are among the main bottlenecks that restrict the rapid large-scale development of EVs.

The lithium-ion batteries (LIBs) are favoured with powering EVs due to their high energy density (200-600Wh/L) and high round trip efficiency (>90%) at cell and pack level. Although the LIB based EVs are not yet comparable with conventional fuels in terms of energy density (Petrol has an energy density of 9500Wh/L, and internal combustion engine (ICE) has an efficiency of 35% [2]), they are clean with better environmental impact. The charging speed has also been a non-negligible factor influencing customers' decision on EV purchases. As indicated by charger suppliers, a typical EV with a 60kWh battery takes about 8 hours to charge fully from empty [3], compared with a petrol/diesel car, which only takes a few minutes to refuel the vehicle. A Chinese EV manufacturer, NIO, is currently at the forefront of the development of a battery swap technology to address this issue [4]. The new technology would take ~10 minutes to swap a nearly drained battery pack with a fully charged battery pack, which significantly saves the time waiting for a LIB based EV to be fully charged. But presently, NIO is the sole manufacturer which is promoting the battery swap technology and the current battery swap facility can only support NIO's EV models. Also, the average cost of a battery swap station is US$ 434,000. Hence economically, it might be difficult for this to be promoted and sustained. Safety-wise, EVs also have their own problems. If catching on fire, an EV would burn a lot more violently therefore making it difficult to be extinguished [5].

As a result of the above, significant efforts have been made to develop iterative battery technology. Post lithium-ion batteries (PLIBs) including lithium-air, lithium-sulfur, lithium-metal and solid-state batteries, have the potential to substitute the LIB. The PLIBSs can offer a much higher energy density, charging speed, and improved safety. However, most of these advanced batteries are still in the stage of fundamental research. Many aspects are the subjects of intensive studies, such as stability. Most of the PLIBs suffer from long term stability. For example, in the charging and discharging process of lithium-air batteries, the side reactions occur on the electrolyte, and cathode can cause severe capacity loss [6]; the lithium polysulfide

intermediates produced in the charging and discharging process of the lithium-sulfur battery can diffuse to the positive and negative electrodes, which also causes permanent capacity loss [7]; the dendrite growth on the lithium anode makes the operation of the lithium metal battery very difficult; the dendrite-free operation of the lithium metal battery is still a challenge; although the solid-state batteries (SSBs) are the most promising candidate of the commercial PLIBs, which is also believed to have stability problems, and are not expected to have commercial application in the EV market until 2030 [8,9].

The powertrain of the EVs is therefore likely to still depend on LIBs. After 25 years of development, the energy density of LIBs is close to the theoretical limit [2]. Many of the current research on LIBs have been focused on their practical application, and battery thermal management system (BTMS) is one of the most essential research topics.

The traction battery pack in the EV is composed of multiple single cells connected in series and parallel. Its performance, lifetime and safety are closely related to the characteristics of the single cells and their temperatures. If the temperature of any single cell is too high or too low, it will affect the safety and performance of the whole battery pack. At low temperatures, significant battery polarization occurs, which can result in a massive decrease in the charge rate and energy capacity. When charging at low temperatures, insertion of lithium ions into the negative electrode is difficult, and dendrites can form on the surface of the negative electrode, which can permanently damage the battery and may cause safety hazards. At high temperatures, the battery could be irreversibly damaged during charging and discharging due to ageing from parasitic reactions and even cause safety accidents such as overheating, burning and explosion. An uneven temperature distribution can cause a difference in the internal resistance of single cells within a battery pack. The long-term use of the cells with different internal resistances can cause a difference in battery ageing. Since the capacity of the battery pack is determined by the cells with the lowest capacity, this will cause a decrease in the battery capacity of the whole pack. Also, the difference in internal resistances caused by temperature differences gives a difference in the open-circuit voltage (OCV) of single cells, which, in extreme conditions, can lead to a short circuit.

A battery thermal management system (BTMS) not only helps the battery pack to dissipate heat but also preheats the battery before the operation so that the battery pack can work in an optimal environment. At present, EV manufacturers mainly use active BTMS, including air cooling and liquid cooling systems. An air-cooling system has a simple structure with a low

manufacturing cost. However, due to the low heat transfer coefficient of forced air convection, the air cooling based BTMS is often unable to meet the requirements of battery packs with high capacity or under fast charging. Besides, the air-cooling channels are typically designed at the surroundings of the battery pack. Hence the heat generated from the core part of the battery usually cannot sufficiently dissipate through air cooling. Even if the surface temperature of the battery is kept within a safe temperature range, the core part of the battery may be on a significantly higher temperature for a longer time, which affects the battery life and even safety. Liquid cooling with a high heat transfer coefficient can provide an excellent cooling capability. At the same time, most liquid cooling systems require a refrigeration unit as the cooling source, which consumes a lot of electricity. Therefore, the cost is generally high due to its complex structure. The liquid cooling system does have a disadvantage of having a risk of coolant leakage, which leads to subsequent high-priced maintenance.

The active cooling systems summarized above consume electrical energy from the traction battery, leading to a decreased EV driving range. The use of passive cooling for the BTMS has the potential to reduce and even eliminate the issue. This is through the inherent thermal regulation behaviour of phase change materials (PCMs), which forms the primary motivation of this PhD study.

1.2. Aim and objectives

This PhD study was aimed to develop a hybrid battery thermal management system based on the use of composite phase change materials (CPCMs) and liquid cooling. It is focused on the thermal management device consisting of two components of the system, the CPCMs and LIBs. The necessity to develop CPCMs was mainly due to the low thermal conductivity of pure PCMs. When applied to thermal management, although the PCMs can adjust the heat source temperature with its temperature regulation ability, their low thermal conductivities hinder the heat transfer. The battery may overheat due to the low heat transfer coefficient between the battery pack and the PCM. Also, the PCM can be heated to above its phase change temperature as the accumulated heat cannot be dissipated to the ambient in time. Eventually, it will lead to the failure of thermal management. Hence in this study, three thermal enhancement materials, including expanded graphite (EG), copper foam and colloidal graphite, were chosen to incorporate with the PCMs to improve their thermal conductivities.

A battery cell is a sophisticated electrochemical system. The behaviour and performance of it need to be understood before developing the BTMS. The thermal characteristics of the LIB

was studied at different current rates of charge and discharge. A thermal model was developed based on the experimental measurements for numerical modelling of the BTMS. The underlying reason for the variation of the battery heat generation rate has also been proposed. The battery performance is closely linked to its temperature and current rate, thereby the relationship between the battery performance and the operation conditions has been investigated.

Finally, the active cooling based BTMS using CPCMs has been experimentally and numerically studied combined with the previous research on the CPCMs and the LIB. The study was to understand the effects of the design and operating conditions on the BTMS performance. The CPCMs can provide good thermal conductivity, leading to temperature uniformity, but the use of too much CPCMs can occupy a large space, leading to a decrease in the energy density of the battery pack. The work studied the influences of current rate, inlet velocity of heat transfer fluid and type of CPCMs on the performance of the BTMS.

In conclusion, the objectives of this PhD study are:

1) To study the properties of the CPCMs containing different thermal enhancement materials
2) To investigate the thermal characteristics and performance of the LIBs under different operation conditions
3) To design, construct and test an active cooling-based battery thermal management device using CPCMs and study the thermal management performance of the system
4) To develop numerical models for the hybrid BTMS to further study the system

1.3. Layout of the thesis

This thesis consists of 7 chapters. Chapter 2 provides a detailed literature review covering the background and most recent research related to this work. Chapter 3 outlines the methodology of this work including thermal and structural characterization of the CPCMs, experimental setup on the battery test and the test protocol, device setup of the BTMS and the test protocol, and mathematical model and numerical method. Chapter 4 discusses the results from the CPCM characterization and compares the properties of different CPCMs. Chapter 5 discusses the results from battery characterization and develops a thermal model for the LIB. The relationship between battery performance and operation condition is also presented in this chapter. Chapter 6 shows the results of the device test. The numerical modelling work is also

discussed in detail in this chapter. Chapter 7 summaries the conclusions of this study, where recommendations for further work are also given based on this study.

Chapter 2 Literature review

In this chapter, relevant literature on the battery thermal management systems is reviewed. Section 2.1 gives a detailed review of lithium-ion batteries, from its early-stage research to recent applications in industry. Different types of lithium-ion batteries are classified based on their shapes. An up-to-date work on the energy efficiency of the lithium-ion battery is summarized. Section 2.2 examines the temperature effect on lithium-ion batteries, including battery ageing, performance degradation, and hazards. Section 2.3 summarizes commercial battery thermal management systems for electric vehicles and products in the market. Section 2.4 reviews in detail the recent research on battery thermal management systems using composite phase change materials.

2.1. Lithium-ion batteries

2.1.1. Development of lithium-ion batteries

In 1970s Michael Stanley Whittingham discovered the mechanism of lithium intercalation when he worked for Exxon Research & Engineering Company, such a concept forms the foundation of the modern LIB. $LiTiS_2$ cathode was therefore developed for high energy density rechargeable batteries [10]. Whittingham described the intercalation process as putting jam in a sandwich. In the chemical terms, the lithium ions can be put into the crystal structure and taken out. Meanwhile, the structure is precisely the same afterwards [11]. The $LiTiS_2$ battery has a discharge voltage of 2.5V with good cycle ability, but the fire hazard of the material stopped it from entering the market. In recent years $LiTiS_2$ has regained research interest in all-solid-state batteries which resolves the risk of fire hazard issue [12,13]. The sulphide solid electrolytes have poor ionic contact with the active materials, and the application of nanoscale TiS_2 significantly increases the reversible capacity and rate capability of the solid-state battery.

John B. Goodenough is another pioneer who greatly promotes the development of modern LIB technology. His research group discovered three most important crystal structures of cathodes, including layered structure, spinel structure and polyanion, as shown in Figure 1, which are the only three classes existing in the market.

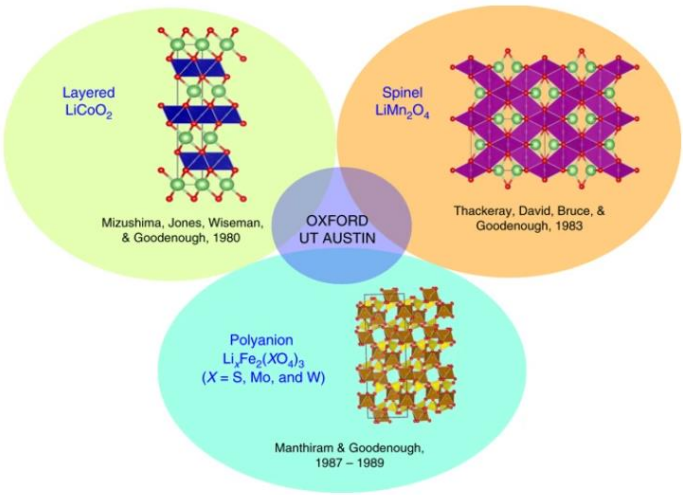

Figure 1 Three types of crystal structure of LIB cathodes discovered by Goodenough's research groups in University of Oxford and University of Texas at Austin [14]

The first commercialized layered structure cathode $LiCoO_2$ (LCO) was developed in 1980 by Goodenough's group. Mizushima et al. [15] prepared a rock salt structure $LiCoO_2$ cathode with a theoretical energy density of 1.11 kWh/kg. The open-circuit voltage (OCV) reached 4V,

which was twice of the $LiTiS_2$ cathode as mentioned previously. The LCO cathode was prepared by heating a pelletized mixture of lithium carbonate and cobalt carbonate at 900 °C for 20 hours, followed by subsequent firings twice. A 3D crystal structure of $LiCoO_2$ is shown in Figure 2, where the lithium ions occupy the octahedral sites in the lithium diffusion plane between the CoO_2 slabs. The Li-ions can diffuse via two routes, namely the Oxygen Dumbbell Hop (ODH) and Tetrahedral Site Hop (TSH) [16,17], as illustrated in Figure 3. The main advantage of the LCO cathode is the close-packed arrangement of the anions, forming a close-packed pseudocubic array. Mizushima et al. also tested $LiVO_2$, $LiCrO_2$, $LiNiO_2$ and $NaFeO_2$, which were not shown promising for battery application. However, the energy density of the LCO cathode was limited to 140mAh/g, and the high price ($30000/ton as of May 2020 from London metal exchange market) and ethical problems of cobalt drive the substitution of cobalt with transition metals. These disadvantages drive the developments of other cathodes.

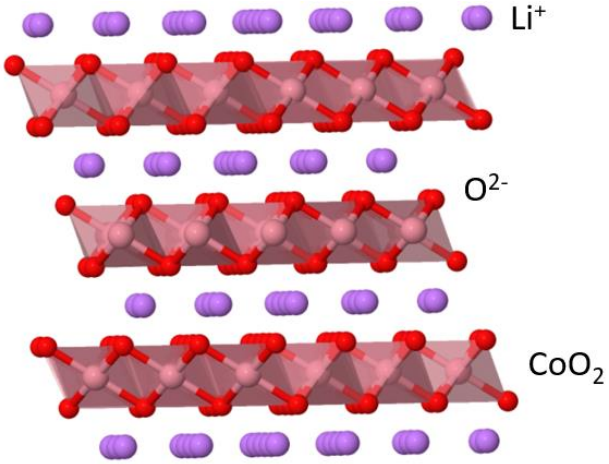

Figure 2 Crystal structure of $LiCoO_2$ [18]

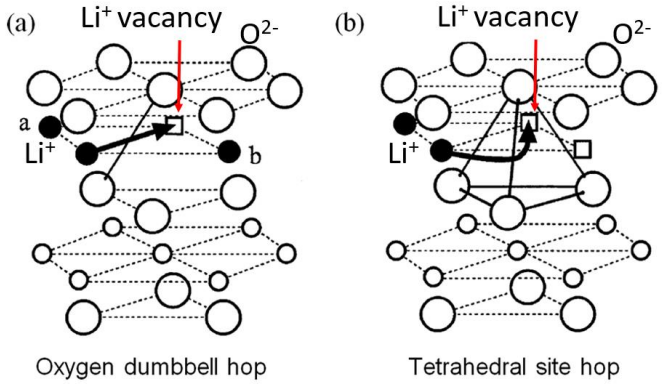

Figure 3 Two lithium-ion migration routes. (a)Oxygen dumbbell hop and (b)Tetrahedral site hop [17]

Mn and Ni have been studied for partial substitution of Co. The octahedral-site stabilization energy (OSSE, energy towards stabilization as the consequence of crystal field theory) of Ni sits between the Co and Mn ions, offering structural stability [14,19]. The Mn ions further provide structural stability as $Mn^{3+/4+}$ helps with reducing Ni^{3+} into stabilized Ni^{2+} without involved in the battery charge/discharge process. Figure 4 shows the 3D crystal structure of the $LiNiMnCoO_2$ (NCM) cathode. The Ni, Mn and Co ions are located at the centre of the O octahedra [20]. Like the parent LCO material, the Li in NCM cathode occupies the space between the MO_6 planes. The Li-ions also diffuse by hopping through neighbouring tetrahedral sites and oxygen dumbbell hopping [21]. Working separately, Thackeray et al. from University of Chicago and Lu et al. from 3M both filed patents in 2001 on the NCM cathode. Thackeray et al. [22] filed a patent of lithium metal oxide electrodes with a general formula $xLiMO_2 \cdot (1-x)Li_2M'O_3$ in which $0<x<1$, and where M is one or more trivalent ion with at least one ion being Ni and Co, and where M' is one or more tetravalent ion including Mn, Mg and Al. Lu et al. [23] filed a similar patent for a cathode with composition with the formula $Li[M^1{}_{(1-x)}Mn_x]O_2$. In which $0<x<1$ and M^1 represents one or more metal elements selecting from Ni, Co, Fe, Cu, Li, Zn and V. The main difference between these two patents is that Thackeray's invention describes a general formulation, while Lu's claim focuses on a formulation with higher Li and Mn content. Compared with LCO, $LiMn_2O_4$ (LMO) and $LiFePO_4$ (LFP) cathodes, the NCM battery has a higher energy density and cycle life. Hence it has been widely used worldwide. As of 2020, the majority of the battery electric vehicle (BEV) models including BYD Yuan, BAIC EU5, Renault Zoe, VW e-Golf, Nissan Leaf, Hyundai Kona, BMW I3, Audi e-Tron, use NCM batteries.

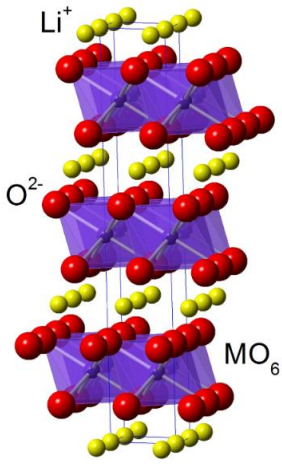

Figure 4 Crystal structure of the $LiNi_xMn_yCo_{1-x-y}O_2$. Ni, Mn and Co are randomly distributed within MO_6 slabs [20]**.**

Another set of materials for partial substitution of Co in the LCO cathode includes Ni, Al, and Co. The energy density of $LiNiCoAlO_2$ (NCA) batteries could reach 200 mAh/g, which is 1.5 times the LCO batteries [24]. The crystal structure of the NCA is similar to NCM, as shown in Figure 4. The difference in structure is instead of Ni, Mn and Co, Ni, Al, and Co are randomly distributed within MO_6 slabs. The presence of Al in NCA battery provides a better thermal stability and a high energy density. The Al ions in the MO_6 sites inhibit the migration of cations, preventing phase transition of the material at high temperature [25].

The second important discovery by Goodenough and team was the manganese spinels cathode. Thackeray et al. [26] chemically and electrochemically inserted lithium into $LiMn_2O_4$ at room temperature. The structure of the spinel $LiMn_2O_4$ is shown in Figure 5. The lithium ions can move between tetrahedral sites by hopping via intermediate octahedral sites in $LiMn_2O_4$. In this way, the ions can diffuse in 3-D. The $Li_{1+x}Mn_2O_4$ system is cubic at x=0 and tetragonal (ca=1.161) at x=1.2. Cubic and tetragonal phases coexist in the range $0.1 \ll x \ll 0.8$. The inserted lithium ions in $LiMn_2O_4$ occupy the interstitial octahedral positions of the spinel structure.

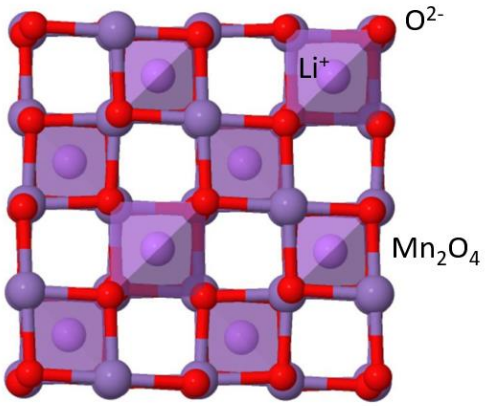

Figure 5 crystal structure of spinel $LiMn_2O_4$ [27]

The LMO batteries have stability problems as electrolyte decomposition occurs when the batteries are charged above 4V, and the Mn_2O_4 in LMO convert into MnO_2 at 190 °C. The third important discovery from John B. Goodenough's team was the stable polyanion oxides, with phospho-olivines as the most successful cathode in 1997. Padhi et al. [28] considered LFP cathode as an inexpensive, non-toxic, environmentally benign candidate for a lower power LIB. The characteristics have now been widely recognized by the industry and proved to be the exact description. The structure of the LFP is shown in Figure 6. The lithium ions can only diffuse

in 1-D, which move by hopping between neighbouring octahedral sites via the intermediate tetrahedral sites which share faces with the two adjacent octahedra. In the initial development, the LFP cathode battery has 3.5V nominal voltage and 0.05mA/cm^2 current density. The energy density was 100 to 110mAh/g with ~0.6 Li insertion/extraction.

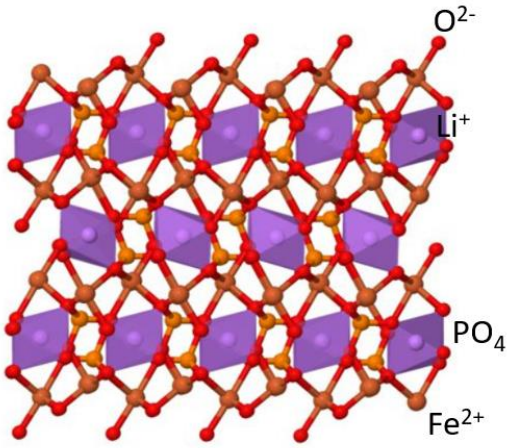

Figure 6 Crystal structure of $LiFePO_4$ [29]

The spinel-structure $Li_4Ti_5O_{12}$ (LTO) is the only anode material which used to name as a type of the LIB, as shown in Figure 7. The Li-ions occupy the tetrahedral sites and diffuse by hopping through neighbouring tetrahedral sites in 3D. The structure was first reported by Deschanvres [30] in 1971, and later the property was measured by Freg et al. [31]. Compare with the most common carbon anode, the LTO anode is much more stable. Particularly the expansion/contraction problem of the carbon-based anode during the charge/discharge is significant, which could detach from the active material, leading to capacity fading, and even short circuit. On the contrary, the LTO anode can accommodate the Li-ions without expansion, and the material has a neglected structure alteration during the charge/discharge. A study by Vijayakumar et al. showed that after 100 cycles, the battery only saw 1% of capacity loss [32].

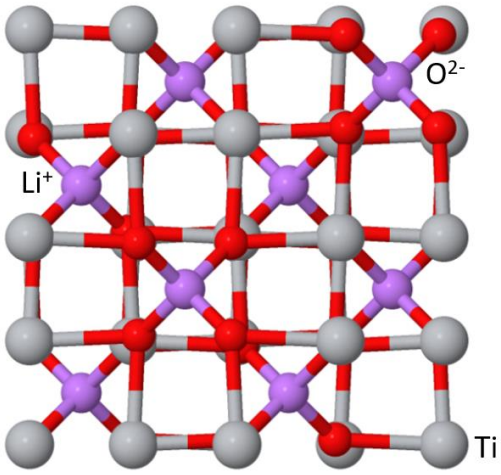

Figure 7 crystal structure of $Li_4Ti_5O_{12}$ [33]

Akira Yoshino developed the first commercial lithium-ion battery prototype in 1983 based on the early research from John B. Goodenough and M. Stanley Whittingham [34,35], who shared the Nobel Prize in Chemistry in 2019. The first LIB has a carbonaceous material as the anode and LCO as the cathode. The LCO battery has a nominal voltage of 3.6V and a high specific energy of 150-240Wh/kg. LCO battery was widely used in digital cameras, laptop, and mobile phones. However, the battery suffers from significant structural instability and server capacity fade in use, especially when it is designed for high specific energy [36]. Hence nowadays very few commercial LCO batteries can be found in the market. NCM, LMO, NCA, LFP, and LTO batteries have been the most popular LIB on the market. The properties and comparison of the different LIBs are given in Table 1.

Table 1 A comparison of LIBs based on different chemistry [37–40]

Battery short name	**NCM**	**LMO**	**NCA**	**LFP**	**LTO**	**LCO**
Commercial product since	2008	1996	1999	1996	2008	1991
Cathode	$LiNiMnCoO_2$	$LiMn_2O_4$	$LiNiCoAlO_2$	$LiFePO_4$	variable	$LiCoO_2$
Anode	graphite	graphite	graphite	graphite	$Li_4Ti_5O_{12}$	graphite

Theoretical energy density (mAh/g)	278 (NCM111)	148	270	170	175	274
Energy density from mass production (mAh/g)	160	110	180	140	50	135
Cycle life	1500-2000	500-1000	1500-2000	<2000	6000-20000	500-1000
Thermal runaway temperature (°C)	210	250	150	310	420	150
Nominal Voltage (V)	3.6	3.7	3.6	3.2	2.4	3.6
Maximum charge rate (C)	1	3	1	1	5	1
Maximum discharge rate (C)	2	10 (for short period)	1	25(for short period)	30(for short period)	1
Applications	Electric Vehicles, Stationary energy storage, Electronics	Power tools, medical device	Electric Vehicles, Stationary energy storage, Electronics	Electric Vehicles, Stationary energy storage	Electric Vehicles	Electronics
Cost as of 2017 ($/kWh)	250-750	250-750	250-750	250-750	500-1500	N/A

Table 2 gives a list of commercial EVs with their battery specifications and battery thermal management method. As shown in Table 2, The NCM batteries have taken up the majority of the EV market share. This is due to its relatively high energy density and stable property. As shown in Figure 8, with different ratios of Ni, Co and Mn, the NCM batteries can be classified into NCM111, NCM333, NCM523, NCM622 and NCM811 (e.g. chemical formula of the NCM 811 is $LiNi_{0.8}Co_{0.1}Mn_{0.1}O_2$). Since Co provides a higher thermal conductivity, a better thermal stability, and a longer cycle life to the NCM, a high Co formula has been chosen when the NCM cathode came to the market. In recent years, the high price and ethical problems of cobalt have driven the manufacturers and scientists to develop NCM batteries with a low Co content. High nickel NCM cathode (Ni element more than 0.6) especially NCM811 has been popular due to the low cost. Although high nickel formulations provide high energy density, it causes a decrease in cycle life and thermal stability.

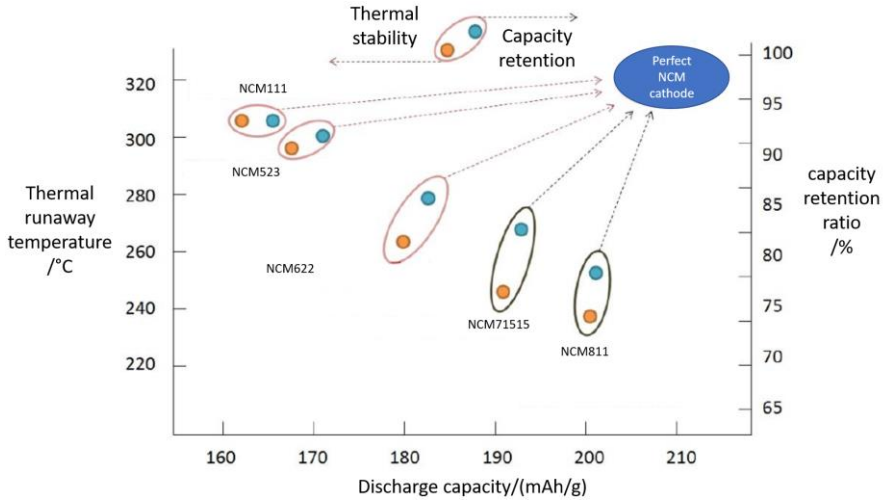

Figure 8 Property of NCM cathode based on different formulation [41]

When it comes to NCA batteries, Tesla is always mentioned. The commercial NCA battery has a high energy density of 250Wh/kg, with 5wt% of Co at the early development stage. In contrast, the commercial low-nickel NCM111 battery only has 220Wh/kg with higher Co ratio. Hence Tesla has been using NCA batteries since its first EV Model S [42]. Until 2015, 18650 cylindrical cells (18mm in diameter, 65mm in height) with NCA cathode and graphite anode have been used in Tesla Model S and Tesla Model X. Since 2017, when Model 3 entered the market, the cells are manufactured into a larger size (21700 cylindrical cells). The anode has been changed into silicone-graphite material, which leads to an energy density increase to 300Wh/kg. Including Model 3, Model X, and Model S, Tesla sold 367, 871 EVs, which accounts for 16% of global PHEV in 2019[1]. The company's selection of battery has always

attracted attention. In 2020 Tesla began to use NCM and LFP batteries in its EVs manufactured in China. This change was because of the local production policy and the technology evolution of NCM battery and LFP battery. The technical barrier of NCA battery resulted in that production of NCA battery in China is not popular. As of 2017, the production of NCA cathode in China was only a few hundred tons, while the production of NCM cathode was 86000 tons, and the production of LFP cathode is 55000 tons [43]. The high nickel NCM battery also achieved an equivalent energy density to NCA battery [44]. Previously the LFP battery was only applied to electric buses or cheap EV models, the energy density at the cell level was only 2/3 of the NCM811 and NCA batteries. Fast charging cannot be applied to LFP battery as the cathode has only 1% of the conductivity of the ternary LIB. Still, mainly the high cobalt price has been driving the change to the LFP battery. As of 2019, the pack level cost of LFP battery was calculated to be $94/kWh while the cost of NCM811 battery was 23% higher with $116/kWh (based on model developed by Everbright securities for batteries produced by CATL [45]).

Table 2 Battery chemistry and cooling method of commercial electric vehicles（Vehicle class：Class A: Microcars, Class B: Superminis, Class C: Small family vehicles, Class E: Executive cars, Class S: Sports cars, Class J: 4 wheel drive (4x4) vehicle. Battery Type: Ni-Mh: Nickel-metal hydride battery，NCA-LIB with $LiNiCoAlO_2$ cathode, NCM-LIB with $LiNiMnCoO_2$ cathode, LFP-LIB with $LiFePO_4$ cathode）

Country	Model	Class	Battery chemistry	Battery capacity/kWh	Battery thermal management method
Japan	Toyota Prius	C	Ni–MH	4.4	Air cooling
	Nissan Leaf	C	LMO	24	Air cooling
	Mitsubishi Outlander PHEV	J	NCM	12	Liquid cooling
USA	Chevrolet Volt	C	NCM	16	Air cooling
	Ford Focus BEV	C	NCM	23	Liquid cooling
	Tesla Model 3	C	NCA	50/62/75	Liquid cooling
	Tesla Model S	E/S	NCA	75/100	Liquid cooling
	Tesla Model X	J	NCA	75	Liquid cooling

Germany	Mercedes s400	E	NCM	70	Direct cooling
	BMW i3	B	NCM	33	Liquid cooling / Direct cooling
	Audi A6 PHEV	E	NCM	14.1	Direct cooling
France	Renault ZOE	B	NCM	44	Air cooling
China	Geely Dorsett EV	C	NCM	45.3	Liquid cooling
	BYD e5	C	LFP	47.5	Air cooling
	BYD Song DM	J	NCM	16.9	Liquid cooling
	JAC iEV6E	A	LFP	33	Air cooling
	JAC iEV7S	J	NCM	39	Liquid cooling
	BAIC EC180	A	NCM	20.3	Air cooling
	BAIC EX260	J	NCM	38.6	Liquid cooling
	SAIC Roewe eRX5	J	NCM	12	Liquid cooling
	SAIC Roewe e950	E	NCM	12	Liquid cooling
	GAC Trumpchi GS4	C	NCM	11.6	Liquid cooling
	GAC Trumpchi GA5	C	NCM	13	Liquid cooling
	NIO ES8	J	NCM	70	Liquid cooling

2.1.2. Physical shapes of lithium-ion batteries

A battery consists of a positive electrode, a negative electrode, an electrolyte which allows lithium-ion diffusion, a separator to separate the positive and negative electrodes, and a current collector. As illustrated in Figure 9, during charging, electrons move to the anode and lithium ions pass through the separator and accumulate on the anode. The discharging process takes the opposite process.

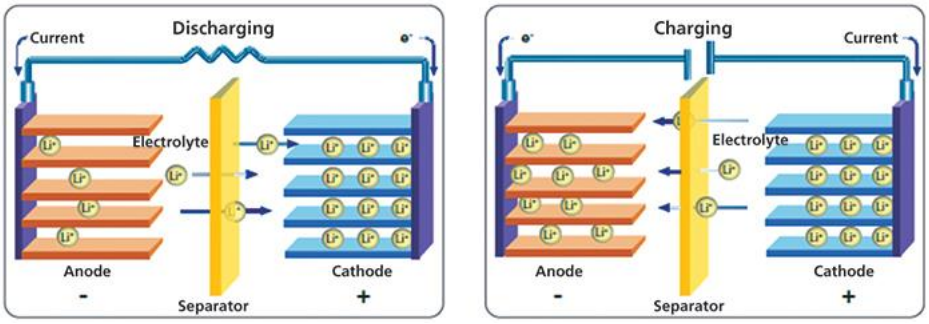

Figure 9 Lithium-ion transport during the battery charge and discharge [46]

Lithium-ion batteries have different shapes, as shown in Figure 10, and they can be divided into cylindrical, prismatic, and pouch cells. All these lithium-ion batteries have anodes, cathodes, separators, electrolyte, and battery housings, although they differ in the configuration and manufacturing process. Both the cylindrical and prismatic cells consist of single sheet anode/cathode/separator, and the electrodes and separator of pouch cells are pre-cut separated sheets. The manufacturing of the cylindrical cell involves the rolling of the anode/cathode/separator sheets into a cylindrical shape, whereas that of prismatic cells include rolling and pressing to the prismatic shape, and the pouch cell compounds are stacked onto each other. The material assembly process follows with the tab welding process when the electrodes of the three types of cells are connected. The housing of the pouch cells is different from the cylindrical and prismatic cells, as the pouch cells packaging are made of polymer-aluminium foils while the housing of the other two types is made of aluminium plate. During the electrolyte filling process, the pouch cells require extra care as the batteries need to be vacuumed. An addition bag is also attached to the pouch cell, which is used to gather the gas generated during the battery formation process, and the additional will be removed later.

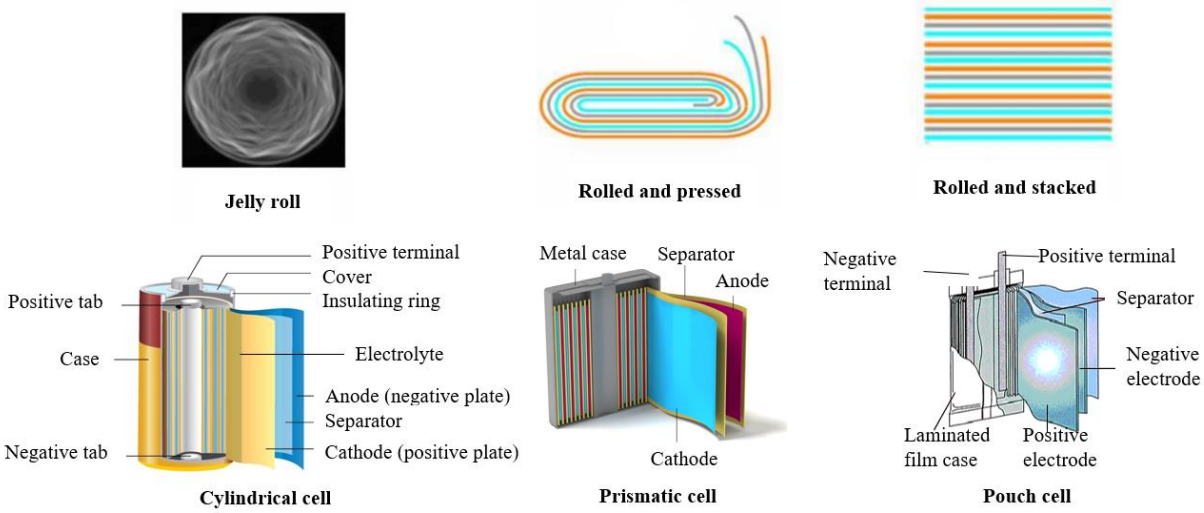

Figure 10 Different types of lithium-ion batteries[47–49]

Apart from the configuration and manufacturing process, the application, cost, durability, and size of the three types of batteries are different. Ciez and Whitacre [50] concluded that cylindrical cells have a cost advantage, mainly due to the economics of scale. Prismatic and pouch cells are believed to have more potentials of cost reduction as it has a larger size.

The commercial cylindrical cell was first developed by Sony in 1991, which was led by Yoshio Nishi [51]. They are largely used as laptop batteries and traction batteries of Tesla EV models. The advantage of the cylindrical shape batteries are the high consistency, durable cases, and low manufacturing cost, and the disadvantage of the cylindrical cells is the low volumetric energy capacity due to the gap between the cylinders. The cylindrical cells in module and pack level do not allow the replacement of the single dead cells, but the entire modules, which is a costly procedure. In use, all the cells need to be well managed and monitored, as the failure or overheating of one single cell could bring problems to the whole battery system, including short circuit and thermal runaway. Tesla has developed an advanced battery management system to manage the batteries in many aspects. All the single cells are in contact with ribbon-like cooling tubes where coolant circulates to remove the excess heat from the battery or warm up the battery when necessary. In precaution of single battery failure, all the cells are welded with fuse once a cell shorts it will disconnect from the module. However, to achieve the safety measures, the manufacturing of the batteries is a sophisticated process. Tesla used the industrial robot to accomplish the assembly and welding of the battery module while the technology has not been seen in other battery pack manufacturers [52]. Pouch cells with high energy density

and low-cost packaging have been widely used in mobile phones. The use of polymer materials in the packaging also makes the battery relatively lightweight compare with other types. The battery can be made into shapes different than the square, which could make full use of the space when it is limited. Apple used a single L shape pouch cells in the iPhone XS to maximize the use of the room [53]. Pouch cells are not applied in the EV industry yet. General motor plans to use large-format pouch cells which provides the flexibility of battery layout in its next-generation EVs [54]. Pouch cells are also considered to be a cost-effective battery packing type as it can be produced in large size. The downside of the pouch cells is the fragility of the casing. To properly use the pouch cells, any stress including vibration, squashing, and warping on the cells are not allowed. The prismatic cells are the most widely used batteries in EV, and durable cases and high energy density make them popular on the market. The prismatic shape allows a high flexible module design for different requirements. Due to its large size, thermal management of prismatic cells is difficult.

2.1.3. Energy efficiency of lithium-ion batteries

Battery performance is usually evaluated in terms of the specific energy (Wh/kg), energy density (Wh/L) and energy efficiency (EE, %). Current research on lithium-ion battery has focused on the improvement of rate capability. Commercial lithium-ion batteries have a high specific energy of 224-263Wh/kg and energy density of 659-741Wh/L [55,56]. The post lithium-ion batteries (PLIBs) which are still at research stage can achieve 700Wh/kg with Bismuth-based anode [57], or even higher 1375Wh/kg with Li_2S cathode [58].

However, practical energy density which measured under actual working condition would exhibit a significant decrease, compared with specific energy density. Li-S cells which were previously developed by Sion Power Corporation could only achieve 550Wh/kg with low discharge rate [59]. Such difference is caused by the existence of EE, which is consists of the Coulombic efficiency (CE) and the voltage efficiency (VE) [60]. The EE is defined as

$$\eta_{EE} = \eta_{CE} \cdot \eta_{VE} \tag{1}$$

where CE is defined as the efficiency with which the charge is transferred in the battery facilitating an electrochemical reaction:

$$\eta_{CE} = \frac{Q_{discharge}}{Q_{charge}} \tag{2}$$

where Q is the electric charge.

and the VE is defined as the ratio of the average discharge voltage to the average charge voltage：

$$\eta_{VE} = \frac{V_{discharge}}{V_{charge}} = \frac{U-V_p}{U+V_p} \quad (3)$$

where V is the operation voltage, U is the open-circuit voltage, V_p is the voltage change caused by polarization.

Commercial lithium-ion batteries with NCA or NCM cathode have near to 100% of CE [61]. With graphite anode, the CE of the battery is reduced only on the first discharge cycle due to irreversible reactions. The irreversible reactions cause the formation of passivating film or solid electrolyte interface on the graphite [62]. After the first discharge, if the CE of the cell is not exactly 100%, the causes could be parasitic reactions which are associated with solid electrolyte interface growth, electrolyte oxidation, transition metal dissolution and positive electrode damage of the lithium-ion battery [63]. PLIBs suffer from low CE, while multiple methods can be used to eliminate the unwanted process and improve the CE to near 100%. Sun et al. [57] reported that the Li_3PO_4 battery with graphene-coated $BiPO_4$ anode could achieve 99.88% of CE efficacy at 500 cycles. Yao et al. [64] reported a lithium-ion battery with silicon hollow nanosphere anode could achieve 99.5% CE. Yang et al. [58] increased the CE of Li_2S from 80% to 97%, when 1% of $LiNO_3$ were added and with silicon anode.

Improvement of VE is still very challenging, especially under abuse working condition, e.g. under high discharge rate and low temperature. Reduced VE is mainly attributed to the battery polarization, which the process that causes the voltage at the terminals of a battery deviates from its open-circuit voltage. Polarization is strongly associated with the battery internal resistance, which includes the pure Ohmic resistance R_O, the charge transfer resistance R_{CT} and the polarization resistance R_P [65,66]. A typical equivalent circuit model is shown in Figure 11 [67,68]. The battery temperature, the state of charge (SoC) and the current rates affect the internal resistance of the lithium-ion battery.

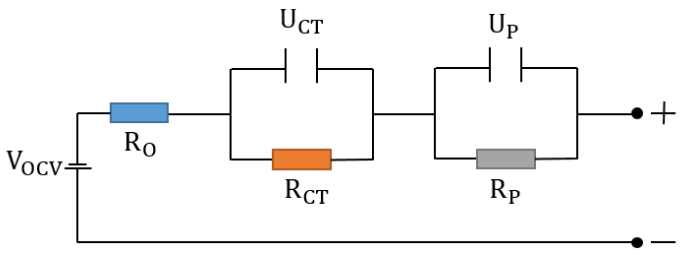

Figure 11 The equivalent circuit model

During discharge, a current pulse is applied, leading to an immediate voltage drop due to the R_O, which comprises electrolyte ionic resistance and electronic resistance. The R_O is affected by temperature, but is independent of the SoC and the current rates [69–71].

The charge transfer resistance R_{CT} is caused by the charge transfer or activation polarization of the reaction at the electrode/electrolyte interface [72]. As the chemical reaction rate depends on temperature, the R_{CT} is temperature dependant, and it substantially increases at low temperatures. Another factor that has an impact on the R_{CT} is SoC. The R_{CT} of the anode reaches the highest at a SoC of 100%, whereas the R_{CT} of the cathode behaves oppositely, namely, the R_{CT} becomes the highest at a zero SoC. As a result, batteries have the lowest R_{CT} when the SOC is at 50% [69,73]. Also, R_{CT} becomes dominant at the very low current rate, especially at low temperatures. Ji et al. [70] found that at -20 °C, the R_{CT} at a 1/1000 C discharge rate is 3 times that at a 1C discharge rate.

The R_P stands for concentration polarization resistance, which is caused by the slow diffusion of solid-phase lithium ions and is usually considered to be a rate-determining step [72]. At an approximately 100% of SoC, the diffusion speed of lithium ions into electrolyte is much slower than electrons into the positive electrode, leading to concentration polarization and a rapidly increased R_P [74]. At a higher current rate, R_P of the positive electrode is even higher and becomes a limiting factor [73,75]. Li et al. observed that the R_P at SoC=50% is lower than that at SoC=100% [76]. At 0% SoC, concentration difference forms again, giving rise to concentration polarization. The R_P is also dependent on temperature, a high concentration polarization at the anode was observed at -20 °C [77].

Jiang et al. [78] studied the effect of SoC, the current rate on the charge polarization behaviour of the LIB. Large polarization was observed. It was found that elevated polarization voltage is linearly proportional to the charge rate. The polarization voltage at initial SoC (0-10%) and final SoC (90-100%) is 2-3 times of the voltage during other stages of charge. Cho et al. [79] quantitatively studied the polarization of a LIB below room temperature and proposed two examples of surface modification and hybridization with an electrochemical capacitor to enhance the low-temperature performance. High cell polarization and lowered power were observed with temperature decrease. The polarization behaviour is more significant under the influence of low operating temperature. From the results of 10s pulse discharge test, the cells were able to remain above the cut-off voltage at 25℃ even under 21C, while at 15, 5 and -5℃ the cell reached the cut-off voltage before 10 s at much lower discharging rates. Meister et al.

[80] investigated different electrode materials for LIBs on a comparative basis concerning their specific energy, discharge capacity, energy efficiency, columbic efficiency and voltage efficiency. The researchers found that silicon/graphite anode with low delithiation potential has the potential to replace current graphite anode. Under increased current rate, the polarization behaviour of the LIB become more significant, hence leads to reduced VE, in turn, to reduced EE. Polarization behaviour is even more significant in PLIBs. Development of a practical lithium-air battery has been a challenge for more than 30 years, mainly due to the large polarization. It leads to low voltage efficiency even under low current rate [81,82].

2.2. Temperature effect on lithium-ion batteries

2.2.1. Heat generation mechanism

Lithium-ion batteries are essentially electrochemical systems, and complex electrochemical reactions occur during the charge and discharge process. The lithium ions intercalate and deintercalate on the contact surface between the electrode and the electrolyte, and release energy. The internal electrochemical reaction is as follows (the cathode material used in the example is LFP）:

Positive

$$Li_xFePO_4 \underset{\text{discharge}}{\overset{charge}{\rightleftharpoons}} Li_{x-z}FePO_4 + zLi^+ + ze^- \quad (4)$$

Negative

$$Li_yC_6 \underset{\text{charge}}{\overset{\text{discharge}}{\rightleftharpoons}} Li_{y-z}C_6 + zLi^+ + ze^- \quad (5)$$

In equation (4), x represents the mole stoichiometry of lithium in lithium iron phosphate; y in equation (5) represents the mole stoichiometry of lithium in the graphite (C_6) structure; z represents the moles of lithium ions participating in the electrochemical reaction.

According to the theory proposed by Newman et al., the heat generation of lithium-ion batteries includes ohmic heat, polarization heat and reaction heat [83].

Bernardi et al. [84] have discussed the thermodynamic energy balance of lithium-ion battery in detail. The irreversible heat is mainly caused by cell overpotential [85,86]:

$$q_{ir} = I(U - V) \quad (6)$$

where I represents the operating current of the battery, U and V represent the open-circuit voltage and battery operating voltage, respectively. The cell overpotential $U - V$ is governed by internal resistance R, which includes the pure Ohmic resistance, the charge transfer overpotential, and mass transfer limitation. It can be further described as:

$$q_{ir} = I(V - U) = I^2R \tag{7}$$

The reversible heat is due to entropy change. The occurrence of the entropy change strongly relates to the lithium ions in the electrodes. As indicated from previous research, it could be due to the disorder of the ions in the electrode crystal [87], or the molar entropy change in the process of lithium intercalation [88]. Usually, in the fast charge and discharge conditions, the reversible heat is much smaller than the irreversible heat [89]. The occurrence of the entropy change strongly relates to the lithium ions in the electrodes. The part of heat due to entropy change can be expressed as:

$$q_r = \frac{d}{dt}T\Delta S \tag{8}$$

where T is the battery operating temperature, ΔS is entropy change. The potential derivative often referees the entropic heat coefficient or temperature coefficient concerning temperature. Hence the following equation can be yielded:

$$q_r = IT\frac{dU}{dT} \tag{9}$$

where $\frac{dU}{dT}$ is the entropy coefficient, which is related to density, state of charge (SoC) and battery temperature. A simplified equation which expresses the heat source in the lithium-ion battery can be defined as follows:

$$q = I^2R + IT\frac{dU}{dT} \tag{10}$$

where heat from mixing is ignored as the commercial battery has good transport properties. Also, the phase change is dismissed as all the species in the battery has the same phase.

2.2.2. Temperature effect on battery lifetime

When the LIB is charged or discharged under unwanted temperature, battery ageing is one the drawbacks. The best operating temperature range of the battery is between 20°C and 50°C, within which the maximum power capacity and acceptable ageing speed can be achieved [90]. At high operating temperature, although good battery performance can be achieved, the reaction rates of many other unwanted reactions are also improved. Those reactions accelerate

the failure of the battery system and cause battery ageing. When cycling under higher temperature, the anode surface will have a constant formation of thin films, thereby accelerating the rate of lithium loss. Meanwhile, the resistance at the negative terminal has also increased significantly. With time the capacity of the battery cell is significantly decreased [91]. Kuper et al. revealed that between 50°C and 60°C, the power capacity of lithium-ion batteries increases with increasing temperature. The temperature range can effectively prevent battery ageing and ensure that the cell temperature is within a safe range [92]. Figure 12 illustrates battery calendar degradation at different temperatures. After five years of operation, the remaining capacity of the battery at 15 ℃ can be 1.5 times of the battery at 55℃. Ramadass et al. [91] concluded that the capacity fade of 18650 lithium-ion battery at elevated temperature comes from three parameters: rate capability loss, primary (Li^+) and secondary ($LiCoO_2$/carbon) active material losses. At high temperature, a repeated film formed on the anode, and it led to the increased rate of lithium ion loss and increased cathode resistance. Vetter et al. [93,94] summarized the mechanisms of capacity degradation and power loss due to battery ageing. Waldmann et al. [95]studied the temperature effect on the ageing and performance of lithium batteries in the range of -20℃ to 70℃. The results showed that when the temperature is lower than 25℃, as the temperature decreases, the ageing speed of lithium batteries increases. When it is higher than 25°C, the temperature increase will also aggravate the battery ageing.

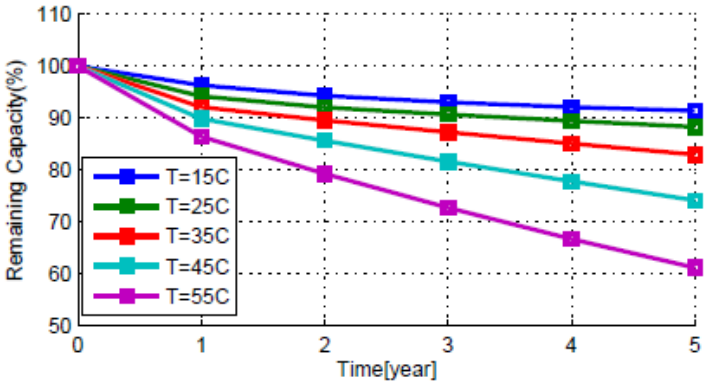

Figure 12 Capacity degradation at different temperatures [96]

Non-uniformity of temperature within both the single battery and the battery pack can also cause a localized deterioration, which will accelerate the battery ageing and reduce the cycle life of the battery [97]. When the different cells of the battery pack are at different temperatures, the characteristics of each cell is slightly different during each charge and discharge cycle, which results in a difference in the SoC. This difference will gradually increase as the battery

cycles. With high temperature difference within the cells, the rate of capacitance loss could be severe [98]. Gogoana et al. experimentally studied the influence of the inconsistency of the internal resistance on discharge. Results showed that internal resistance is very susceptible to temperature [99].

Both high and low temperatures will have a severe impact on the performance of lithium batteries. Temperature nonuniformity will also cause the capacity difference of singles cells and eventually affect the pack performance. To improve the electrochemical performance, extend the service life of the battery, and maintain the power performance at a high level, it is essential to design a BTMS that can reasonably and effectively control the temperature.

2.2.3. Temperature effect on battery performance

The battery is essentially an electrochemical system. The Arrhenius equation (Eq.11) defines the relationship between the operating temperature and the rate of the battery system [100]. It can be told that the rate constant increases exponentially when the active temperature increases, as the rate of the chemical reaction doubles for every 10 degrees rise in temperature. Hence, the battery system is sensible to operation temperature.

$$k = Ae^{-E_a/RT} \tag{11}$$

where k is the rate constant, A is a constant that defines the rate due to the frequency of collisions between modules, e is a mathematical constant, E_a is the activation energy for the reaction, R is the universal gas constant, T is the absolute temperature.

At lower temperatures, the performance of lithium-ion batteries is significantly reduced. According to the Nernst equation, OCV is strongly related to temperature [101]. Under low temperature, the OCV will significantly decrease, which affects the battery power and usable capacity. The high resistance and low ion diffusion rate at the anode/electrolyte interface will reduce the energy and power of the battery at low temperatures. Battery capacity will irreversibly lose at low temperatures. Zhang et al. [102] investigated the charge and discharge characteristics of a commercial 18650 lithium-ion battery. The results showed that the discharge power is significantly reduced with the decrease of temperature, and the discharge power is entirely lost at -10 °C. The discharge energy of the battery also decreased with increased power, significantly below 10 °C. However, the battery is still able to deliver high power at low temperature.

In the early stage researches, it was pointed out that the electrolyte is the main factor affecting the performance of lithium batteries [103]. The electrical conductivity of the solution decreases as the temperature decreases, hence in a cold environment, the mobility of lithium ions is suppressed, resulting in a significant increase in internal resistance [104]. Therefore many research on electrolytes focuses on the development of electrolytes with low freezing point and high ionic conductivity, which suits the low-temperature environment [105–107]. Shiao and Smart et al. [108,109] investigated a series of low-temperature lithium-ion electrolytes, with anode and cathode being the mesophase carbon microspheres and $LiNiCoO_2$, respectively. The authors performed a characterization on battery discharge behaviour under different rates (C/100 to 3C) in a wide temperature range (+30 ~ -70℃). The results showed that all carbon-based electrolytes have excellent electrical conductivity under low temperature.

Some researchers believe that high charge transfer resistance (R_{CT}) is the main factor which suppresses the lithium-ion battery performance [104,110,111]. Zhang et al. [112] investigated the battery system containing $LiBF_4$ or $LiBF_6$ electrolyte. When the environment temperature dropped below -20°C, the R_{CT} increased significantly. The R_{CT} is also largely affected by the SoC of the battery. Under low temperatures, the charging process of lithium-ion batteries is more problematic than the discharge process. The main reason for the poor performance of lithium-ion batteries at low temperatures was attributed to the problematic diffusion of lithium ions into the carbon anode. A later study Zhang et al. [113] investigated lithium-ion diffusion coefficient of lithium-ion batteries at low temperature. When the temperature is under 0℃, the lithium-ion diffusion rate is significantly reduced. The lithium-ion diffusion rate in delithiated graphite (discharge process) is lower than that of lithiated graphite (charge process). Hence under low-temperature charging is much more complicated than discharging.

2.2.4. Battery fires in electric vehicle

As shown in Figure 13, at low operating temperature, the reaction rate of the battery system is reduced. It leads to reduced current and affects the charging and discharging cycle. Meanwhile, the plating of metallic lithium occurs on the negative electrode. It can cause irreversible damage to the battery. At extremely low temperature, the cathode of the LIB can break down and causes a short circuit. Elevated battery temperature increases the reaction rate that causes a further increase in temperature, leading to a destructive result. Thermal runaway occurs spontaneously once the temperature of the battery is over 80℃. The solid electrolyte interface (SEI) film close to the carbon electrode tends to decompose when the temperature is between 90 ~120 ℃. When

the temperature exceeds 120℃, the decomposed SEI film will not be able to protect negative materials. It will react with electrolyte and produce combustible gas. With the temperature increase, the polyethylene (PE) separator also starts to melt. Decomposition of positive material occurs between 150~ 310℃, and oxygen is produced from the reactions. At 200℃, the electrolyte will decompose and produce combustible gas. With the temperature increases to 240~ 350℃, as the SEI film is decomposed at the temperature, the binders begin to react violently with the lithiated graphite and produce a lot of heat (1500J/g from [114]). Along with the air expansion due to heat generation, the produced combustible gas and oxygen will react and cause fire and explosion [115]. Eventually, the aluminium current collector and the case will melt. Hence battery operation under harsh temperature environment is hazardous for large LIB packs and affect the battery life and safety.

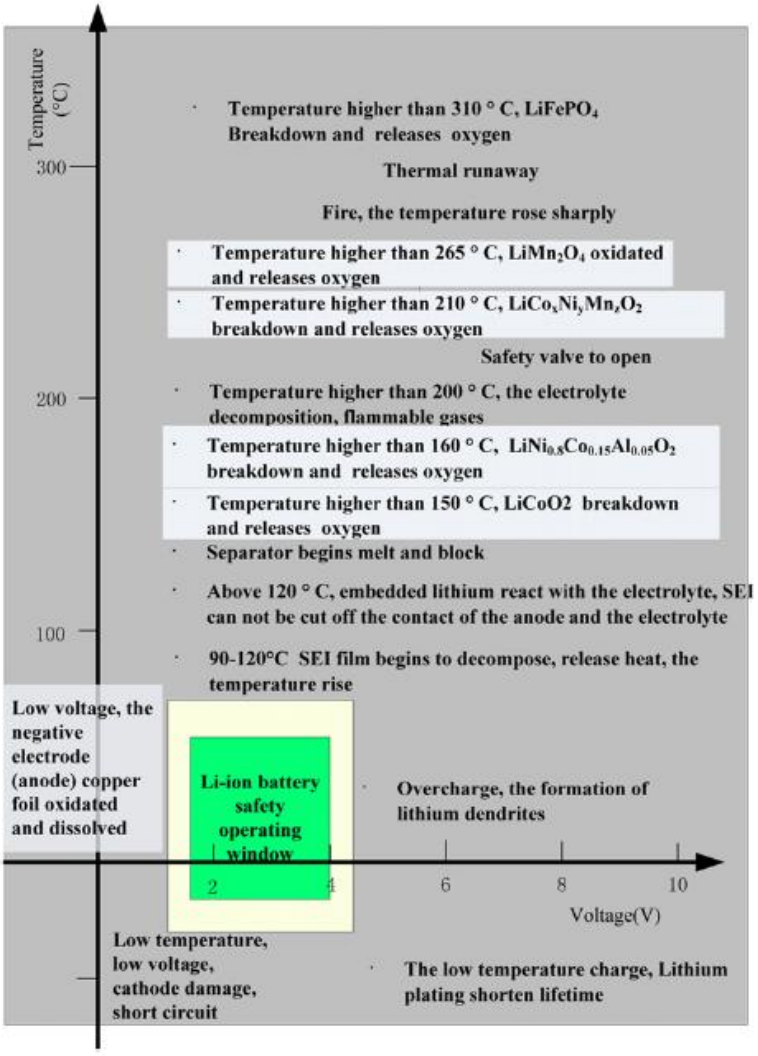

Figure 13 Reactions inside NCA battery under different operation environment [115]

EV now is not only a symbol of green transport, but also represents the extraordinary driving experience with excellent acceleration and advanced driver-assistance system. However, the safety of the EV is still less mature than the internal combustion engine vehicles. The PHEV sale was 2.2 million in 2019 accounts for 2.5% market share [1]. With the increase of EV deployment, fire accidents have been increasing in recent years. For most of the PHEV, especially self-ignition accidents, the fire starts in the powertrain, namely the battery pack. Table 3 listed some of the PHEV fire accidents since 2005. The causes of accidents are varied. It could be (1) loose cable connection (2) short circuit because of battery deformation in collision (3) short circuits because of worn wires (4) overcharged battery as the consequence of the failure of the battery management system. Although the fire accidents are not always related to battery, the vulnerable nature of the LIB makes people associate the accident with battery malfunction/damage. In some cases, the battery pack is not the cause of the fire, but it might be ignited later and become the major fuel to feed the fire.

Table 3 PHEV fire accidents since 2005 [116–121]

Number	Date	Location	Accident	Cause
1	2008.06	Columbia, United States	Toyota Prius (PHEV) with modified lithium-ion battery pack caught fire on the highway.	Loose bolt connections cause the battery to overheat
2	2011.05	Burlington, United States	A Chevrolet Volt (PHEV) caught fire after undergoing a side stick impact test and destroyed nearby vehicles	The side impact damaged the cooling system and the battery module, and the leakage of conductive coolant caused a short circuit and ignited the combustible gas leaking from the battery
5	2013.10	Seattle, United States	Tesla Model S (BEV) ran over large metal objects on the highway	The battery pack is penetrated and deformed by a metal object, causing

				a short circuit, and igniting the battery
6	2015.04	Shenzhen, China	Wuzhoulong electric bus (BEV) caught fire while charging in the garage	Battery thermal management system failed during the charging, and the battery pack was overcharged
8	2016.01	Jelsta, Norway	Tesla Model S (BEV) caught fire while charging at a supercharger station	Short circuit when charging
9	2016.04	Shenzhen, China	Wuzhoulong electric bus (BEV) caught fire	Short circuit caused by worn wire
10	2016.06	Beijing, China	JAC IEV5 (BEV) caught fire	Battery pack overheating caused by loose wire connections
11	2018.03	Bangkok, Thailand	Porsche Panamera (PHEV)	Charging cable plugged to socket in the living room without built-in safety systems
12	2019.04	Shanghai, China	Models S (BEV) caught fire spontaneously	Battery short circuit
13	2019.06	Wuhan, China	KIA Kona Electric (BEV) caught fire spontaneously	Battery explosion without knowing the cause
14	2019.08	Sejong City, Korea	NIO ES8 (BEV) caught fire spontaneously	Wear out of the sensor wiring cause short circuit
15	2020.05	Changsha, China	Li Xiang one (PHEV) caught fire	Protective pad ignited by the exhaust pipe

	spontaneously when driving

Fire accidents of EV always attract attention. Due to the large sale number, Tesla EVs account for a large portion of fire accidents. From 2013 to 2019, it was counted by the media that Tesla has at least 20 reported incidents [122]. Fire accidents are worldwide, especially in the United States, European countries (Figure 14a), Mexico, and China. In March 2017, two Model S at the Shanghai Jinqiao Tesla Super Charging Station caught fire (Figure 14b). The fire was caused by "voltage instability" which caused one of the cars to catch fire, which subsequently caused another car next to it to be burnt down as well [123]. One month later, a Model X caught fire and exploded after a collision in Guangzhou, China. In January 2018, another Tesla in Chongqing, China spontaneously combusted due to battery quality, without charging or collision (Figure 14c) [124]. Tesla uses battery packs consisting of more than 8000 cylindrical 18650 batteries, which are placed on the chassis of their vehicles. If the car collides, there is a high chance that the battery pack is hit. It will cause the deformation of the pack and cause a short circuit, and eventually cause the battery to catch fire. Also, to reduce weight and cost, some Model S and Model X models removed the insulation layer outside the battery module, which increases the possibility of spontaneous combustion of the battery pack during charging or after a collision. Although Tesla vehicles have the most advanced battery management system in the market, the large number of batteries will inevitably lead to inconsistent battery attenuation. The inconsistency of battery capacity will form a circulating current inside the battery pack, accelerate the loss of the battery, and cause it to self-discharge. It will further lead to higher circulation and reduce battery pack capacity. With its EP9 model set the record the fastest lap by an electric vehicle for some Grand Prix circuits, NIO has been one of the most popular EV manufacturers. In 2019 NIO's ES8 has several spontaneous combustion accidents (Figure 14d) and the company has recalled 4803 ES8 models [117]. The voltage sampling sensor wiring of the NEV-P50 battery modules on the NIO ES8 has been continuously squeezed by the upper cover plate, causing the insulation material to wear out. In extreme cases, it causes the wiring harness insulation layer to burn and cause the battery pack thermal runaway.

Figure 14 (a) Austria (2017) Tesla Model S, battery short circuit due to the force deformation of the chassis in a collision, [123]**; (b) Shanghai, China (2017) two Tesla Model S caught fire at a charging station** [123]**; (c) Chongqing, China (2018) Tesla Model S spontaneously ignites due to battery failure** [125]**; (d) Shanghai, China (2020), NIO ES8 caught fire at charging station** [117]

Although it was claimed by EV manufacturers that EV is ten times less likely to experience a fire than a gas car [122], it is more difficult to put out an EV fire mainly because of the battery. Ordinary foam or dry chemicals would not work, and it could require 9 tons of water to extinguish the fire [5]. Even worse the EV could reignite after the earlier fire extinguished. The accumulated heat in the battery pack could not fully dissipate hence the EV that has experienced fire needs to be kept away from any objects for a few days. If the whole vehicle is fully immersed into a water tank, the fire can be fully extinguished, which makes the fire extinguishing much more difficult. In a rare case, a BMW i8 was dumped into a huge tank with 13 tons of water for 24 hours to make sure the vehicle could not catch fire again [126]. A guide from Tesla pointed out that immersion of the EV into water tank is necessary.

With increasing demand on the driving range, charging speed and vehicle performance of EV, the power and capacity of the battery pack is increasing. The trend will last until the next generation batteries with significantly improved energy density and safety become available on the market. According to the analysis, the most promising full solid-state battery will not have commercial application in the EV market until 2030 [8,9]. The only solution to have a safe and long-life battery pack is the battery management system (BMS), with the BTMS to be one of the core functions. The BMS is the safety control system which manages the individual cells of a battery module and the entire battery pack. It involves voltage, current and temperature monitoring of the cells, state of charge, state of health, state of power, state of energy and state of function estimation and the BTMS module. An efficient BTMS could either be air cooling, liquid cooling, direct cooling, or PCM cooling. In cold areas, the BTMS needs to have a heating method for a comfortable store and start-up of the battery system, which could be PCM heating and PCT/ heating element heating.

Many countries and international organizations have issued mandatory standards for LIBs used in EV, e.g. United Nation standards: UN 38.3, UN R100, International Electrotechnical Commission (IEC) standard: IEC 62133, IEC 63056, IEC 62660.1, IEC 62660.2, IEC 62660.3, International Organization for Standardization (ISO): ISO16750.1, ISO16750.2, ISO16750.3, ISO16750.4, ISO16750.5, Institute of Electrical and Electronics Engineers (IEEE): IEEE1625, IEEE1725, IEEE2030.3, China standards: GB/ T 31484-2015, GB/ T 31485-2015, GB/ T31486-215. All these standards specify the safety, reliability requirement of the LIB and provide test methods of abuse use and short circuit of the battery. However, current standards no matter it is issued by a country or international organization such as IEC/ ISO/ IEEE, they are deficient in specifying the requirement of a generic BMS, especially the BTMS part. The gap needs to be understood, and more complex standards and test methods can be then proposed. In this way, the battery system can be properly handled through the lifetime and reduce the risks and hazards. Cell temperature monitoring should be part of the BMS function, so once the cell temperature is above 40 ℃ or below 20 ℃, BMS can actuate BTMS control and send cooling/ heating request.

2.3. Commercial battery thermal management systems

2.3.1. Battery cooling systems

Table 2 listed the BTMS of the EVs with different classes, battery capacity, battery chemistry and from other manufacturers. There are three types of commercial BTMSs: air cooling, liquid cooling, and direct cooling.

Air cooling BTMS uses air to remove the heat generated from LIB. As shown in Figure 15, it has a simple structure hence is advantageous in cost. It is commonly used in the early stage EV models, as previously EV models use LIBs with less active chemistry, e.g. nickel-metal hydride battery (Ni-MH) and LMO. Currently, most electric busses and some EV models from Japanese/ Korean manufactures such as Honda Insight, Toyota Prius, Nissan Leaf and Kia Soul EV uses this type of BTMS. However, the air-cooling method has its inherent limitation of low convective heat transfer coefficient, which limits its application. Studies have shown that under stressful conditions, i.e. at high discharge rates or high ambient temperatures, air cooling is not efficient enough to manage the thermal performance of lithium-ion battery pack [127].

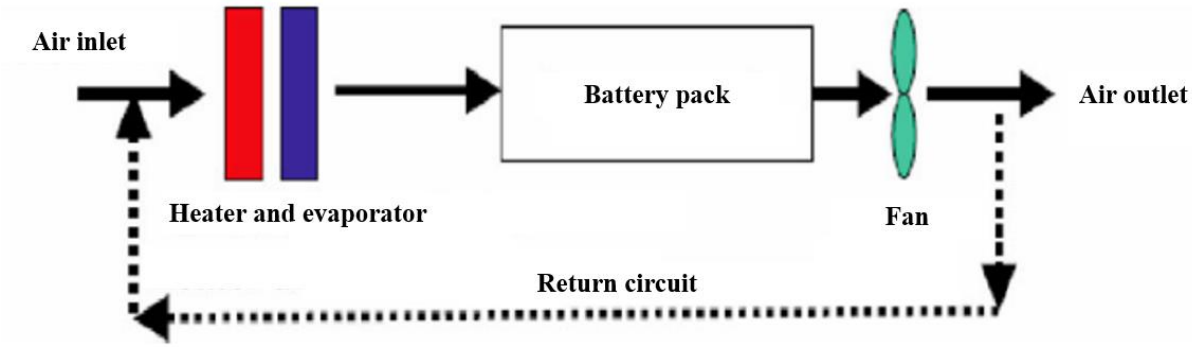

Figure 15 Schematic of air cooling BTMS

As shown in Table 2, most EV models now use more active LIB with NCM or NCA cathode, and they equipped with the liquid cooling method. Liquid cooling BTMS uses heat exchanger and cooling circuit together to remove the battery heat (Figure 16). Comparing with air cooling, liquid cooling method (uses typically 50%/ 50% water/ Ethylene glycol mixture as coolant) has much higher convective heat transfer coefficient. It is capable of cooling LIBs with active chemistry and under high current rate and high operation/ ambient temperature. However, the liquid cooling BTMS has a complex structure, which leads to a relatively large volume and high cost. Conductive fluid should also be avoided if the thermal management system is also responsible for the cooling of AC-DC and DC-DC converter.

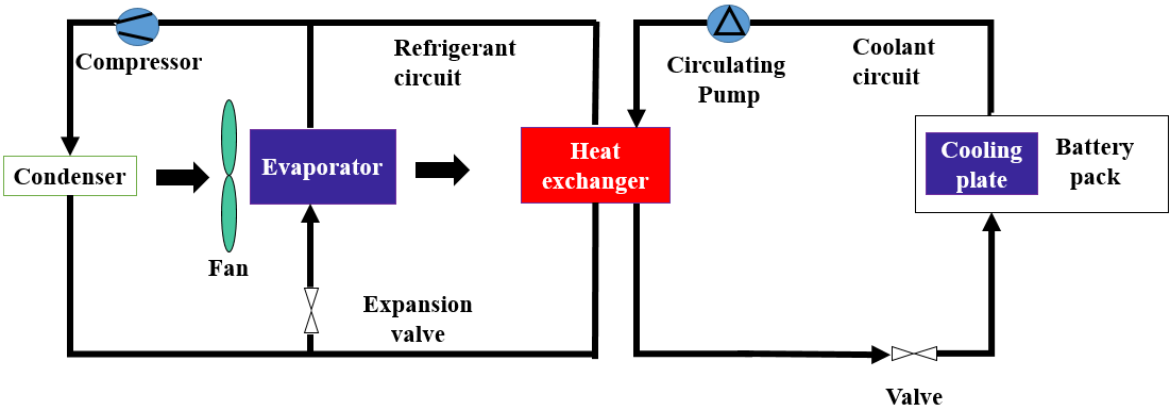

Figure 16 Schematic of liquid cooling BTMS

Direct cooling is another cooling method which now is used in EV models from German manufactures, e.g. BMW i3 and Mercedes S400. It uses the refrigerant (e.g. R134a) to "directly" cool down the LIB. As shown in Figure 17, the refrigerant flows into two branches after it is condensed in the condenser. In one brand the refrigerant will evaporate in the evaporate and provide cold air to the vehicle cabin. In another branch, the refrigerant will take the heat from the LIB in the cooling plate. The two coolant branches will then converge into one loop and condense in the condenser. The disadvantage of this method is it has a long refrigerant loop, and the amount of refrigerant is large, which brings high cost.

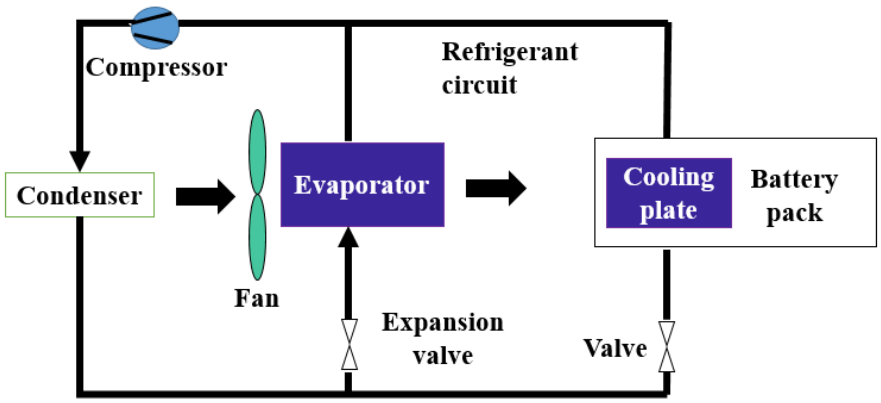

Figure 17 Schematic of direct cooling BTMS

2.3.2. Heating systems

Existing electric vehicle models generally use external battery heating methods, including

convection heating and direct heating methods. Convection heating methods have air convection heating and liquid convection heating. The system design is similar to air cooling and liquid cooling systems, except that the convection heating system is additionally equipped with heating elements. Convection heating is widely supplied in the market's electric vehicle thermal management system. European and American electric vehicle models such as some high-end models of Tesla, Ford Focus Electric Edition, Smart electric drive, and some Chinese electric vehicle models such as NIO ES8 and Weimar EX5 Both are equipped with liquid convection heating systems. Japanese and Korean electric vehicle models such as Nissan Leaf and Kia Soul EV are equipped with air convection heating systems. Direct heating is widely used in cheap models and non-electric car electrification. It uses typically direct polymer PTC heating, which is generally placed on the surface/side of the battery and the battery is heated using power battery power.

2.3.3. Application in electric vehicles

Battery thermal management system is usually a part of the vehicle thermal management system including electric motor cooling system, BTMS and air conditioning system.

Liquid cooling/ heating thermal management systems are used in a variety of models. Figure 18 shows the schematic of the system in Ford Focus electric model. The electric motor three-way valve acts as a thermal switch. When the motor starts, if the motor temperature is within the normal range, the water pump pumps the coolant passes through the DC-DC converter, the electric motor, the heater three-way valve and the electric motor three-way valve, and eventually returns to the water pump. As the coolant continues to absorb heat and its temperature rises, the coolant will additionally flow through the radiator then back to the water pump. For battery thermal management, when the temperature of the lower and upper batteries are above 35 °C, the battery is cooled by another coolant circuit which is further cooled by a cooler. When the battery pack is charged in a cold climate, if the coolant temperature in the battery coolant circuit is lower than 10 °C, the polymer PTC heater starts working. It heats the coolant, which further heats the batteries. The electric motor and DC/ DC converter coolant circuit is linked with the battery coolant circuit. The battery three-way valve allows the coolant in the electric motor and DC/ DC converter coolant circuit to enter the battery coolant circuit during the driving of the electric vehicle, thereby helping to heat the battery. The electric motor and DC/ DC converter coolant is prevented from flowing into the battery coolant circuit when it is over 80 °C, which may cause battery damage or even thermal runaway.

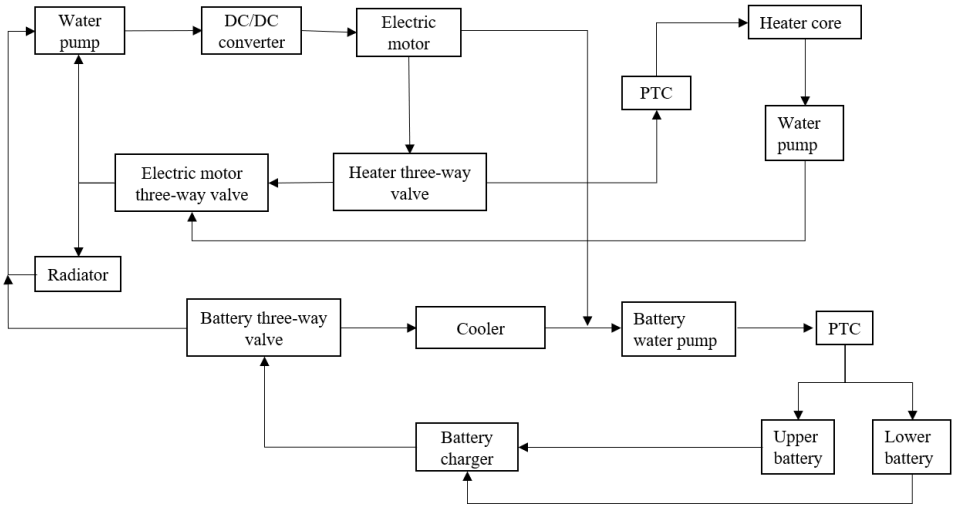

Figure 18 Thermal management system of Ford Focus electric model, single-mode liquid cooling/ heating and waste heat recovery system [128]

As the top-selling pure electric vehicle, Tesla integrates many advanced technologies from different industries, and have developed many novel designs on its cars, especially on the BTMS. As shown in Figure 19, Tesla's BTMS uses liquid cooling and PTC indirect heating method and combines waste heat recovery from its electric motor and electronic systems. Tesla's BTMS can use different operating modes based on component temperature and have better control of battery temperature.

When the thermal management system is in serial mode, in cold weather, the heat generated from the electric motor will be transferred to the battery pack for heating purpose (green line). Some Tesla models, such as the Tesla Model 3, use a technology called “series-parallel control” which can heat the battery pack when the vehicle is undercharging. Its motor starts to rotate and generates heat, the heat is then transferred from the motor stator to the battery pack for preheating. Also, some Tesla models are equipped with PTC heating, which allows heating the battery through heating the coolant first indirectly. When battery exceeds its operating temperature, the chiller in the coolant circuit starts to work, which can reduce coolant temperature. In parallel mode, the coolant circuit for battery temperature control is isolated from motor coolant circuit.

Tesla’s pure electric vehicle uses many high energy density 18650 lithium-ion batteries (up to 7, 140 cells). To maintain battery temperature uniformity, Tesla's BTMS needs to perform efficient thermal management of single cells. As shown in Figure 19 (c) and Figure 19 (d), the

cooling pipes meander through every single cell in the battery pack, and to ensure efficient heat transfer. The cooling pipes have good contact with the battery through flexible fins.

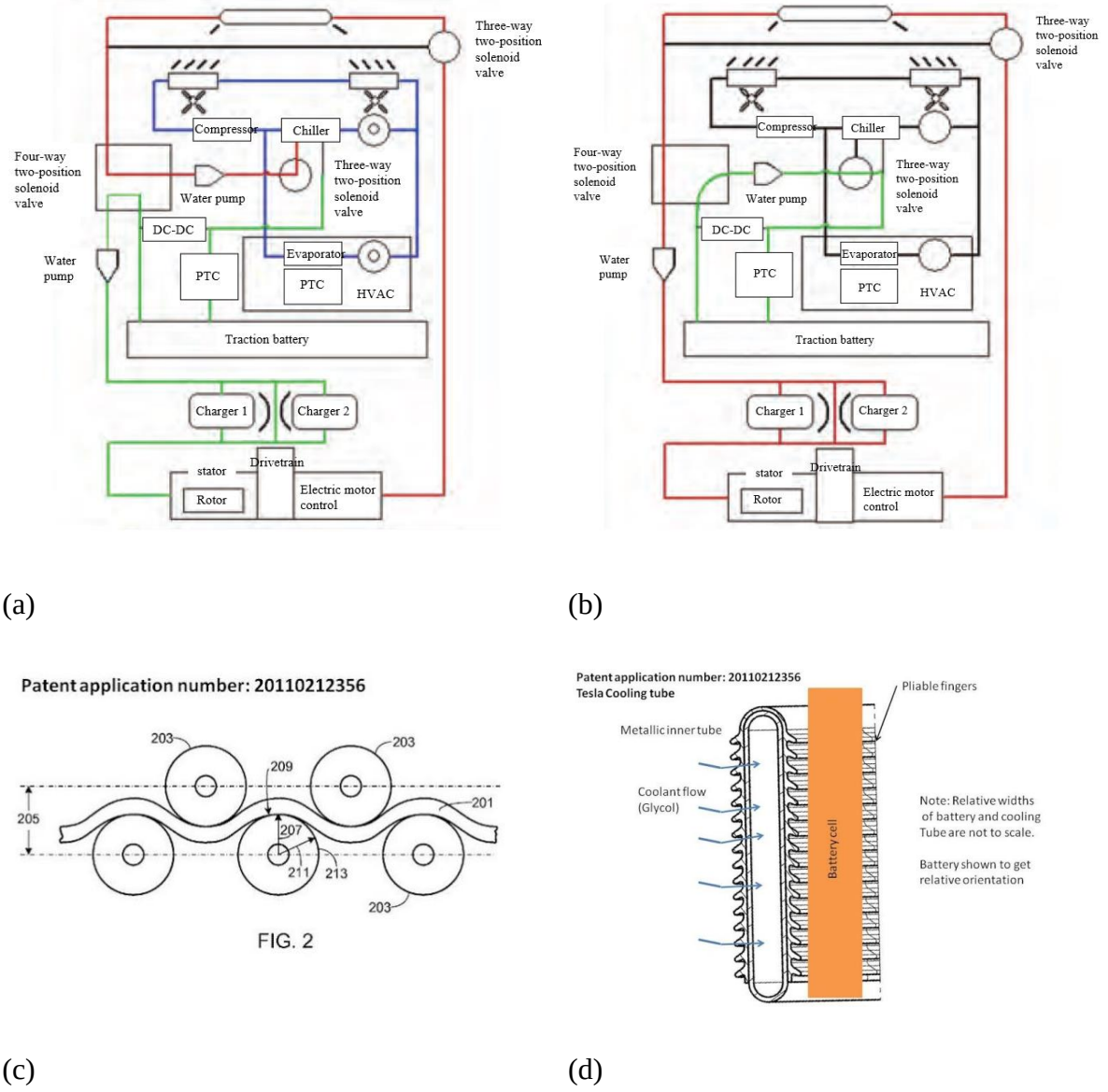

Figure 19 Thermal management system of tesla electric vehicle, dual-mode liquid cooling/ heating and waste heat recovery system (a) Series mode (b) Parallel mode (c) Arrangement of the single cells and the cooling tube (d) Good contact between the single cells and the cooling tube [128,129]

Thermal management system for BMW i3's drive system and battery pack are two independent circulation systems. The system includes a motor controller, DC/ DC converter and the battery charger. The cooling circuit of the motor electronic device is in serial connection with the electric motor's cooling circuit. Different from the BTMS from other models, the battery is cooled directly by the refrigerant, and the refrigerant pipeline is directly arranged inside the

power battery case. In cold weather, the battery is heated by polymer PTC elements which are arranged along the cooling channel.

Figure 20 shows an air cooling and direct heating based BTMS, which was proposed by Hyundai and Kia [130]. In this patented system, the battery pack is cooled by air where the cooling channels are adjacent to the prismatic cells. Heating elements are installed on both sides of the battery pack and is fixed to the battery pack by double-sided adhesive. The temperature sensor is used to monitor the battery temperature. When the battery temperature is low, the heating units on both sides of the battery start to work to heat the battery. When the battery temperature is too high, the air begins to flow, and the battery is cooled through the cooling channels.

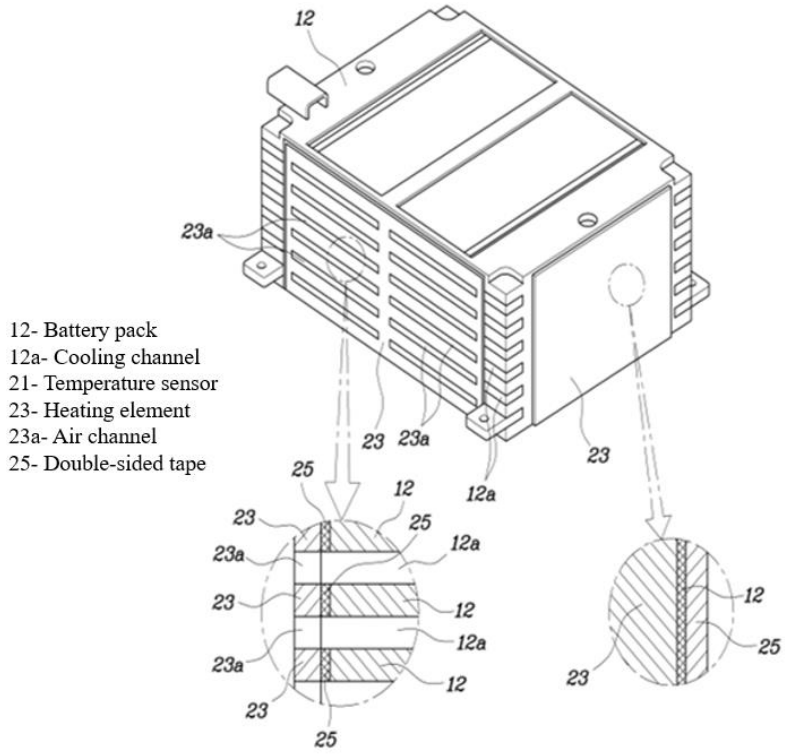

Figure 20 Patented Hyundai / Kia BTMS [130]

Although currently PCM based BTMS is not applied in any EV models in the market, many vehicle and battery manufactures forecast the potential of PCM application in BTMS and filed patents worldwide.

Chinese vehicle manufacture BYD patented design of the battery pack filled with CPCM [131]. As shown in Figure 21, the PCM filled the gap of the battery container to act as a thermal reservoir. The power battery pack is bonded to the base through a thermally conductive

adhesive material, and then the floor is fixed to the chassis. When the battery pack is working, the PCM absorbs the heat generated from the battery pack and conducts it to the container without using any electric power to dissipate heat.

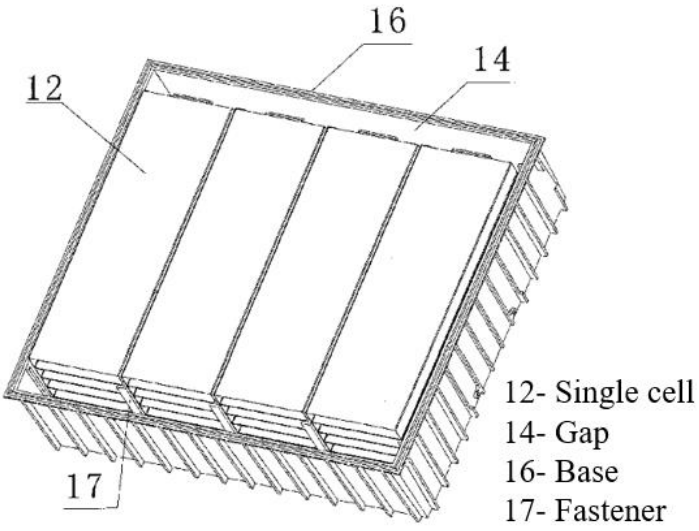

Figure 21 Patented BYD BTMS[131]

General Motors was granted with a patent for a battery pack with PCM cooling, as shown in Figure 22 [132]. The compressible isolator sheets are made of both polystyrene foam and PCM. Hence it can absorb and release the heat generated from the battery.

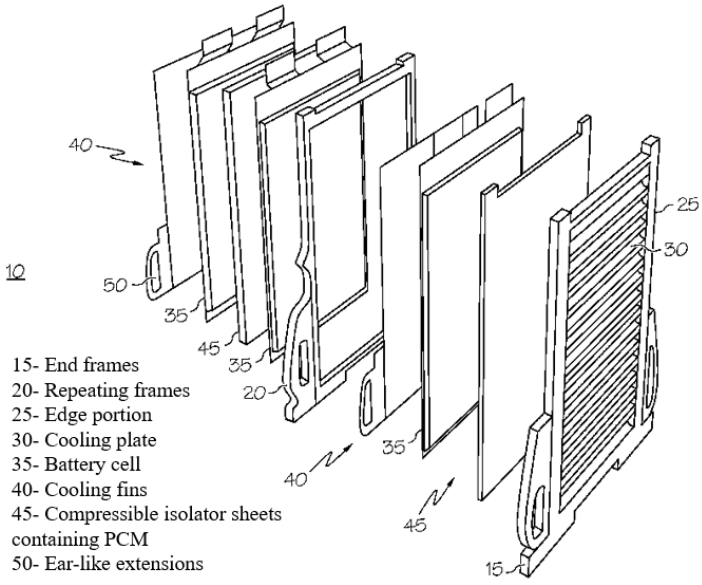

Figure 22 Patented GM BTMS [132]

Midtronics Inc proposed a BTMS for cylindrical batteries with PCMs[133]. As shown in Figure 23, cylindrical batteries with protrusions or fins are surrounded by PCM. The bumps and fins are efficient in increasing the contact area between the PCM and the battery pack.

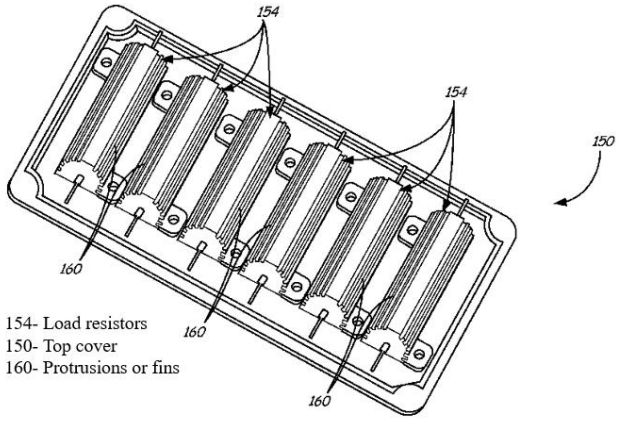

Figure 23 Patented Midtronics Inc BTMS [133]

American company All Cell Tech[134] has commercialized the BTMS based on CPCM and claims that products at difference capacity level from e-bike batteries to grid-connected systems can be provided. As shown in Figure 24, the CPCM is evenly distributed within the gap between the battery pack and the case, the temperature difference between cells can be efficiently controlled between 3-5 ˚C meanwhile the maximum temperature of the batteries can also be maintained at a safe level. The company claims that with PCMs the maximum temperature of the battery pack can be reduced by 15 ˚C.

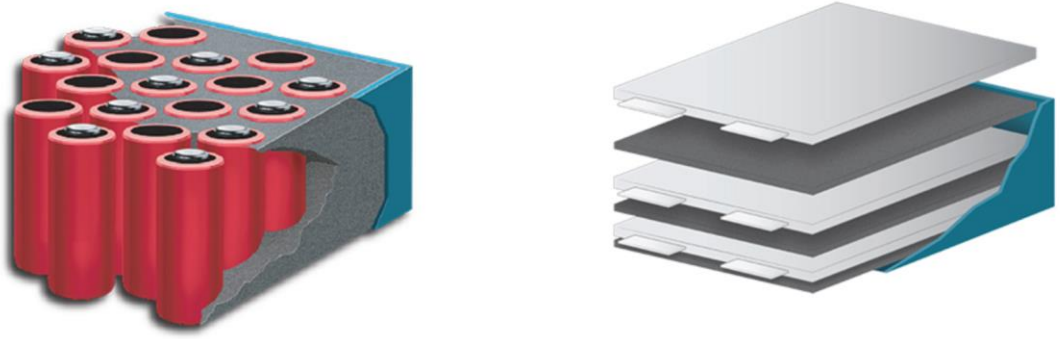

Figure 24 Product from All Cell Tech [134]

2.4. Current research on battery thermal management system with phase change material

2.4.1. Phase change materials and the enhancement materials

The idea of using PCM for BTMS was firstly proposed by Hallaj and Selman [135]. They introduced a mathematical model of the heat transfer between the PCM and the battery in their work. This model adopts the enthalpy equation, and it is described as Eq.12:

$$\nabla \cdot (k\nabla T) + s = \rho \frac{\partial H(T)}{\partial t} \tag{12}$$

where T is the temperature, k is the thermal conductivity, s is the heat generation per volume, ρ is the density, H is the enthalpy and t is the time.

Most PCMs also have abundant source and is not toxic, which is ideal for industrial application. A PCM based BTMS, therefore, has the potential to control battery packs operated in the desired temperature range effectively, while maintaining temperature uniformity within battery cells. PCM based BTMSs usually are designed to have lithium-ion battery pack surrounded by PCM modules/plates. Figure 25 illustrates the designs of the BTMS for standard cylindrical batteries and prismatic batteries. For cylindrical batteries, cells are usually inserted into pre-cut BTMS modules, while for prismatic batteries, PCM plates are sandwiched between the cells.

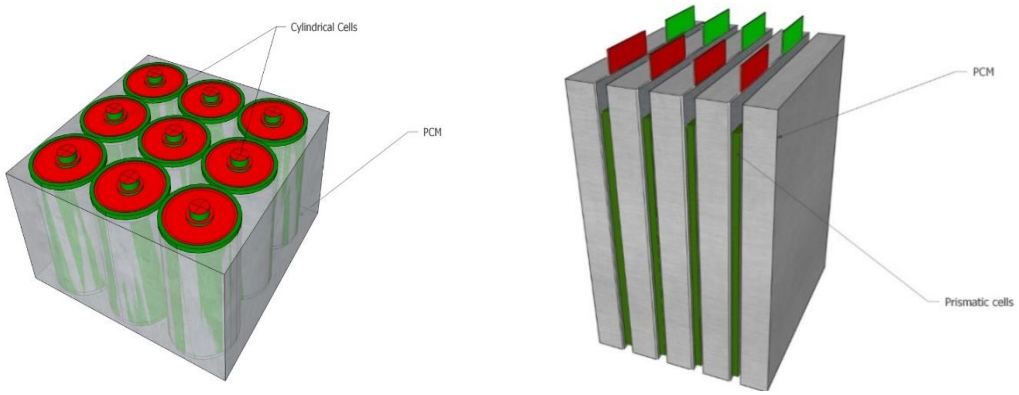

(a) (b)

Figure 25 Typical designs of BTMS of lithium-ion batteries using PCMs. (a): PCM block which is designed for easy cylindrical cells insertion. (b): Flat sheet PCMs sandwiched between prismatic cells.

Figure 26 illustrates the mechanism of the PCM based BTMS. It is a three-stage process that corresponds to the sensible heat, latent heat and sensible heat. When battery heats up from low

temperature, the PCM temperature increases along with the battery temperature and the heat is stored as sensible heat. As soon as the temperature reaches the melting temperature, the heat generated from the battery will be stored as the form of latent heat, and both PCM and battery temperature will be maintained at the phase change temperature. Once the latent heat is consumed both the PCM temperature and battery temperature will increase, and the heat is again stored in PCM as latent heat.

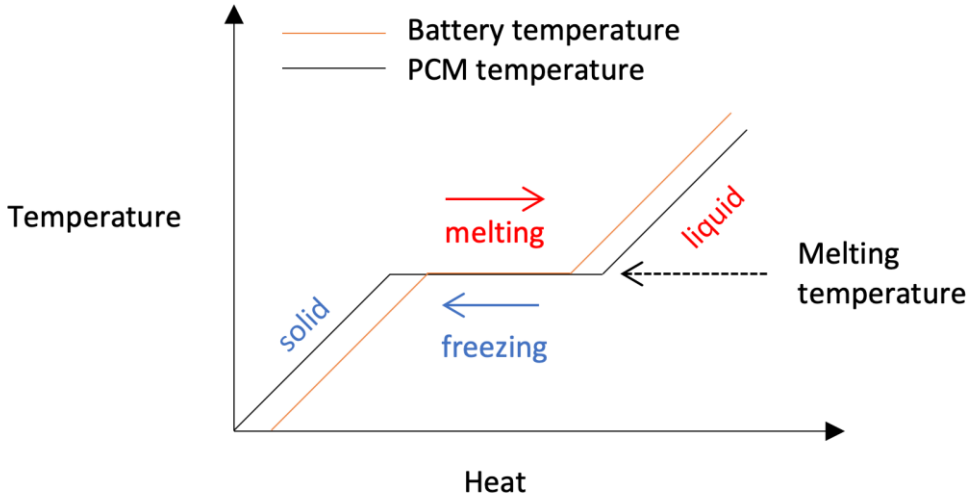

Figure 26 Mechanism of BTMS based on PCM.

The advantage of BTMS based on PCM can be concluded as following: (1) PCM could maintain temperature uniformity within single cells and battery packs. (2) PCM can absorb and release a large amount of heat during phase change and keep their temperature unchanged. Hence, the temperature of the battery pack can be regulated passively. Since the idea was proposed, many researchers carried out researches on (1) improvement on thermal and mechanical property of PCM, mostly focuses on thermal conductivity and encapsulation ability of PCM (2) combination of passive BTMS based on PCM and conventional active BTMS.

The optimum operating temperature of lithium-ion batteries is between 20- 50 ^{o}C, phase change temperature of PCM is accordingly limited to this range. Currently available PCMs for BTMS include hydrated salts, fatty acid, polyethene glycol and paraffin. Table 4 presents a list of the PCMs and main properties of the materials that are selected for BTMS of Lithium-ion batteries in EVs. As one can notice, looking at Table 4, the most common PCM employed for BTMS is paraffin. Its melting temperature is usually chosen between 30-50 ^{o}C. Paraffin wax has elevated latent heat, but low thermal conductivity (between 0.2–0.3 W/m·K). The other non-paraffin materials also have the limitation of low thermal conductivity.

Table 4 List of PCMs adopted elsewhere, and their thermal properties

Ref.	PCM	Melting temperature [˚C]	Thermal conductivity [W/m·K]	Specific heat [kJ/kg·K]	Latent enthalpy [kJ/kg]
[136]	Paraffin RT28 HC, provided by Rubitherm	28	0.2	2	245
[137]	n-Heptadecane paraffin	21.9	0.146	2.226	214
[137]	n-Octadecane paraffin	28	0.149	2.66	241
[138]	Paraffin RT44 HC, provided by Rubitherm	42.76-49.24	0.2	2	255
[139]	Eicosane	36.65	0.27	-	241
[139]	$Na_2SO_410H_2O$	32.25	0.544	-	254
[139]	$Zn(NO_3)_26H_2O$	36.25	0.31	-	147
[140]	RPCM ®, provided by the Glacier Tek Inc	18	0.55	2.1	195
[141]	Polyethene glycol 1000	35-40	0.23	2.142	159
[142]	PCM44(a eutectic mixture of $Mg(NO_3)_26H_2O$–	44	0.47	1.28-1.73	292

	$MgCl_2 6H_2O$–NH_4NO_3)

Most PCMs, however, suffer from a disadvantage of low thermal conductivity. As a result, thermal conductivity enhancement materials such as expanded graphite (EG) [143], metal foams [144] and carbon fibres [145], have been incorporated into PCMs to overcome the issue. These studies showed that CPCMs with a significantly improved thermal conductivity could transfer the heat generated from battery packs efficiently, hence providing a potentially enhanced BTMS. Table 5 presents a list of PCM/enhanced material composite and their thermal properties. Although most of the PCM/enhanced material composites receive a decrease in their latent heat, the increase in their thermal conductivities is significant.

Table 5 List of PCM/enhanced material composite, and their thermal properties (Part of this table adapted and reproduced from [146]

Phase Change Material composite	**Melting temperature [˚C]**	**Thermal conductivity [W/m·K]**	**Specific heat [kJ/kg·K]**	**Latent enthalpy [kJ/kg]**
Paraffin/ graphite composite	42-45	16.6	1.98	123
RT-42, provided by Rubitherm/ EG composite	55	16.6	1.98	185
A copper mesh (CM)-enhanced paraffin /EG composite	42	7.65	-	141.6
Paraffin/ EG/ low density polyethylene composite	44.5–50.2	1.38	2.48	87.4
Paraffin/ graphite sheets composite	21.6–25.5	3.95	2.39	132.6
Hexadecane/ aluminium particles composite	23.16–24.9	1.25	-	167

N-octadecane/ composite	**EG**	28.13-30.39	1.07	-	189
N-docosane/ composite	**EG**	40.2	0.82	-	178.3
N-octadecane/ inorganic		26.9	0.6213	-	123

Among all the materials, carbon-based nanomaterials have been proved to be excellent choices due to their high thermal conductivity and good compatibility with organic PCMs. Ramakrishnan [147] enhanced the thermal conductivity of paraffin/hydrophobic expanded perlite composites with graphite, carbon nanotube and graphene nanoplates. Results showed that addition of 0.5wt% carbon-based material could improve the thermal conductivity with 30% to 49%. Sari et al. [148,149] investigated thermal property enhancement ability of carbon nanotube. The researchers found that when 1wt% and 2.5wt% of carbon nanotube were added into polyethene glycol/raw diatomite composite and myristic acid/silica fume composite, the thermal conductivity can be improved by and 43.8% and 93%, respectively.

EG is another promising carbon-based material with excellent thermal property and cost advantage. The porous material has pores and voids, which is consisted of many large and thin graphite flakes. The graphite flakes have high in-plane thermal conductivity, and it provides EG with high thermal conductivity [150]. The capillary forces of the pores and voids in EG can pull PCM into the matrix. In this way, it confines the PCM in the pores and voids and increases the thermal conductivity of the composite [151]. Karaipekli et al. [152] improved the thermal conductivity of stearic acid using EG. Results showed a linear relationship between the thermal conductivity and mass fraction of EG, with 10% of EG the thermal conductivity was increased by 266.6% and reached 1.1 W/m·K Sari et al. [153] developed a novel palmitic acid/EG composite with excellent thermal stability. FTIR results confirmed that after 3000 times of thermal cycling, the chemical structure of the composite material remains the same. DSC results also showed that change of melting and solidification temperature and latent heat of the composites were at an acceptable level. Sari et al. [154] also studied the paraffin/EG composite material and found that with 10wt% EG the thermal conductivity of the composite was measured to be 0.82 W/m·K. Zhang et al. [155] investigated the flammability of EG/paraffin/high-density polyethene composites. The results showed that flame retardancy of

the composite can be improved with the existence of EG, as EG could form a char layer with good strength and stability under heating.

Metal foam with high thermal conductivity and high porosity has been popular in recent years. Wang et al. [144] tested the thermal conductivity of a paraffin/aluminium foam composite. The theoretical thermal conductivity of the CPCM can be 218 times larger than the value of pure PCM. Li et al. [138] studied a passive BTMS based on paraffin/copper foam composite. The authors also compared the system with two other control cases: a passive battery thermal management based on paraffin and an air-cooling BTMS. CPCM resulted in the lowest battery temperature and most uniform temperature distribution within the cells and battery packs. The study also revealed that the battery temperature decreased with decreased porosity of aluminium foam.

The polymer materials are also commonly used as the supporting material in the CPCM. The advantage of using polymer is it overcomes the leakage problem when PCM liquefy, hence creates the "solid-solid" phase change. Wu et al. [156] developed a from stable paraffin/olefin block copolymer/expanded graphite composite with the excellent thermal property. The researchers found that with 20wt% OBC, noticeable leakage of PCM was not observed on the composite, and EG could further prevent the PCM from leakage. Xiao et al. [157] proposed a new material development strategy through the polymerization of octadecyl acrylate and crosslinkers to form a polymer PCM. The aliphatic chains are chemically bonded to the skeleton hence provides excellent form stability. The composite does not have any leakage after long term operation and has good thermal stability even under 250 ˚C. Liu et a. [158] reported a hyper-crosslinked polystyrene PCMs through Lewis acid catalysis. Polystyrene was used as the encapsulation material in the composite. The composites were heated under a pressure force module at 80 ˚C for 5 hours, and no leakage was observed.

2.4.2. Battery thermal management system based on metal foam/PCM composite

Metal foam is commonly used for the development of CPCM due to its high thermal conductivity and porous structure. Li et al. [138] examined the performance of a passive BTMS using a sandwich structure with copper foam plates saturated with paraffin in between prismatic cells. Battery surface temperature was well controlled under 1C and 3C discharge rates with both pure PCM and copper foam-based CPCM, while with air convection the temperature exceeded the safety limit. Copper foam with different porosities of 0.9, 0.95 and 0.97 and

different pore density of 10PPI, 20PPI and 40PPI were investigated. Researchers found that lower porosity and pore density could help with reducing the battery surface temperature.

Similar results were also discovered by Hussain et al. [159]. Hussain et al. investigated the application of nickel foam/paraffin composite in BTMS experimentally, as shown in Figure 27. The influence of the pore density and porosity of the nickel foam on the performance of the BTMS were studied, and the results were compared with natural air cooling and pure PCM cooling. The results showed natural cooling was not able to control the battery temperature under the safety limit. Both PCM and nickel foam/PCM were able to reduce the battery temperature significantly, and compared with pure PCM, 24-31% of temperature reduction can be achieved with nickel foam/paraffin campsite. The geometric parameter study of the nickel foam showed that lower porosity and pore density of the nickel foam could help with controlling the battery surface temperature.

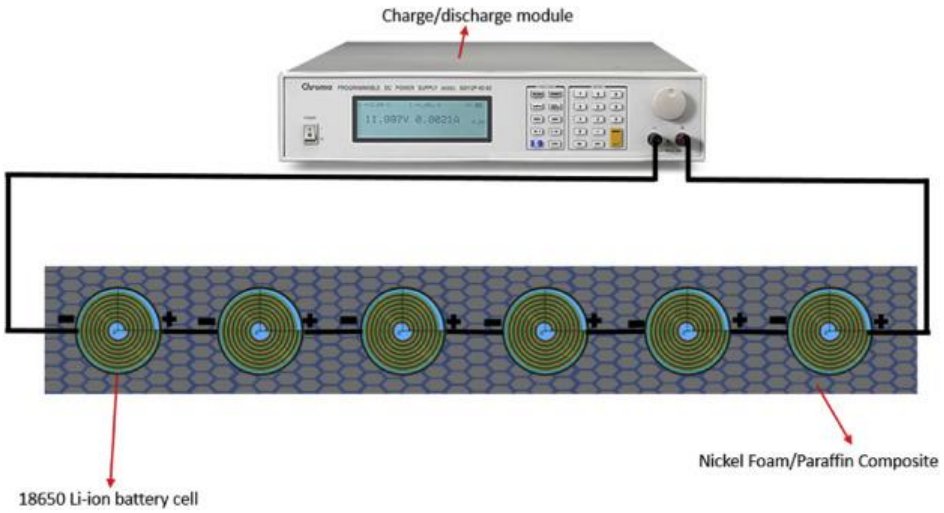

Figure 27 Schematic diagram of battery pack [6S] surrounded by nickel foam-paraffin composite [159]

Hussain et al. [160] further enhanced the thermal conductivity of the nickel foam/paraffin CPCM through coating nickel foam with graphene layer using chemical vapour deposition (Figure 28). After infiltrating into the graphene-coated nickel foam, the thermal conductivity of the PCM was improved by 23 times. Meanwhile, both its latent and specific heat are decreased by 30%. The developed materials were tested with a battery pack connected in 6S configuration. At 0.5C discharge rate, with graphene-coated nickel foam CPCM, the temperature of the battery surface is decreased by 17% compared with nickel foam.

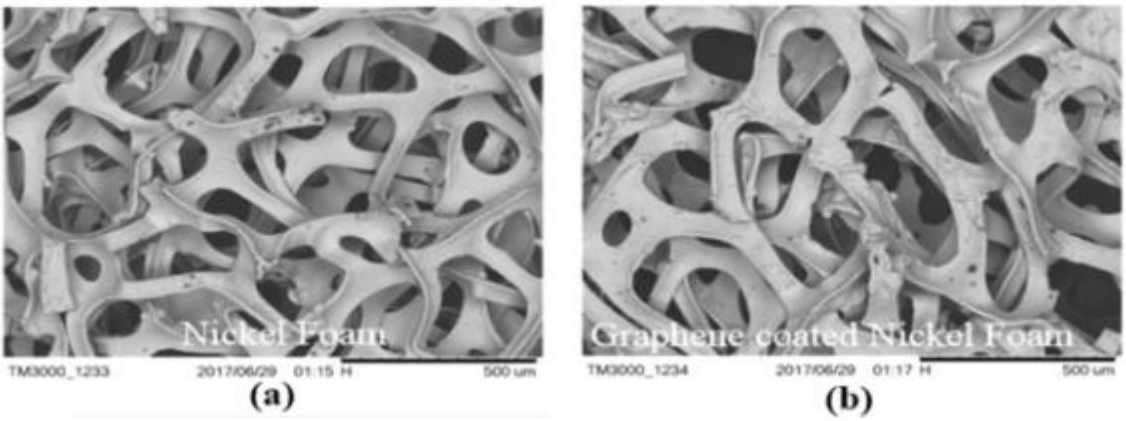

Figure 28 Graphene coated nickel foam. (a) Scanning electron microscopy image of nickel foam (b) Scanning electron microscopy image of graphene-coated nickel foam [160]

Qu et al. [161] studied a passive BTMS using paraffin/copper foam composite with a 2-D transient model numerically and experimentally. The schematic of the passive thermal management system is shown in Figure 29. Single prismatic battery (3.8V, 10Ah) were used in the research to examine the performance of the BTMS. Natural convection of liquid paraffin and local thermal non-equilibrium effect in the copper foam were considered in the model. The results showed that the surface temperature of the paraffin/copper foam composite was significantly reduced compared with isothermal and air convection modes, under 1C and 3C discharge.

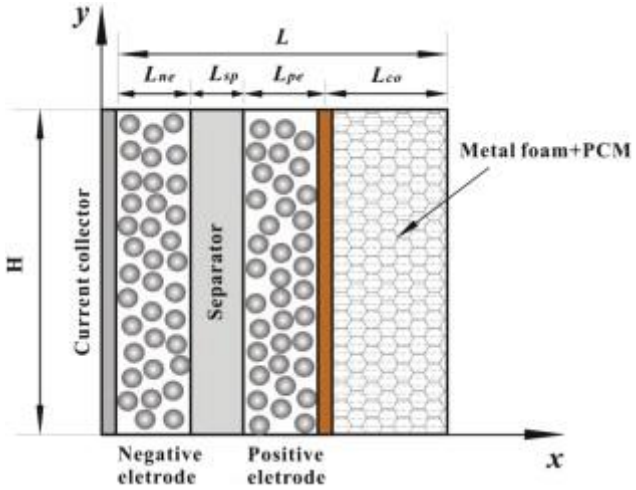

Figure 29 Schematic of the passive thermal management system [161]

Zhang et al. [162] investigated the melting behaviour of aluminium foam/PCM composite numerically and experimentally. 3D models of metal foam were built using both body-centred cubic and face-centred method. The results showed that the metal foam skeleton could enhance

the heat transfer as compared with pure PCM, the melting time of the PCM with both structures were reduced by 26-28%. The metal foam study showed that conduction heat transfer is the primary method of heat transfer in PCM with metal foam skeleton during melting. In contrast, the primary method of heat transfer during pure PCM melting is convection. Temperature uniformity of the CPCM can be improved with a larger interfacial area as the heat transfer coefficient is improved.

Alipanah and Li [163] carried out a numerical study on the BTMS using aluminium foam/PCM. They compared the performance of the BTMS based on different PCMs and metal foam/PCM composites. Aluminium foams with different porosities were also studied. Constant heat flux was applied to examine the thermal management performance. The results showed that through comparing different aluminium foam-based PCMs, PCMs with higher diffusivity and lower Stefan number provides better temperature uniformity and better temperature control. Aluminium foam with lower porosity (0.88) was able to achieve better battery thermal management performance.

Pan et al. [164] studied using copper fibre/paraffin composite in the BTMS. They tested the BTMS with a battery pack consisting of 15 Panasonic NCR18650PF cells in 3S*5P arrangement. The schematic of the mould is shown in Figure 30. Different test methods of natural cooling, pure paraffin cooling, copper foam/paraffin cooling and copper fibre/paraffin cooling were tested. The results showed that compare with the natural air cooling, CPCM cooling can decrease the temperature increase by 50%, and the maximum temperature was kept below 60 ℃ under 2.4C discharge. When copper fibre/paraffin CPCM was applied, good temperature uniformity was also achieved as the temperature difference within the battery pack was controlled within 2 ℃. The authors believed that 90% porosity copper fibre sintered skeleton offers the best performance of the CPCM.

Figure 30 Schematic of the sintering mould [164].

Khateeb et al. [165] studied the performance of a BTMS with aluminium foam-based CPCM for three charge/discharge cycles to understand the thermal stability of a battery module. A lithium-ion battery pack consisted of 18 commercial 18650 batteries was used to test the performance of the BTMS. They found that the battery temperature was well controlled during the first charge/discharge cycle. The PCM was fully melted after the second cycle. Then the thermal management performance of BTMS with CPCM was not sufficient after three cycles, leading to risks of battery thermal runaway.

2.4.3. Battery thermal management system based on EG/PCM composite

EG has also been widely applied in the research of BTMS based on CPCM. EG has the advantage of excellent thermal conductivity and good compatibility with organic PCMs. Compacted EG has a porous structure with the high surface area to volume ratio. The capillary forces of compressed EG matrix can pull PCM into the matrix. In this way, it increases the thermal conductivity of the CPCM. During the melting/solidification cycle, the EG matrix also prevents the leakage of PCM [151].

Jiang et al. [151] investigated the BTMS performance of paraffin/EG with the different mass fraction of EG. The prepared material is shown in Figure 31. Single 26650 $LiFePO_4$ cells were used to test the performance of the CPCM. Results showed that the performance of BTMS was significantly improved with the incorporation of EG. The thermal conductivity of the CPCM is enhanced, and the leakage of PCM is prevented. With 20% of EG loading, under 5C discharge rate, the cell temperature increase was controlled within 20°C. They believe that CPCM with 16-20wt% of EG is at its optimum condition due to its excellent thermal management performance and stable shape.

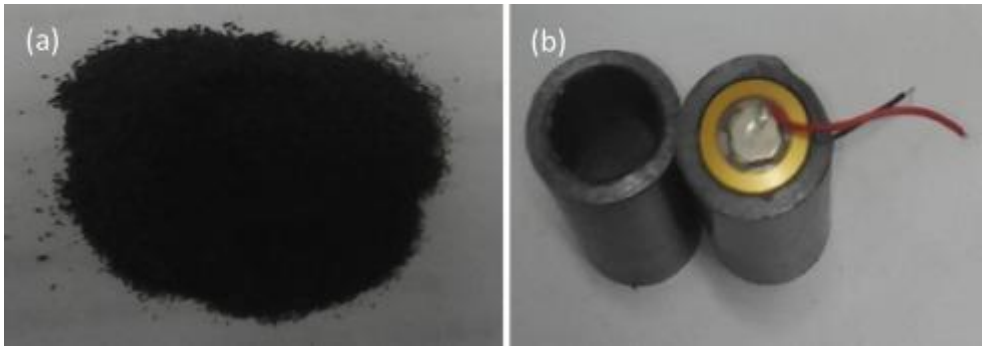

Figure 31 (a) Optical images of CPCM powder and (b) impacted CPCM samples [151]

Mills et al. [143] impregnated porous graphite matrix with paraffin in their study. The porous graphite matrix was fabricated by compacting EG. Different densities of the CPCM from 50g/L

to 350g/L were prepared. The experimental results showed that CPCM had a thermal conductivity that is 20-130 times greater than the value of pure PCM. The CPCM showed larger thermal conductivity with the direction perpendicular to the direction of compacting.

Ling et al. [166] studied the performance of BTM based on PCM/EG composite at low temperature. The BTMS based on CPCM was tested with a lithium-ion battery pack consisting of 20 commercial 18650 lithium-ion batteries at 5 and −10 °C and at different discharge rates. The results showed that with the CPCM can slow down the temperature decreasing of the battery pack. The temperature uniformity of the battery pack was also improved. Also, the voltage differences between the single cells were also reduced.

Alzoubi et al. [167] added silicon polymer into PCM/EG composites to improve the flexibility and compressibility of the CPCM. The composite was tested through-plane and in-plane relative to the EG compaction direction. The materials show anisotropic thermal and mechanical properties. A model of the compression test was also built based on Maxwell–Kelvin viscoelastic model. It reveals that EG provides ductility and viscous characteristics while PCM provided brittleness characteristics to the material.

Zhang et al. [155] added intumescent flame retardant (IFR) into EG/paraffin/high-density polyethene composite to improve its retardancy. The results showed that with the addition of IFR, the flame retardancy of the composite could also be significantly improved. EG could further enhance the retardancy as EG could form a char layer with good strength and stability under heating.

Luo et al. [168] prepared a novel BTMS module consisting of the dual melting temperature paraffin, expanded graphite and epoxy resin with a mass ratio of 5:2:3. A graphite film was also combined with the module to enhance the in-plane thermal conductivity. The BTMS was tested with a battery pack consisting of 9 commercial 18650 lithium-ion batteries in the arrangement of 3S*3P. They claimed that the paraffin could provide double buffer effect that minimizes the temperature increase of the battery and temperature difference between the batteries due to the broad phase transition range. After six cycles, the maximum temperature of the battery was observed to be 44.8 °C which was below the safety threshold. Addition of epoxy resin ensures the mechanical properties of the CPCM were maintained at a high level.

Wu et al. [169] proposed a BTMS based on PCM using copper mesh (CM)/EG/paraffin composite, as shown in Figure 32. The BTMS was tested with a battery pack consisting of 5

$LiFePO_4$ batteries (12Ah). They compared the novel method with traditional air natural convection and PCM plate method. The results showed CM-enhanced CPCM plate has a better performance of thermal management in heat dissipation and temperature uniformity, especially at high discharge rate. CM-enhanced CPCM plate can also improve the heat transfer ability of the BTMS under forced air cooling.

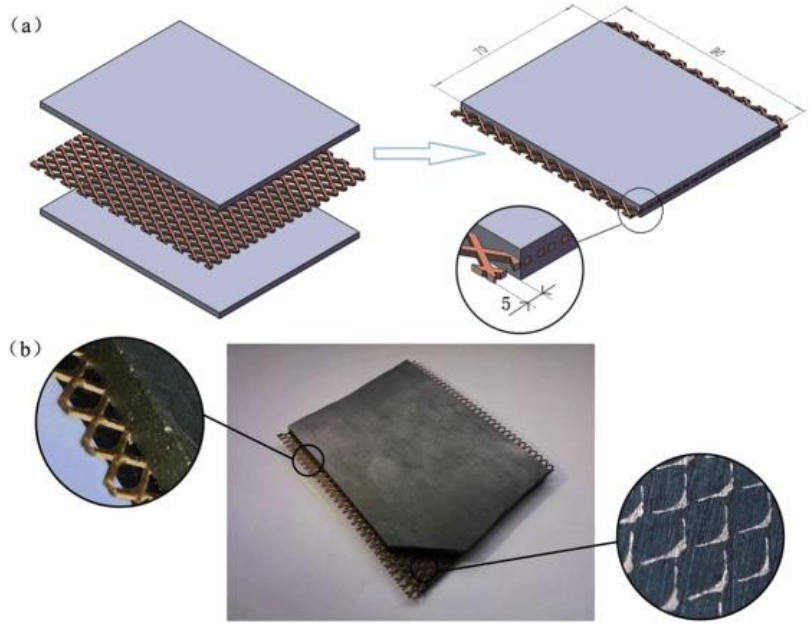

Figure 32 (a) Fabrication scheme and (b) photograph of CM-PCMP [169]

2.4.4. Battery thermal management system based on nano additives

Nano additives including graphene nanoplates, carbon nanotubes and boron-nitride nanosheet have been integrated with PCM to increase its thermal property. Some studies have observed excellent improvement in the thermal conductivity of the PCM.

Zou et al. [170] developed a novel CPCM using graphene and multi-walled carbon nanotubes (MWCNT) which can improve the performance of BTMS. With the addition of 1% carbon addictive (the mass ratio of MWCNT/graphene is 3:7), both thermal conductivity of the PCM and viscosity of the liquid CPCM is improved. The rapid rise of the liquid PCM temperature can also be restrained.

Mortazavi et al. [171] developed multiscale modelling techniques to explore the efficiency of the BTMS with CPCM. Thermal conductivity of graphene reinforced paraffin and hexagonal boron-nitride nanosheet reinforced paraffin were evaluated numerically. Newman's electrochemical model was employed to simulate battery heat generation. The BTMS was tested with a battery system consisted of 6 Hitachi's batteries (4.4Ah capacity each). They

found that, compared with pure paraffin, although thermal conductivity of paraffin nanocomposites was enhanced by several times, a significant improvement on the performance of BTMS was not observed. Study on heat transfer of nanocomposites revealed that hexagonal boron nitride nanosheet provides better thermal conductance to paraffin than graphene nanofilms.

Bahiraei et al. [172] explored the heat transfer performance of BTMS with paraffin-embedded with different carbon-based nanoparticle addictive. They found that the thermal conductivity of the CPCM was improved with up to 1100% when 10wt% graphite nanopowder were used. Dynamic viscosity of the CPCM was also improved, which leads to natural convection suppression and weaker temperature control comparted to pure paraffin.

Temel [173] investigated the performance of BTMS using RT-44 paraffin and graphene nanoplate (GNP)/RT44 with different mass fractions. The BTMS was tested with 12 heaters with the same geometric diameter of 18650 lithium-ion batteries. Results showed that the thermal conductivity of 7% GNP/ 93% RT-44 CPCM was improved by 230% in the solid phase and 130% in the liquid phase when compared with pure PCM. 7% GNP/ 93% RT-44 CPCM is able to prolong the battery effective protection time as 7.9 and 1.96 times compared to natural convection and pure PCM cooling, respectively. The CPCM also significantly reduced the maximum temperature difference within the battery pack.

Javani et al. [174] developed a passive BTMS for EV, which is consisted of shell/tube heat exchanger and CNT/GNP enhanced PCM. They found that due to limited space in the vehicle, BTMS based on pure PCM was not able to be employed in the EV. With the addition of CNT and GNP into PCM, the thermal conductivity of the PCM was increased. It leads to the decease on the size of the heat exchanger and BTMS.

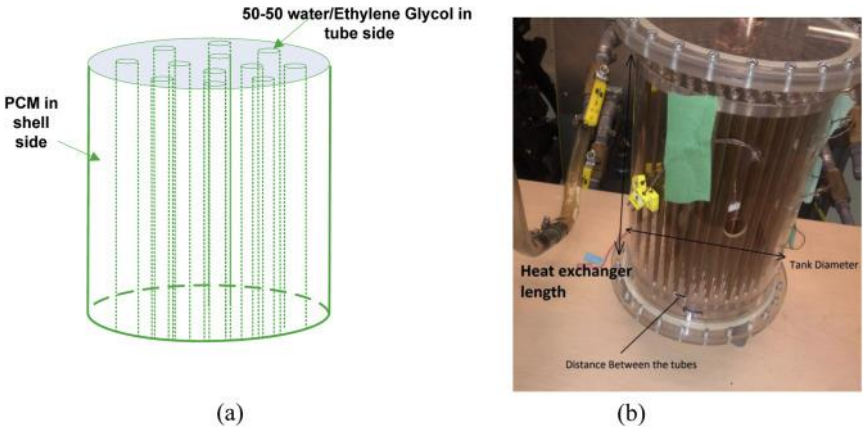

Figure 33 (a) Physical model of the heat exchanger, (b) optimized and manufactured latent heat thermal energy storage [174]

2.4.5. Battery thermal management system based on polymers

When PCM is applied in BTMS, there are challenges such as electric insulation consideration, PCM leakage, thermal contact resistance[175] and poor mechanical properties. Many researchers have studied incorporating polymer into PCM and have achieved CPCM with good electric insulation, good encapsulation ability, good homogeneity, suitable mechanical property and low volume change. However, polymer-based CPCM may suffer from low latent heat, as to archive good shape stability, a relatively large mass ratio of the polymer will be used and lead to decreased latent heat. Thermal conducive enhancement material also needs to be included in the CPCM due to the low thermal conductivity of most polymers, which further reduces the latent heat of the CPCM.

Wang et al. [176] developed a BTMS based on polymer enhanced PCM for the battery module of autonomous underwater vehicles. They chose acrylonitrile butadiene styrene and polyphenylene sulfide as the enhancement material. The polymers were able to provide excellent form stability to the composite. RT48 paraffin dominated BTSM can efficiently keep the battery temperature at the range of 321K to 325K, and the temperature differences were controlled less than 3.4K.

Lv et al. [177] tested the performance of BTMS based on a ternary CPCM, including EG, paraffin and LDPE coupled with low fins. The BTMS with tested with a battery pack consisting of 24 commercial 18650 lithium-ion batteries (6S*4P configuration). Results have shown that the LDPE framework was able to enhance the mechanical property of the CPCM and prevent PCM leakage. The BTMS presented excellent heat dispassion ability, under high discharge rate

3.5C, the temperature of the battery pack was still kept under 50°C, and the temperature difference was limited within 5°C.

As future work, Lv et al. [178] added nano-silica (NS) into EG/paraffin/LDPE CPCM. NS could further enhance the encapsulation and mechanical property of the PCM. The rigid nano-framework skeleton and adsorption property of NS can retain paraffin even in the liquid phase, and increased the inhomogeneity and reduce PCM leakage and volume change. The authors tested the BTMS with 6 commercial lithium-ion batteries in 1S*6P arrangement. With 5.5 wt% of NS, the temperature was 5.9°C lower than CPCM without NS addition.

Lei et al. [179] developed a cellulose/boron nitride nanosheet (BNNS)/polyethylene glycol (PEG) composite through vacuum impregnation and cold compressing. The CPCM has an excellent in-plate thermal conductivity of 4.76W/m·K and latent heat of 136.6J/g with 10 vol% BNNS loading. The developed CPCM also has excellent shape stability as it can endure 500 times of its weight even under high temperature (101°C).

Shi et al. [180] developed a polydimethylsiloxane /paraffin material which exhibits excellent mechanical property and performance on thermal management. The CPCM itself is soft, which is ideal for flexible electronic. The CPCM could also become transparent after melting, which could be the visual warning of excessive temperature increase.

Olefin block copolymer (OBC) from Dow Chemical Company has unique block architecture and excellent mechanical property[181]. OBC also shares a similar chain structure with paraffin (higher alkanes), hence has excellent compatibility with paraffin. Many researchers have used OBC as supporting material to develop CPCM with suitable shape memory property and flexibility.

Zhang et al. [181] developed OBC/paraffin CPCM with excellent shape memory property. The tensile test confirmed that the CPCM could maintain the mechanical property with elongation at breaker at 1500%.

Li et al. [182] developed OBC/EG/paraffin CPCM with high chemical stability, high latent capacity and encapsulation property. The novel CPCM has low bending strength above the melting temperature of paraffin, which benefits the installation and machinability of the CPCM. The CPCM has a rigid body when it is cooled under the melting temperature, which endows the material with resistance to deformation.

Huang et al. [183] investigated the performance of BTMS based on various flexible form stable CPCMs numerically and experimentally. OBC and HDPE were chosen as the supporting material in CPCM. Five heaters with identical dimensions of the 18650 lithium-ion battery were used to examine the performance of the BTMS. They found that OBC based CPCM has better thermal control performance than HDPE based CPCM, as the OBC based CPCM is flexible and can fill the gap between the CPCM and the battery pack, hence lead to lower thermal contact resistance (1/4 of HDPE based CPCM). They also found that CPCM with lower melting temperature (e.g. 33°C) is ideal for battery pack with a small power level and under low ambient temperature. In comparison, CPCM with higher melting temperature (e.g. 47°C) may be suitable for battery pack with high power level and under high ambient temperature.

2.4.6. Hybrid battery thermal management system

Many published studies on the performance of CPCM based BTMS showed reasonable control on battery temperature with one cycle of the battery operation. However, due to weight and volume limitations in EVs, the size of the BTMS module is limited. Hence it limits the amount the CPCM can be used. BTMS with only CPCM, may not be able to control battery temperature under an abusive operation condition (large heat generation), such as repeated charge/discharge cycle and charge/discharge at a high current rate. Even under mild conditions, not in all cases, the CPCMs are sufficient to facilitate the heat dissipation of the battery pack. Most heat is generated by battery pack during discharging, and stored heat in CPCM can only be dissipated to ambient through active method during charging and rest period. If the charging and rest period is not short, and the temperature of CPCM cannot decrease to ambient temperature before the next discharging cycle, the performance of the BTMS will be drastically affected. A hybrid BTMS is believed to be a more efficiency and reliability choice under such conditions. The use of liquid/air cooling provides an extra cooling ability, on top of the CPCM based cooling, leading to a reduced weight of the BTMS and an enhanced temperature uniformity of traction batteries.

2.4.6.1. Air cooling assisted battery thermal management system

He et al. [184] developed a hybrid BTMS based on forced air cooling and EG/copper foam/paraffin composite cooling. The BTMS was able to control the maximum operating temperature of an 80 Ah battery pack under 48°C and maintain the temperature difference within 3.9°C. EG in the developed composite plays the role of confining paraffin meanwhile transfer the heat generated from battery to the copper foam skeleton, and copper foam was able

to transfer the heat through the composite. Eventually, the heat was removed with forced air convection.

Lv et al. [185] tested and compared two different heating strategies for forced-air heating and silicone plate heating. The tested battery pack is consisted of 24 commercial 18650 batteries and surrounded by a BTMS based on aluminium fin/paraffin/expanded graphite/low-density polyethene composite. Results showed that forced-air heating did not achieve better performance than direct silicone plate heating. Silicone plate heating with high power achieved the best performance with 632 seconds of heating time to 10°C and low-temperature difference of 3.55°C.

Huang et al. [186] designed PCM and heat pipe assisted BTMSs with air cooling or liquid cooling. Thirty lithium-ion batteries were connected in parallel with a capacity of 33000 mAh to investigate the performance of the BTMSs. With different discharge rate applied, they found that that heat pipe was able to transfer heat promptly and provide temperature uniformity to the battery pack. BTMS based on heat pipe/liquid cooling was able to control the battery temperature at 50°C under 3C discharge rate, and achieve 3°C reduction compared with pure PCM cooling and heat pipe/air cooling.

Wang et al. [187] developed an air cooling assisted BTMS with copper foam/paraffin CPCM experimentally and numerically. Ten pouch cells, each with a capacity of 10Ah were connected to examine the performance of the BTMS. The results showed that the BTMS was able to keep the battery temperature under 42 °C under 4C discharge rate. Under three times of thermal cycling, the maximum battery temperature was still able to be controlled below 52°C.

Shi et al. [188] investigated the performance of a BTMS using copper foam/n-Eicosane CPCM and air cooling (Figure 34). A prismatic cell with 10Ah capacity was used to examine the performance of the BTMS. A non-steady model was proposed to predict the temperature behaviour of the battery. The results showed that the BTMS could effectively control the temperature of the battery. Both the reduction of convection thermal resistance between the battery and the energy unit and the increase of the thermal conductivity of the energy unit can effectively decrease the battery temperature.

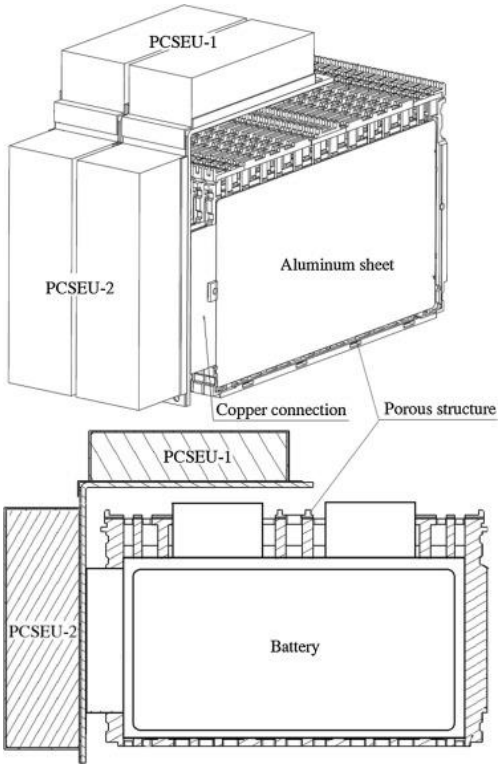

Figure 34 The schematic diagram of the ITMS with PCM [188]

Ling et al. [189] tested a BTMS based on PCM with 20 Samsung 18650 lithium-ion batteries connected in 5S4P. They found that under discharge rates of 1.5C and 2C, the temperature of the battery pack increased above the safety limit after two charge/discharge cycles. Hence active air cooling was introduced into the passive BTMS to enhance the cooling ability. Results showed that the hybrid unit was able to control the battery temperature below 50°C even under high current rates for multiple cycles. It has been concluded that in the hybrid system, PCM is able to suppress temperature rise and provide temperature uniformity. Air cooling is essential as it recovers the thermal energy storage capacity of PCM.

Qin et al. [190] investigated a BTMS based on PCM and air cooling numerically and experimentally. As shown in Figure 35, the BTMS consists of 4 commercial 18650 lithium-ion batteries and 12 PCM modules. The BTMS was tested under both passive and active cooling strategies. They found that under 3C rate, the maximum battery temperature and the maximum battery temperature difference were reduced by 16°C and 1.2°C, respectively. Based on the numerical model, the BTMS was further optimized, and 5mm recommended for the gap between cells.

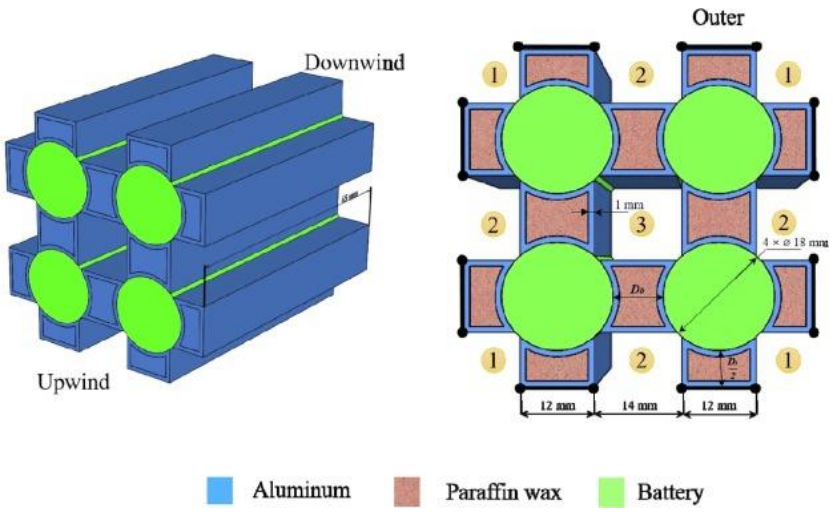

Figure 35 BTMS based on air and PCM cooling [190]

Huang et al. [191] carried out a global sensitivity analysis on an air-cooling based BTMS using EG based PCM. A Kriging-based high-dimensional model representation method was employed, and the effect of design variables on the performance of the BTMS was revealed. Computational efficiency was improved as the relationship between the design variable, and the performance of the BTMS was achieved. The results showed that heat fins assisted PCM/EG structure is essential for the BTMS as better cooling efficiency and temperature uniformity can be achieved. They found that improved inlet velocity of air is beneficial for enhancing the cooling performance of BTMS, while it will become insignificant after it exceeds its limit. The proposed BTMS was also optimized with the developed model. The optimal model could achieve 38.72% and 40.09% of reduction on maximum temperature and maximum temperature difference, respectively.

Jiang et al. [192] developed a hybrid BTMS using both forced air cooling and EG/paraffin composite cooling. Each 18650 battery was first placed into a case made of 16wt% EG/84wt% paraffin composite. Five cells were connected in series and fitted inside an aluminium tube, eventually five aluminium tubes where arrayed in parallel and mounted with baffles. The developed module was tested under different initial temperatures, discharge rate and air convection methods. Thermal behaviour of the battery pack was further investigated numerically with and without baffles. The results showed that with forced air cooling only the battery temperature could reach 72°C and created 20°C of temperature difference. While forced-air effectively reduced the PCM solidification time with 42 minutes of difference under 28 °C without baffle. The use of EG/paraffin case significantly reduced the battery temperature,

and the maximum temperature was observed within 41-44°C with 1-2°C of temperature difference.

Wu et al. [193] tested the thermal performance of a heat pipe assisted BTMS using both EG/paraffin composite and forced air cooling. The developed module contains five prismatic batteries with 12Ah capacity in series connection. Two CPCM plate embedded with heat pipes was attached on both sides of the battery module to create a compact sandwich structure. The module was tested under different forced air inlet velocity of 0, 1, 2 and 3m/s. The results showed that with the benefit of forced air cooling, battery temperature was able to be controlled under 50 °C. Temperature uniformity can be improved with the use of CPCM. Heat pipe could decrease the temperature of the part of the battery, which is close to the condenser side. It could also effectively control the battery temperature under multiple operation cycles.

2.4.6.2. Liquid cooling assisted battery thermal management system

Hemery et al. [136] tested a mock-up battery module consisted of 27 heaters under natural air cooling, forced air cooling and hybrid cooling based on liquid cooling and PCM cooling (Figure 36). The results showed that high inlet velocity was required for battery cooling, which increases fan power. With air cooling, the battery temperature exceeded the battery safety limit under failure test, and the thermal runaway spreads quickly from the defected battery to the surrounding batteries. With hybrid cooling, results showed that temperature uniformity was provided to the battery pack. The temperature of the defected battery was also kept under the safety limit under the failure test.

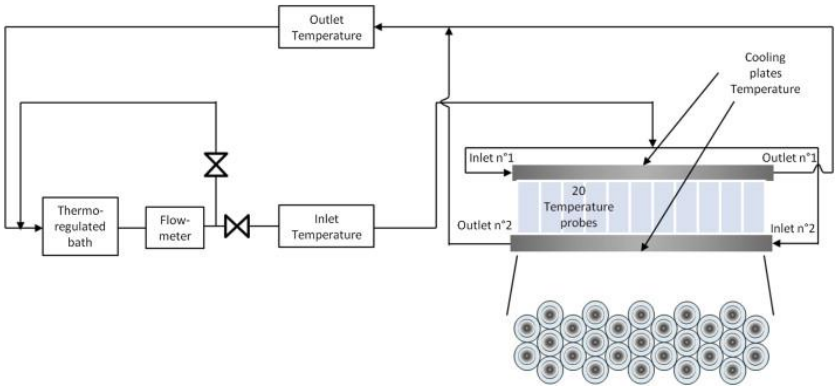

Figure 36 Experimental setup of the semi-passive BTMS [136]

Liu et al. [194] numerically studied the effects of ambient temperature, liquid flow conditions (Reynolds number) and discharge rate on the performance of BTMS with different cooling methods. A battery module consisted of 20 prismatic cells (20Ah total capacity) was used to

examine the performance of the BTMS. They found that liquid cooling was generally more effective in reducing the battery temperature while PCM cooling provided temperature uniformity to the battery pack. Increase of Reynold number could enhance the cooling ability of liquid cooling. Although air cooling was preferred at sub-zero ambient temperature, as heat generated from the battery should be retained to warm the battery rather than be removed.

Zheng et al. [195] numerically investigated the performance of a liquid cooling dominated BTMS with PCM cooling. A battery module consisted of 110 prismatic cells in 10*11 arrangement (10 Ah capacity per cell) was charged under 8C rate to demonstrate the capability of the BTMS. Results showed that liquid cooling contributes 80% of the cooling ability of the BTMS. The importance of the CPCM was it boost the heat conduction between the coolant, and the cell, hence high thermal conductivity is required for the CPCM.

An et al. [196] numerically investigated the performance of the liquid cooling based BTMS using CPCM under various flow velocities, channel arrangement and different PCMs. A lithium-ion battery pack consisted of 25 Panasonic 18650 lithium-ion batteries in 5S5P arrangement was discharge at 3C to examine the BTMS performance. Increased flow velocity was able to improve the heat dispassion ability of the BTMS efficiently. In contrast, the increase has a limit, and little enhancement was observed when the velocity was over 0.08m/s. When cooling channels were set at four corners, the optimal cooling performance was achieved. Compared with pure PCM, CPCM was found to have better cooling performance. They concluded that with a velocity of 0.04m/s and 6wt% EG CPCM, the best cooling performance was provided from the BTMS.

2.5. Summary of Chapter 2

The development of lithium-ion battery started from the discovery of lithium intercalation mechanism by Michael Stanley Whittingham, broke through by John B. Goodenough and commercialized by Akira Yoshino. The applications of lithium-ion batteries have been everywhere, especially since 2010, with the massive deployment of EVs started. The market is currently occupied by NCM, NCA, and LFP batteries, with NCM and NCA being the majority due to the higher energy density. The battery heating issue is mainly resulted from the battery polarization, which has always been a threat as it can cause battery ageing even fire accident. To control battery temperature, the use of BTMS is essential. EV with BTMS usually uses air/liquid/refrigerant as the cooling/heating medium without any energy storage method. The incorporation of phase change material with the BTMS could provide temperature uniformity

to the battery, and extra cooling load benefited from the inherent phase change behaviour of PCM. The low thermal conductivity disadvantage of PCMs can be overcome by using thermal enhancement materials including metal foam, expanded graphite and nano additives. All the thermal enhancement materials could significantly improve the thermal property of the PCM. Addition of polymer material could preserve the phase change material even when it is liquid state hence provide stability to the CPCM. Future commercial BTMS is recommended to use hybrid BTMS which is consisted of both active cooling and CPCM cooling. Active cooling is powerful to manage the battery temperature, and with the incorporation of the CPCM, part of the generated heat can be stored in CPCM, which can help with reducing the electricity consummation of active cooling method.

The literature review suggests research on BTMS with CPCM is popular while there are some research gaps need to be overcome. Firstly, in the research of CPCM, there has been inadequate studies of particle size effect on the thermal property of CPCMs. Studies on fire retardancy of CPCM is limited while the battery system is fragile to fire hazards. Secondly, many published papers did not include accurate descriptions of the battery heat generating behaviours in their study, while the heat generation rate can fluctuate wildly in the charge/discharge process. Thirdly, in the investigation of BTMS, there have been very few studies compared the performance of different CPCMs in the BTMS. There are not many studies on continuous operations of BTMS, while extreme operations could lead to the failure of the BTMS and cause fire accidents. The above gaps drive me to carry out the research on the CPCM, lithium-ion batteries, and active cooling based BTMS using CPCM, which are presented in the following chapters.

Chapter 3 Material and Methodology

This chapter explains the methodologies, including the experimental and modelling methods. Section 3.1 describes the materials and their characterisation as well as battery characterisation method. Section 3.2 introduces the modelling methods, including the establishment of the physical model, mathematical model, and the model validation.

3.1. Experiment

3.1.1. Material characterisation

3.1.1.1. Raw materials

Table 6 Physical properties of the phase change materials

Physical properties	**Parameter**	
	RT28HC	RT35HC
Peak melting temperature（°C）	28	36
Peak solidification temperature （°C）	26	34
Specific heat（kJ/kg·K）	2	2
Latent heat (kJ/kg）	230	210
Density（Liquid）（kg/m^3）	0.77	0.77
Density（Solid）（kg/m^3）	0.88	0.88
Flash point（°C）	165	177

Paraffins (RT28HC and RT35HC) were purchased from Rubitherm as the phase change materials for this study, characteristics of the PCMs are listed in Table 6 (Rubitherm supplied the properties). The RT28HC and RT35HC were chosen for the CPCM study as it has a relatively high latent heat among the PCMs and has a suitable range of phase change temperature for the battery thermal management. Three types of expanded graphites (EGs) with different particle sizes termed EG1, EG2 and EG3, were purchased from Donghai Anfa International Trade Company Ltd. EG1 and EG2 were in large micrometres range (i.e. hundreds μm), while EG3 was in lower micrometres range (i.e. ~10 μm). These EG particles were sieved manually (an example of the setup shown in Figure 38). The sizes of these EG particles were then examined using a scanning electron microscope (SEM), and later statistically analysed using ImageJ. Their dimensional information is given in Figure 37. Most of the EG1 have a particle size of 800-1000 μm in length, and 360-540 μm in width. Most of the EG2 have a particle size of 160-200 μm in length, and 90-100 μm in width. Most of the EG3 have a particle size of 9-12 μm in length, and 3.5-4.5 μm in width.

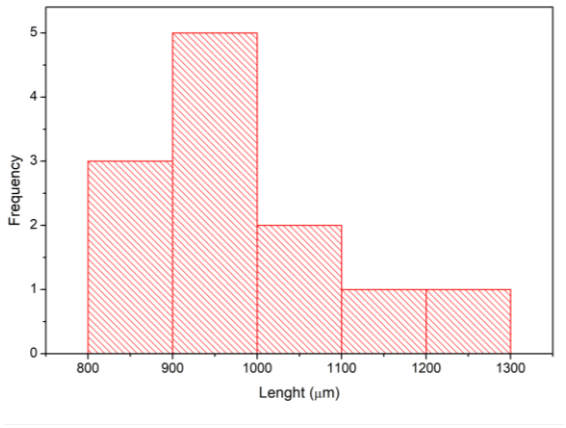

(a)

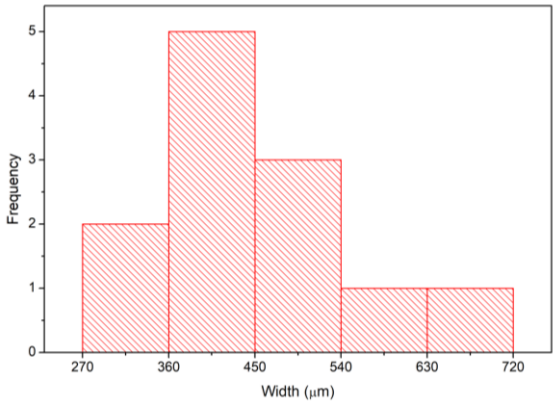

(b)

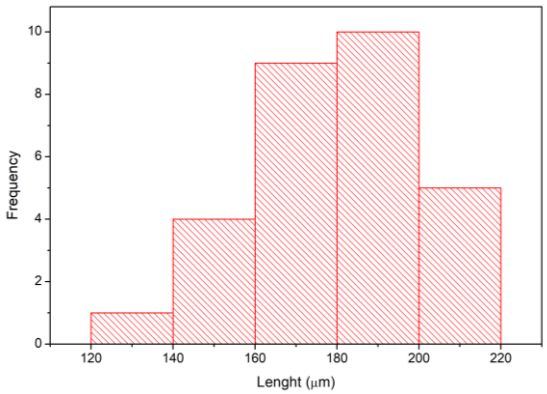

(c)

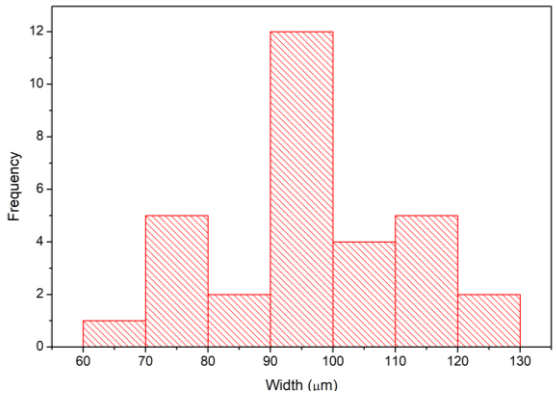

(d)

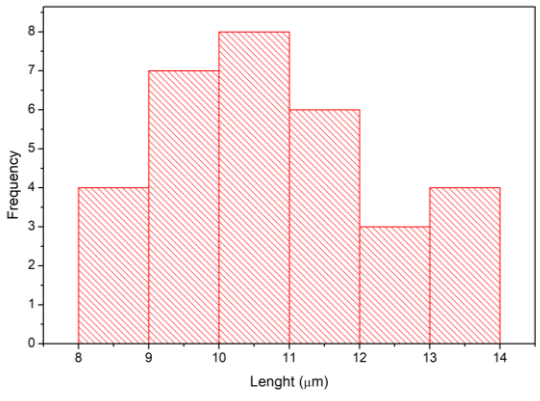

(e)

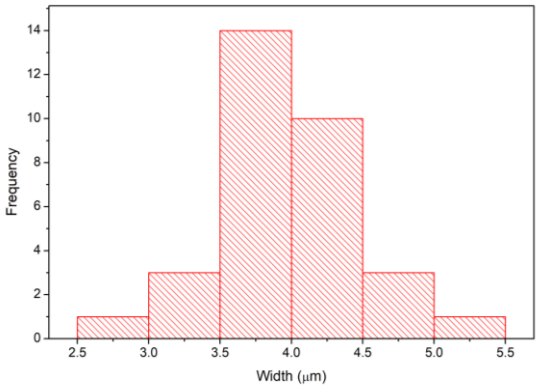

(f)

Figure 37 Particle size distribution of EGs. (a) and (b) are the length and width of EG1, respectively. (c) and (d) are the length and width of EG2, respectively. (e) and (f) are the length and width of EG3, respectively.

Figure 38 Example of the sieving set up for material preparation of EG.

Copper foams with different pore sizes and porosities were purchased from Wuhan Jing Chu Chen Pharmaceutical Chemical Co. Ltd, China. Their dimensional information is given in Table 7. The copper foams have a material density of 8930kg/m^3 and a skeleton thermal conductivity of 398 W/m.k

Table 7 Pore sizes and porosities of the copper foams

Type of copper foam	Pore size (PPI)	Porosity (%)
Copper foam 1	20	99
Copper foam 2	50	92
Copper foam 3	100	81

Industrial grade colloidal graphite powder was used as a thermal enhancement material in CPCM investigation. The colloidal graphite powder has a particle size of 300 mesh and was purchased from Shenzhen Huananxinyang Tech Co. Ltd, China. Laboratory grade melamine was used as the fire retardant in the study, which was purchased from Sigma-Aldrich, UK.

3.1.1.2. Preparation of the composite phase change material

Shape stabilised EG/RT28HC composites were prepared by physical blending and impregnating the PCM into different sizes of EGs. A typical process involves the following: Paraffin was pre-melted using a magnetic hotplate stirrer first. Then EG was slowly added to

the melted paraffin with continuous stirring. The mixture was stirred for 10 minutes to ensure the homogeneity of the mix. Next, the mixture was transferred into an ultrasonic water bath to accelerate the impregnation of liquid paraffin. After the impregnation, the surface of EG was coated with paraffin, and the pores of the EG were filled with paraffin. The prepared sample was then cooled to the room temperature and compacted using a Lloyd LS100 Plus materials testing machine. Samples were compressed into a solid matrix with a flat cylindrical shape. The process of sample preparation is illustrated in Figure 39.

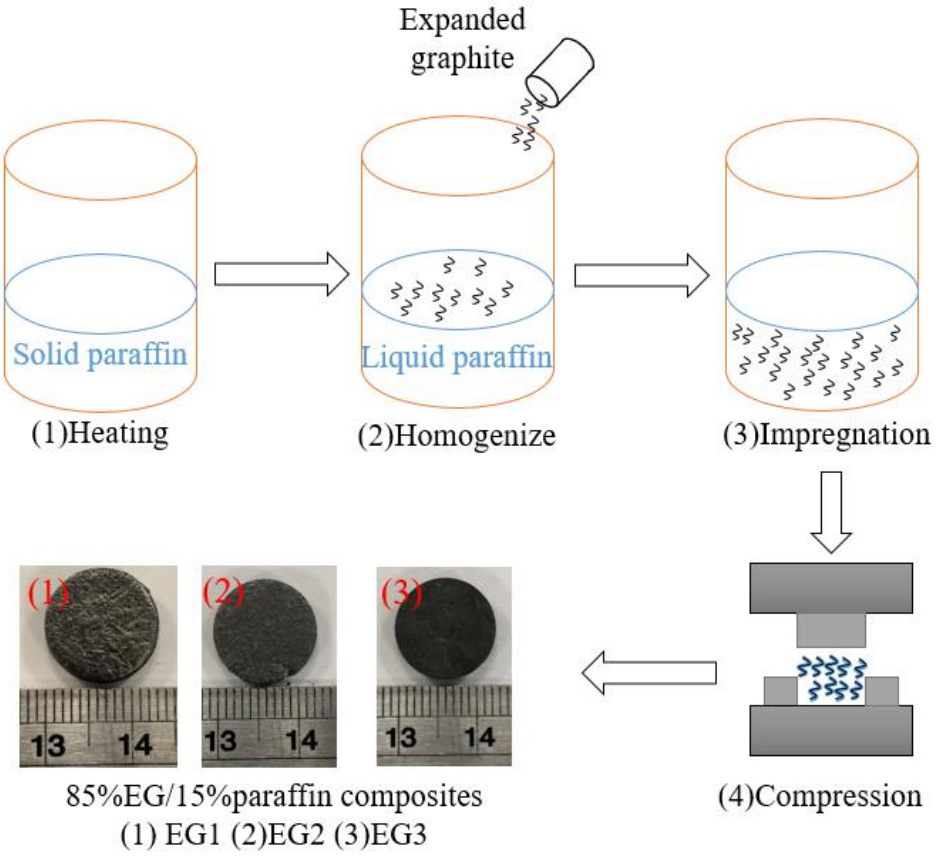

Figure 39 Process of the CPCM sample preparation

The samples were weighed within the error of ± 0.1mg. The prepared samples had the same weight of 0.24g, 13mm in diameter and roughly 3mm in height. All samples should have the same density as this property is directly related to the thermal conductivity and porosity estimation of composites. Wang et al. found out that an increased compression pressure on EG will cause the change of thermal conductivity and permeability [197]. Because the selected EGs possess different density initially, thus the compression strength was ranging from 0.2 to 30KN to attain a similar density of final composites. During the compression, no leakage of paraffin was observed, which indicated the sufficient adsorption of the paraffin. Composites

were prepared with paraffin and different particle sizes of EG, with the EG mass ratio in a 5% increment from 15- 25%. The compression ratio from raw material to the tablet can be more than 10 times. The high compression ratio will create difficulty and high cost for the scale-up of the preparation method as large customized mould and dedicated compression machine will be required.

The copper foam/RT35HC composites were prepared under vacuum. As shown in Figure 40, a copper foam and a pre-set amount of paraffin was placed in a vacuum chamber first. The chamber was then closed and sealed. The vacuum pump started to work and to remove the air in the vacuum chamber, especially air confined in the pores of the copper foam, and was kept under an absolute pressure of 50Pa. A hot plate was set at 60°C, and held for 60 mins to melt the paraffin fully. The hot plate was then switched off, allowing the vacuum chamber and the material to cool overnight naturally. In the next day, the fully solidified paraffin with copper foam trapped inside was removed from the chamber. Excess paraffin was carefully removed, and finally, the preparation of the copper foam/paraffin composite was finished. The vacuum environment for material preparation was essential as the pores and voids of the copper foam could hold the PCM hence significantly improves the thermal properties. If the materials were prepared in an ambient environment, there is always air trapped in the copper foam which would stop the infiltration of paraffin, leading to a reduced weight of paraffin absorbed, and a lower energy density of the composite. The confinement of air in the copper foam/paraffin composite also consequently lowers the thermal conductivity of the composite as the thermal conductivity of air is only 0.02W/m·K.

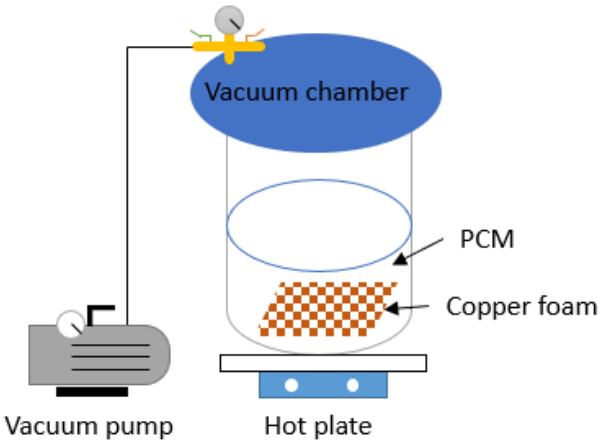

Figure 40 Experimental set up for the copper foam/paraffin composite preparation

The colloidal graphite and melamine were heated in the oven at 100°C for 12 hours to remove moisture. The mixtures of colloidal graphite, melamine and RT28HC were then heated and mixed using a magnetic stirrer at 60°C according to the composition shown in Table 8.

Table 8 Composition of the graphite-based composites

Sample number	Composition（wt%）
1	10% colloidal graphite/90% RT28HC
2	20% colloidal graphite/80% RT28HC
3	30% colloidal graphite/70% RT28HC
4	40% colloidal graphite/60% RT28HC
5	1% Melamine/ 40% colloidal graphite / 59% RT28HC
6	3% Melamine/ 40% colloidal graphite / 57% RT28HC
7	5% Melamine/ 40% colloidal graphite / 55% RT28HC
8	10% Melamine /40% colloidal graphite / 50% RT28HC
9	15% Melamine /40% colloidal graphite / 45% RT28HC

3.1.1.3. Material characterisation

The surface morphology of the raw materials and the CPCMs were observed using a scanning electronic microscope (SEM, HITACHI Microscope TM3030). The observations were performed at different magnifications with different acceleration voltages. The SEM also has an Energy Dispersive X-ray Spectrometry for element analysis.

A Nano-CT system (XRT, Bruker SKYSCAN 2211) was used to attain the internal structure and porosity information of paraffin/EG composites. The XRT is a non-destructive technique wherein thousands of 2D raw images are acquired from different angular positions of the composite. Using the 2D reconstructed images of the samples will be able to build a 3D volume rendering which enables the observation of the impregnated PCM in EG matrixes. The 3D model gives the structure parameter of the EG matrix and distribution condition of the PCM. Flat-panel X-ray detector was used, and 1200 images were generated with the scanning step angle of 0.3°. To obtain the structure parameters from the 3D models, VOI (volume of interest) needs to be carefully defined firstly. It refers to the sub-volume of the dataset within which EG matrix is precisely included. The images also need to be segmented, i.e. to confirm the suitable grey level (0-255) threshold. Same segmentation method was applied to all the samples. After

segmentation, voxels that represent the porosity were efficiently distinguished from the EG constituent. An example of the 3D binary XRT image and the grey level frequency histogram after segmentation is shown in Figure 41. The specific surface area was defined as the object surface area per object volume space. Pore volume is the difference between the VOI and the EG matrix volume. The porosity was calculated as follows:

$$\%\text{Porosity} = 1 - \frac{EG\ matrix\ volume}{VOI\ volume} \tag{13}$$

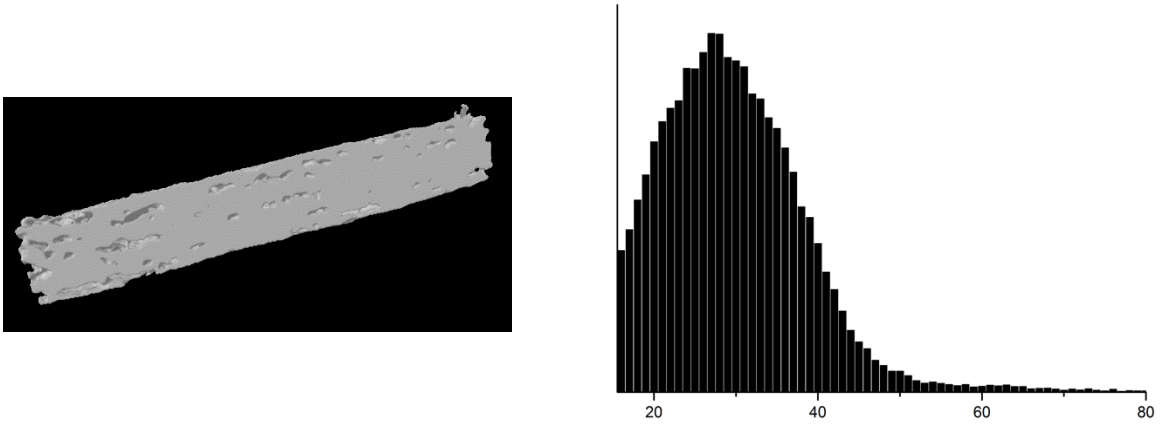

Figure 41 One of the cut surface of the EG1 3D binary image (Left), selected grey level of the image (right)

Other methods for pore structure study including mercury intrusion porosimetry and surface area and porosity analyser (Brunauer–Emmett–Teller theory) were attempted but found not suitable for EG characterization. The mercury damaged the fragile expanded graphite hence no results was achieved, and neither from the surface area and porosity analyser.

Thermal properties of EG/paraffin composites, such as latent heat, specific heat, melting and solidification temperatures, were measured by using a differential scanning calorimeter (DSC, Mettler Toledo DSC 3). The tests were performed in a nitrogen atmosphere over 0- 50°C (heating) and 50- 0°C (cooling) at a heating/cooling rate of 5°C/min. Samples were weighted using a high precision balance (Mettler Toledo XP6U Micro Comparator) with the readability of 0.0001 mg. The weight of the samples was controlled in the range of 3-6mg. All samples were tested under three heating and cooling cycles for repeatability. Specific heat was measured using a sapphire as a reference according to DIN 51007 [198]:

$$C_p = \frac{(\dot{q}_{meas} - \dot{q}_{bl})}{m_{sam}} * \frac{m_{sap}}{(\dot{q}_{sap} - \dot{q}_{bl})} * C_{p.sap} \tag{14}$$

where m_{sap} and $C_{p.sap}$ are known, which represent the weight and specific heat of the sapphire, respectively. $\dot{q}_{sap}$ and $\dot{q}_{bl}$ denote the heat flow applied to the sapphire and blank samples, respectively. $\dot{q}_{meas}$ is the measured total heat flow and m_{sam} is the measured sample weight.

Thermal conductivities of EG/paraffin composites and graphite/paraffin composites were measured by a Laser Flash Apparatus (LFA, NETZSCH LFA 427). The measurements were performed under a nitrogen atmosphere from 30 to 70 °C with a measurement interval of 10°C. At each of the temperature setpoints, the measurement was repeated five times to ascertain the correct values.

A thermal hot bridge (THB, LINSEIS THB 500) was used to measure the thermal conductivity of copper foam/paraffin composites. The reason for choosing a different method was that LFA is only suitable for small samples with a maximum size of 12.7mm in diameter and 3mm in height. Copper foam with high porosity/low PPI could have pores of several millimetres in diameter hence it is considered appropriate to measure with the LFA. The thermal hot bridge was an efficient method to measure samples in bulk size. The THB sensor needs to be sandwiched between two identical pieces of the copper foam/paraffin composite samples. The test was performed under ambient temperature and repeated for five times. Between each test, there was 60s of wait time for the material temperature to reach an equilibrium.

The thermal stability of the materials was characterised by a simultaneous thermal analyser (STA, NETZSCH STA 449 F3 Jupiter) from 25- 400°C with a heating rate of 10°C/min. Leakage phenomenon was also studied by comparing the weight of the samples before and after cycling. The samples were cycled between 15- 45°C for 50 times, and weight loss were calculated according to the following equation [199] :

$$weight\ loss\% = 100\% - \frac{(m_{before} - m_{after})}{m_{before} * w} * 100\% \quad (15)$$

where m_{before} is the weight of the sample before cycling, m_{after} is the weight of the sample after cycling, w is the mass fraction of the paraffin.

3.1.2. Battery characterisation

3.1.2.1. Thermal behaviour characterisation

Commercial 18650 lithium-ion batteries (Panasonic NCR18650B) were chosen for this work. The specifications of the lithium-ion batteries are shown in Table 9.

Table 9 Specifications of a single lithium-ion battery used in this work [67,200,201]

Chemistry	**$LiNiCoAlO_2$**
Nominal capacity	3.35Ah
Nominal voltage	3.6V
Operating temperature	Charge from 273K to 318K Discharge from 253K to 333K
Weight	48.5g
Charge cut-off voltage	4.17V
Discharge cut-off voltage	2.5V
Maximum charge rate	0.5C
Maximum discharge rate	2C
Specific heat	823(J/kg-K)

Before each experiment, each cell was tested for its static capacity using an ampere-hour integral method. Only batteries that meet the nominal capacity were chosen for subsequent experiments. The single battery cells were discharged at C/1 rate and terminated at the discharge cut-off voltage. The following equation was then used to calculate the static capacity:

$$Q = \int_0^T U(t)I(t)dt \tag{16}$$

where Q is the static capacity, U is the voltage, I is the current, and t is the discharge time of the battery.

The internal resistance of the lithium-ion batteries was measured using the hybrid pulse power characterisation method from the PNGV Battery Test Manual [202]. The measurements were done at the 20°C. The test profile consisted of 10 steps, separated by 10% of the depth of discharge (DOD). The test began with a fully charged battery and ended at 90% DOD. Each of the batteries was discharged at C/1 rate for 18s at each DOD. Then it followed with 1-hour rest

period to allow the cell return to a charging equilibrium condition before the next step of the test. The discharge resistance is simply the ratio of voltage to current, given by:

$$R = \frac{\Delta V}{\Delta I} = \frac{U - V_1}{I} \tag{17}$$

where R is the internal resistance, U is the open-circuit voltage before discharge, V_1 is the voltage after discharge, and I is the discharge current.

The ohmic resistance (R_O), charge transfer resistance (R_{CT}) and concentration polarization resistance (R_P) were estimated at different time scales. The R_O was calculated from an instantaneous voltage drop up to 0.1s. Currently accurate measurements of the R_{CT} and R_P, are still a challenge, and there is so far a lack of suitable method [72]. Hence, the sum of R_{CT} and R_P was calculated from the voltage drop between 0.2 and 10s. In the respective time scale, the R_{CT} and R_P were the major contributors to the total resistance.

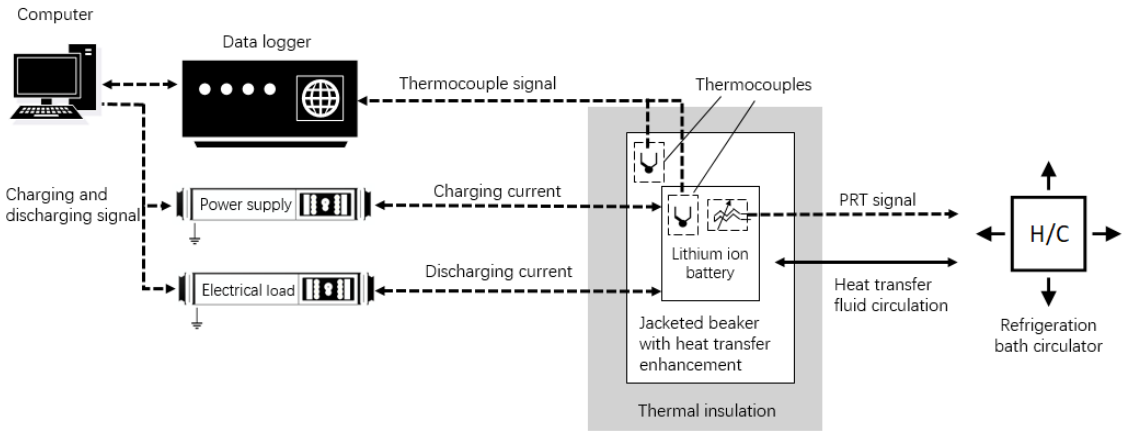

(a)

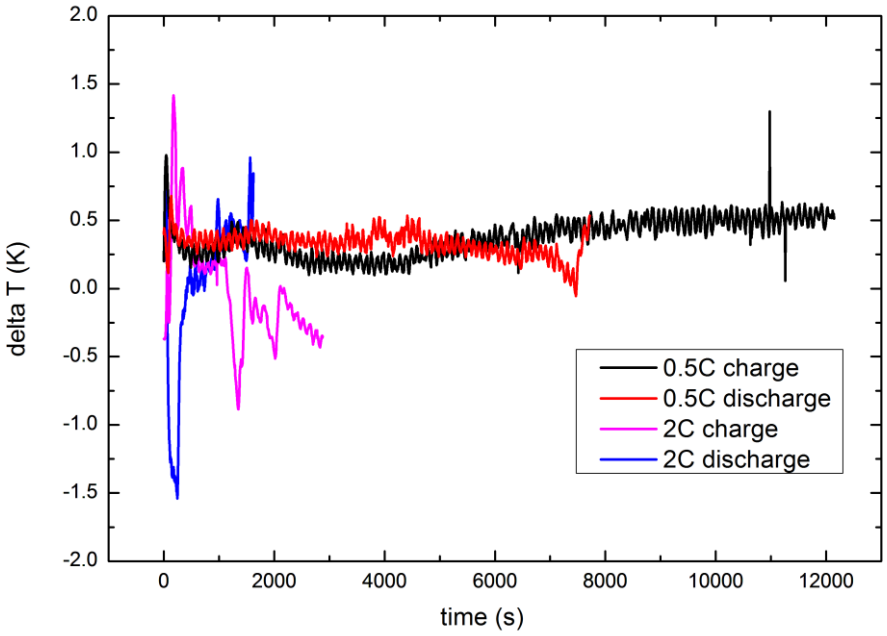

(b)

Figure 42 Proposed experimental set up for battery thermal characterisation: (a) schematic illustration; (b) temperature difference between platinum resistance thermometer (PRT) and circulator fluid

Thermal characteristic of lithium-ion batteries was studied using an experimental set up illustrated in Figure 42 (a). The charge and discharge of batteries were done by using a DC power supply (model: PS9000 2U, EA-Elektro-Automatik, error < 0.1%), and an electronic DC Load (model: EL9000B, EA-Elektro-Automatik, error < 0.1%), respectively. The DC power supply and electronic DC load were also used to record the current and voltage. The lithium-ion battery was placed in a jacketed beaker. A bath circulator was connected to the beaker to provide a temperature environment. The beaker was fitted inside with aluminium fins to achieve temperature consistency between the battery and the beaker. It makes the beaker the "environment" of the battery. A PRT which is connected to the bath circulator was attached on the battery to monitor the temperature of the battery. It determines the working temperature of the bath circulator. A thermocouple was attached on the cell to record the cell temperature. An additional thermocouple was attached on the inner wall of the beaker to monitor the environment temperature. Necessary insulation measures were taken to assure the accuracy of the experiment.

Usually, the experimental measurements of the lithium-ion battery thermal behaviour are carried by accelerating rate calorimeters (ARC) [203]. However, I did not have access to the ARC. An experimental setup with the same principle of the ARC was designed and shown in Figure 42 (a). The battery was fully charged and discharged at 0.5C and 2C current rate during the test. Through the discharge period, the cell was discharged at the galvanostatic mode until the voltage dropped to 2.5V. During the charge period, the single cell was first charged at the galvanostatic mode until it reached 4.17V, then followed by the potentiostatic mode until the current drops to 0.1 A. When the charge/discharge process began, the bath circulator simultaneously starts working. The bath circulator had a built-in function of delta T limiter, which kept the temperature difference between the PRT and the circulator fluid within 1.5K. In this way, the temperature difference of the battery and the environment was within 1.5K, so it created a nearly adiabatic condition. The temperature difference between the PRT and circulator fluid is shown in Figure 42 (b).Temperature increase of the battery was recorded, which was later associated with battery property and converted into heat generation rate.

3.1.2.2. Performance characterisation

An experimental set up was built to examine the battery performance at different conditions. A schematic of the experimental setup is shown in Figure 43. Before the experiment, each battery was tested by an ampere-hour integral method to assure the capacity of the batteries.

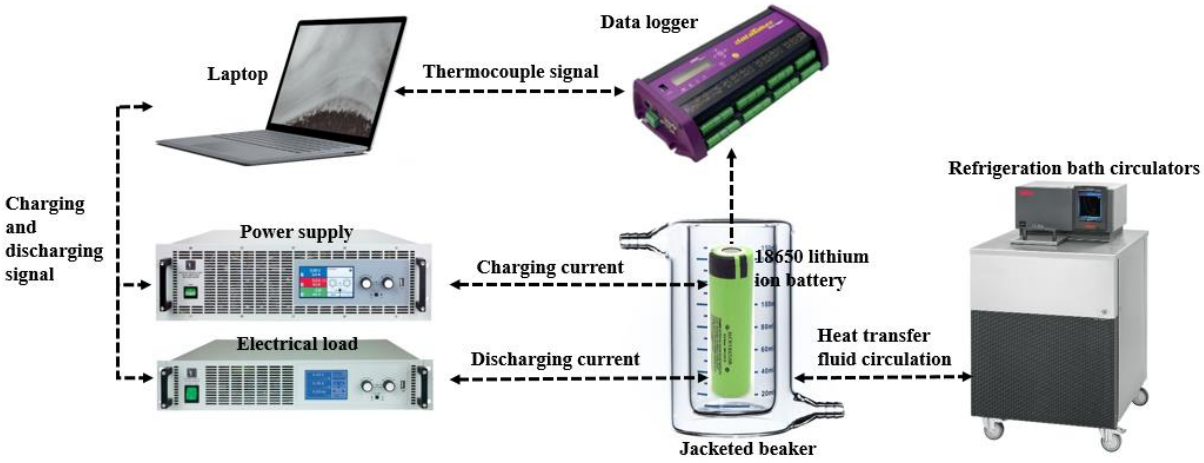

Figure 43 Schematic of the experimental setup for battery efficiency characterisation

Batteries were charged using a DC power supply (model: PS9000 2U, EA-Elektro-Automatik, error < 0.1%), and discharged using an electronic DC Load (model: EL9000B, EA-Elektro-

Automatik, error < 0.1%). The current and voltage were also recorded using the power supply, and the electronic load and the logging interval was set to 50ms. A data logger (model: DT85, Data Taker) was used to monitor the temperature of the lithium-ion battery. Each battery was attached with three thermocouples, and one additional thermocouple was used to record the ambient temperature. A refrigeration bath circulator (model: CC902, Huber) was connected with the jacketed beaker to control the ambient temperature of the lithium-ion battery. The battery was fully charged and discharged at 0.5C, 1C and 2C current rate during the test. The test temperatures of the cell were 20°C, 30°C, 40°C, 50°C, and 60°C. Through the discharge period, the cell was discharged at the galvanostatic mode until the voltage dropped to 2.5V. During the charge period, the single cell was first charged at the galvanostatic mode until it reached 4.17V, then followed by the potentiostatic mode until the current drops to 0.1 A. After each test, the battery was rested for 3 hours to allow the cell to return to a charging equilibrium condition before the next step of the test.

3.1.3. Battery thermal management device

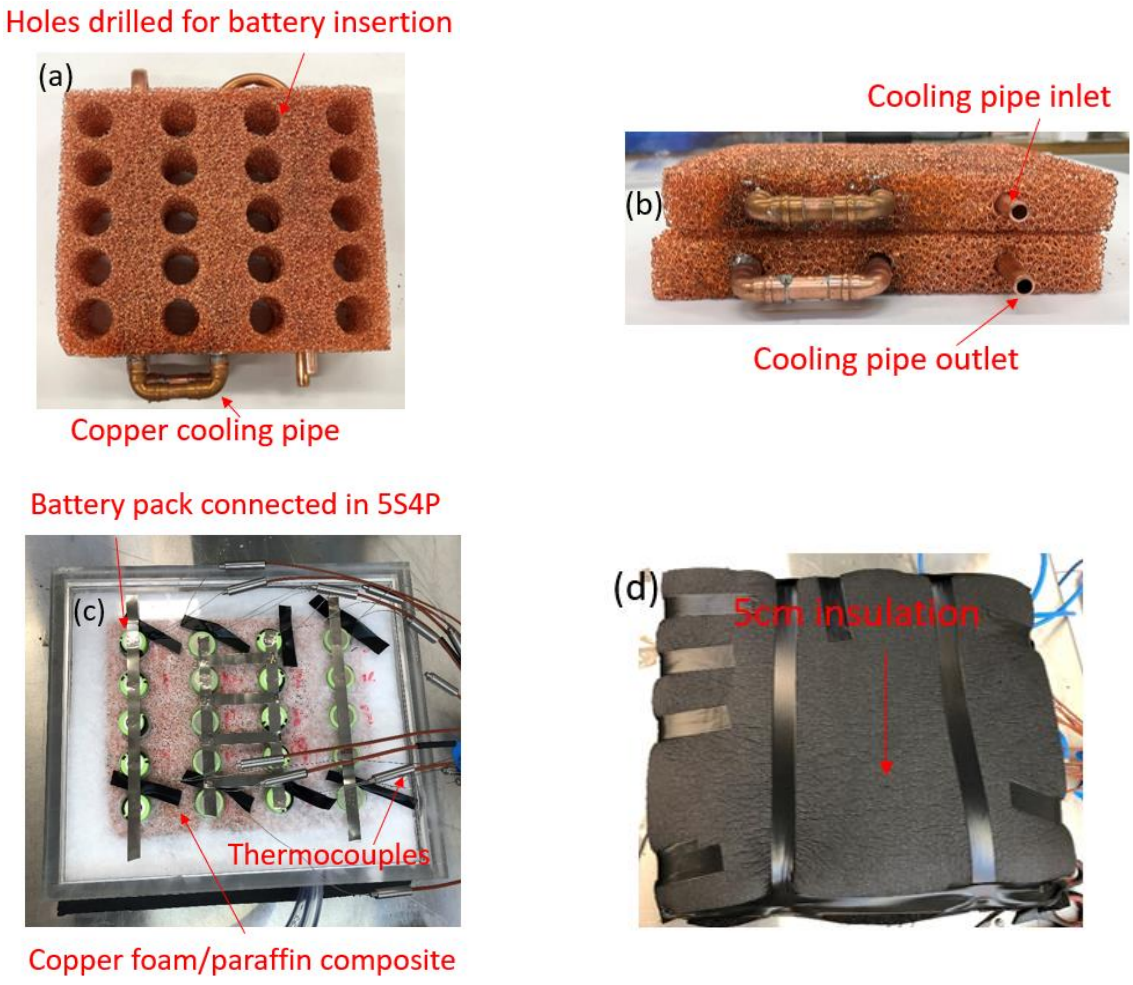

Figure 44 Photos of the devices set up. (a) top view of the copper foam and cooling pipe set up. (b) front view of the copper foam and cooling pipe set up (c) battery thermal management device (d) battery thermal management device with proper insulation

As shown in Figure 44 (a), two pieces of copper foam with a diameter of 180mm*150mm*30mm was used to build the matrix of the copper foam/paraffin composite. A single piece of copper foam with 65mm thickness was not able to manufacture. Hence two pieces with 32mm were chosen. Each copper foam was predrilled 20 holes with 20mm diameter from top to bottom for later battery insertion. Three holes with a diameter of 5mm were drilled on the copper foam from front to behind for the placement of copper pipes (Figure 44 (b)). The copper pipes were then inserted into the copper foam and welded as the channel for active water cooling. The two copper foams were then placed in an acrylic box. Cell 1, 6, 11, and 16 (layout is shown in Figure 46) were attached with two thermocouples near the top and bottom of the cylindrical. The two thermocouples were for measuring the top part and bottom part of the batteries. Batteries were then inserted into the copper foam and welded using spot welder to construct a battery pack connected in 4 in series and 5 in parallel. Liquid paraffin RT35HC were poured into the acrylic box (Physical property is shown in Table 6). The whole device was left in a vacuum oven at 40 °C overnight to ensure the full infiltration of paraffin into the copper foam (Figure 44 (c)). As shown in Figure 44 (d), eventually the device is insulated with 5cm foam insulation.

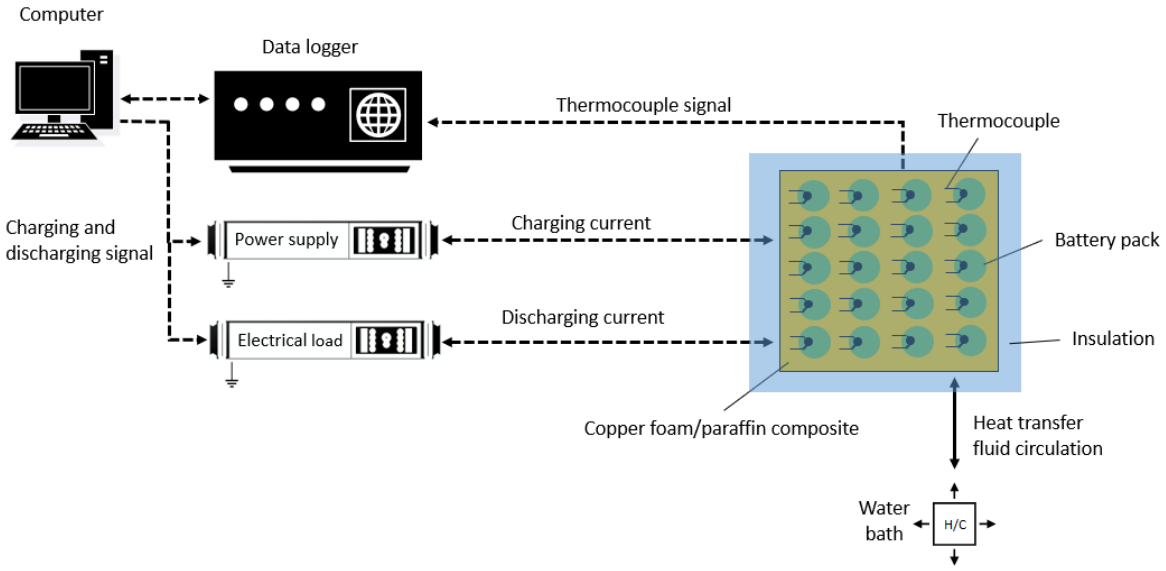

Figure 45 Schematic illustration of the battery thermal management device test setup

As shown in Figure 45, the test setup was like the thermal behaviour characterisation and efficiency characterisation set up (Figure 43). The DC power supply and the electronic DC Load were used to charge and discharge the battery pack, respectively. The DC power supply and electronic DC load were also used to record the current and voltage. A bath circulator was connected to the pipe to provide temperature control. Before each test, the bath circulator operated at the set temperature until the temperature of the whole device was controlled at the desired temperature. The battery pack was tested under 25°C. The battery pack was fully charged and discharged in each of the charge-discharge cycles. During charge, the batteries were first charged in the galvanostatic mode at a 0.5C rate (8A), with a voltage cut-off limit of 16.8V, followed by the potentiostatic mode until current drops to 325mA. Through the discharge process, the batteries were discharged in the galvanostatic mode at a 0.5C rate (8A) or 1C rate (16A), until the voltage drops to the discharge cut-off voltage (10.4V).

3.2. Model development

3.2.1. Physics model

As shown in Figure 46, a 3D numerical model was built based on the experimental set up of the battery thermal management device. The pipe arrangement was horizontal to the batteries in a parallel connection. Simulations started with an initial temperature of 298K throughout the domain. Water was used as the HTF with given inlet velocity of 0.02m/s, 0.01m/s, 0.005m/s, 0.003m/s and 0.001m/s. The BTMS was also studied without liquid cooling. Pressure outlet was set at the cooling channel outlet. The round copper pipes had 5mm in outer diameter, the volume of the copper pipes inside the CPCM module was 10598mm^3, and the heat transfer area of the between the outside round tube wall and the CPCM module was 8478mm^2.

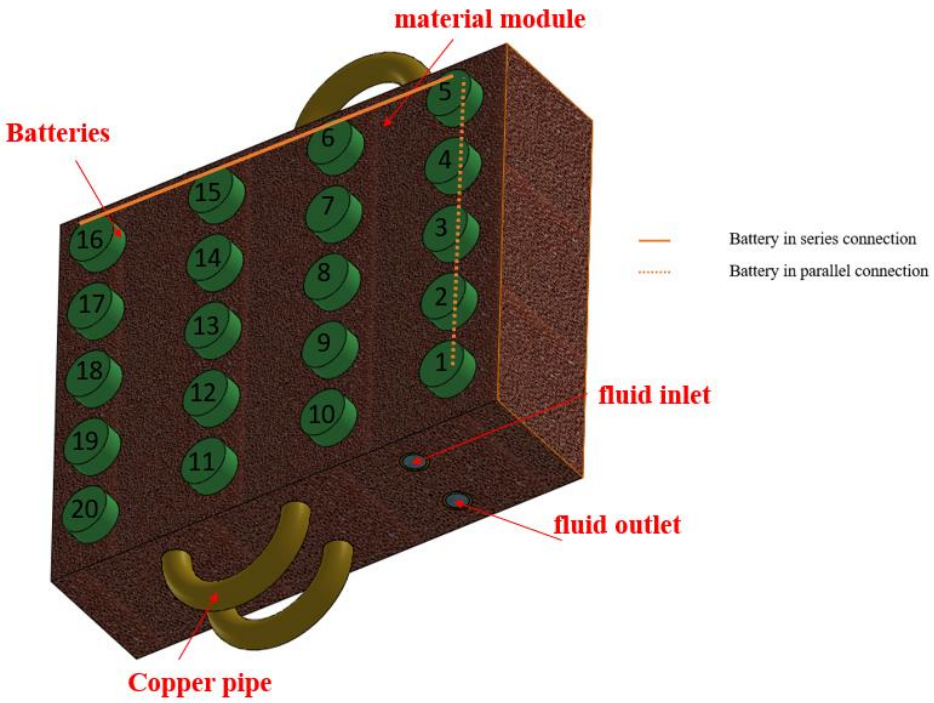

Figure 46 Schematic diagram of the 3D active cooling based BTMS with CPCM using round pipes

As shown in Figure 47, a different 2D model based on tabular pipes with higher heat transfer area and higher copper foam volume was also built. The tabular pipes had 2mm in width and 65mm in height, the volume inside the CPCM module was 58500mm^3, which was 5.5 times of the round tube. The heat transfer area between the tabular tube and the CPCM was 58500mm^2, which was 7 times of the round tube. The BTMS module is similar to Tesla's BTMS, which has been regarded as safe and efficient under fast charging conditions. A battery pack which contains 20 cylindrical cells was placed in the BTMS module. The ribbon-shaped metallic cooling channel with a width of 2mm was used, which snaked through the battery pack. The cooling channel arrangement was horizontal to the batteries in series connection. Cells have gaps of 7.8 mm in horizontal direction and 3.6mm in vertical direction. The gaps between the batteries and the cooling pipe were filled with CPCM. The heat generated from the individual cells was transferred to the CPCM first, then to the cooling liquid flowing through the cooling pipe. The battery cells were indicated as Cell 1 to Cell 20. Simulations started with an initial temperature of 298K throughout the domain. Water was used as the HTF with given inlet velocity of 0.1m/s, 0.01m/s and 0.001m/s. Pressure outlet was set at the cooling channel outlet.

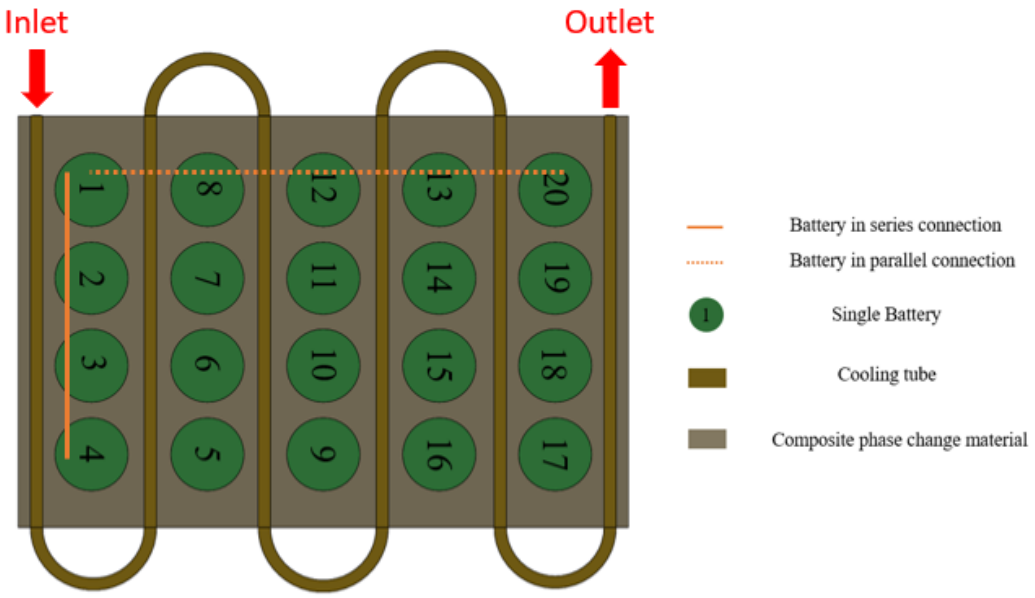

Figure 47 Schematic diagram of the 2D active cooling based BTMS with CPCM using tabular pipes

Two paraffin-based CPCMs were studied, one with EG and the other with copper foam as thermal enhancement materials. The 25wt% EG/75wt% PCM composite was considered, and the copper foam with 92% porosity was used in the copper foam/PCM composite. The thermophysical properties of the materials are summarised in Table 10.

Table 10 Thermophysical properties of paraffin, EG/paraffin composite, and copper

	Paraffin	**Large particle size expanded graphite/Paraffin**	**Copper**
Melting temperature (K)	308	308	
Latent heat (kJ/kg)	210	175	
Thermal conductivity(W/m·K)	0.2	3.59	385
Liquid phase density (kg/m^3)	770	1000	
Solid phase density (kg/m^3)	880	1000	8920
Specific heat (j/kg·K)	2000	1790	380

Viscosity in the liquid state (kg/m. s)	0.005

3.2.2. Mathematical model

The mathematical model is established using the following assumptions:

- The thermophysical properties of the CPCMs are considered as isotropic and homogeneous.
- The heat generation in the battery is regarded as being uniformly distributed.
- The top, bottom and surroundings of the BTMS module are assumed to be adiabatic.

Based on these assumptions, the continuity, momentum and energy equations are written as follows:

The mass balance for 2D modelling:

$$\frac{\partial \rho}{\partial t} + \frac{\partial (\rho u)}{\partial x} + \frac{\partial (\rho v)}{\partial y} = 0 \tag{18}$$

The mass balance for the 3D modelling:

$$\frac{\partial \rho}{\partial t} + \frac{\partial (\rho u)}{\partial x} + \frac{\partial (\rho v)}{\partial y} + \frac{\partial (\rho w)}{\partial z} = 0 \tag{19}$$

The momentum balance for the 2D modelling:

$$\text{X-direction} \quad \rho\left(\frac{\partial u}{\partial t} + u\frac{\partial u}{\partial x} + v\frac{\partial u}{\partial y}\right) = \mu\left(\frac{\partial^2 u}{\partial x^2} + \frac{\partial^2 u}{\partial y^2}\right) - \frac{\partial P}{\partial x} + S_x \tag{20}$$

$$\text{Y-direction} \quad \rho\left(\frac{\partial v}{\partial t} + u\frac{\partial v}{\partial x} + v\frac{\partial v}{\partial y}\right) = \mu\left(\frac{\partial^2 v}{\partial x^2} + \frac{\partial^2 v}{\partial y^2}\right) - \frac{\partial P}{\partial y} + S_y \tag{21}$$

The momentum balance for the 3D modelling:

$$\text{X-direction} \quad \rho\left(\frac{\partial u}{\partial t} + u\frac{\partial u}{\partial x} + v\frac{\partial u}{\partial y} + w\frac{\partial u}{\partial z}\right) = \mu\left(\frac{\partial^2 u}{\partial x^2} + \frac{\partial^2 u}{\partial y^2} + \frac{\partial^2 u}{\partial z^2}\right) - \frac{\partial P}{\partial x} + S_x \tag{22}$$

$$\text{Y-direction} \quad \rho\left(\frac{\partial v}{\partial t} + u\frac{\partial v}{\partial x} + v\frac{\partial v}{\partial y} + w\frac{\partial v}{\partial z}\right) = \mu\left(\frac{\partial^2 v}{\partial x^2} + \frac{\partial^2 v}{\partial y^2} + \frac{\partial^2 v}{\partial z^2}\right) - \frac{\partial P}{\partial y} + S_y \tag{23}$$

$$\text{Z-direction} \quad \rho\left(\frac{\partial w}{\partial t} + u\frac{\partial w}{\partial x} + v\frac{\partial w}{\partial y} + w\frac{\partial w}{\partial z}\right) = \mu\left(\frac{\partial^2 w}{\partial x^2} + \frac{\partial^2 w}{\partial y^2} + \frac{\partial^2 w}{\partial z^2}\right) - \frac{\partial P}{\partial z} + S_z \tag{24}$$

The energy balance:

$$\text{EG-PCM composite for 2D modelling:} \quad \frac{\partial (\rho_c H_c)}{\partial t} = \frac{\partial}{\partial x}\left(k_c \frac{\partial T_c}{\partial x}\right) + \frac{\partial}{\partial y}\left(k_c \frac{\partial T_c}{\partial y}\right) \tag{25}$$

Metal foam/PCM composite - PCM zone for 2D modelling:

$$\varepsilon(\rho c)_{pcm}\frac{\partial T_p}{\partial t}+\varepsilon(\rho c)_{pcm}\left(u\frac{\partial T_{pcm}}{\partial x}+v\frac{\partial T_{pcm}}{\partial y}\right)=k_{pcm}\left(\frac{\partial^2 T_{pcm}}{\partial x^2}+\frac{\partial^2 T_{pcm}}{\partial y^2}\right)+h_{sf}A_{sf}\left(T_{pcm}-T_{me}\right)-\varepsilon\rho_{pcm}L\frac{\partial\beta}{\partial t} \quad (26)$$

PCM zone for 3D modelling:

$$\varepsilon(\rho c)_{pcm}\frac{\partial T_p}{\partial t}+\varepsilon(\rho c)_{pcm}\left(u\frac{\partial T_{pcm}}{\partial x}+v\frac{\partial T_{pcm}}{\partial y}+w\frac{\partial T_{pcm}}{\partial z}\right)=k_{pcm}\left(\frac{\partial^2 T_{pcm}}{\partial x^2}+\frac{\partial^2 T_{pcm}}{\partial y^2}+\frac{\partial^2 T_{pcm}}{\partial z^2}\right)+h_{sf}A_{sf}\left(T_{pcm}-T_{me}\right)-\varepsilon\rho_{pcm}L\frac{\partial\beta}{\partial t} \quad (27)$$

For metal foam/PCM composite - metal foam zone for 2D modelling:

$$(1-\varepsilon)(\rho c)_{me}\frac{\partial T_{me}}{\partial t}=k_{me}\left(\frac{\partial^2 T_{me}}{\partial x^2}+\frac{\partial^2 T_{me}}{\partial y^2}\right)+h_{sf}A_{sf}\left(T_{me}-T_{pcm}\right) \quad (28)$$

metal foam zone for 3D modelling:

$$(1-\varepsilon)(\rho c)_{me}\frac{\partial T_{me}}{\partial t}=k_{me}\left(\frac{\partial^2 T_{me}}{\partial x^2}+\frac{\partial^2 T_{me}}{\partial y^2}+\frac{\partial^2 T_{me}}{\partial z^2}\right)+h_{sf}A_{sf}\left(T_{me}-T_{pcm}\right) \quad (29)$$

The phase-transition of the PCM was solved with the enthalpy-porosity approach [204], and the melting and solidifying processes were simulated with the melting and solidification model. The natural convection and thermal radiation that occurred within the CPCM are neglected due to confinement of the PCM in the interparticle voids of the EG/PCM composite [205]. The non-equilibrium thermal model was employed for describing heat transfer phenomenon in the metal foam based CPCM, with the energy equations solved separately for porous media and PCM [206]. Among the above equations, ρ is the density; u, v and w stand for the x, y and z coordinates velocities, respectively; subscripts of f, c and me respectively represent the HTF, composite and metal foam; k is the thermal conductivity; ε is metal foam porosity; h_{sf} and A_{sf} refer to the local heat transfer coefficient and the surface, respectively;

H relates to the enthalpy sum of the sensible (h) and latent forms (ΔH):

$$H=h+\Delta H \quad (30)$$

$$h=h_{ref}+\int_{T_{ref}}^{T}C_p\,dT \quad (31)$$

$$\Delta H=\beta L \quad (32)$$

$$\beta = \begin{cases} 0 & if\ T_{pcm} \le T_s \\ \frac{T_{pcm}-T_s}{T_l-T_s} & if\ T_s \le T_{pcm} \le T_l \\ 1 & if\ T_{pcm} \ge T_l \end{cases} \quad (33)$$

where h_{ref}, T_{ref} and C_p are the reference enthalpy, the reference temperature and the specific heat of PCM at constant pressure, respectively, and L is the latent heat, β is the liquid fraction; S_x, S_y, and S_z are momentum sink given by of $S_i = Cu_i(1-\beta)^2/(\beta^3+\gamma)$ with *i= x, y, or z*; C is a constant reflecting of the mushy zone, and a numerical number of 10^5 is assigned in this study; γ refers to a small constant that used to avoid division by zero.

A few parameters for the metal foam/paraffin composite has been evaluated before solving the above equations, and they are summarised as follows. First, the metal foam and PCM effective thermal conductivities of k_{me} and k_{pcm} are calculated using a three-structured model [207]:

$$k_{pcm} = k_{eff} = \frac{\sqrt{2}}{2(R_A+R_B+R_B+R_D)}\Big|_{k_{me}=0} \quad (34)$$

$$k_{me} = k_{eff} = \frac{\sqrt{2}}{2(R_A+R_B+R_B+R_D)}\Big|_{k_{pcm}=0} \quad (35)$$

$$R_A = \frac{4\sigma}{(2e^2+\pi\sigma(1-e))k_{me}+(4-2e^2-\pi\sigma(1-e))k_{pcm}} \quad (36)$$

$$R_B = \frac{(e-2\sigma)^2}{(e-2\sigma)e^2k_{me}+(2e-4\sigma-(e-2\sigma)e^2)k_{pcm}} \quad (37)$$

$$R_C = \frac{(\sqrt{2}-2e)^2}{2\pi\sigma^2(1-2e\sqrt{2})k_{me}+2(\sqrt{2}-2e-\pi\sigma^2(1-2e\sqrt{2}))k_{pcm}} \quad (38)$$

$$R_D = \frac{2e}{e^2k_{me}+(4-e^2)k_{pcm}} \quad (39)$$

$$\sigma = \sqrt{\frac{\sqrt{2}(2-(5/8)e^3\sqrt{2}-2\varepsilon)}{\pi(3-4e\sqrt{2}-e)}} \quad (40)$$

$$e = 0.339 \quad (41)$$

Second, the structural characteristics of metal foam including permeability, *A*, inertia coefficient, C_i, and porosity (ε)-pore density (ω)-ligament diameter (d_f) relationship, they can be determined by the following equations [208]:

$$\frac{A}{d_p^2} = 0.00073(1-\varepsilon)^{-0.224}\left(\frac{d_f}{d_p}\right)^{-1.11} \quad (42)$$

$$C_i = 0.00212(1-\varepsilon)^{-0.132}\left(\frac{d_f}{d_p}\right)^{-1.63} \tag{43}$$

$$\frac{d_f}{d_p} = 1.18\sqrt{\frac{1-\varepsilon}{3\pi}\left(\frac{1}{1-e^{-(1-\varepsilon)/0.04}}\right)} \tag{44}$$

$$d_p = \frac{0.0254}{\omega} \tag{45}$$

Last, the local heat transfer coefficient between the PCM and copper foam, h_{sf}, and interfacial surface area, A_{sf}, they are from Zhukauskas's model and Calmidi and Mahajan's model [207,208].

$$h_{sf} = \begin{cases} \frac{0.76Re_d^{0.4}Pr^{0.73}k_{pcm}}{d_f} & 1 \le Re_d \le 40 \\ \frac{0.76Re_d^{0.4}Pr^{0.73}k_{pcm}}{d_f} & 40 \le Re_d \le 10^3 \\ \frac{0.76Re_d^{0.4}Pr^{0.73}k_{pcm}}{d_f} & 10^3 \le Re_d \le 2\times 10^5 \end{cases} \tag{46}$$

$$Re_d = \rho\sqrt{u^2+v^2}\frac{d_f}{\varepsilon\mu} \tag{47}$$

$$A_{sf} = \frac{3\pi d_f(1-e^{-(1-\varepsilon)/0.04})}{(0.59d_p)^2} \tag{48}$$

3.2.3. Modelling details and model validation

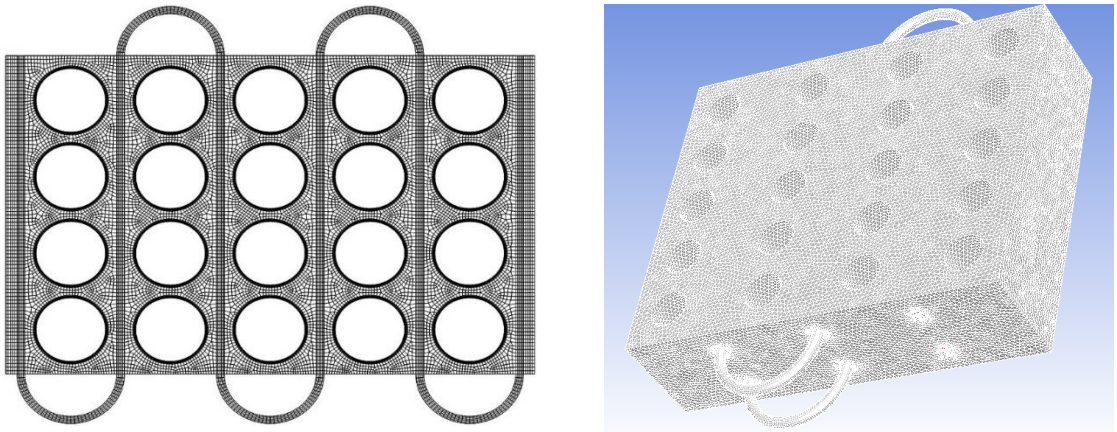

(a) (b)

Figure 48 Meshing of the computational domain (a) 2D modelling (b) 3D modelling

Figure 48 shows the meshing of the modelling domain. The 2D meshing was established using the grid of combined structured and unstructured cells by the Gambit software, and the 3D meshing was built by the meshing function in Ansys® meshing. Different mesh sizes were

examined, and the results showed that a total of 24,198 cells for the 2D modelling, which were able to ensure the grid independence without consuming too much computational resource. A total of 2,169,322 cells were used for 3D modelling. The whole computational domain was initially set at a temperature of T_i which was the same as the experimental value, and a zero velocity. A velocity inlet boundary was defined where the HTF velocity and temperature were set as constant. At the outlet, a fully developed outflow condition was performed. The interfaces between the fluid pipe and PCM as well as that between the PCM and battery cells were set as coupled-wall boundary conditions for heat transfer. Insulated boundary conditions were assumed for the outside walls of the modelling domain. A commercial software of Ansys Fluent was used for the modelling, and software of Gambit was adopted for mesh generating. The User Define Function files were interpreted to calculate the HTF thermophysical properties and also the PCM-metal foam interfacial heat transfer coefficient. The scheme of Second-Order Upwind was employed to solve the momentum and energy equations, and Pressure Staggering Option Scheme was used for pressure correction. The Under-Relaxation factors of 0.5, 1, 0.3 and 0.9 were respectively taken for the velocity, energy, pressure correction and liquid fraction. The time-step effect on the calculation was attentively checked before the modelling. The calculation convergence was evaluated at each time step, and the residuals were below 10^{-4} under all calculation conditions, and the energy residuals were less than 10^{-6} when converged.

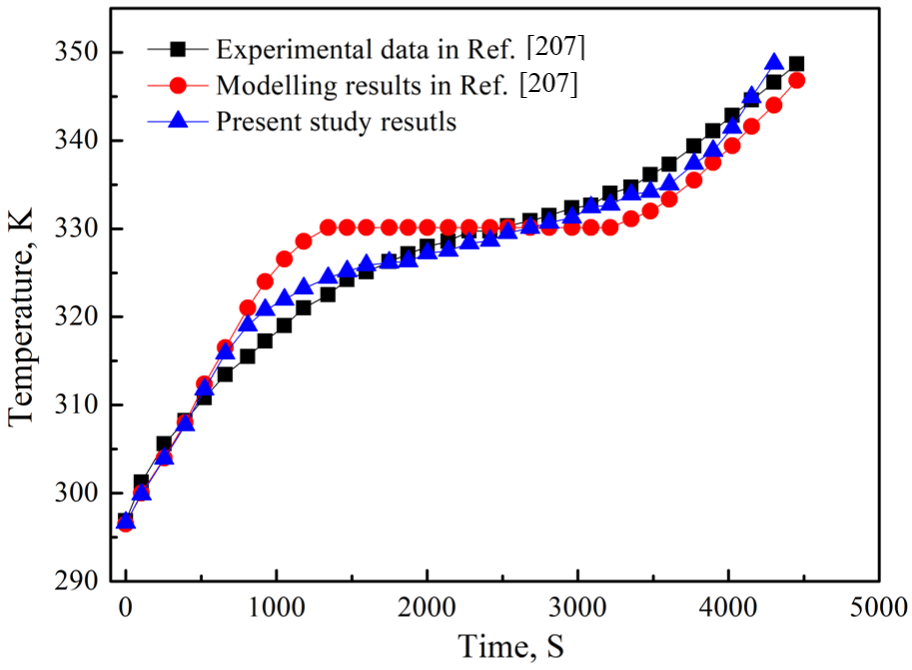

Figure 49 Comparison between numerical modelling and experimental results from Zhao et al. [207] **for metal foam/PCM composite**

To ensure the reliability and confidence of the numerical model for the metal foam/PCM composite, a validation simulation based on the 2D model was carried out to compare the modelling results with experimental literature data. The modelling case based on the work reported by Zhao et al. [207] was run for a rectangular configuration (0.2 × 0.025 m) containing metal foam embedded with paraffin wax as the PCM. The numerical code for the validation was the same as that for this study. During the comparison, the initial temperature for the whole computational area was set as 20 °C, and the heat flux was kept as 1.6 kW/m^2. As shown in Figure 49, a reasonable good agreement between the modelling and experiments has been achieved, giving the confidence in the use of the models and the numerical methods as described above for the present study. An investigation on the copper foam/paraffin composite, which was detailed discussed in chapter 4 also validates the copper foam/paraffin model.

Chapter 4 Characterization of composite phase change materials

In this chapter, three different composite phase change materials were studied for their thermal properties, microstructures, surface morphologies and safety improvement. The particle size effect of expanded graphite on the thermal properties of the expanded graphite/paraffin composites was investigated first. The thermal conductivity of the copper foam/paraffin composites was then also experimentally measured, which was used for the numerical modelling work. The flame retardancy of the colloidal/paraffin composites was improved with the addition of the melamine. The research on expanded graphite [209] has been previously published in Applied Thermal Engineering in 2020.

4.1. Expanded graphite /paraffin composite phase change materials

4.1.1. Microstructure of the composites

4.1.1.1. Morphology observations

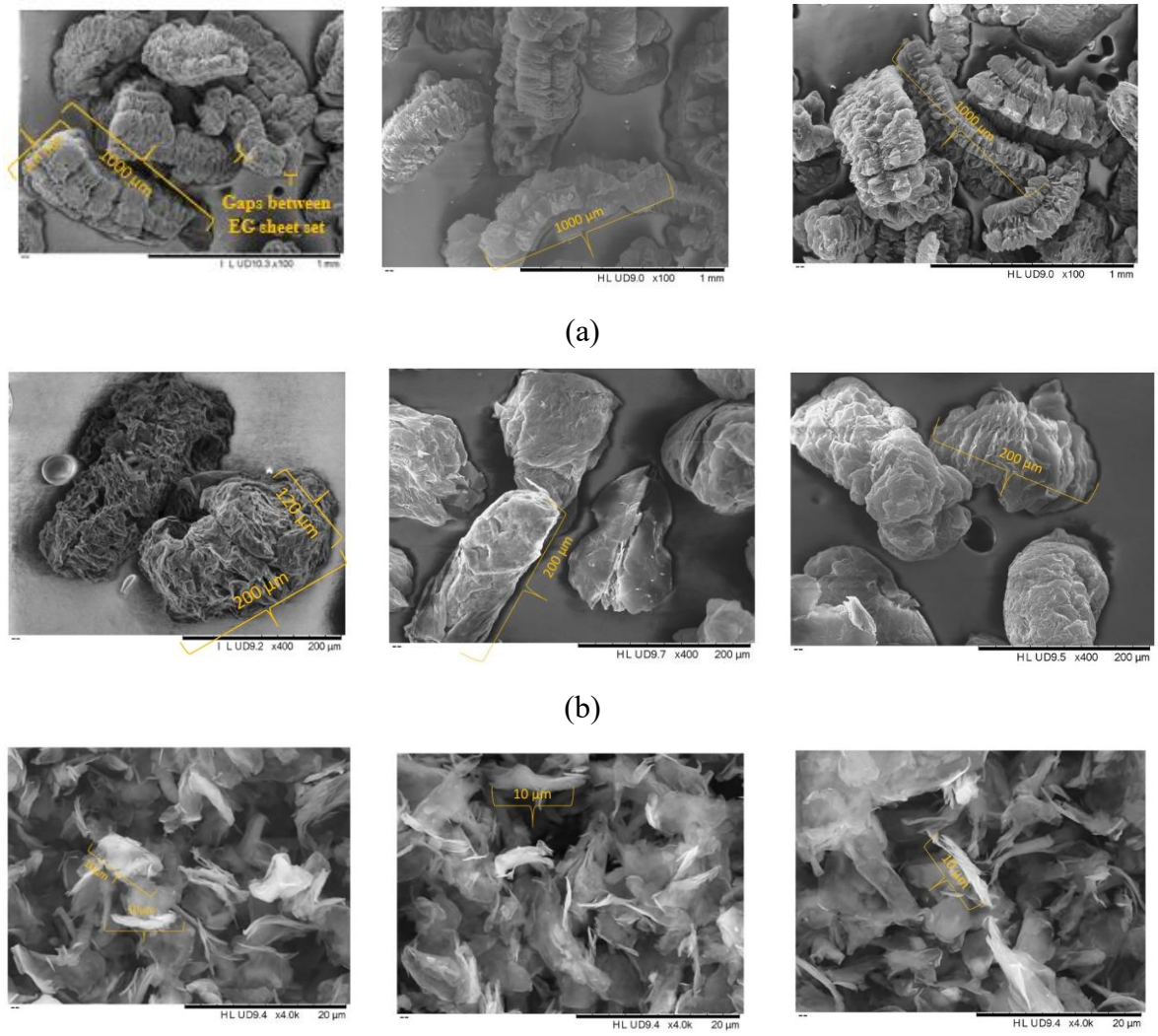

(a)

(b)

(c)

Figure 50 Particle size observation of different EG particles: (a) EG1, (b) EG2, (c) EG3

Figure 50 shows SEM images of the purchased EG particles. A distinct difference in the morphology can be observed between EG3 and the other two EGs. EG1 and EG2 are in large micrometres scale with a loose vermicular shape. On the surface of EG1, sets of graphite sheets are seen in parallel, with gaps with an approximate size of (30µm × 200 µm) in between each of graphite sheet sets. EG3 are micro-scale and take the form of graphite sheets arranged irregularly.

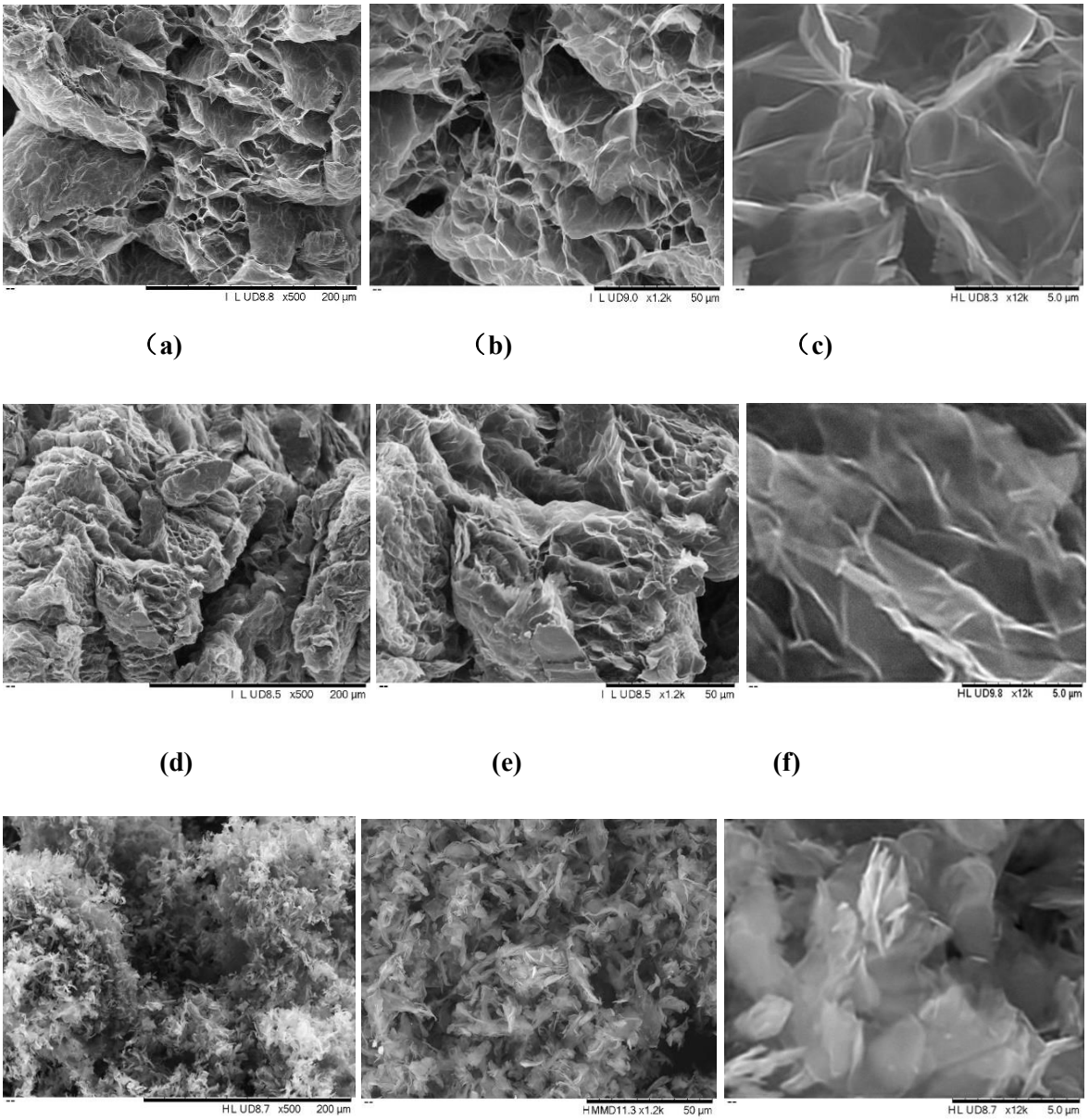

Figure 51 Pores of varied sizes on the surface of infiltrated EG1, EG2 and EG3 particles. (a) EG1 (×500) (b) EG1 (×1200) (c) EG1 (×12000); (d) EG2 (×500) (e) EG2 (×1200) (f) EG2 (×12000); (g) EG3 (×500) (h) EG3 (×1200) (i) EG3 (×12000)

Continually zooming into the surface of EG1 and EG2 particles, as shown in Figure 51, pores with varying sizes in a range of 1-60 µm are apparent. These pores intersect with each other, forming an irregular networking structure. However, when the particle size of the EGs is reduced to a low micrometre scale (i.e. EG3), there is a lack of the connected networking

structure, and particles are primarily in the form of loose graphite sheets, see Figure 51 (g, h and i).

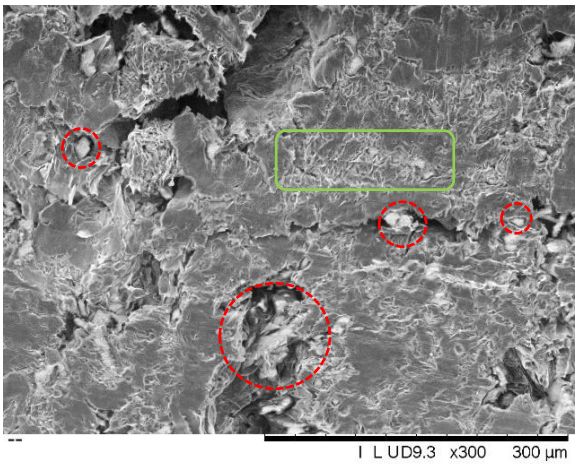

(a)

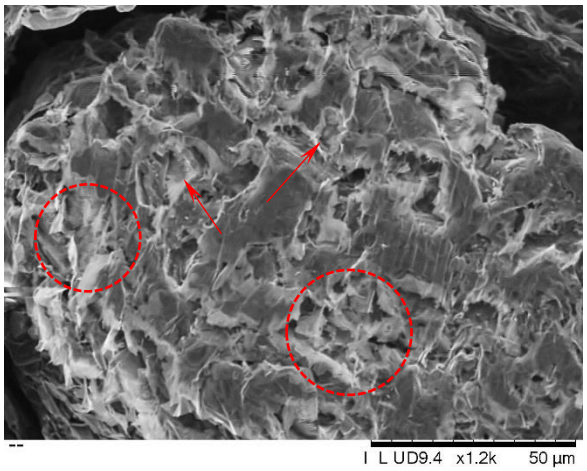

(b)

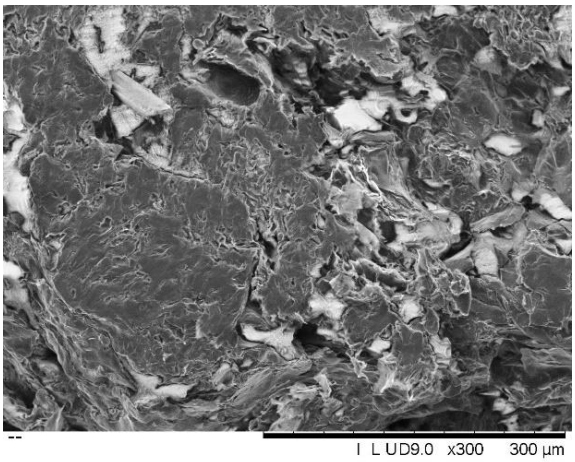

(c)

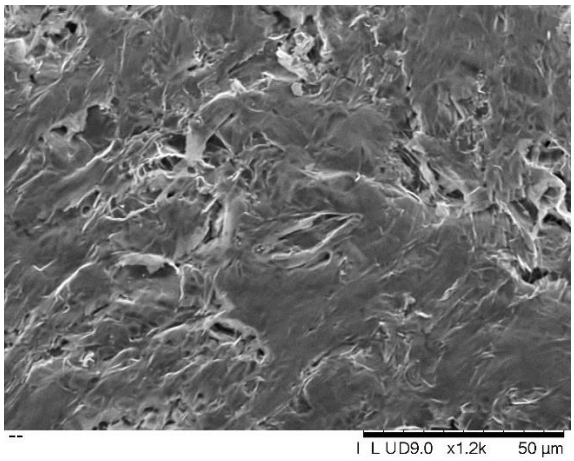

(d)

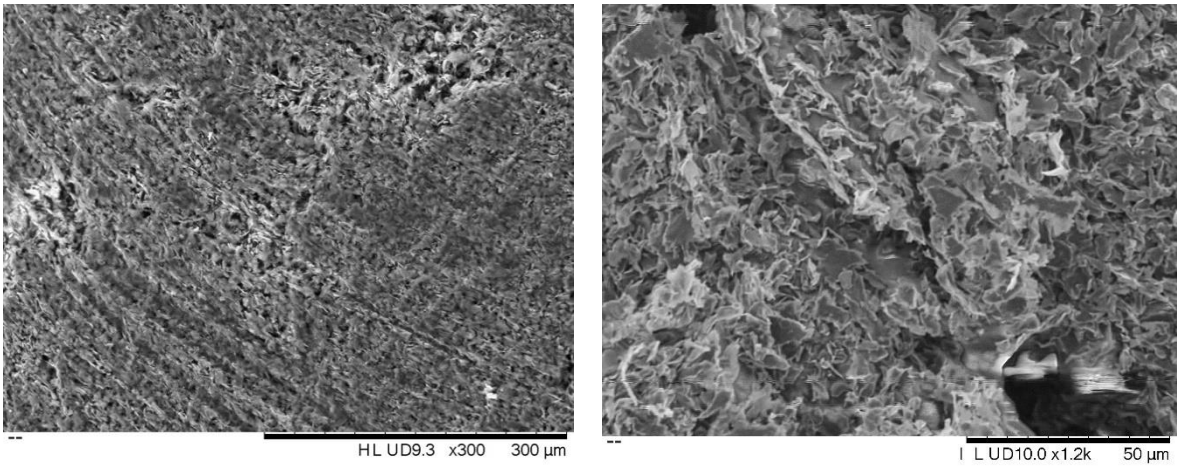

(e) **(f)**

Figure 52 Cross-sectional positions of composites at different magnification. Light area- RT28HC, Dark area- EG (a) EG1 Composite, ×300. (b) EG1 Composite, ×1200. (c) EG2 Composite, ×300. (d) EG2 Composite, ×1200. (e) EG3 Composite, ×300. (f) EG3 Composite, ×1200.

Figure 52 presents the cross-sectional positions of the composite tablets made from different types of EGs. Paraffin is seen to exhibit good compatibility with EGs, and when paraffin is confined in the graphite pores interaction is likely to occur between the paraffin and graphite layer. Patrik et al. [210] carried out a detailed X-ray diffraction study on low-density polyethene, paraffin and expanded graphite composites. Their results suggested the partial intercalation of the paraffin wax chains between the graphite layers. The highest intercalation was observed with the highest amount of EG and paraffin wax. The existence of the various pore sizes in the EG matrixes, especially of EG1 and EG2, is therefore considered to contribute to the adsorption of most of the paraffin.

These different structural arrangements of EGs have a great impact on paraffin absorption. The SEM pictures (Figure 52) indicate that composites based on EG1 and EG2 behave differently towards paraffin, compared with composites based on EG3. For composites made from EG1 and EG2, paraffin is absorbed into large pores and the gaps among EG particles, crystallised and aggregated into big particles (see Figure 52 a and c). In addition to this, owing to the capillary force, a mass of the paraffin is seemed to be retained in relatively small pores of the networked structures. In these circumstances, the morphology of paraffin appears to be in needle shapes as indicated in the green area of Figure 52 a. Moreover, the paraffin can be easily impregnated into the void and pore structures of the large micro size EG, also due to the high

wetting ability of paraffin in the liquid phase. Li et al. [211] observed the EG with 180 μm size formed a large number of microvoids on the EG. The voids were constituted by parallel and collapsed layers, which were concluded by them to be a key reason for the EG's excellent adsorption.

On the contrary, by reasoning of lacking the compact networked structure, the capability of the absorption reduced a great extent. Only a small amount of the PCM was confined in the voids formed among loosed EG3 particles. Most of the paraffin sit on the surface of graphite sheets, so largely white colour can be seen in Figure 52 (e) and (f).

The compact networked structure of EG1 and EG2 matrixes are expected to provide good thermal behaviour to the composites. While in the case of EG3 composites, interfacial thermal resistance is expected among the small particles, which would hinder the heat transfer among the composites. Subsequently, the phase change temperature, thermal conductivity and thermal degradation temperature are expected to be affected by the structures, which will be discussed in the following chapters with evidence.

4.1.1.2. 3D structural characterization of the pure EG matrix and paraffin/EG composites

Pure EG matrix made of different particle sizes were imaged in 3D using the Nano-CT system (XRT). The porosity and specific surface area of the EG matrixes were obtained from the 3D binary images (see Table 11). It was found that EG1 and EG2 have a relatively large porosity and a high specific area compared with EG3.

Table 11 Structure parameters of the pure EG matrix.

Material	Porosity (%)	Specific area (1/mm)
EG1	38.01	13.07
EG2	30.06	11.86
EG3	18.03	9.04

The pore size distribution of different pure EG matrixes before the absorption is shown in Figure 53 (a). It illustrates that EG3 has a relatively narrow porosity distribution. The pore size of EG3 is also relatively small, sitting within 27-180 μm. The pore sizes of EG1 and EG2

mainly locate in the range of 135 - 243 µm, which are relatively larger than the EG3 matrix. The latter one mostly consists of small particles without significant compact pore structure. These small particles are loosely arranged to form unconnected voids (see Figure 51 g-i), the void size is relatively small, compared with the porous structure in EG1 and EG2 matrixes. These observations can also be confirmed by SEM images. EG/paraffin composites were also studied preliminarily. The 3D surface-rendered models are shown in Figure 53 (b). Different material components are visualised in different colours according to the material density (x-ray opacity). The brown colour indicates a low density which is EG, and the blue colour denotes a high density which is paraffin. The results demonstrate the impact of particle size on the EG matrix/PCM absorption. The pronounced colour difference illustrates that EG matrixes with a connected porous structure have a better capability for PCM uptake and confinement. EG1 and EG2 have connected pore structures, and PCM are confined in the pores of EG. Hence few blue coloured zones are observed at the cross-section of the 3D model. However, in the case of composites with EG3, PCM is not observed in pores but held in the void between small EG particles. The cross-section of the 3D model corresponds to blue colour, which is paraffin, indicating the bad uptake of paraffin into the EG.

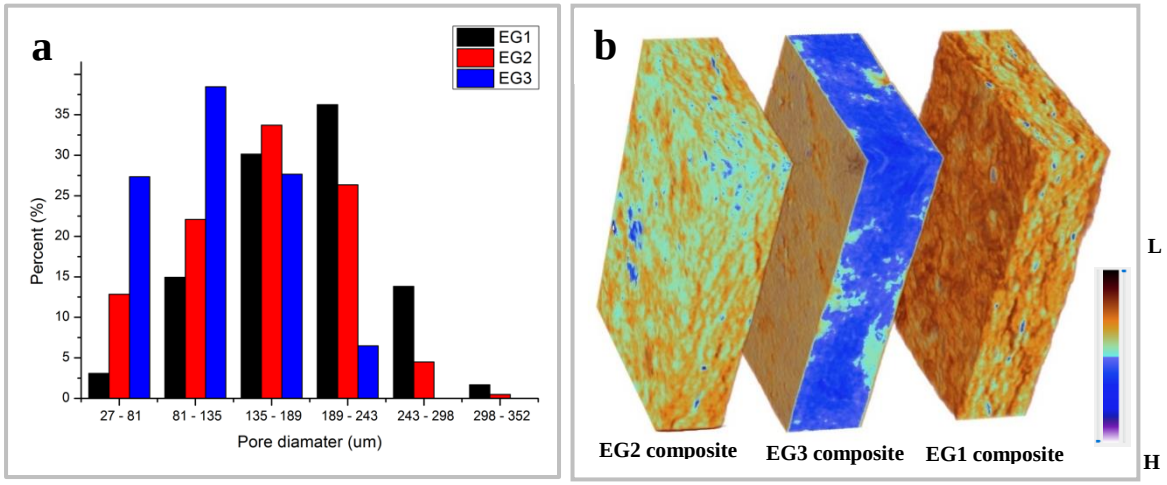

Figure 53 (a) Pore size distribution of EG matrixes, calculated from the binary images (b) 3d surface-rendered models of the cross-section of EG/Paraffin composite with 25wt% of EG loading (brown to blue scale bar indicates the density changing from low to high)

4.1.2. Thermal characterization

4.1.2.1. Phase change behaviour study

The phase change temperature of the composites is affected by both thermal conductivity and the porous structure of the EGs in a complex manner. The melting peak temperature ($T_{p,m}$) and

solidification peak temperature ($T_{p,s}$) are chosen for illustrating the melting and solidification behaviours of the composites. It should be mentioned that the following analysis is only valid for a small size sample which is discussed in this paper. For a scaled-up system (e.g. in the application with a full-size EV battery system), the phase change behaviour might be different due to different heat transfer and kinetics.

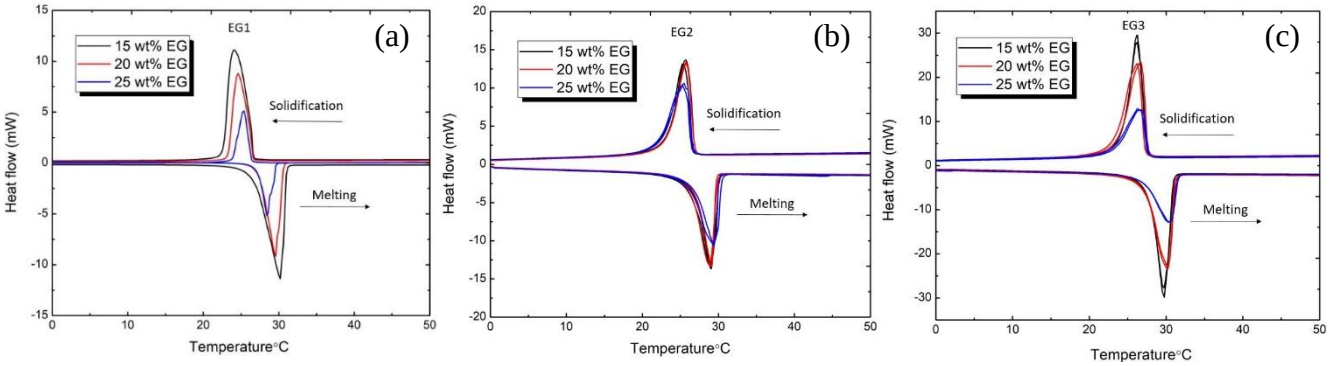

Figure 54 DSC scanning curve for EG based composites. (a) EG1 based composites (b) EG2 based composites (c) EG3 based composites (sample mass for DSC measurement were different hence the heat flow does not always increase with the increase of the mass ratio of paraffin)

Figure 54 shows the DSC results of the composites, which displays the well-defined peaks, which are associated with the melting and solidification processes. The position of the peaks varies with the different mass contents of EGs.

Table 12 Peak melting temperatures obtained from DSC measurement

Material		$T_{p,m}$ (°C)	$T_{p,s}$ (°C)	ΔT= $T_{p,m}$-$T_{p,s}$
EG1	15wt%	29.9	24.33	5.57
	20wt%	29.45	24.77	4.68
	25wt%	28.32	25.48	2.84
EG2	15wt%	28.85	23.31	5.54
	20wt%	28.38	24.62	3.76
	25wt%	28.16	24.75	3.41

EG3	15wt%	28.19	25.79	2.4
	20wt%	28.17	26.34	1.83
	25wt%	28.16	25.72	2.44
RT28HC		28.02	26.24	1.78

Table 12 gives the peak temperatures obtained from the DSC measurements and their differences. It can be found that the maximum differences of $T_{p,m}$ and $T_{p,s}$ between the composites and the raw PCM are 1.88 and 2.93 °C, respectively. The $T_{p,m}$ of both EG1 and EG2 based composites is increased compared with the pure RT28HC. In contrast to the $T_{p,m}$, the shift of the $T_{p,s}$ of EG1 and EG2 from bulk RT28HC is negative. Pronounced hysteresis between solidification and melting is observed in the present of EG. The temperature difference (ΔT) between $T_{p,m}$ and $T_{p,s}$ of the composites increases by up to 3.79 °C, compared with the raw PCM. The shift on the phase change temperature of the PCM has also been observed by some other researchers [212–214].

The change of the phase change behaviour could be affected by the interface between the PCM surface and the pore surface. Alkane form solid adsorbed monolayers at a graphite surface, which can affect the interfacial phenomena of adhesion. A strong interaction between the PCM surface and the pore surface can give an elevated melting temperature and depressed solidification temperature.

From the above, one can see that the structure of the confined PCM is relevant to the melting and freezing temperature. As observed in this study, EG matrix has a tight network structure. The pore networking effect influences the hysteresis. The interconnected pores affect the melting and solidification of the PCM and cause a large hysteresis, leading to different thermal properties, compared with the pure PCM.

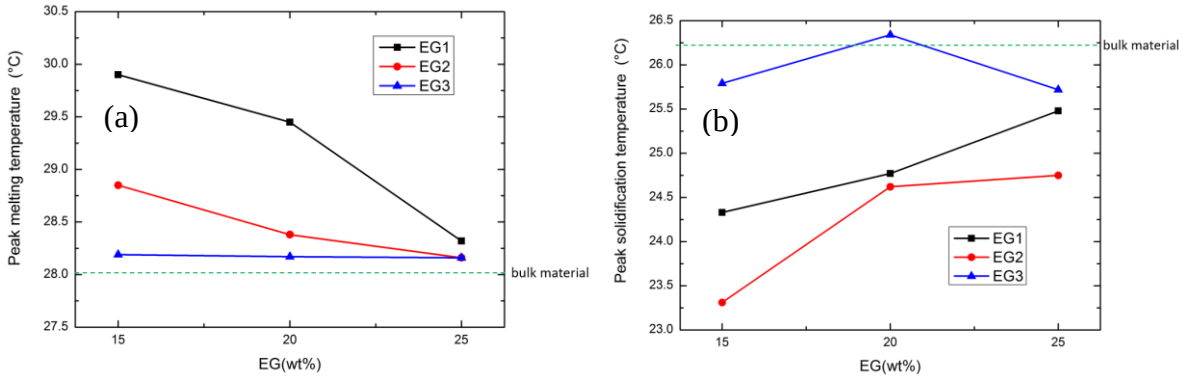

Figure 55 Melting and solidification peak temperatures of EG based composites in comparison with the bulk PCM

The morphology of EG is not the only factor that affects the phase change temperature of the PCM. Figure 55 illustrates the impact of the EG content on the PCM phase change behaviour. The melting temperature of the EG1 and EG2 based composites decreases with the increase of EG mass percentage, with the composites containing 25wt% EG content having the lowest $T_{p,m}$, close to the $T_{p,m}$ of the pure PCM. The $T_{p,s}$ in this case increases with increasing mass percentage of the EG. $T_{p,s}$ of the composites with 25wt% EG content is also close to the $T_{p,s}$ of the pure PCM. Hence the hysteresis of EG1 and EG2 based composites reduces with increasing EG content.

The difference in the thermal conductivity of composites is expected to contribute to the differences discussed above. As increased EG content increases the thermal conductivity of composites, strengthening the heat transfer among the composites. In the case of solidification, heterogeneous nucleation of the PCM also benefits from the increased EG content.

The $T_{p,m}$ and $T_{p,s}$ of EG3 based composites are not observed to have an apparent phase change temperature changes. As indicated in the SEM study (see Figure 51 and Figure 52), EG3 does not appear to have a complex networked structure because of the small particle size. Although a limited number of micro-pores ($\sim 15\mu m$) still exist among the EG3 particles, it has an insignificant impact on the phase change behaviour of the PCM.

4.1.2.2. Latent heat and specific heat study

Table 13 tabulates that the latent heat and specific heat of the composites as a function of EG mass percentage. The latent heat (L) was obtained by the integration of the area under the peak with an extrapolated baseline. The results of the latent heat measurement of the EG composites with different mass percentages are also shown in Figure 56.

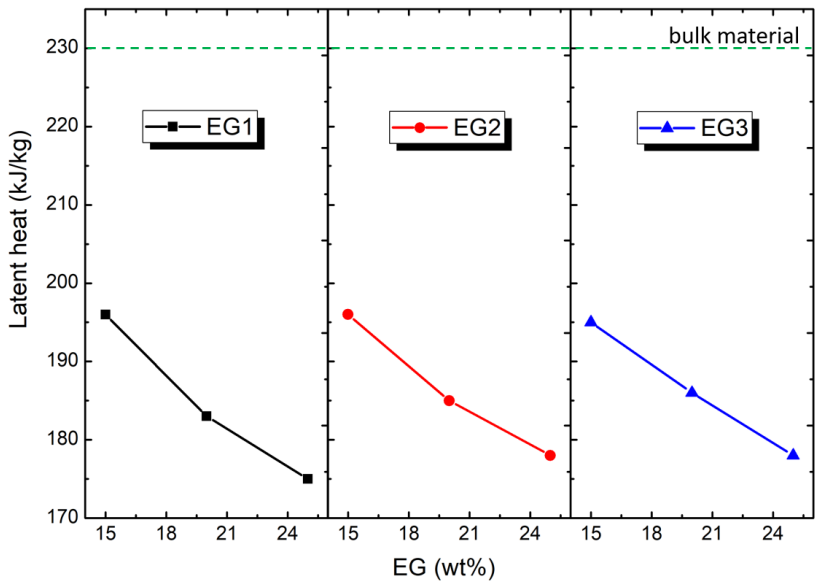

Figure 56 Variation of latent heat versus EG mass percentage at different EG particle size

Table 13 Latent heat and the specific heat (of both liquid and solid phases) of composites obtained from the DSC measurements

Material		**Latent heat (kJ/kg)**	**specific heat (kJ/kg • K)**	
			Solid state	Liquid state
EG1	15wt%	196± 1.47	1.16± 0.03	2.13± 0.07
	20wt%	183± 1.15	0.88± 0.06	1.79± 0.12
	25wt%	175± 1.73	0.76± 0.13	1.12± 0.11
EG2	15wt%	196± 0.75	2.19± 0.12	2.81± 0.06
	20wt%	189± 1.00	1.83± 0.06	2.35± 0.05
	25wt%	178± 1.14	1.79± 0.11	2.1± 0.06
EG3	15wt%	195± 1.48	1.65± 0.05	1.92± 0.09
	20wt%	186± 0.84	1.52± 0.06	1.91± 0.09

25wt%	178± 1.53	1.43± 0.08	1.82± 0.07

The latent heat of composites is inversely proportional to the EG content, which decreases by 5% for every 5wt% increase in EG content.

The results of the specific heat of the composites are also listed in Table 13. The specific heat of EG is in the range of 0.47 ~ 0.65 kJ/(kg·K) at ambient temperature [215], while RT28HC has a specific heat of 2 kJ/(kg·K) at the same condition. With more EG added, the specific heat of the composite decreases as EG has a lower specific heat than the RT28HC.

4.1.2.3. Thermal stability study

The thermal stabilities of the composites with different mass percentages and different particle sizes of EG were evaluated by the TG analyses. In this PhD study, the onset (degradation) temperature ($T_{on,d}$) is chosen as the criteria for studying the thermal characteristics of the composites. As shown in Figure 57 (a), an extrapolated onset temperature ($T_{on,d}$) indicates the beginning of the weight loss.

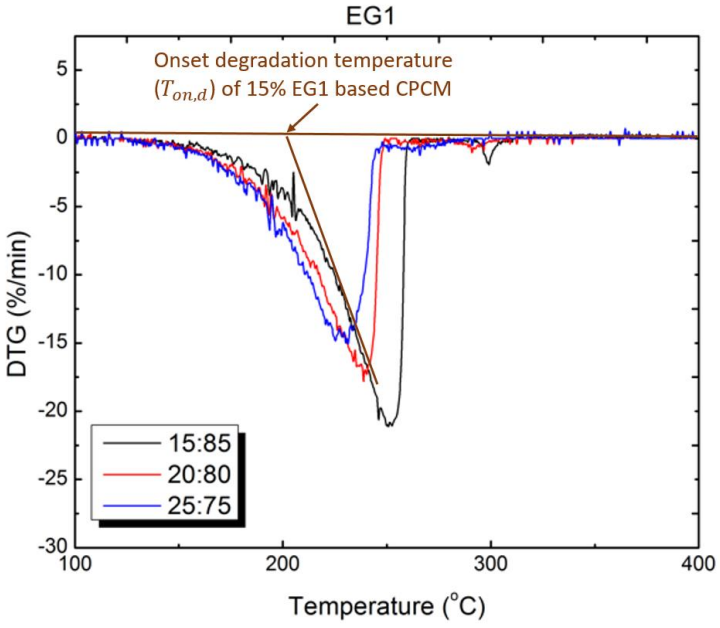

(a)

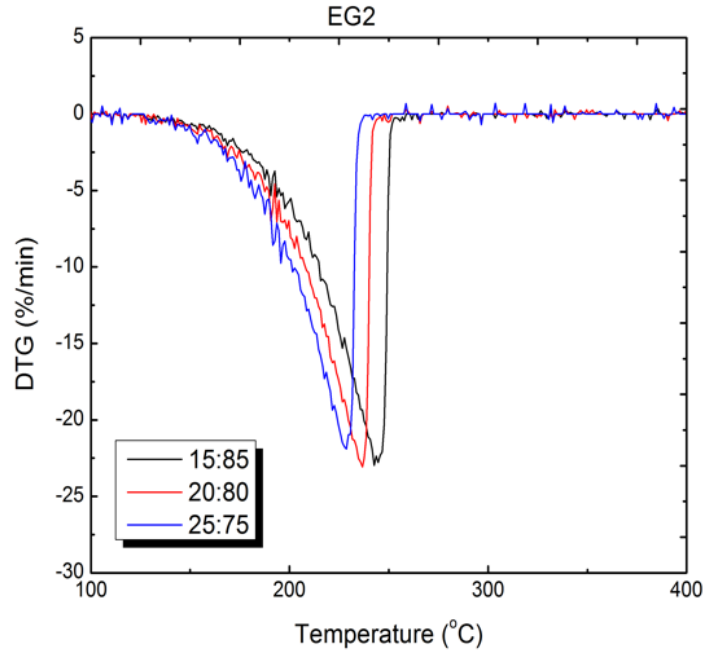

(b)

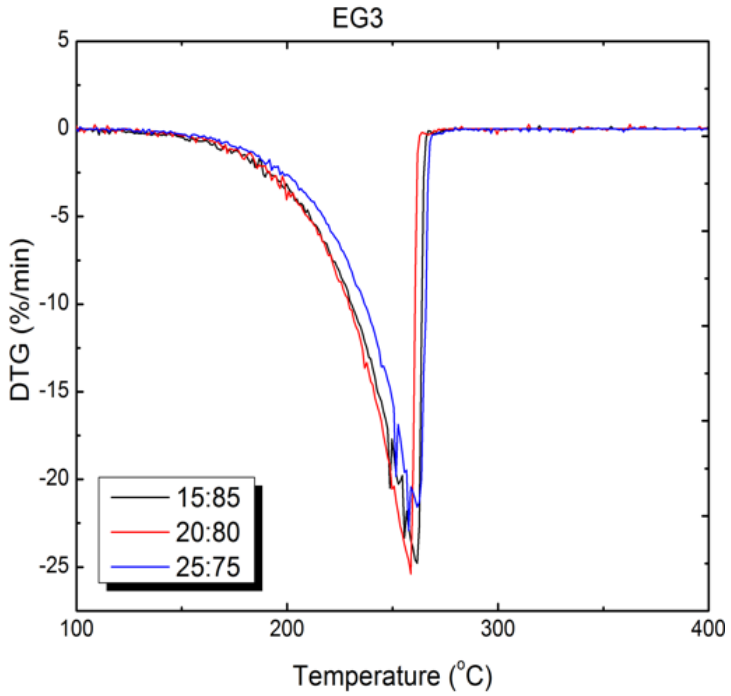

(c)

Figure 57 DTG curve for EG based composites. (a)EG1 based composites (b)EG2 based composites (c)EG3 based composites

The derivative thermogravimetry (DTG) result of the composites is shown in Figure 57. The degradation temperatures and the charred residue amount after the degradation are shown in Table 14.

Table 14 Thermal stability properties obtained from the DTG curve ($T_{on,d}$ is onset degradation temperature)

Materials		$T_{on,d}$ **(ºC)**	**Charred residue (%)**
EG1	15wt%	219	16.40
	20wt%	205	19.96
	25wt%	196	27.15
EG2	15wt%	212	15.98
	20wt%	207	21.66
	25wt%	199	25.60
EG3	15wt%	227	14.83
	20wt%	227	19.55
	25wt%	230	25.91
RT28HC		196	0.38

It can be seen from Figure 57 that the thermal degradation process completes in one step for all composites, corresponding to the degradation of RT28HC. A larger amount of the charred residues was observed from measurements of the composites with more weight percentage of EG content. This is because the degradation temperature of EG is more than 800 ºC. Besides, the charred amount was almost consistent with the EG content of the corresponding composite. Therefore, the residue from the degradation tests is mainly EG.

$T_{on,d}$ is influenced by the particle size and mass percentage of the EG. The $T_{on,d}$ of RT28HC is 196ºC. It could be observed from the results that EG had a positive effect on the degradation

of composites, leading to a significant increase in the degradation temperatures. The maximum increase in the $T_{on,d}$ of composites is 34 ºC compared with pure RT28HC.

From Figure 57 and Table 14, one could conclude that the existence of EG has a great contribution to the thermal stability of the composites. In the case of EG with a large particle size (i.e. EG1 and EG2), the PCM is confined in the pores of the EG particles. The porous structure of the EG particles is therefore advantageous for slowing the escape of the volatile products generated during thermal degradation. Hence it hinders the degradation process, and improves the thermal stability of the composites. Although EG3 with a small particle size has an unconnected porous structure, it also increases the degradation temperature of the composites and has a positive effect on the thermal stability. The fine EG particles from a matrix that could also help with slowing down the escape of the paraffin vapour. Interfacial thermal resistance reduces the heat transfer in the composite, which could further increase the thermal degradation temperature.

The amount of EG content plays a role in the degradation process. For EG1 and EG2 based composites, a higher weight percentage of EG leads to a lower thermal degradation temperature. When comparing the composites at different mass percentages of EG1, 23 ºC of difference is observed for the $T_{on,d}$. The differences between the $T_{on,d}$ is 13 ºC in the case of EG2 based composites. A higher EG content gives a greater thermal conductivity of the composites. In such a way, it strengthens the heat transfer inside the composite, thus leading to a lower degradation temperature. Composites contained EG3 do not show a significant difference in the degradation temperatures.

4.1.2.4. Leakage study

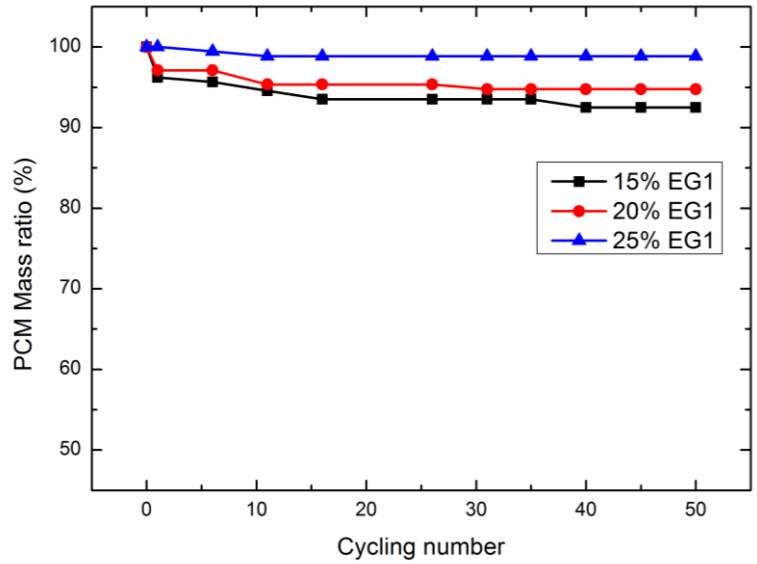

(a)

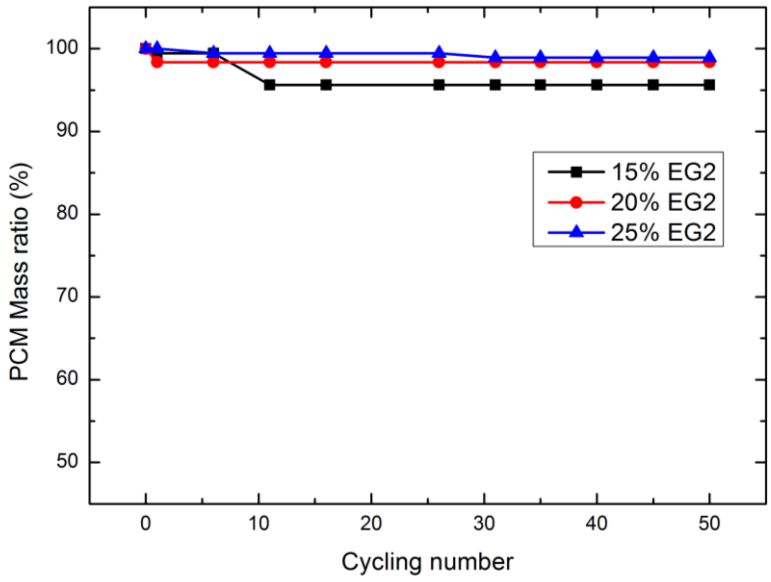

(b)

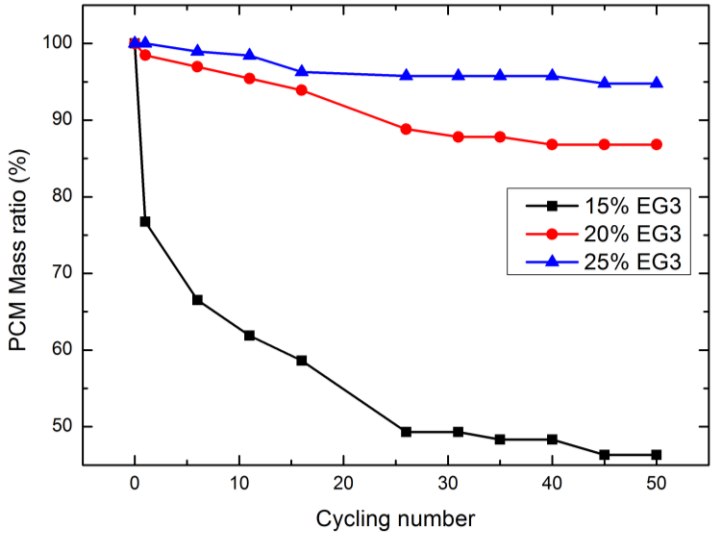

(c)

Figure 58 PCM mass ratio change after 50 thermal cyclings. (a)EG1 based composites (b)EG2 based composites (c)EG3 based composites

The leakage phenomena of the composites were studied through thermal cycling tests. Figure 58 shows the mass ratio change of the PCM in the composites made of EG 1, EG2 and EG3 with 10wt%, 15wt% and 25wt% EG content after 50 thermal cycles. The most pronounced leakage occurs in EG3 composite with 15wt% EG. After the first cycle, 24wt% of PCM leaks out of the composite, and the leakage then continues at a rate of 5wt% PCM per 5 cycles until 25 cycles. The PCM leakage of the EG3 composites is improved when the mass ratio of EG increases. After 50 cycles, EG3 composite with 20wt% EG retains 87wt% PCM, and EG3 composite with 25wt% EG has no significant leakage.

Regarding the composites using large particle sized EG, the composites containing 20wt% and 25wt% EG are observed to be form stable after 50 cycles, with less than 5wt% PCM leakage. The composites with 15wt% of large EG particles show slightly worse cycling stability, and 15wt% EG1 composite and 15wt% EG2 composites are found to have 8wt% and 6wt% PCM leakage after 50 cycles, respectively.

From the results above, it can be concluded that the mass ratio of EG is the determining factor for the cycling stability of EG based composites. After 50 cycles, most of the PCM remained in the composites with 20wt% and 25wt% large EG particles. The leakage also significantly reduced when the mass ratio of EG3 in the composite increased to 20% and 25%. Particle size is another factor which influences the composite cycling stability. Comparing EG3 with EG1,

after 50 cycles the remaining PCM mass ratios of EG3 are 46%, 8wt% and 4wt% less than EG1 with 15wt%, 20wt% and 25wt% EG contents, respectively. The difference in the stability between these composites is due to structurally dissimilar of the different particle sizes of EG. Large EG particles have pores and voids which are able to confine the PCM, while small EG particles are lack of pore structure and are not able to preserve the PCM.

4.1.2.5. Thermal conductivity study

The thermal conductivity measurement results of the composites with different mass percentages and particle sizes of EG is shown in Figure 59 and Table 15. The measurements were carried out using the laser flash apparatus.

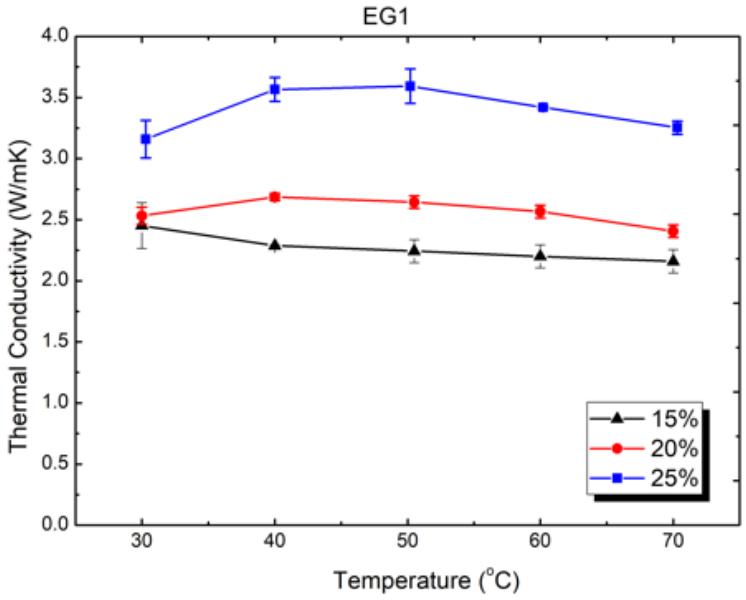

(a)

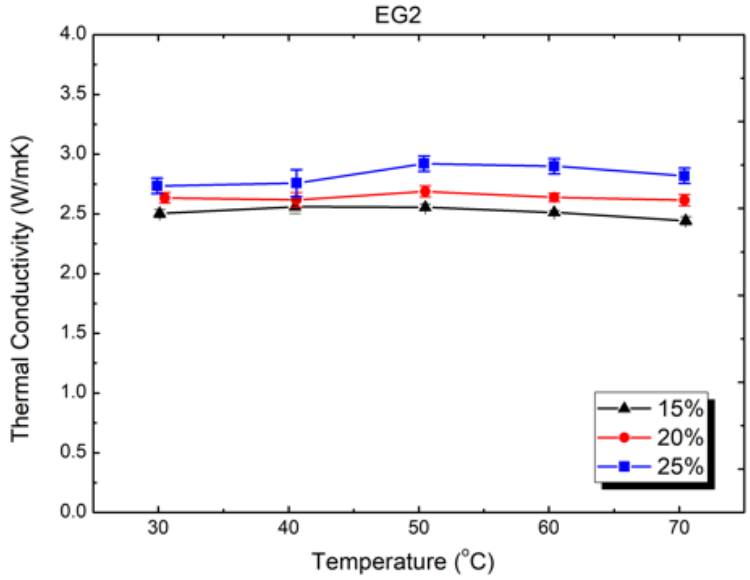

(b)

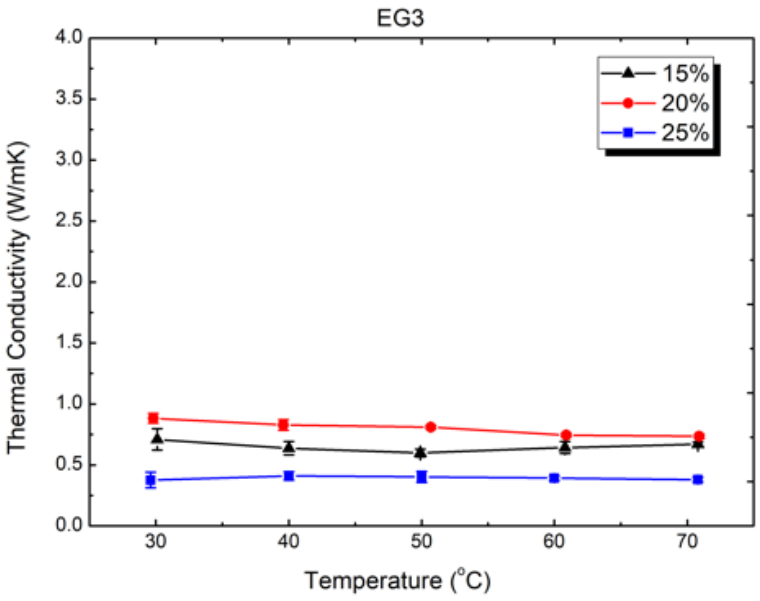

(c)

Figure 59 Thermal conductivity of solid and liquid phases as a function of temperature. (a) EG1 EG based composites (b) EG2 EG based composites (c) EG3 EG based composites

With the addition of EG, the thermal conductivity of the composites is improved effectively. The larger the particle size of the EG, the more pronounced the effect on the thermal conductivity of the composites. The thermal conductivity of the composites increases in the order of EG1≈ EG2> EG3. For instance, with 25wt% of EG loading, EG1, EG2, and EG3 composites have a thermal conductivity of 3.16, 2.74 and 0.38 W/m·K at 30°C, respectively

Regarding the large micrometres scale EG, the thermal conductivity increases with the EG loading. However, in the case of EG3, the rising tendency is unnoticeable. The decreased thermal conductivity with reduced particle size could be attributed to the effect of interfacial thermal resistance. When the particle is small, the interfacial thermal resistance dominates the influence on the thermal conductivity of the composites. Nevertheless, if the particle size is relatively large, the thermal conductivity of the composites is decided by the bulk property. In Figure 59 (c), the sudden drop in the thermal conductivity of the EG3 composites suggests that interfacial thermal resistance exists among the small graphite particles.

Table 15 Thermal conductivity data obtained from the LFA measurement.

		Thermal conductivity (W/m • K)				
Material		30ºC	40ºC	50ºC	60ºC	70ºC
EG1	15wt%	2.45± 0.19	2.29± 0.01	2.24± 0.09	2.20± 0.09	2.16±0.09
	20wt%	2.53± 0.07	2.69± 0.03	2.64± 0.05	2.57± 0.05	2.41±0.05
	25wt%	3.16± 0.15	3.57± 0.10	3.59± 0.14	3.42± 0.01	3.25±0.06
EG2	15wt%	2.50± 0.03	2.56± 0.06	2.56± 0.03	2.51± 0.02	2.44±0.03
	20wt%	2.64± 0.04	2.62± 0.06	2.69± 0.05	2.64± 0.04	2.62±0.05
	25wt%	2.74± 0.06	2.76± 0.11	2.92± 0.07	2.90± 0.06	2.82±0.06
EG3	15wt%	0.71± 0.09	0.64± 0.06	0.60± 0.03	0.64± 0.05	0.67±0.02
	20wt%	0.88± 0.04	0.83± 0.04	0.81± 0.02	0.74± 0.01	0.74±0.02
	25wt%	0.38± 0.06	0.41± 0.04	0.40± 0.05	0.39± 0.02	0.38±0.02

Thermal conductivities of composites/mixtures have been a subject of numerous studies. Many models have been proposed for the estimation of the effective thermal conductivity. In this study, the two-form Maxwell-Eucken model was also used for estimating the thermal conductivity of EG composites. The model is given as following [216]:

$$K = \frac{k_1 V_1 + k_2 V_2 \frac{3k_1}{2k_1 + k_2}}{V_1 + V \frac{3k_1}{2k_1 + k_2}} \quad (49)$$

where K is the effective thermal conductivity of the composites, k_1 is the thermal conductivity of the continuous phase (EG), V_1 is the volume fraction of the continuous phase, k_2 is the thermal conductivity of the dispersed phase (paraffin), V_2 is the volume fraction of the dispersed phase.

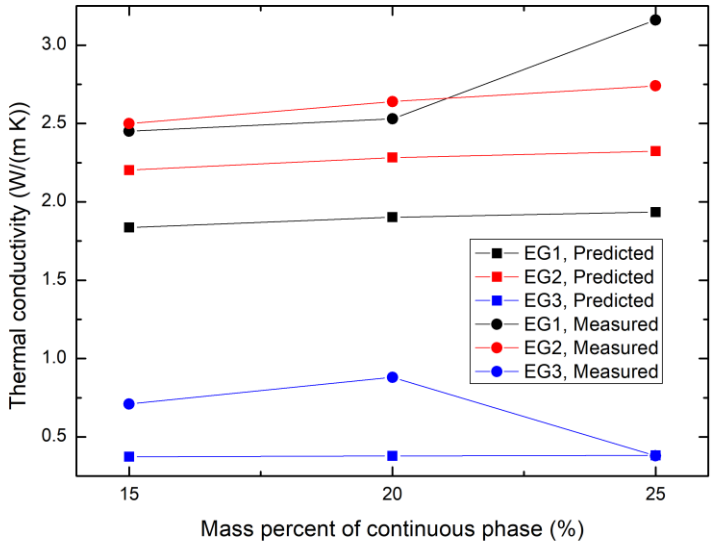

Figure 60 A comparison between the theoretical predictions and experimental measured thermal conductivities of EG composites

The thermal conductivity of pure EG1, EG2 and EG3 matrix was measured to be 3.23, 3.92 and 0.5 W/m·K, respectively. Xia et al. [213] observed the distribution of EG in the EG/PCM composites using a polarizing optical microscope and found that EG matrix forms a continuous phase when the mass percentage of EG in the composite is more than 4%. In this study, the mass fraction of the EG was more than 15wt%, hence the EG matrix presented as the continuous phase, and RT28HC was the dispersed phase. It can also be observed from the SEM picture of the cut surface of composites (Figure 52) that EG matrix existed continuously. The volume fraction of the continuous phase was achieved from the measured value. The volume fraction of the dispersed phase was calculated from the weight and density of the dispersed phase at solid-state. The predicated data is shown in Figure 60. The results show that the predicted data has good agreement with experimental data.

4.2. Copper foam/ paraffin composite phase change materials

4.2.1. Morphology observation

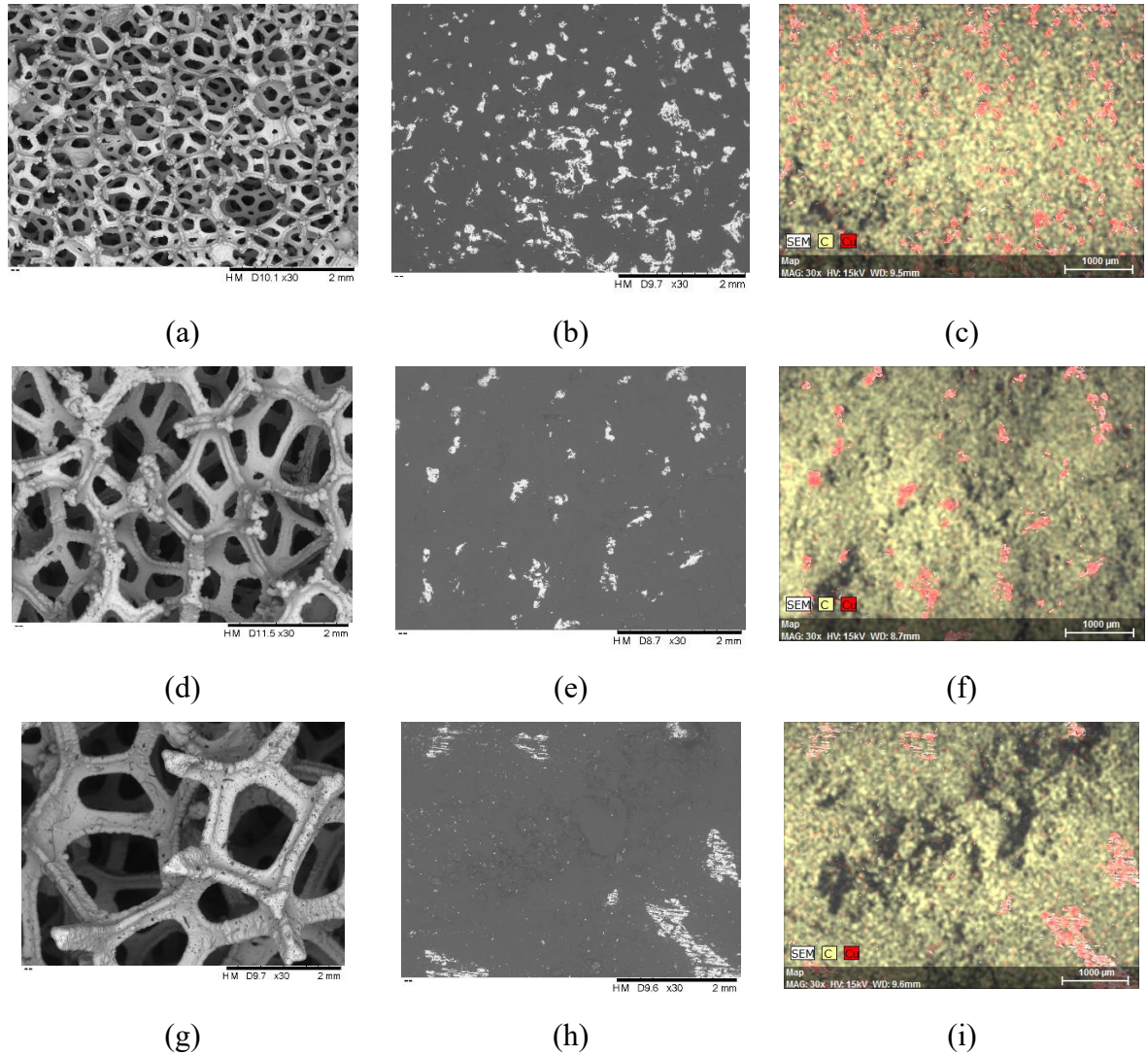

Figure 61 SEM observation of the composites at 30 times magnification. (a) copper foam 1 (b) composite 1 (c) EDS element mapping of composite 1 (d) copper foam 2 (e) composite 2 (f) EDS element mapping of composite 2 (g) copper foam 3 (h) composite 3 (i) EDS element mapping of composite 3

Morphology observations of the copper foam and the composites are shown in Figure 61. Figure 61 (a) (d) (g) indicate that the pore size of the composites increases from copper 1 to copper 3. These can also be observed from SEM images of the composite. As shown in Figure 61 (c) (f) (i) the element mapping indicates that the white zones in Figure 61 (b) (e) (h) are copper foam skeleton and the dark zones are paraffin. The white zones reduce from composite 1 to composite 3.

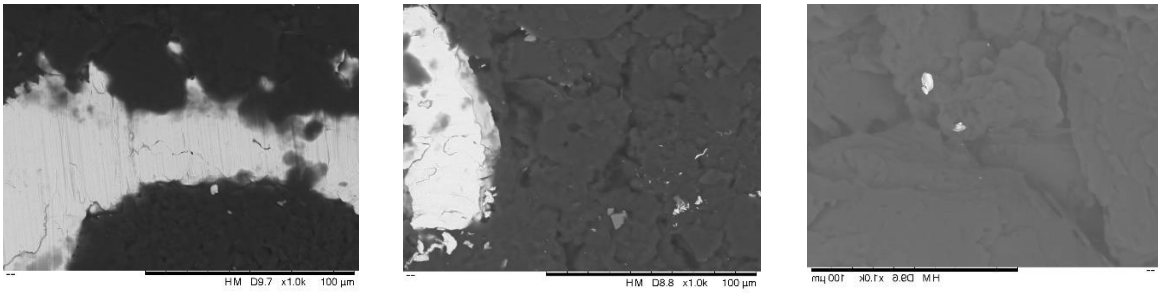

(a) (b) (c)

Figure 62 SEM observation of the composites at 1000 times magnification (a) composite 1 (b) composite 2 (c) composite 3

Further zooming into the composites, Figure 62 is obtained, which shows the morphology of the composites with a 1000 time magnification. One can see that the paraffin has been closely integrated with the copper foam skeleton, leading to the excellent adsorption of paraffin.

4.2.2. Thermal characterization

Since the copper foam with high porosity/low PPI could have pores of several millimetres in diameter, the samples will be too large to fit the measuring crucibles of the DSC. The composites are prepared under vacuum and eliminate the air bubble traps inside the copper foam skeleton. The SEM analysis (Figure 62) also shows that the copper foam skeleton has good adsorption of the paraffin. The latent heat of the composites can be theoretically calculated based on the absorbed weight of PCM into the copper foam skeleton. The results are showing in Figure 63. The composite 1 (99% porosity) and composite 3 (81% porosity) have latent heat of 190 kJ/kg and 62 kJ/kg, respectively. Compare the latent heat of composite 1 and composite 3, with 18% of porosity difference the difference of latent can be 67% of composite 1. The latent heat of composite 2 (92% porosity) sits in the middle, which is 111 kJ/kg.

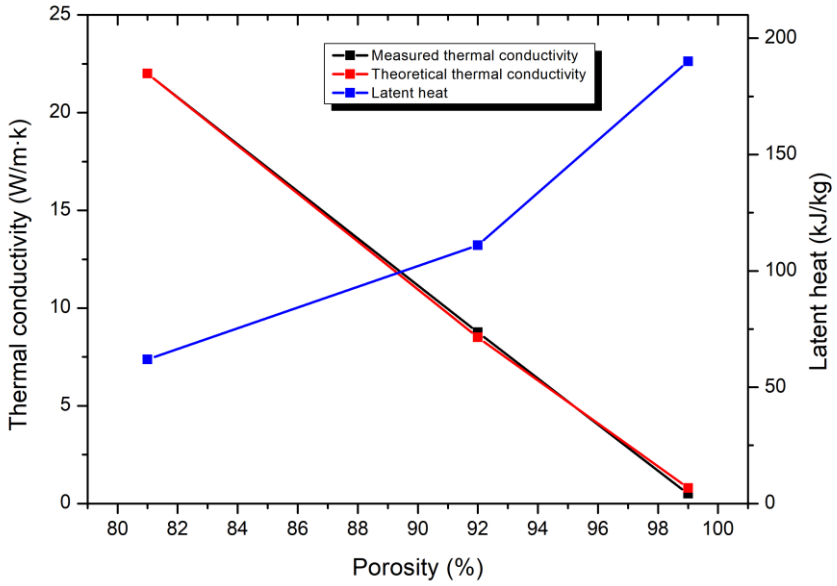

Figure 63 Thermal properties of the different composites. Copper foam skeleton of composite 1 has a porosity of 98%, copper foam skeleton of composite 2 has a porosity of 92%, copper foam skeleton of composite 3 has a porosity of 81%

The thermal conductivity of the copper foam/paraffin composite was characterized using the thermal hot bridge with results plotted in Figure 63. With only 18% of porosity difference, the thermal conductivity shows a great contrast. Composite 1 has a thermal conductivity of 0.5 W/m·K, which is 2.5 times of the pure paraffin. The composite 3 has a thermal conductivity of 22 W/m·K, which is 110 times of the pure paraffin and 44 times of composite 1.

Measured thermal conductivities were compared with the theoretical thermal conductivities of the composites, which were calculated based on the model proposed by zhao et al. [207] (equation 34-41). The results of the theoretical calculations are also shown in Figure 63. It shows a good consistency between the measured and theoretical values. It is important as the operation of the thermal hot bridge replies on experience. The measurement time and current of the heating wire of the device need to be adjusted each time empirically according to the estimated thermal conductivity, size, and surface roughness of the samples, which may cause an error due to human error.

Using copper foam as the composite skeleton and thermal enhancement material is truly double-edged. With 81% porosity, the thermal conductivity could reach 22 W/m·K, which sees an improvement of 110 times compared to pure paraffin. In contrast, the latent heat of the

composite is only 62 kJ/kg, which is 30% of the original paraffin. With 99% porosity, the composite has a latent heat of 190 kJ/kg, while the thermal conductivity is only 0.5 W/m·K. The 92% porosity has a thermal conductivity of 8.76 W/m·K and latent heat of 111 kJ/kg. When applied to battery thermal management, copper foam porosity should be carefully selected first to make sure the composite has sufficiently high enough thermal conductivity for heat dissipation and the latent heat can be then decided.

In the real application of copper foam/paraffin composite, if ordinary copper foam as mentioned in current research is used, the composite needs to be placed in a container. The large pores of ordinary copper foam could not confine the paraffin in its pores, once above the melting temperature, the paraffin will leak from the copper foam. This can be addressed by developing novel copper foam with nanopores. Research on copper foam with the anti-leaking property was carried out by Grosu et al. [217]. The hierarchical macro-nanoporous metals have both macro and nanopores. The developed novel copper foam PCM composite has excellent anti-leakage performance due to strong capillary force in nanopores, together with high energy density due to high porosity created by macropores.

4.3. Colloidal graphite /paraffin composite phase change materials

4.3.1. Thermal characterization

4.3.1.1. Phase change behaviour study

For comparison purpose, colloidal graphite was also added to RT28HC phase change material. Figure 64 shows the heat flow from the DSC measurement curve (Figure 64a) and latent heat (Figure 64b) of samples 1-4 (containing 10wt%, 20wt%, 30wt%, and 40wt% colloidal graphite particles). With 10% graphite content, the latent heat of the composite is 196 kJ/kg. When the graphite mass ratio increases to 40%, the latent heat is observed to be 135 kJ/kg. Then latent heat of the composites reduces by 20 kJ/kg with every 10% increase of the graphite mass ratio. The experimental results show that the latent heat of composites is inversely proportional to the mass ratio of the graphite content. The latent heat is provided by RT28HC. With the increase of graphite content in mass ratio, the mass ratio of the RT28HC decreases hence the latent heat decrease.

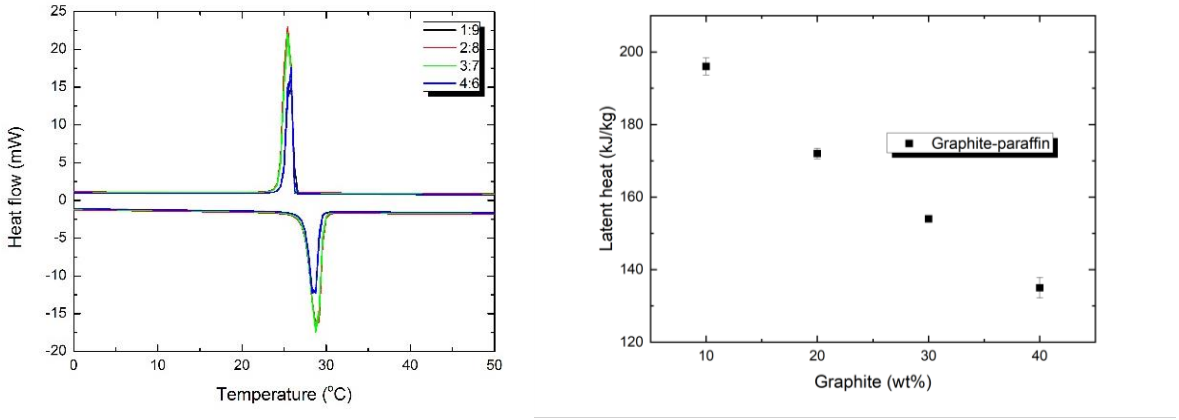

Figure 64 Phase change behaviour and latent heat of colloidal graphite /paraffin composite. (a) DSC scanning curve of composite 1-4 (b) Latent heat of composite 1-4

4.3.1.2. Thermal conductivity study

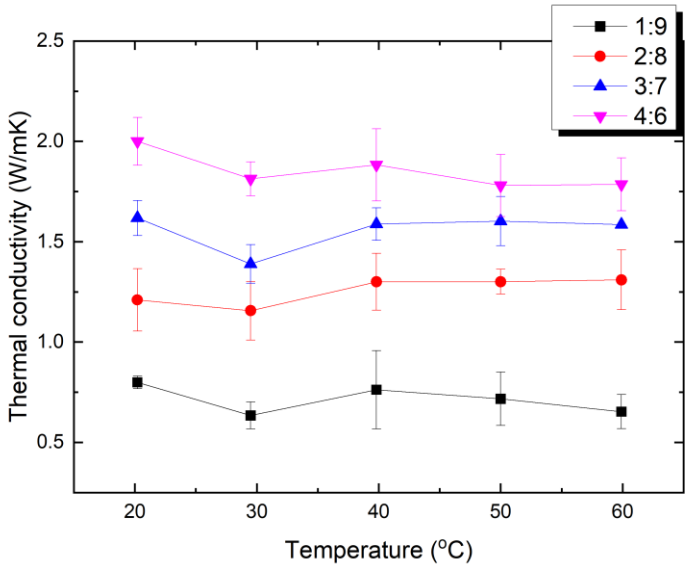

Figure 65 Thermal conductivity of colloidal graphite /paraffin composite 1-4

Organic PCMs usually have low thermal conductivity. Adding high thermal conductivity materials to organic phase change materials is a commonly used method to improve the thermal conductivity of materials. Different proportions of colloidal graphite were added to RT28HC to improve its thermal conductivity. The thermal conductivity of the composites with different mass ratios of graphite was experimentally measured by laser flash apparatus.

Figure 65 shows the thermal conductivity of the composites prepared by adding different mass ratio of graphite content. The samples were measured at the temperature range of 20-60°C. It can be seen from the figure that the addition of graphite can effectively enhance the thermal

conductivity of the paraffin, and the thermal conductivity increases with the increase of the mass ratio of graphite. At 20°C, and the thermal conductivity of composites with 10%, 20%, 30% and 40% of graphite content was 3.995 times, 6.05 times, 9.09 times and 10.27 times of the thermal conductivity of the pure materials (about 0.2 W/m·K), respectively. The thermal conductivity measured at different temperatures did not show much deviation from the thermal conductivity measured at 20°C, even after the phase change. Table 16 shows the values of thermal conductivity of composite 1-4 measured under different temperatures.

Table 16 Thermal conductivity of colloidal graphite/paraffin composite 1-4

Colloidal graphite/paraffin composites				
	1：9	**2：8**	**3：7**	**4：6**
20°C	0.799±0.032	1.21±0.156	1.618±0.088	2.053±0.119
30°C	0.634±0.067	1.156±0.147	1.39±0.096	1.813±0.085
40°C	0.762±0.195	1.3±0.142	1.588±0.081	1.883±0.18
50°C	0.717±0.133	1.301±0.062	1.603±0.122	1.78±0.155
60°C	0.653±0.085	1.31±0.149	1.586±0.004	1.786±0.132

4.3.1.3. Thermal stability study

Thermal stability is an essential property of thermal energy storage materials, especially in an electric vehicle application. Figure 66 is the thermogravimetric analysis of pure paraffin and composites. Adding graphite to paraffin caused a difference in thermal stability property. Compared with the $T_{on,d}$ of the pure paraffin (196°C), the onset degradation temperature of the composites was improved. The evaporation of the paraffin could have been delayed from the protection of the graphite content. When comparing composites with a different mass ratio of the graphite, there was no significant difference.

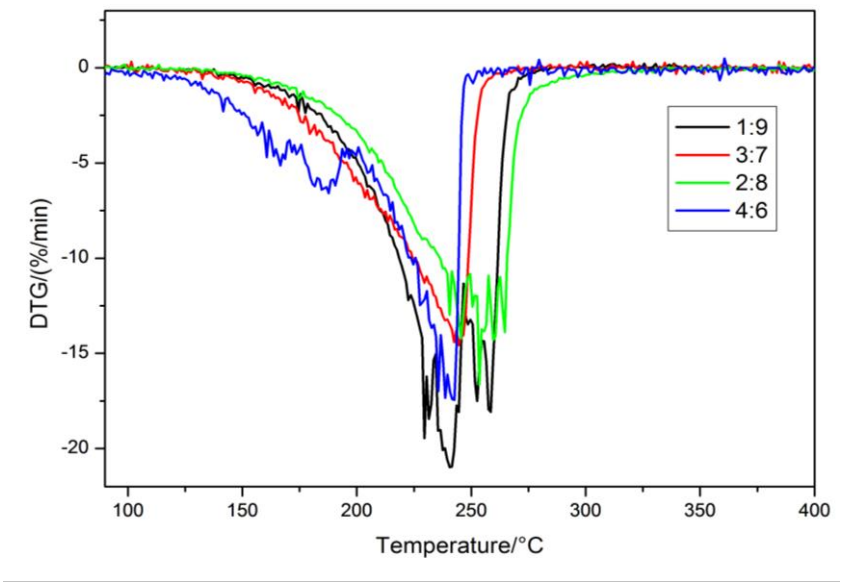

Figure 66 TG curve for colloidal graphite/paraffin composites

Table 17 Thermal stability properties of the colloidal graphite-based samples ($T_{on,d}$ is onset degradation temperature)

Sample number	composition（wt%）	$T_{on,d}$/°C
1	10% graphite/90% RT28HC	210
2	20% graphite/80% RT28HC	215
3	30% graphite/70% RT28HC	205
4	40% graphite/60% RT28HC	208

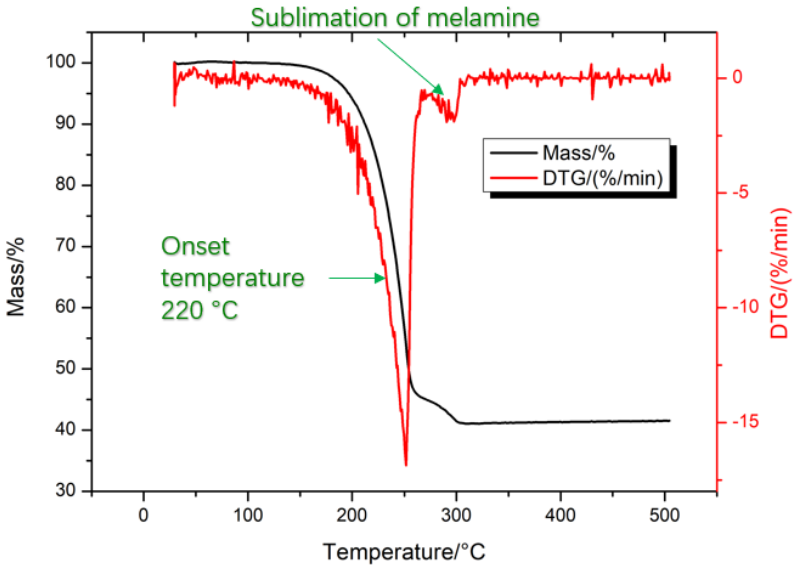

Figure 67 DTG curve for melamine/colloidal graphite/paraffin composites

To further improve the thermal stability of the composites, melamine was added into the composites. As can be observed from Figure 67, adding 5% melamine material can increase the $T_{on,d}$of the material by 12°C to 220°C. The endset degradation temperature ($T_{end,d}$) of the composites was the most significantly affected parameter. As shown in Figure 68, with melamine content increases from 1wt% to 15wt%, the $T_{end,d}$ increased from 245 °C to 334 °C, forms a gradient of 89 °C. Addition of melamine could not only delay the start of the degradation process but also hugely affect the degradation process. Much higher temperature will be needed to undergo the full decomposition of the material. Multiple reasons can be contributed to the improvement of thermal stability. With the test samples being heated in the furnace of STA, the melamine had undergone evaporation/decomposition. The process of evaporation and decomposition of melamine absorbed a lot of heat, which led to an increase in the decomposition temperature of the composite material. Melamine vapour contains nitrogen, which is a non-combustible gas and dilutes the gas paraffin produced from the evaporation/decomposition of RT28HC. It was effectively increasing its decomposition temperature. Besides, the decomposition products of melamine can effectively form a carbon layer on the surface of composite, thereby inhibiting the evaporation of paraffin, and increased the decomposition temperature.

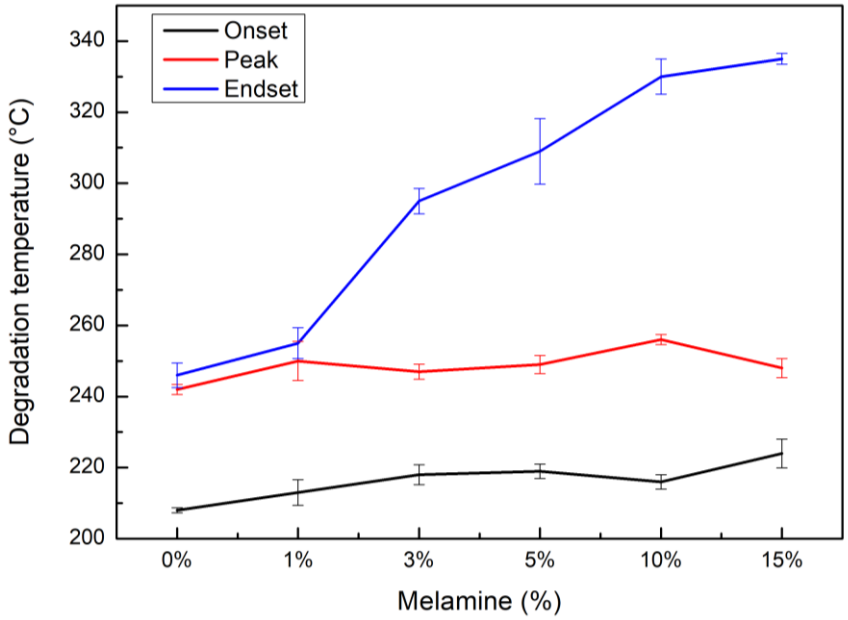

Figure 68 Effect of melamine on the improvement of thermal degradation temperature of the composite. With higher mass ratio of the melamine, $T_{end,d}$ was significantly increased

4.4. Summary of the chapter 4

In this chapter, paraffin-based CPCM using EG, copper foam and colloidal graphite as the thermal enhanced material was studied. The structural and thermal property of the different composites has been investigated.

It has been observed that EG particles with different particle size have different structures, results in dissimilarities on EG matrix structures. SEM pictures showed that large EG particles (i.e. EG1 and EG2) with loose vermicular shape possessed interconnected pore structure, while the small EG particles (i.e. EG3) was primarily in the form of loose graphite sheets without connected networking structure. 3D structure characterization revealed that large EG matrix had higher porosity and larger pore/void size comparing with the small EG matrix. Different structural arrangements of EG had a significant impact on paraffin adsorptions, hence affects the thermal behaviour of EG/paraffin composites. The interconnected pore structure of large EG matrix confined PCM in the pores and voids and led to an increased temperature hysteresis comparing with the pure paraffin. The pore structure of the large EG matrix could help with confining the EG, and it had advantageous in slowing the escape of the volatile products generated during thermal degradation. The confinement behaviour was further confirmed in the thermal cycling test. The test showed composites using large particle size EG has a

significantly lower PCM loss than composites using small size EG. It was also revealed that the mass ratio of the EG content is the determining factor of the composite cycling stability. Thermal stability of composites containing large EG particles was effectively improved as indicated by the results from TG analysis. The thermal conductivity of composites with large EG particles increased by 1360% - 1695% because of the high thermal conductivity of the EG matrix. In the case of small EG particles, interfacial thermal resistance dominates the influence on thermal conductivity, which results in less improvement in thermal conductivity. A 90 ~ 340% increment on thermal conductivity was obtained regarding different EG contents. Interfacial thermal resistance also helped with improving the thermal stability of the composite.

Copper foam/paraffin composites with different porosity of copper foam were investigated regarding its morphology and thermal property. The SEM pictures confirmed the good adsorption of PCM into the copper foam skeleton. The experimental measurement validated the copper foam/paraffin composite model, which was used for numerical modelling. The porosity of the copper foam could have a significant effect on the thermal property of the composites. With 18% of porosity difference, the difference in latent heat can be 128kJ/kg and the difference in thermal conductivity reached 20.5W/m·K.

The thermal properties of the colloidal graphite/paraffin composite were studied. The latent heat of the composites is inversely proportional to the mass ratio of the colloidal graphite, and there was 20 kJ/kg of difference with every 10wt% of graphite content difference. The thermal conductivity of the composite is proportional to the mass per cent of colloidal graphite in the composite, and with 40wt% of colloidal graphite, the composite can achieve thermal conductivity of 2W/m·K at 20 °C. With the addition of melamine, the end set degradation temperature can be significantly increased. With 15wt% of melamine, the $T_{end,d}$ reached 334 °C, which was increased by 126 °C when compared with 0% melamine.

Table 18 Comparison of the paraffin-based composites using expanded graphite, copper foam or colloidal graphite as the thermal enhancement material

Material composition	Latent heat (kJ/kg)	Thermal conductivity (W/m·K)	Cost ($/kg)
15wt% EG1/85% paraffin	196	2.45	9
99% porosity copper foam/paraffin	190	0.5	40
10wt% colloidal graphite/ 90wt% paraffin	196	0.8	9

（The cost is based on the purchase price of the raw materials from market in China. The copper foam was purchased at a price of $345/kg, expanded graphite with 400 μm in diameter was purchased at the price of $5/kg, colloidal graphite was purchased at a price of $0.5/kg. RT28HC was purchased at the price of $10/kg. The factor of manufacturing cost is not considered as it can be varied in different countries/areas）

A comparison on the paraffin-based composites is summarized below in Table 18. With the latent heat in the range of 190-200 kJ/kg, the 15wt% EG/85% paraffin composite has the highest thermal conductivity, which is 4.9 times of 99% porosity copper foam/paraffin composite and 3.1 times of 10wt% colloidal graphite/ 90wt% paraffin composite. Since the battery thermal management system will be practically applied to industrial products, the cost of the materials needs to be calculated. The cost of EG based composite and colloidal based composites are $9/kg. Due to the high cost of copper foam and high density of copper skeleton, even with 99% porosity, the cost of the material was still $40/kg, which is 4.4 times of the other materials. It can be concluded that from this research, the EG/paraffin composite is the best choice for industrial application due to its advantage in thermal property and cost. While the copper foam/paraffin composite has a high cost, however thermal conductivity of it can reach 22W/m·K with 81% porosity copper foam which is way above the other materials. The high thermal conductivity could dissipate the heat to the ambient very fast, which is useful for battery under high current rate cycling operation. It can be applied to sectors which do not consider cost as the main factor, e.g. military use. Hence in the numerical studied both the EG/paraffin and copper foam/paraffin composites has been investigated.

Chapter 5 Characterization of lithium-ion batteries

This chapter presents the work on the thermal characteristics and the performance of lithium-ion batteries studied in the PhD study. Firstly, the heat flux of a battery under different charge/discharge current rates is discussed. The relationship between the heat flux and internal resistance is described. Secondly, the performance, including the specific energy and specific power of the lithium-ion batteries is discussed under different operation temperatures and different current rates.

5.1 Battery characteristics.

5.1. Thermal characterization

Consider a battery has an average heat capacity, C_p, its the heat generation can be estimated by the following equation:

$$\dot{q} = mC_p \frac{dT}{dt} + h_{sf} a(T - T_a) + \varepsilon_{em} a(T^4 - T_a^4) - ka \frac{\partial T}{\partial l} \quad (50)$$

where m is the weight of LIB, $\frac{dT}{dt}$ is the rate of the temperature increase, h_{sf} is heat transfer coefficient, a is surface area, T is the temperature of LIB, T_a is the temperature of ambient, ε_{em} is the emissivity, k is thermal conductivity, and l is the length of heat conduction. The first item on the right side represents the thermal energy generated during battery operation, the remaining three items on the right side represent the heat loss by convection, radiation and conduction, respectively;

The experiment was always carried out in an adiabatic condition. The heat loss due to convection and radiation can be neglected. In fact, the temperature difference between the single battery and the surrounding is less than 1.5K. The entire cell is also nearly in a uniform temperature due to the small contact area within the cell. Hence the heat conduction is negligible as well. Therefore, the following simplified equation can be used for the study:

$$\dot{q} = mC_p \frac{dT}{dt} \quad (51)$$

The heat flux in equation (53) can be further calculated based on the surface area:

$$\vec{q} = \frac{\dot{q}}{a} \quad (52)$$

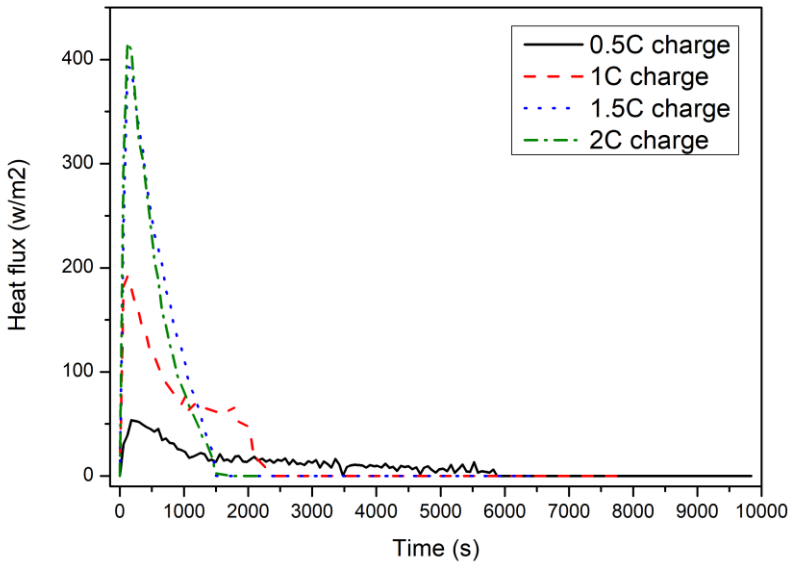

(a)

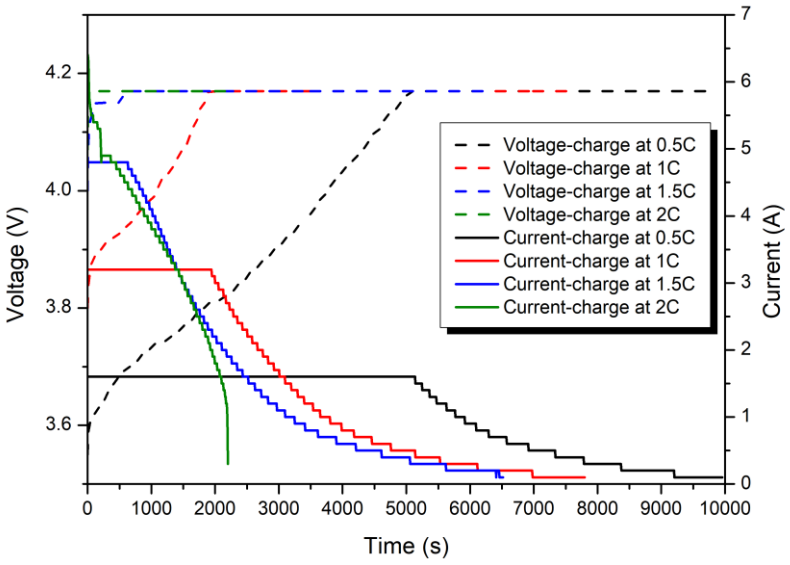

(b)

Figure 69 Characteristics of Panasonic NCR18650B charged at 0.5C, 1C, 1.5C and 2C: (a) Time evolution of the heat flux $\vec{q}$; (b) Variation of the voltage and current as a function of time

Figure 69 shows the characteristics of a single battery charged at different current rates. The heat flux as a function of time is plotted in Figure 69(a) during charge, demonstrating that the $\vec{q}$ of the charging process depends on the current rate; the higher the current rate, the larger the $\vec{q}$. The reason for this is associated with heat generation of the battery, which consists of both

reversible heat and irreversible heat. The reversible heat is achieved based on the change of entropy of the chemical reaction, which is proportional to the current rate. The irreversible heat is based on the resistance, *R*, which is proportional to the square of the current rate [218].

The $\vec{q}$ of the battery charge process can be divided into several stages, which is affected by *R* (see section 3.1.2 in chapter 3). At the initial stage of the changing process (ref. to Figure 69(a)), the $\vec{q}$ increases rapidly to reach a peak in the first 120-180s, especially at high charge rates. A similar observation was also observed by Barai et al. [72] and attributed to the effect of *R*. The R_O and sum of R_{CT} and R_P were measured using hybrid pulse power characterisation method at every 10% of depth of discharge. As shown in Figure 70, at 20 ^{o}C, the R_O keeps constant (~ 0.13 Ω) at different SoCs, the sum of R_{CT} and R_P is relatively low (~0.05 Ω) at 100% SoC. The R_O becomes a dominant factor in the battery system immediately after the charge begins. After a few hundred milliseconds, the oxidation reaction at the negative electrode happens, and it requires activation energy, which further generates the R_{CT}. Then the concentration polarization starts to affect the *R*. Lithium ions are released into the electrolyte, and electrons are transferred into the positive electrode. The diffusion speed of lithium ions is much slower than the electrons, which causes concentration difference, leading to the generation of the R_P, especially at high charge/discharge rates. For 0.5C, 1C and 1.5C, the $\vec{q}$ changes with the charge rate. However, the peak values of $\vec{q}$ at 1.5C and 2C are similar, which are 393 W/m^2 and 416 W/m^2, respectively. It is reflected by the voltage data, as shown in Figure 69(b). At 120s, the battery voltage under both 1.5C and 2C rates are close to the cut-off limits, which are 4.14V and 4.17V, respectively. The rapid voltage increase is mainly due to the concentration polarization.

After the heat flux reaches the peak, the $\vec{q}$ starts to decrease with a trend consistent with the current change. Under the 1.5C and 2C rates, the $\vec{q}$ starts to decrease rapidly after 120s, so do the current rates. While under 1C rate, a clear 3-stage process can be observed, with the $\vec{q}$ dropping fast with time first, followed by a slow rate of decrease and finally a fast drop again. Under the 0.5C rate, a 2-stage process is apparent with the $\vec{q}$ decreasing relatively quick first, followed by a slow decreasing process. During this period, the excess activation energy is not required for the reaction, and a stable concentration gradient is formed. Hence both R_{CT} and R_P decrease to a low level. As shown in Figure 70, the R_{CT} and R_P drop to ~0.01 Ω at 50% SoC. The R_O still takes a role in the battery system as it does not change with SoC.

The final stage is a period within which the $\vec{q}$ is zero. The reason for this is that, during this period, although the sum R_{CT} and R_P reaches a peak value of ~0.09 Ω, the battery is charged at potentiostatic mode, which means a low current rate. As shown in Figure 69 (b), the current rate gradually decreases, and hence the heat generation is negligible. Similarly, no heat generation period has been observed in other published studies, using accelerating rate calorimeters (ARC) to characterize the battery heat generation [203].

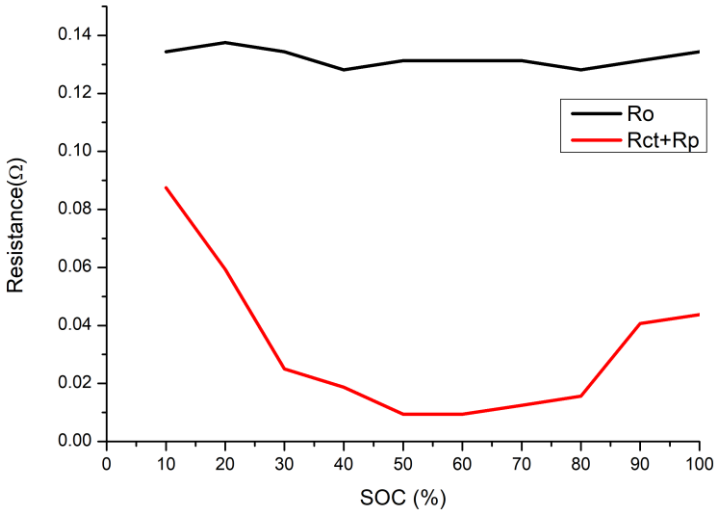

Figure 70 Internal resistance of a testing lithium-ion battery at different SoC at 20 ºC

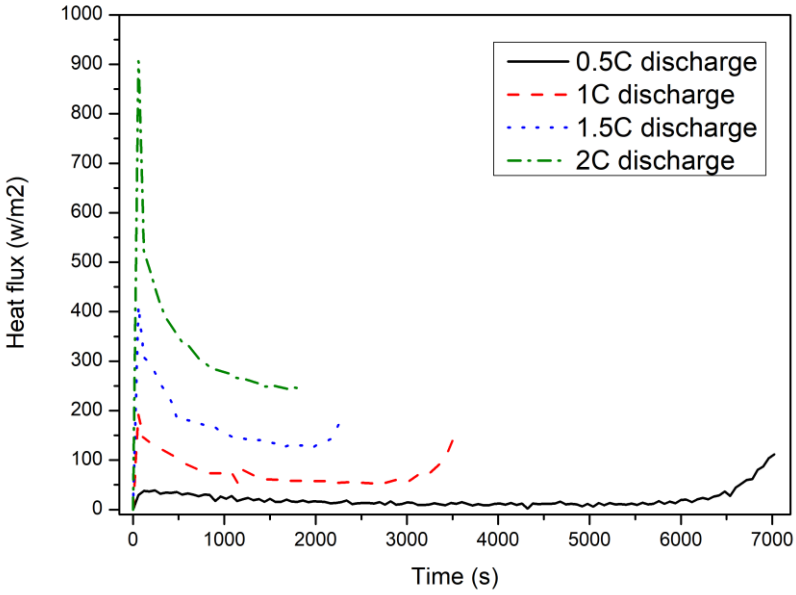

(a)

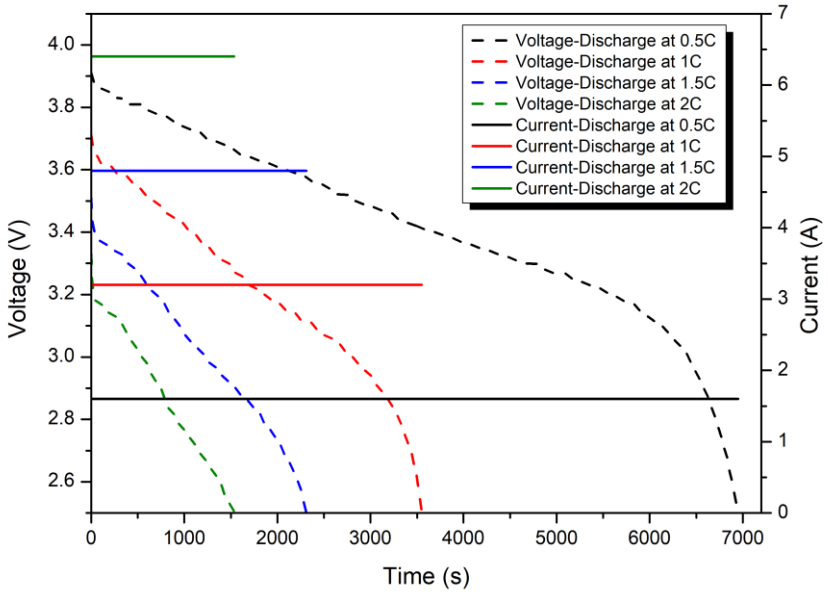

(b)

Figure 71 Characteristics of a Panasonic NCR18650B discharged at 0.5C, 1C, 1.5C and 2C: (a) The heat flux $\vec{q}$ (b) The voltage and current

Figure 71(a) shows the heat flux profile of a battery discharge process as a function of time. The heat flux $\vec{q}$ is also seen to depend on the current rate; a high discharge rate leads to a high $\vec{q}$. Similar to the charge process, the discharge process can also be divided into stages. When the discharge starts, the $\vec{q}$ reaches its maximum value almost instantly and the peak value increases with the increasing current rate; at 0.5, 1, 1.5 and 2C, the peak values of $\vec{q}$ are respectively 40, 192, 411 and 917 W/m^2. This significant increase in $\vec{q}$ at the initial stage is attributed to the effect of the R. After the peak heat flux, the $\vec{q}$ decreases with time due to the stabilization of the R_{CT} and R_P, and the rate of decrease declines with time. For the 0.5C, 1C and 1.5C rates, the last stage of discharge is different from the final stage of the charging process towards, where the voltage under these current rates decreases dramatically, whereas the $\vec{q}$ rises. At the end of the discharge process, the values of the $\vec{q}$ at 0.5C, 1C and 1.5C rates are respectively 111, 157 and 181 W/m^2. During this period the positive cathode is rich in lithium ions due to a poor ability to absorb lithium ions, leading to the generation of the R_{CT} and R_P. As shown in Figure 70, the sum of the R_{CT} and R_P at 10% SoC reaches its peak of 0.09 Ω. However, at the 2C discharge rate, the $\vec{q}$ does not show an increase towards to the end

of the process. This could be the reason that the R at high discharge rates is always at a high point, which could not give a sudden increase.

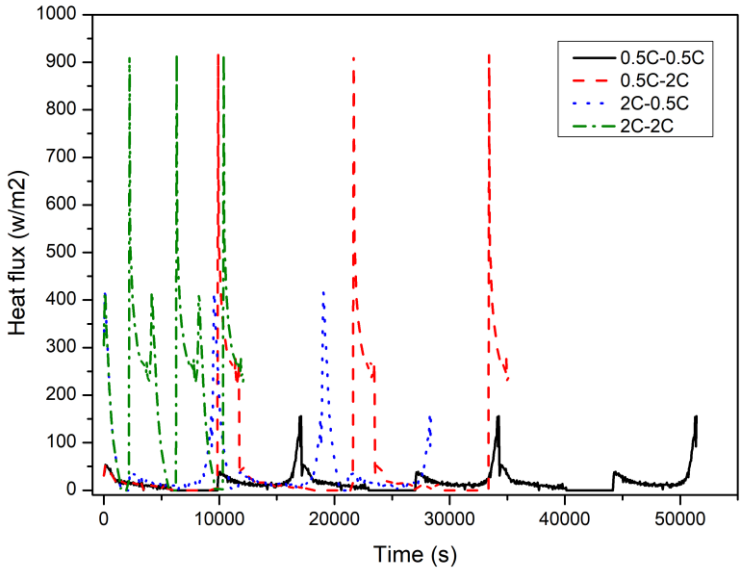

Figure 72 Heat flux of a lithium-ion battery under 3 cycles of charge and discharge at different rates

In order to examine the performance of the active cooling based BTMS with CPCM, different operation conditions were studied. Figure 72 shows the results obtained by using the thermal characteristics of the battery over three charge-discharge cycles at 0.5C and 2C charge/discharge rates as the input. The reasons the taking the two rates are that the 0.5C current rate can serve the normal charge with a regular EV driving profile, and 2C current rate can represent the fast charge with a fast EV driving profile. An active cooling based BTMS with CPCM was studied numerically. The definition of a proper operation here refers to constraints including an upper limit of the battery temperature and maximum temperature difference within individual cells. As indicated by the battery supplier, the maximum working temperature of the lithium-ion battery is 333K, and the temperature difference within a single cell in a battery module should not exceed 5K.

5.2. Energy efficiency characterization

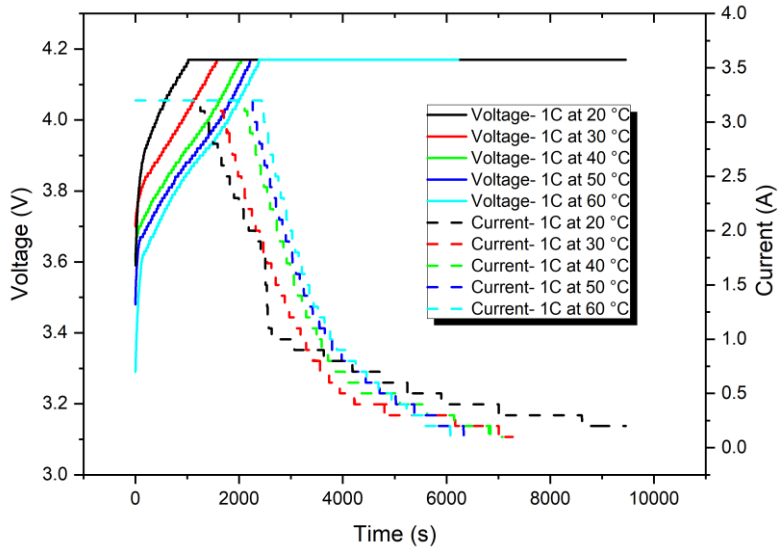

(a)

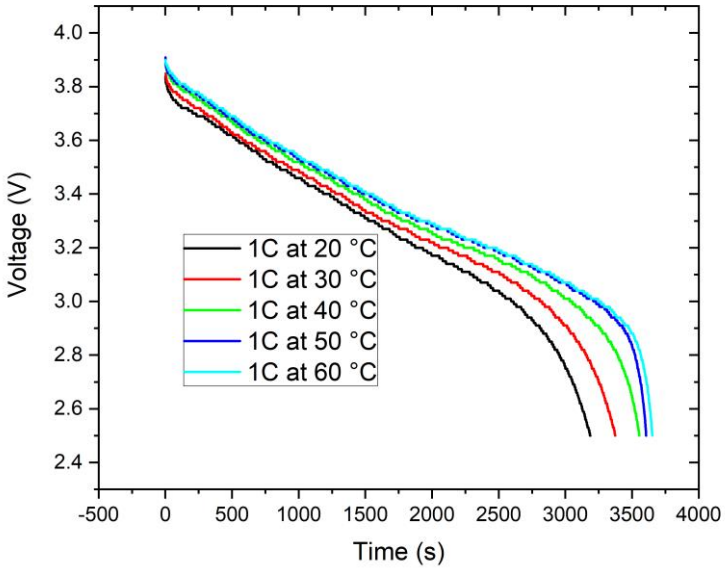

(b)

Figure 73 (a) Charge voltage and current and (b) discharge voltage of Panasonic NCR18650B battery under 1C current rate and 20, 30, 40, 50, and 60 ºC

When charged under a 1C current rate, the cell first undergoes a constant current charging progress. As can be observed in Figure 73 (a), the charge voltage at 0s of charge starts from 3.3V to 3.6V at different charge temperatures, and the battery has a lower start voltage at a higher temperature. The dependency of the start voltage on temperature is attributed to battery polarization, which leads to the sudden voltage increase when the battery charging starts, and is caused by the internal resistance includes the R_O, R_{CT} and R_P. Once the battery starts to operate the internal resistance begins to affect the battery. The R_O immediately causes the voltage increase, followed by R_{CT} and R_P, leading to a further increase in the start voltage of the battery.

At the start of the battery charge, the voltage increases and hits the 4.17V upper cell voltage limit. The time for this process ranges from 1000s to 2400s at different charge temperatures, and a shorter period is needed to reach the upper limit when the battery is charged under lower temperature. The difference can also be explained by battery polarization. Low temperature causes high internal resistance, leading to unexpected high initial battery voltage and unanticipated shorter plateau of the current during the charging process. The constant current charge process of the battery provides most of the energy in one charge. There have been many reports on the fast charging technology on mobile phones and electric vehicle, claiming that 80% of the battery energy can be charged within 30 minutes [219,220]. The 80% limit is precisely the constant current charge process where the battery can be charged under 2C or even higher current rate. After the constant current charge, the battery is charged under constant voltage process, and the current of the battery decreases until it reaches the current lower limit (65mA with Panasonic NCR18650B battery). The constant voltage charge process under a low current charge is much less efficient than a constant current process, as indicated in Figure 73 (a). 80% of the total charge time could only provide 20% of the electrical energy. The current of the battery under different temperatures also varies, which is consistent with the voltage change. The time of the constant voltage charge process of the cell under 20 ^{o}C is the longest. It is because a smaller portion of the electrical energy is charged into the battery compared with the cell under high temperatures, and the remaining space needs to be filled with a slow constant voltage process. Charging at 60 ^{o}C, the current of the battery remains at a constant value for the longest period and starts to drop at the 2400s. However, the subsequent dramatic declining leads to the overall charging completion at the earliest around 6000s. The results have shown that higher temperature could significantly increase the charge speed with a longer fast constant current charge period and a shorter slow constant voltage charge period.

When discharged under 1C current rate, the cell undergoes a constant current discharging. The open circuit voltage (OCV) of the battery is at 4.18V. As shown in Figure 73 (b), when the discharge starts, the degree of battery polarization is also different. The starting discharge voltages of the cells under 20, 30, 40, 50, and 60 ^{o}C are observed to be 3.81V, 3.85V, 3.88V, 3.89V and 3.9V, respectively. The sudden voltage drop is also caused by battery polarization which is essentially the effect of internal resistance. The internal resistance is temperature-dependent, and the lower the temperature, the higher the battery polarization. The discharge cut off voltage of the Panasonic NCR18650B is 2.5V, with a lower starting discharge voltage, the voltage range for the battery to discharge is undoubtedly smaller, leading to a shorter discharge time and lower discharge energy. With the cell continues to discharge, the cell voltage had a steep decline, the rapid decrease is caused by the increase of charge transfer resistance R_{CT} and the polarization resistance R_P when it close to the end of discharge. As shown in Figure 70, the R_{CT} and R_P are the lowest at 50% SoC and increase when the SoC is further decreased. The rapid drop of the battery voltage is seen in the range of 2700s to 3500s at different discharge temperatures. The time is temperature-dependent which is also due to the internal resistance. An elevated internal resistance of the battery causes more heat generated during the discharge (the irreversible heat), reduces the energy which can be taken from the battery, and eventually affects the energy efficiency of the battery. The current effect on the battery charge and discharge performance is further studied in the following section.

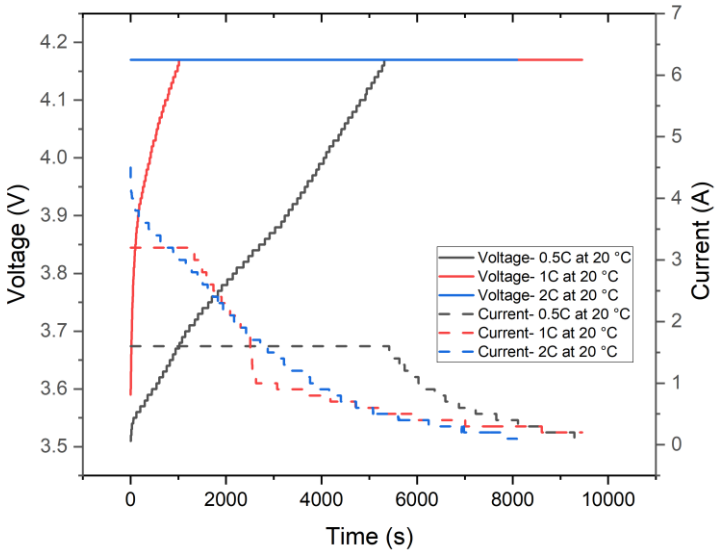

(a)

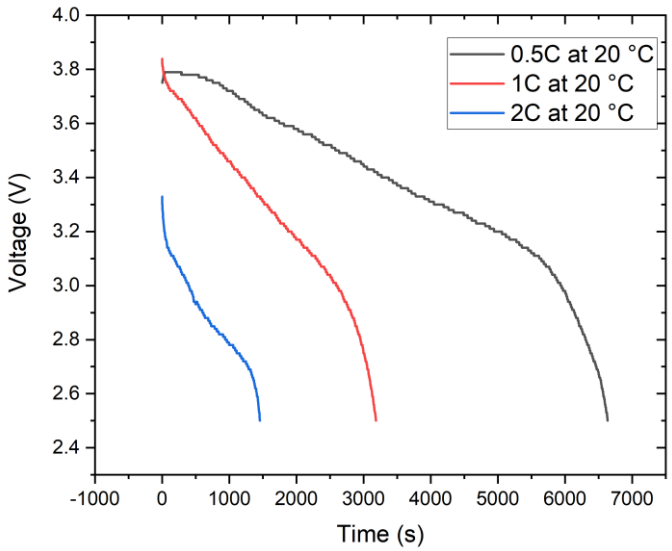

(b)

Figure 74 (a) Charge voltage and current and (b) discharge voltage of Panasonic NCR18650B battery under 0.5C, 1C and 2C current rate under 20ºC

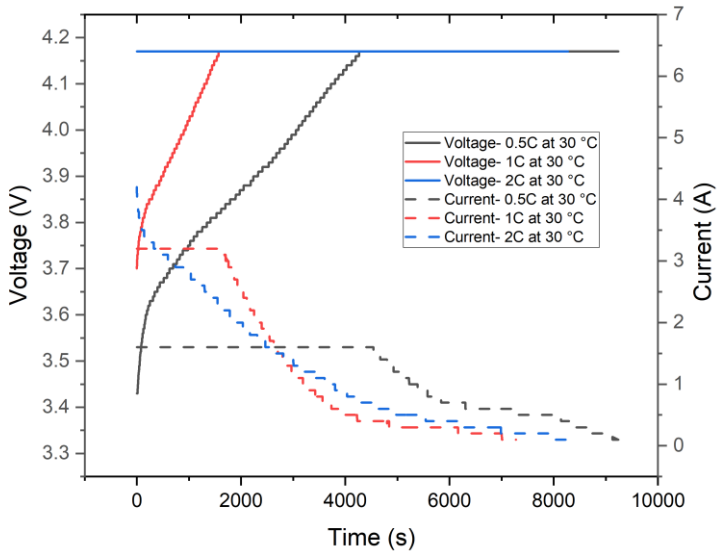

(a)

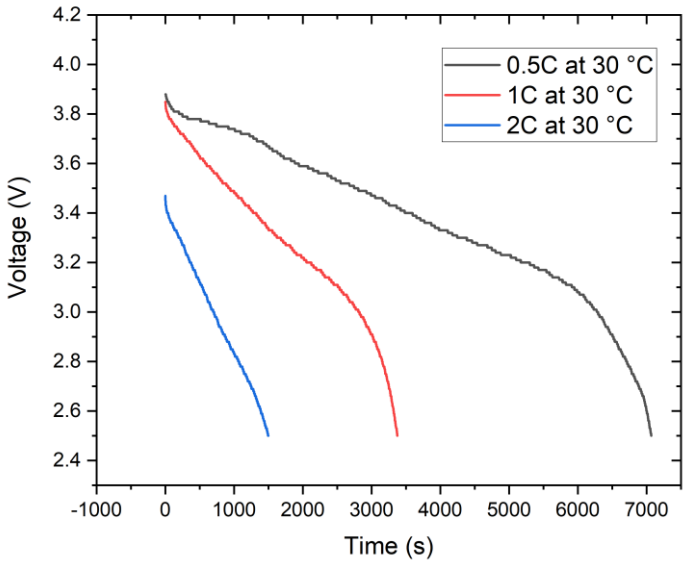

(b)

Figure 75 (a) Charge voltage and current and (b) discharge voltage of Panasonic NCR18650B battery under 0.5C, 1C and 2C current rate under 30ºC

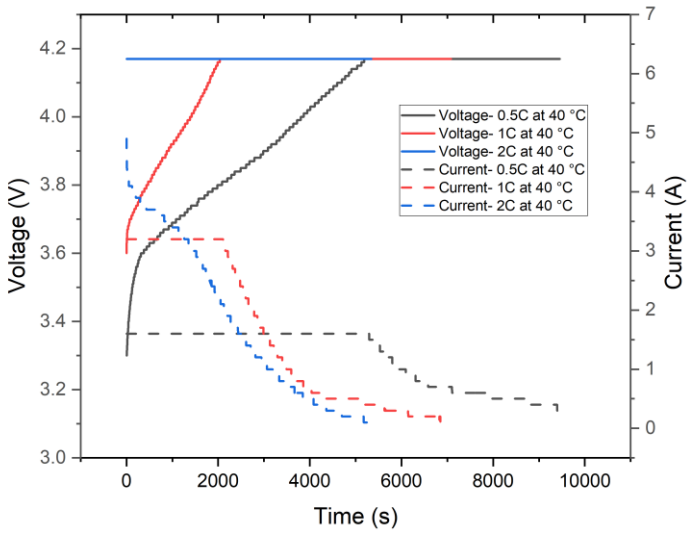

(a)

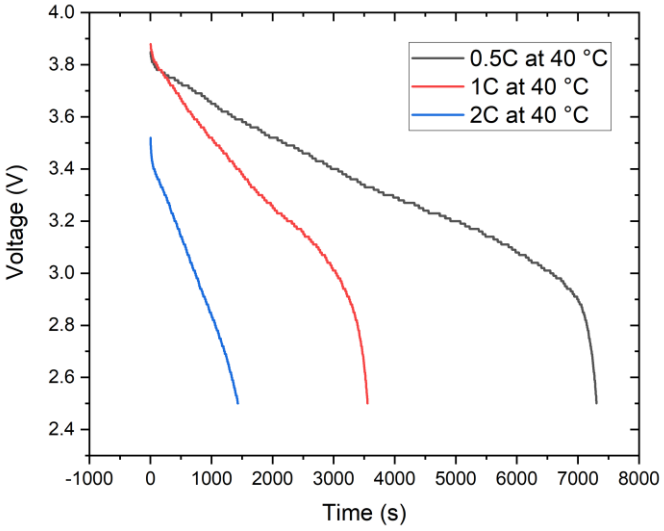

(b)

Figure 76 (a) Charge voltage and current and (b) discharge voltage of Panasonic NCR18650B battery under 0.5C, 1C and 2C current rate under 40ºC

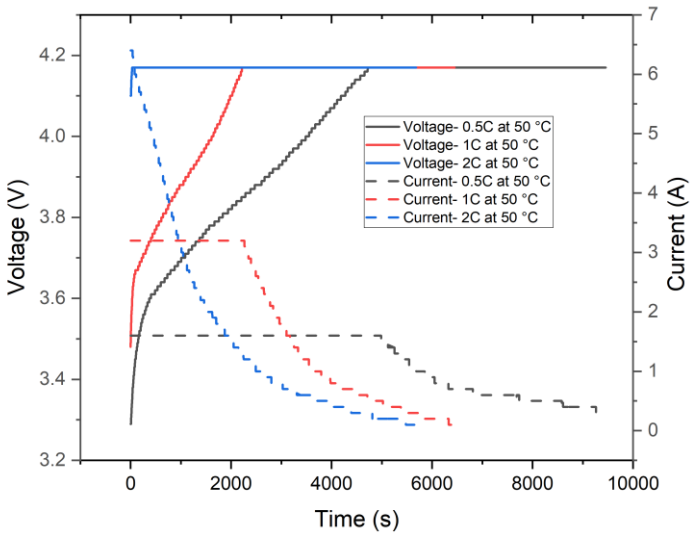

(a)

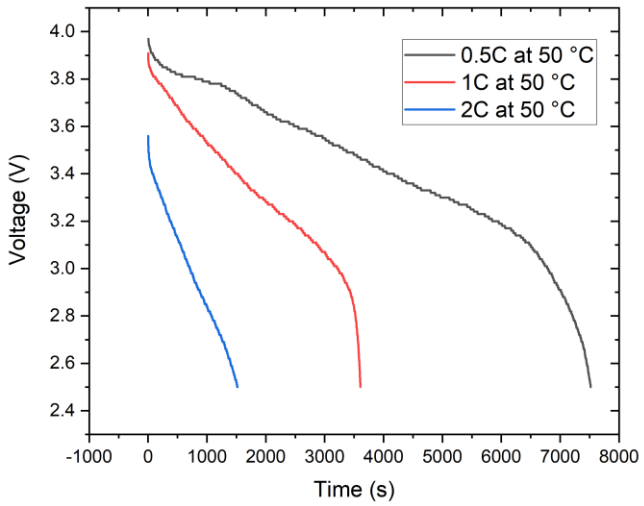

(b)

Figure 77 (a) Charge voltage and current and (b) discharge voltage of Panasonic NCR18650B battery under 0.5C, 1C and 2C current rate under 50ºC

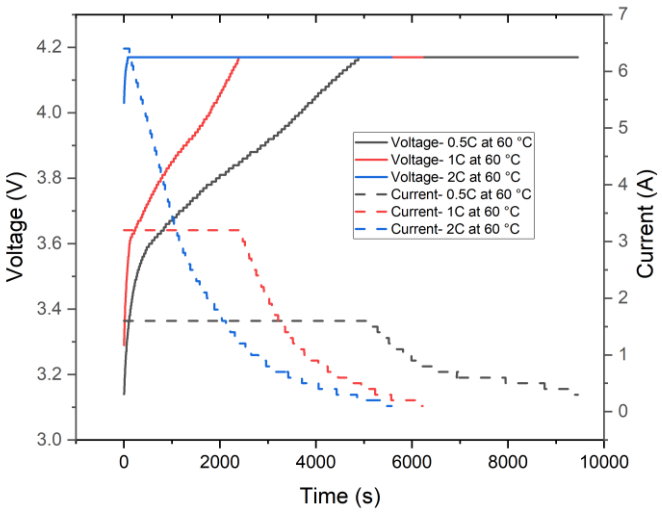

(a)

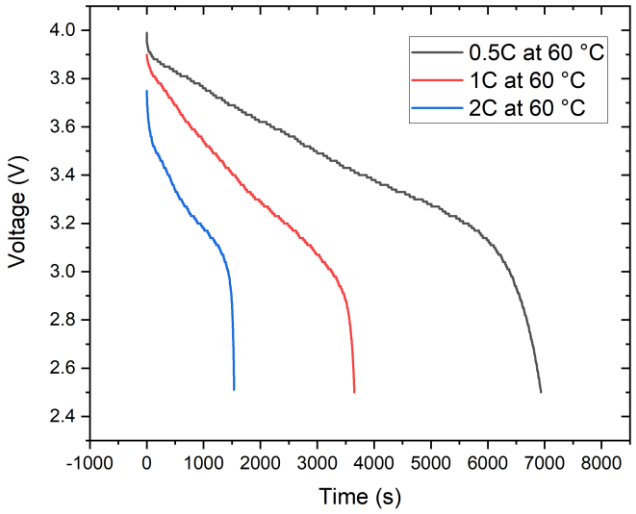

(b)

Figure 78 (a) Charge voltage and current and (b) discharge voltage of Panasonic NCR18650B battery under 0.5C, 1C and 2C current rate under 60ºC

As can be observed from Figure 74 to Figure 78, the current rate has a significant effect on the battery charge and discharge process. These results indicate that in all cases under 2C current rate, the battery polarization is the most significant, especially when the battery is charged. Comparing the 2C charging curve under 20-40 ºC as shown from Figure 74 (a) to Figure 76 (a), the charge voltage starts at the upper limit of 4.17V which means the battery is charged under a constant voltage from the very beginning. A high current rate is the leading causes of the severe battery polarization, at this point, a low charge/discharge temperature would aggravate the situation. In the case of 1C charge rate, the starting charge voltage ranges from 3.6 to 3.7V with a constant current charge period of 1000 to 2000s. At the same temperature range, the battery polarization is further suppressed under 0.5C. The starting charge voltage is from 3.3 to 3.4V, and the constant current charge periods ranges from 4200 to 4500s. When the battery temperature increases to 50 ºC, under 2C current rate, the starting voltage is observed to be at 4.1V, and 50s of constant charge process is observed (Figure 77(a)). At the same temperature, the constant current charge periods is the 2100s and 4500s under 1C and 0.5C, respectively, which is 42 and 90 times that under 2C. Figure 78 (a) shows that when the battery is charged under 2C at 60 ºC, the starting charge voltage of the battery is at 4V, and the constant current charge process maintains for 100s. Compared with 0.5C and 2C, there is more than 0.7V of difference. The constant current charge processes under 0.5C and 1C last 2500s

and 4300s, respectively. The current of the battery under 2C discharge rate starts at 6.4A, which is 2 and 4 times that under 1C and 0.5C charge, respectively. However, the current under 2C discharge declines much faster than that under 1C and 0.5C. At 60 ^{o}C, the current under 2C drops under the 1C current at 1000s and under the 0.5C current at the 2000s. Looking at Figure 74(b) to Figure 78 (b), the battery polarization under 2C discharge process is less significant, as the starting voltage still dropped gradually to 3.7V at 60 ^{o}C, 3.6V at 50 ^{o}C, 3.55V at 40 ^{o}C, 3.5V at 30 ^{o}C, and 3.35V at 20 ^{o}C. The starting voltages of 1C and 0.5C are similar and are maintained above 3.7V even at 20 ^{o}C.

The results of the battery charging process have shown that the current rate could have a significant effect on battery charging behaviour, and the temperature could further influence the charging process. The battery polarization is severe under 2C current rate. The constant charge time decreases with the increase of charge current rate, under abusive 2C charge rate and at 20-40 ^{o}C, the constant charge period is observed to be 0s. Even at a high temperature of 60 ^{o}C when the chemical reactions are active if charged under 2C current rate, the constant charge period is only 1/45 that under 0.5C. During the discharge process, the less significant current effect is observed under the discharge process compared with the charging process, while the starting discharge voltage difference between 0.5C and 2C is still 0.5V at 20 ^{o}C.

The specific energy and power of the battery when charged/discharged under different current rates and different temperatures are shown in Figure 79 to Figure 81. Most of the results show a linear relationship under the same current rate, the linear fitted curve is also plotted with the summary of the curves shown in Table 19 to Table 21.

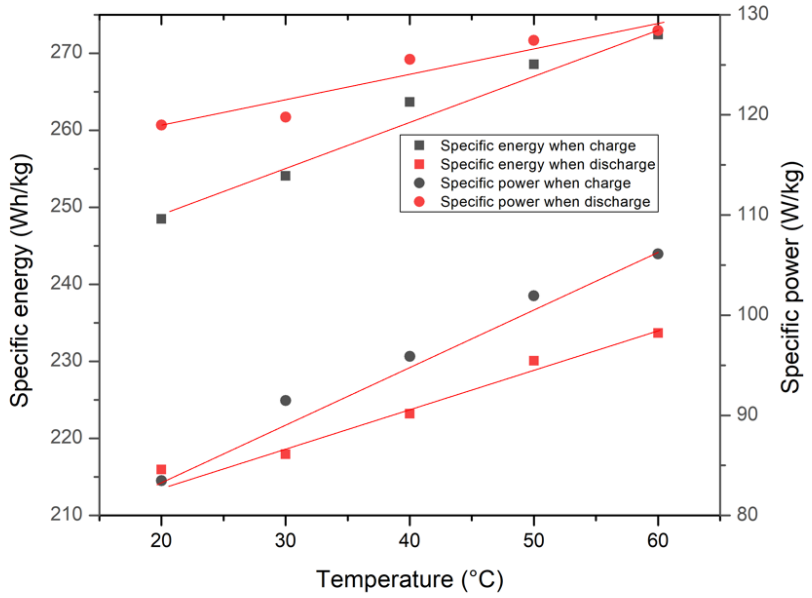

Figure 79 Specific energy and specific power under 0.5C charge/discharge as a function of temperature. Red lines are linear fitting curves

Table 19 Summary of the fitted curve of the specific energy and specific power under 0.5C current from 20-60 ºC

		Intercept		**Slope**		**Statistics**
		Value	Standard Error	Value	Standard Error	Adj. R-Square
Charge	Specific energy	236.49	2.39	0.62	0.05	0.96
	Specific power	73.47	1.53	0.55	0.03	0.98
Discharge	Specific energy	205.16	1.92	0.47	0.04	0.96
	Specific power	113.41	1.93	0.26	0.04	0.89

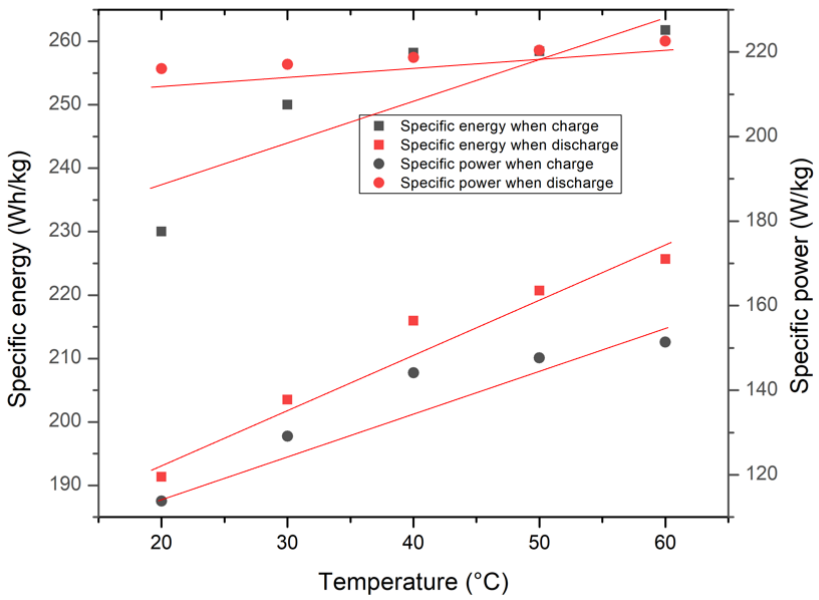

Figure 80 Specific energy and specific power under 1C charge/discharge as a function of temperature. Red lines are linear fitting curves

Table 20 Summary of the fitted curve of the specific energy and specific power under 1C current from 20-60 ºC

		Intercept		**Slope**		**Statistics**
		Value	Standard Error	Value	Standard Error	Adj. R-Square
Charge	Specific energy	225.39	10.98	0.67	0.25	0.59
	Specific power	99.70	7.45	0.93	0.1	0.87
Discharge	Specific energy	177.06	4.78	0.85	0.11	0.93
	Specific power	212.43	0.50	0.16	0.01	0.97

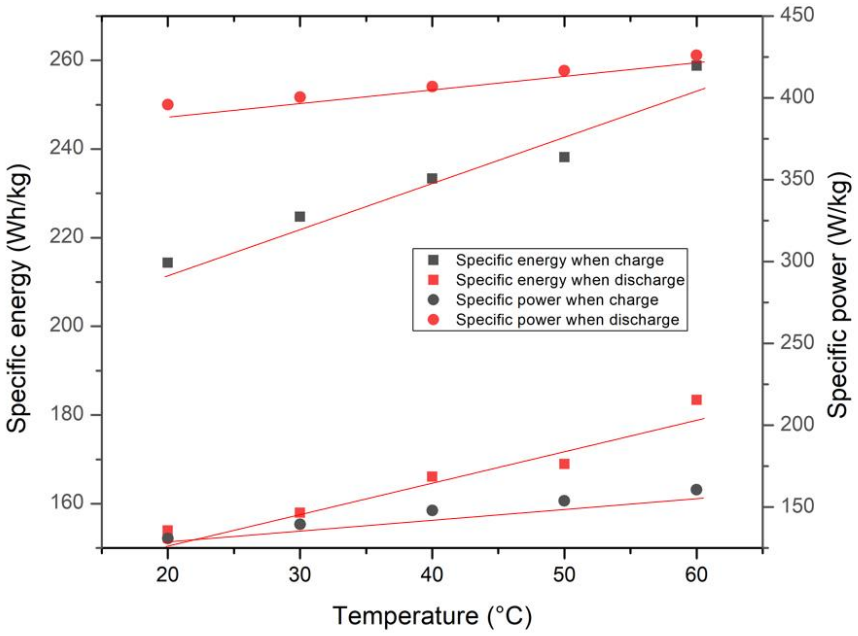

Figure 81 Specific energy and specific power under 2C charge/discharge as a function of temperature. Red lines are linear fitting curves

Table 21 Summary of the fitted curve of the specific energy and specific power under 2C current from 20-60 ºC

		Intercept		**Slope**		**Statistics**
		Value	Standard Error	Value	Standard Error	Adj. R-Square
Charge	Specific energy	192.94	5.85	1.02	0.13	0.93
	Specific power	116.92	1.40	0.73	0.03	0.99
Discharge	Specific energy	138.07	4.43	0.69	0.10	0.91
	Specific power	378.51	2.78	0.76	0.06	0.97

As can be observed in Figure 79, when charged under 0.5C at 20 ºC, the specific energy is 248wh/kg. As indicated in Table 19, with every 10 ºC of the temperature increase, the energy charged into the battery is increased by 6.2 Wh/kg. The same increase can be observed for the

specific power. The specific power under 0.5C at 20 ^{o}C is 83 W/kg, and the increment is 5.6 W/kg with every 10 ^{o}C of temperature increase. The discharge process is also significantly affected by temperature. The discharge specific energy under 0.5C at 20 ^{o}C is 216 Wh/kg, and with an every 10 ^{o}C increase, the specific energy increases by 4.8 Wh/kg. The discharge power under 0.5C at 20 ^{o}C is 119 W/kg, and the increment is 2.7 W/kg for every 10 ^{o}C increase. The discharge specific energy is lower than the charge specific energy while the discharge specific power is higher than the charge specific power. Although the coulombic efficiency (the efficiency with which charge is transferred in the battery facilitating an electrochemical reaction) of the commercial LIB can reach 99%, the existence of battery polarization determines that the voltage efficiency (ratio of the average discharge voltage to the average charge voltage) is normally under 95%. This can be aggravated under abusive discharge conditions, e.g. low temperatures and high discharge current rates. Therefore, the charged energy, which is the input into the battery, cannot be fully extracted when discharged. While the reason for the high specific discharge power is under discharge, the battery has a constant current. As can be observed from Figure 74 to Figure 78, the majority of the charging process is under a constant voltage with a decreasing current, which causes a long operation time and a low power.

When the charge/discharge current rate is increased to 1C current rate, the battery can deliver a much improved power but a slightly decreased energy. Figure 80 shows under 1C charge rate and at 20 ^{o}C, the specific energy of the cell is 230.04 Wh/kg, which is 18Wh/kg lower than the value under the 0.5C rate. As the current rate is increased, the specific charge power under 1C is 113 W/kg, which is 31W/kg higher than that under 0.5C operation. At 20 ^{o}C, the discharge specific power is significantly increased to 216W/kg, which is almost twice of that under a 0.5C operation.

When the cell is discharged under 2C current rate at 20 ^{o}C, the specific power is almost 2 times that under 1C and 4 times that under 0.5C (Figure 81). However, the specific energy is 80% and 71% under 1C and 0.5C, respectively. A higher current rate causes a more severe polarization, and a lot of electrical energy has been dissipated as irreversible heat, as reflected in Figure 71 (a), which shows that the heat flux under 2C discharge is much higher than 1C and 0.5C. When temperature increases, the loss of electrical energy under 2C current rate is eased. At 60 ^{o}C the specific energy under 2C discharge is 81% and 79% that under 1C and 0.5C, respectively. In the case of 2C charge, the loss of electrical energy due to the high current

rate is not very significant. At 20 °C the specific energy is 214 Wh/kg, which is 86% that under 0.5C, while the charge time is only 55% that under a 0.5C operation. With the charge temperature increased to 60 °C, the difference in the specific energy between 2C and 0.5C only gives a 5% difference, while the charge time can be saved by 37% under a 2C current rate.

Battery charging under a high current rate is very common, which benefits the electric vehicle market. One of the factors that limit the development of electric vehicle is the much longer battery charge time than the refuel of petrol or diesel. The results suggest that charge under a high current rate could achieve a much-improved power with a shorter charge speed, but a slightly reduced energy efficiency. The appears to support the reliability of fast charging technology. Although charging under a high current rate could cause a relatively high temperature of the lithium-ion battery, an efficient battery thermal management system can be a solution.

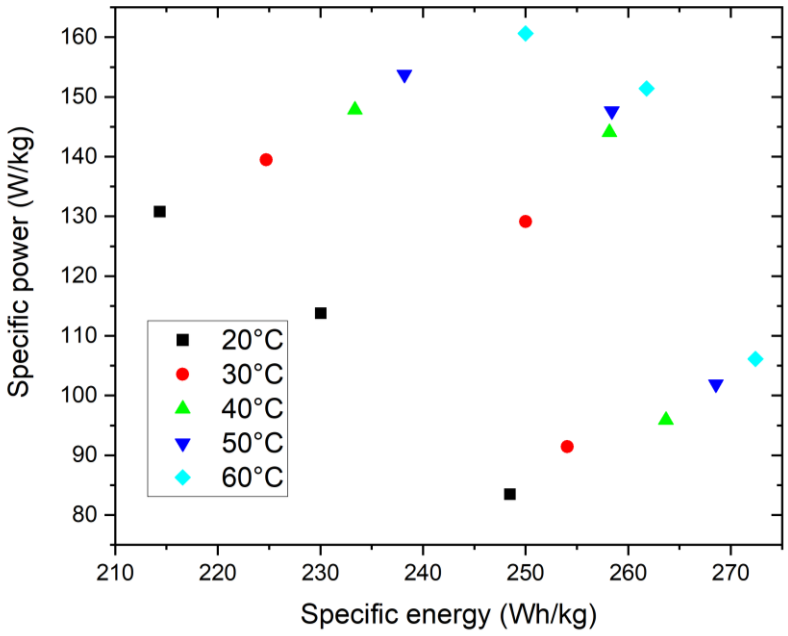

Figure 82 Ragone plot for a battery charged under 20-60 °C

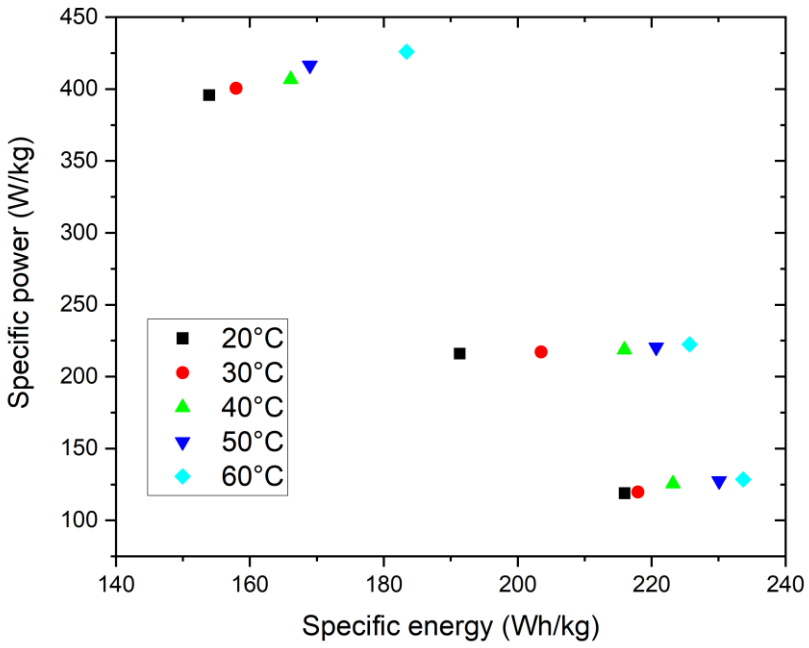

Figure 83 Ragone plot for a battery discharged at 20-60 ºC. Red lines are linear fitting curves

To further summarise the results, Ragone plots of the specific power as a function of specific energy are produced, see Figure 82. The results from the battery charging under different temperatures. It shows that high power and high energy could be achieved at a relatively high battery temperature. The battery specific energy is less sensitive to power at 60 ºC, as when the specific power increases from 106 to 160 W/kg, the specific energy only decreases by 22 Wh/kg. In the case of 20 ºC, when the specific power increases from 83 to 131 Wh/kg, the specific energy decreases by 34Wh/kg. Another conclusion is that the specific energy generally decreases with increasing power when charged under the same temperature.

The discharge behaviour under different temperatures is shown in Figure 83. Temperature effect on the battery energy can be observed from the results. At the same specific power, the specific energy generally increases with increasing temperature.

The round-trip efficiency (RTE) has been widely used to indicate the efficiency of energy storage technologies, including pumped-hydro energy storage, liquid air energy storage, flywheel energy storage, etc. When applied to battery energy storage, it is defined as the energy input to the battery can be retrieved:

$$\eta_{rt} = \frac{Q_{electricityoutput}}{Q_{electricityinput}} \tag{53}$$

The RTE of the battery when discharged under different current rates and different temperatures are shown in Figure 84. As can be observed from the figure, the current rate has the most significant effect on the RTE. At 20 °C, the difference of RTE between 0.5C and 2C current rates was 25%. Under all current rates, the RTE gradually increases with increasing temperature. The RTE difference between 0.5C and 2C current rate is reduced to 19% at 60 °C.

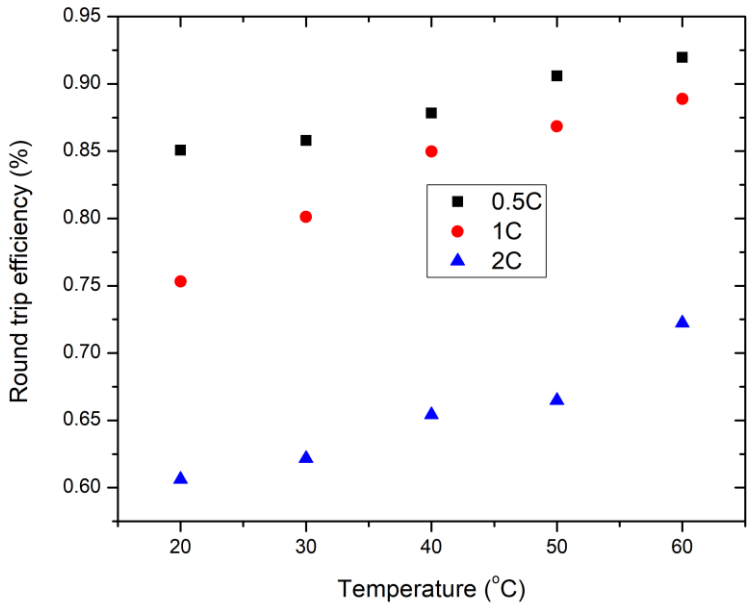

Figure 84 Round trip efficiency of the battery as a function of temperature when discharged under 0.5C, 1C and 2C current rate (the input energy when the battery was charged at 30 °C and under 0.5C current rate was chosen as the charging energy)

5.3. Summary of chapter 5

Heat flux of lithium-ion battery during both charge and discharge process is highly dependent on the current rates; a higher current rate leads to a higher heat flux. Heat flux during both charge and discharge processes exhibit multiple stages, which is affected by the R_{CT} and R_P. R_{CT} and R_P are relatively higher at high and low SoC, low and stable at 50% SoC. As a result,

the heat flux of the battery reached its peak when the charge/discharge began, then decreased along with the decrease of R_{CT} and R_P. At the end of the discharge, heat flux started to increase again due to the elevated R_{CT} and R_P, except at a high current rate. Although R_{CT} and R_P are also high during the end of the charging process, the battery was charged at potentiostatic mode, and the current rate is low, so the heat generation became negligible.

The battery performance is highly dependent on the current rate and operating temperature. Under low operation temperature, battery polarization is aggravated and causes reduced constant current charging time and discharging time. It prolongs the charging time and decreases the discharging time and leads to reduced battery performance in terms of the specific energy and specific power. Under 0.5C discharge current rate, the specific energy and specific power at 20 ^{o}C is 93% and 82% of which at 60 ^{o}C, respectively. The high current rate could further aggravate battery polarization. The LIB could observe much shorten constant current charging time and discharging time. At 20 ^{o}C, when the discharge rate is improved to 2C, the battery will have 28% of loss in specific energy. Although the high current rate causes reduced specific energy due to heat generation, it greatly saves the charging time. The specific power is increased proportionally to the current rate. At 60 ^{o}C, the charge time under 2C current rate is only 63% of which under 0.5C with only 5% of specific energy loss.

Chapter 6 Experimental and numerical investigation into active cooling-based battery thermal management system using composite phase change materials

This chapter presents the work on thermal management of two active cooling-based battery thermal management systems using composite phase change materials with different designs. The work on the battery thermal management system using a round tube focuses on the effect of inlet velocity of cooling liquid and the current rate on the thermal management performance. The work on the battery thermal management system using a tabular tube focuses on the effect of material type on the thermal management performance under multi charge-discharge cycles. The research on battery thermal management system using tabular shaped cooling channels [221] has been previously published in International Journal of Energy Research in 2020.

6.1. Battery thermal management system using round-shaped cooling channels

6.1.2. Experimental investigation on the battery thermal management system

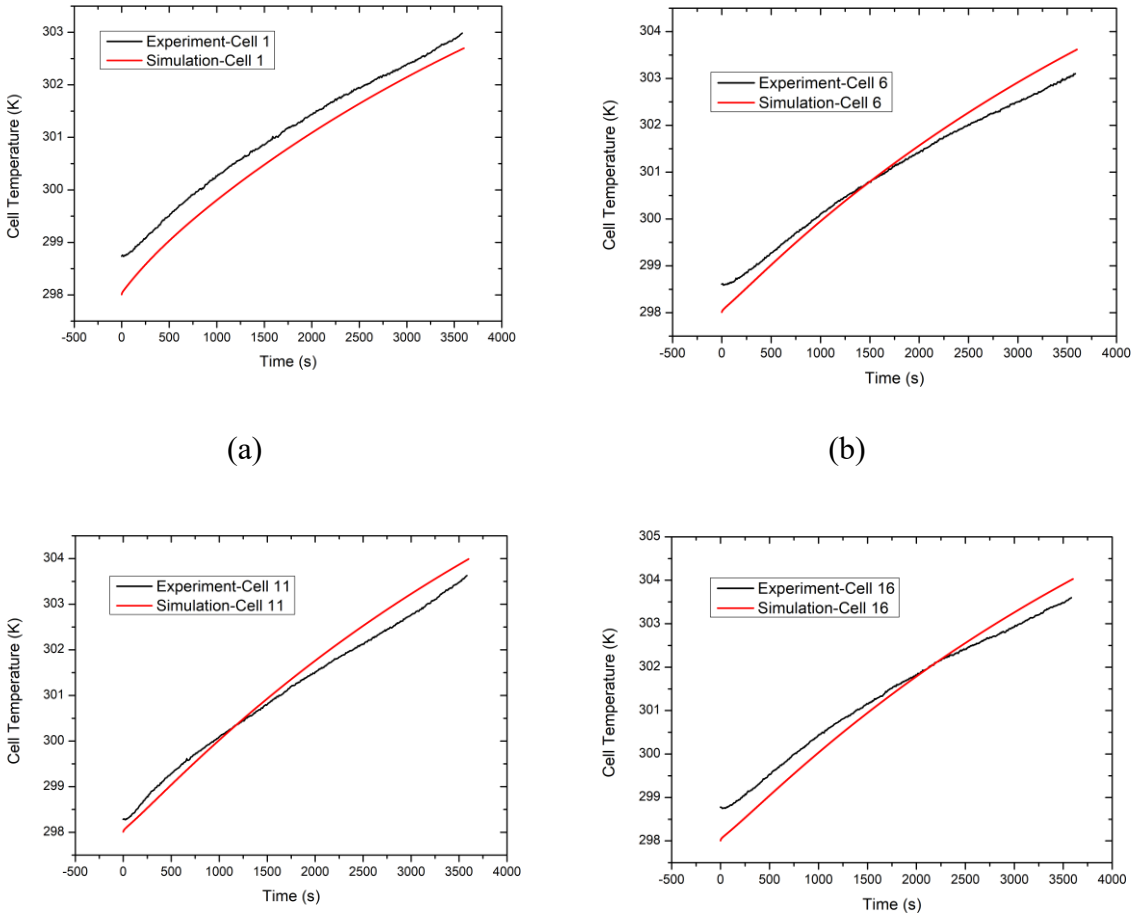

Figure 85 Average cell temperature (T_{ave}) as a function of time from the experimental test (solid lines) and numerical modelling (dash lines). The cell was discharged under 1C current rate at an initial discharge temperature of 298K, with inlet velocity of the heat transfer fluid (HTF) to be 0.005 m/s. (a) Cell 1 (b) Cell 6 (c) Cell 11 (d) Cell 16

Figure 85 shows the average cell temperature, T_{ave}, as a function of time for cells 1, 6, 11 and 16, see Figure 46 for battery layout. One can see that the measured and calculated T_{ave} increases with time from 298K to 303-304K. The simulation results show an excellent match with T_{ave} from the device test, with a maximum temperature difference (ΔT_{max}) below 0.5K. This indicates a good accuracy of the model.

Since the BTMS module was spitted into two parts with two layers of cooling tubes, both the temperature of the top and bottom parts of the cells were monitored using thermocouples.

Table 22 Cell temperature difference (ΔT) between the upper and lower part of the cells. The device was tested under 0.5C discharge at 298K, with the inlet velocity of the HTF to be 0.02, 0.01, 0.005, 0.003, 0.001 and 0 m/s.

	Cell temperature difference (K)					
Cell number	0.02m/s	0.01m/s	0.005m/s	0.003m/s	0.001m/s	0m/s
1	0.1	0.04	0.04	0.06	0.02	0.25
6	0.25	0.14	0.14	0.1	0.08	0.03

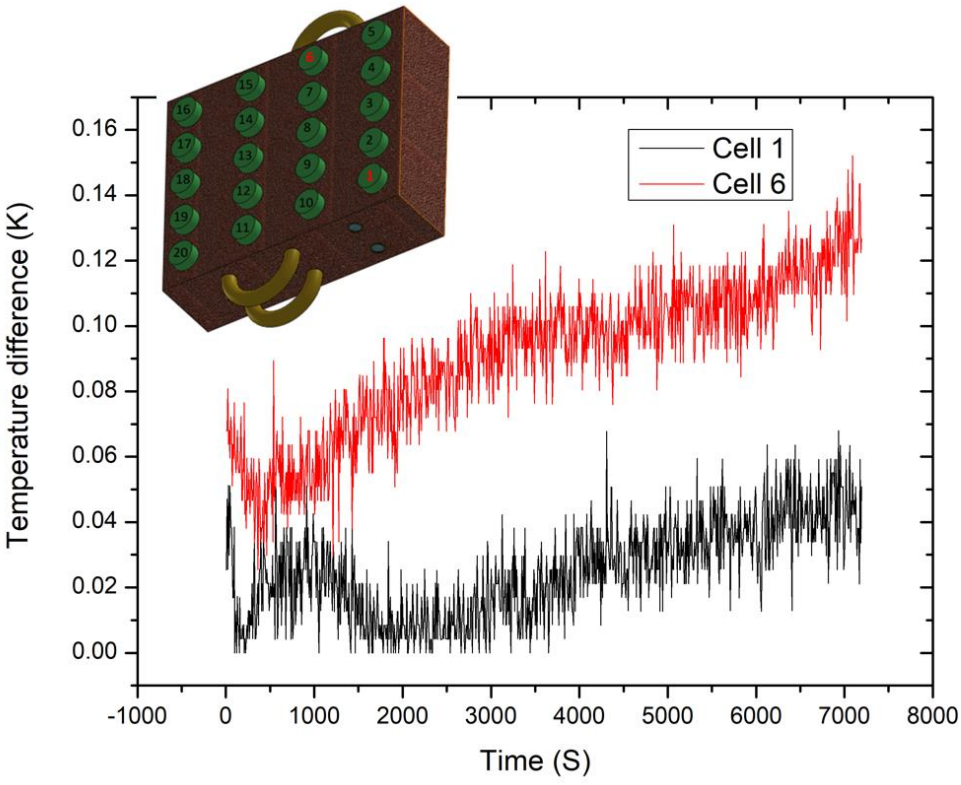

Figure 86 Cell temperature difference as a function of time between the upper and lower part of the cells. The device was tested under 0.5C discharge at an initial discharge temperature of 298K, with the inlet velocity of the HTF to be 0.005 m/s

Table 22 lists the ΔT of the 2 cells close to the inlet of the HTF, with Figure 86 showing an example of the results. As can be observed, there was little difference between the upper and lower parts, which is important for the performance and safety of battery operation.

With the heat transferred to the HTF from the batteries close to the fluid inlet, the cells at the back of the flow path would have been heated up, leading to a more significant temperature difference.

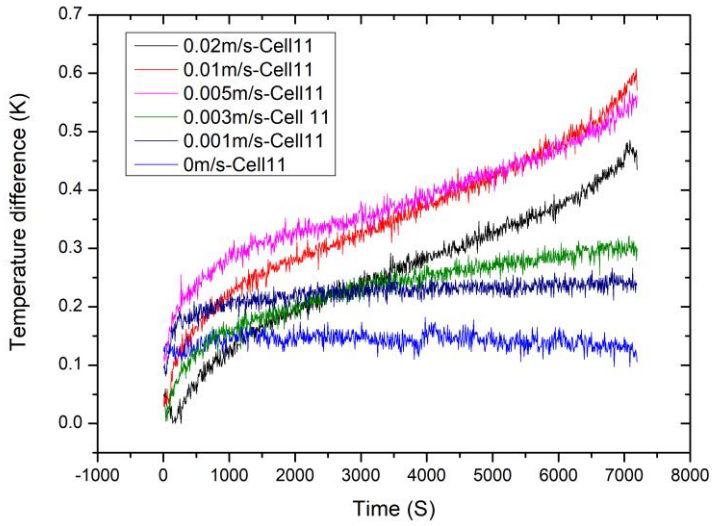

Figure 87 Temperature difference as a function of time between the upper and lower part of the cell 11. The device was tested under 0.5C discharge at an initial discharge temperature of 298K, with the inlet velocity of the HTF to be 0.02, 0.01, 0.005, 0.003, 0.001 and 0 m/s

Figure 87 shows that, without HTF cooling, ΔT within the cell 11 is negligible with only 0.1K. ΔT within the cell starts to increase with HTF cooling. Although the differences are all within a reasonable range, this still brings risk to the battery operation. With a relatively low inlet velocity (0.003 and 0.001m/s), ΔT tends to be less significant as it is less than 0.3K. At a higher inlet velocity of 0.005 and 0.01m/s, ΔT reaches 0.6K. At $\nu_{f,\mathrm{in}} = 0.02\mathrm{m/s}$, ΔT drops due to the effective cooling from the HTF.

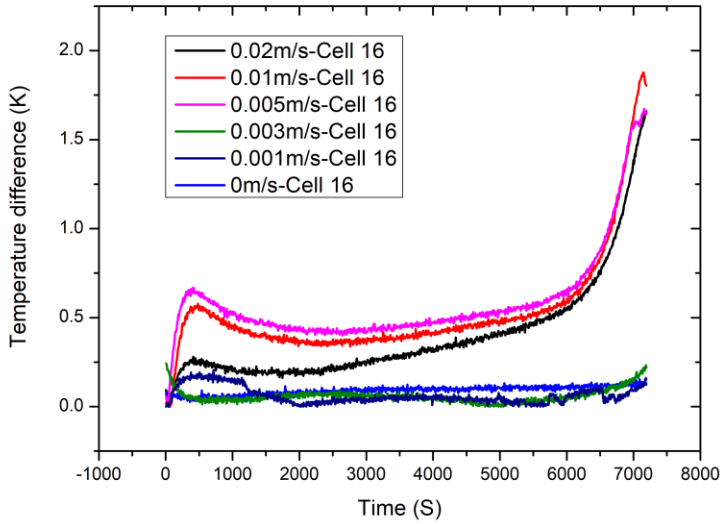

Figure 88 Temperature difference as a function of time between the upper and lower part of the cell 16. The device was tested under 0.5C discharge at 298K, with the inlet velocity of the HTF to be 0.02, 0.01, 0.005, 0.003, 0.001 and 0 m/s

With the HTF flowing to the cell 16, which is the farthest from the inlet of the HTF, ΔT becomes more significant. This can be observed in Figure 88. At $\nu_{f,\mathrm{in}} = 0.02.\ 0.01$ and $0.005\mathrm{m/s}$, ΔT is observed to be between 1.6K and 1.8K, whereas under a lower inlet velocity, the maximum cell temperature difference is 0.25K. Like cell 11, $\nu_{f,\mathrm{in}} = 0.01$ and $0.005\mathrm{m/s}$ give ΔT the most significant values. This has also been observed in the numerical results; see below for more details.

6.1.2. Numerical investigation on the battery thermal management system

6.1.2.1. Effect of inlet velocity of heat transfer fluid on battery module temperature

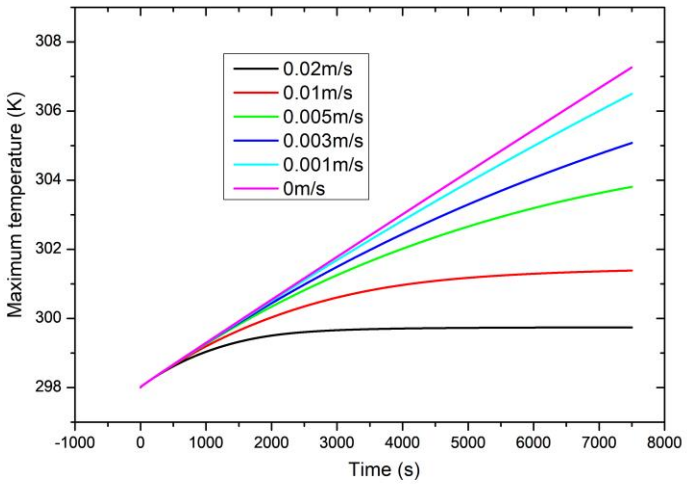

Figure 89 Maximum cell temperature (T_{max}) as a function of time when the device was tested under 0.5C discharge at an initial discharge temperature of 298K, with the inlet velocity of the HTF to be 0.02, 0.01, 0.005, 0.003, 0.001 and 0 m/s

Figure 89 shows the maximum temperature T_{max} as a function of time. High inlet velocity of HTF gives a low T_{max}. The battery temperature has only a 2K increase from the initial value at $\nu_{f,\mathrm{in}} = 0.02\mathrm{m/s}$. T_{max} increases gradually with reducing inlet velocity, when $\nu_{f,\mathrm{in}} = 0\mathrm{m/s}$, the battery has a linear temperature increase against the discharging time, and T_{max} reaches 307K when discharge is ended.

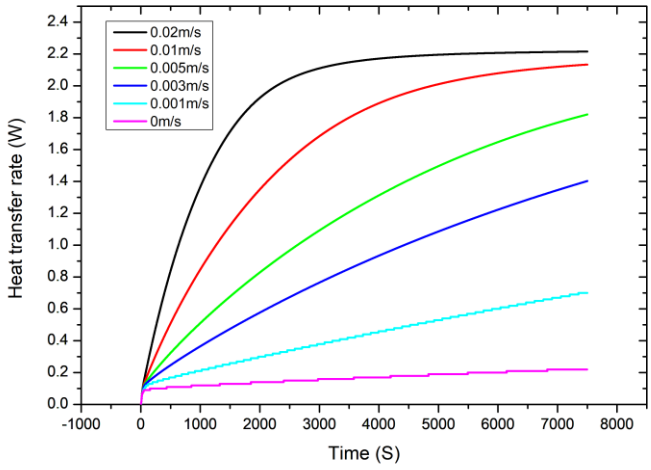

Figure 90 Heat transfer rate between the CPCM module and the heat transfer fluid as a function of time when the device was tested under 0.5C discharge at an initial discharge

temperature of 298K, with the inlet velocity of the HTF to be 0.02, 0.01, 0.005, 0.003, 0.001 and 0 m/s

The velocity effect on the BTMS cooling performance has also been reflected by the heat transfer rate between the CPCM model and the HTF. Figure 90 shows that under the same discharging period, the heat transfer rate increases with increasing inlet velocity of HTF, and reaches 2.2W at $\nu_{f,\text{in}} = 0.02\text{m/s}$, which is the highest under the conditions studied. With the same discharge current rate, this gives the greatest thermal control on the maximum battery temperature.

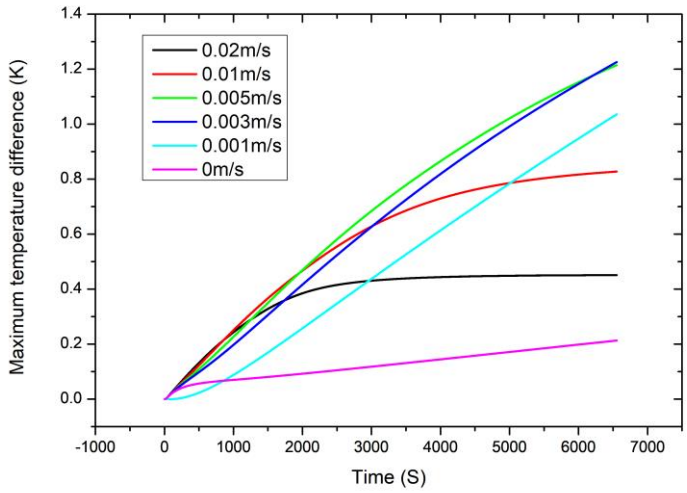

Figure 91 Maximum temperature difference (ΔT_{max}) within single cells as a function of time when the device was tested under 0.5C discharge at an initial discharge temperature of 298K, with the inlet velocity of the HTF to be 0.02, 0.01, 0.005, 0.003, 0.001 and 0 m/s

A meticulous study shows that, for a single cell, the growing trend of ΔT_{max}changes with the increasing HTF velocity. ΔT_{max} within the battery module can also be reduced with HTF velocities higher than 0.01m/s, which elevates the cell temperature difference. The heat accumulates in the HTF which heats up the cells at the back of the cell. As can be observed from Figure 91, ΔT_{max} is only 0.2K when there is only CPCM cooling. ΔT_{max} reaches 1.2K with the use of HTF at $\nu_{f,\text{in}} = 0.003 \text{ and } 0.005\text{m/s}$. Although ΔT_{max} decreases with the increase of inlet velocity, it is still 0.4K at $\nu_{f,\text{in}} = 0.02\text{m/s}$.

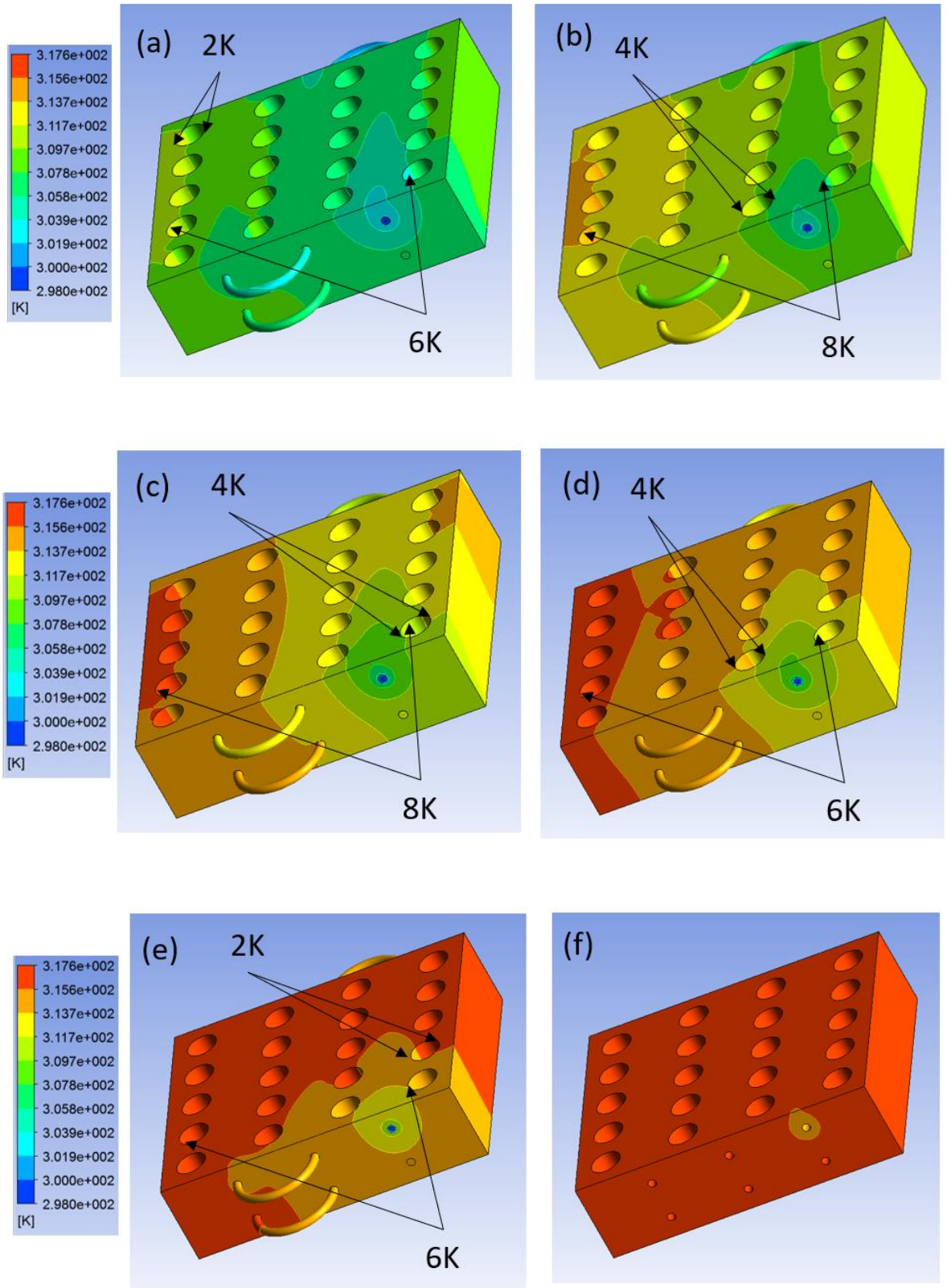

Figure 92 Temperature distribution of the BTMS module at the end of the operation with different cooling methods. The BTMS module was discharged under 2C current rate at an

initial discharge temperature of 298K (a) $\nu_{f,\mathrm{in}} = 0.02\mathrm{m/s}$ (b) $\nu_{f,\mathrm{in}} = 0.01\mathrm{m/s}$ (c) $\nu_{f,\mathrm{in}} = 0.005\mathrm{m/s}$ (d) $\nu_{f,\mathrm{in}} = 0.003\mathrm{m/s}$ (e) $\nu_{f,\mathrm{in}} = 0.001\mathrm{m/s}$ (f) 1C discharge, $\nu_{f,\mathrm{in}} = 0\mathrm{m/s}$

Under a 2C discharge current rate, ΔT_{max} is more significant. Figure 92 shows the temperature distribution within the BTMS module at different inlet velocities of HTF. At the highest velocity of $\nu_{f,\mathrm{in}} = 0.02\mathrm{m/s}$, ΔT_{max} within different cells is 6K (Figure 92(a)). ΔT_{max} increases to 8K with a lower inlet velocity of $\nu_{f,\mathrm{in}} = 0.01$ and $0.005\mathrm{m/s}$, and it drops back to 6K with a further decrease in the inlet velocity to $\nu_{f,\mathrm{in}} = 0.003$ and $0.001\mathrm{m/s}$. The same behaviour can also be observed on ΔT_{max} within the same cell in the module (Figure 92). At $\nu_{f,\mathrm{in}} = 0.02\mathrm{m/s}$, ΔT_{max} within the same cell is 2K, and it increases to 4K at $\nu_{f,\mathrm{in}} = 0.01, 0.005$ and $0.003\mathrm{m/s}$. Where the inlet velocity drops to 0.001m/s, ΔT_{max} is again 2K. Without the HTF cooling, ΔT_{max} is neither be observed within different cells nor in the same cell. Although the temperature difference is controlled well under both high and low inlet velocities, under a high discharge current rate, a high inlet velocity is still required to further bring down the maximum battery temperature.

6.1.2.2. Effect of current rate on battery module temperature

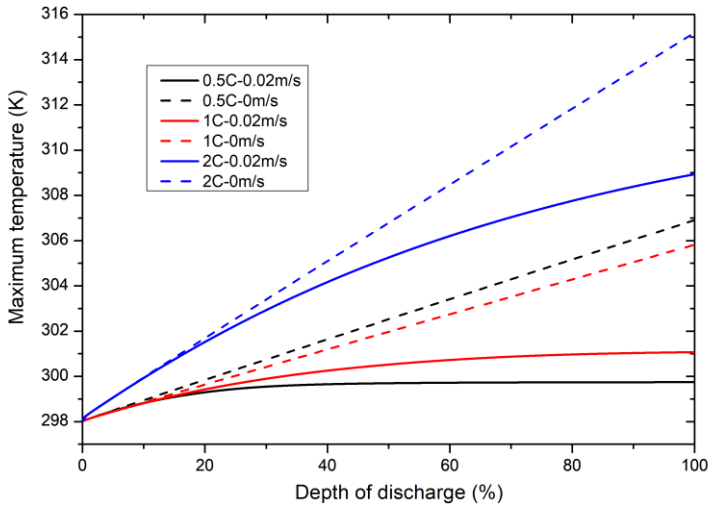

Figure 93 Maximum cell temperature as a function of the depth of discharge when the device was tested under 0.5C, 1C and 2C discharge at an initial discharge temperature of 298K, with the inlet velocity of the HTF to be 0.02 and 0 m/s

T_{max} is found to be affected by the battery discharge current rate, which is shown in Figure 93. One can see that under a high inlet velocity of liquid cooling ($\nu_{f,\mathrm{in}} = 0.02\mathrm{m/s}$), T_{max} under

0.5C and 1C is around 300K, while under 2C T_{max} increases by 8K, reaching 308K. At $v_{f,\mathrm{in}} = 0\mathrm{m/s}$ there is also a 8K of temperature difference when comparing T_{max} between 2C and 1C/0.5C.

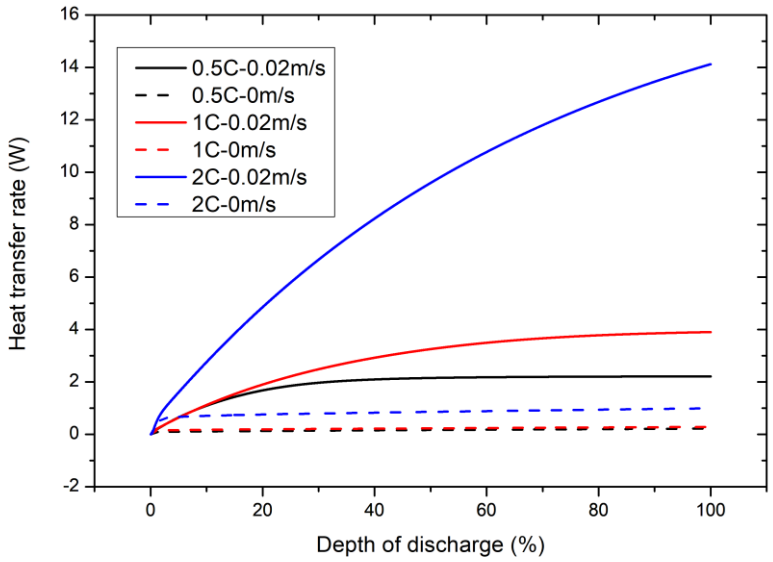

Figure 94 Heat transfer rate between the CPCM module and the heat transfer fluid as a function of time when the device was tested under 0.5C discharge at an initial discharge temperature of 298K, with the inlet velocity of the HTF to be 0.02, 0.01, 0.005, 0.003, 0.001 and 0 m/s

A higher discharge current rate can cause a high heat transfer rate within the BTMS module. This is shown in Figure 94, one can see the heat transfer rate between the CPCM module and HTF is 14W at the end of discharge, when discharged under 2C at $v_{f,\mathrm{in}} = 0.02\mathrm{m/s}$. With the same inlet velocity, the heat transfer rate was only 4W and 2W under 1C and 0.5C, respectively. Without HTF cooling, the difference of heat transfer rate is small with only 1W of difference.

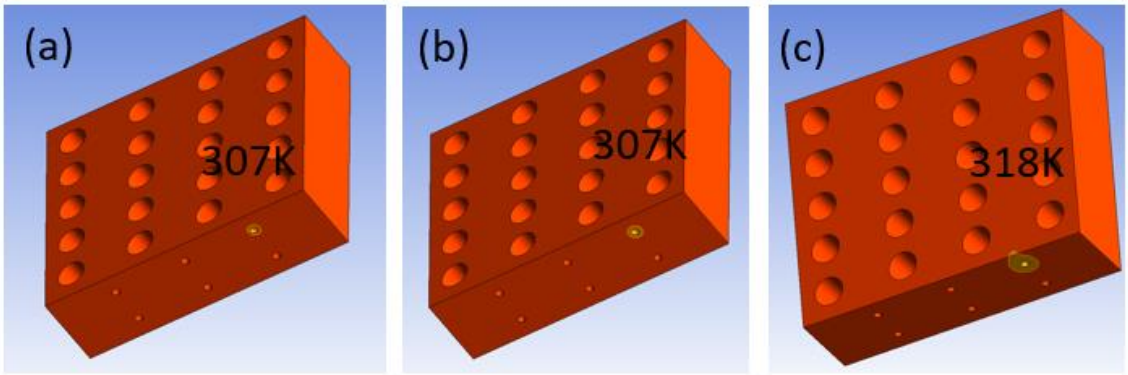

Figure 95 Temperature of the BTMS module at the end of the operation with different cooling methods. The BTMS module was discharged at an initial discharge temperature of 298K and without HTF cooling (a) 0.5C discharge (b) 1C discharge (c) 2C discharge

As shown in Figure 95, although the temperature of the BTMS reaches the maximum when there is no HTF cooling, under all discharge rates, there was no temperature difference between the cells.

The current rate influences the cell temperature difference when the HTF cooling is used. The temperature gradient is also built up within the BTSM, as can be observed in Figure 96. Under 0.5C discharge and at $\nu_{f,\mathrm{in}} = 0.003\mathrm{m/s}$, there is a 3K of ΔT_{max} within different cells. ΔT_{max} within the battery module increases to 6K when the discharge rate is increased to 2C (Figure 96 (e)), forming a 3K of temperature difference compared with ΔT_{max} at $\nu_{f,\mathrm{in}} = 0.003\mathrm{m/s}$. Temperature difference above 5K can lead to different OCV between single cells, leading to a short circuit. With more cycling of the battery module, the degree of battery ageing is different. Eventually, the single cells will have different capacities and hence affect the safety and performance. When the inlet velocity of HTF is increased to 0.02m/s, ΔT_{max} within different cells is reduced to 1K in the case of 0.5C and 1C discharge. Under 2C discharge rate, the value is 6K.

Controlling the temperature difference within the same cell is also crucial as high temperature differences can also cause hazards. Under 0.5C and 1C discharge, ΔT_{max} within a single cell can be controlled below 3K when discharged at $\nu_{f,\mathrm{in}} = 0.003\mathrm{m/s}$ (Figure 96 (a) and (c)). Under the same velocity, ΔT_{max} increases to 4K at a discharge rate of 2C. By increasing the

velocity to $0.02\mathrm{m/s}$, ΔT_{max} within a cell is reduced to 2K which is still 1K higher than that under 0.5C and 1C.

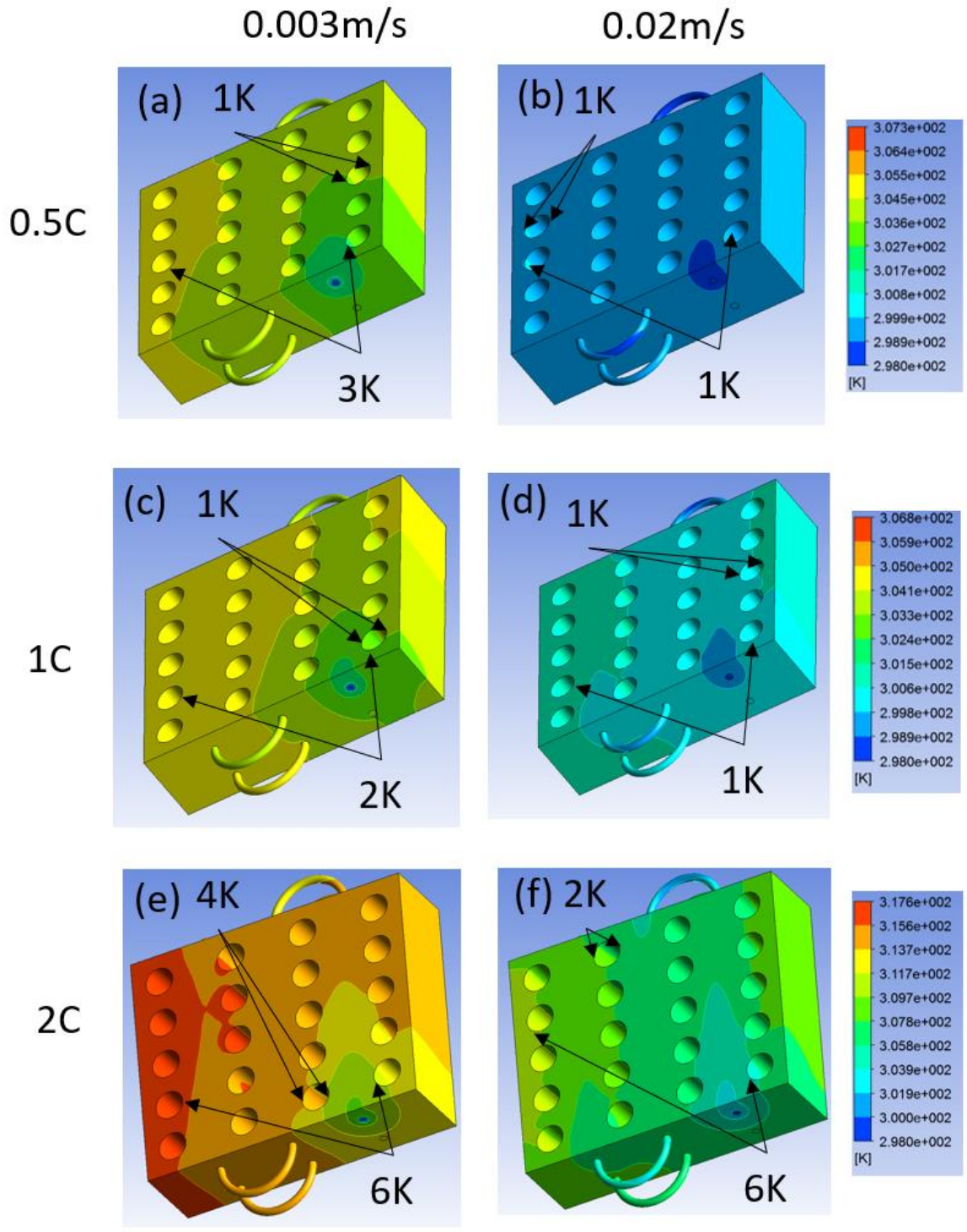

Figure 96 Temperature distribution of the BTMS module at the end of the operation with different cooling methods. The BTMS module was discharged at an initial discharge temperature of 298K (a) 0.5C discharge, $\mathbf{v_{f,in} = 0m/s}$ (b) 0.5C discharge, $\mathbf{v_{f,in} = 0.003m/s}$ (c)

0.5C discharge, $\nu_{f,\mathrm{in}} = 0.02\mathrm{m/s}$ (d) 1C discharge, $\nu_{f,\mathrm{in}} = 0\mathrm{m/s}$ (e) 1C discharge, $\nu_{f,\mathrm{in}} = 0.003\mathrm{m/s}$ (f) 1C discharge, $\nu_{f,\mathrm{in}} = 0.02\mathrm{m/s}$ (g) 2C discharge, $\nu_{f,\mathrm{in}} = 0\mathrm{m/s}$ (h) 2C discharge, $\nu_{f,\mathrm{in}} = 0.003\mathrm{m/s}$ (i) 2C discharge, $\nu_{f,\mathrm{in}} = 0.02\mathrm{m/s}$

6.2. Battery thermal management system using tabular shaped cooling channels

From this section onward, the results of BTMS using tabular shaped are presented for continuous multi-charge and discharge cycles. The effects of material type, liquid cooling capacity and battery current rate on the performance of BTMS are discussed. As mentioned in Section 3.2.1, the cooling channels occupy more space within the CPCM module while the heat transfer area of the tabular channels is 7 times higher than the round tube design.

6.2.1. Single charge/discharge

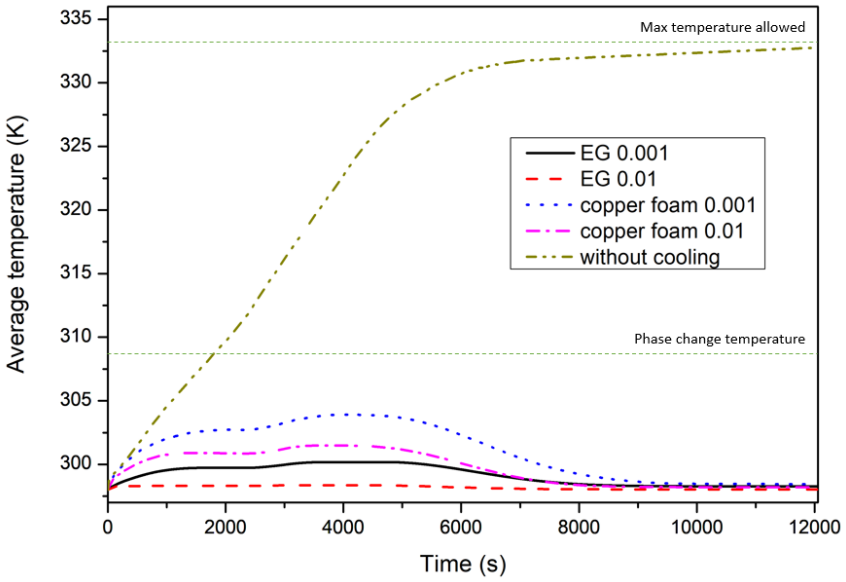

(a) 0.5C charge

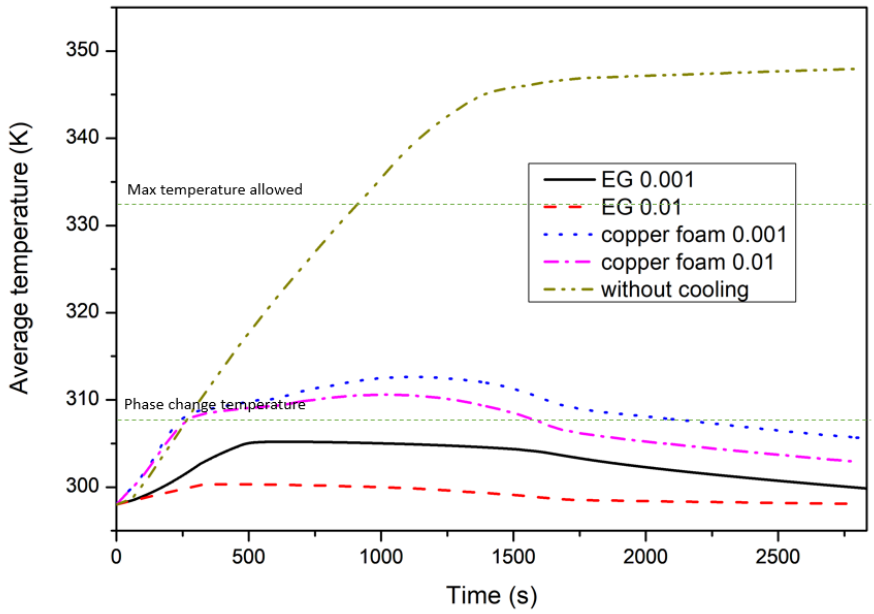

(b) 2C charge

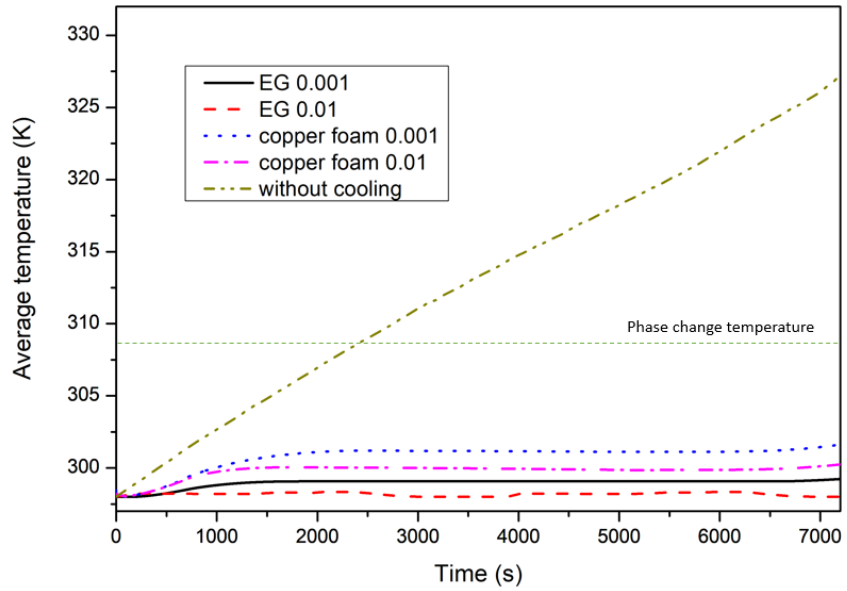

(c) 0.5C discharge

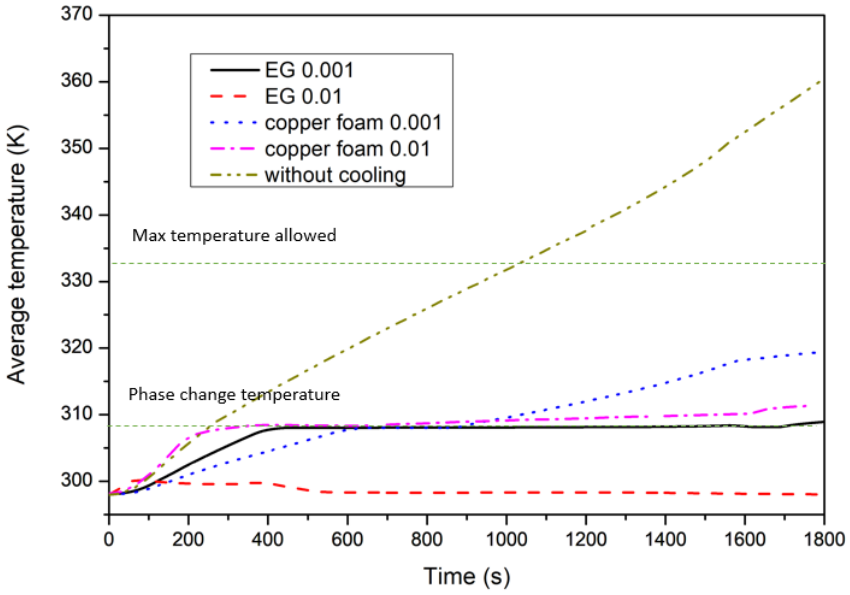

(d) 2C discharge

Figure 97 Time evolution of average battery surface temperature within the battery pack without cooling (under adiabatic condition), and at heat transfer fluid inlet velocity $\mathbf{v}_{f,\mathrm{in}} = 0.001$ and $0.01\mathrm{m/s}$ with EG based CPCM and copper foam-based CPCM for cooling, under (a) 0.5C charge (b) 2C charge (c) 0.5C discharge and (d) 2C discharge

Figure 97 shows the average temperature, T_{ave} on the battery surface as a function of time under different operation conditions with different charge/discharge rates. The temperature variation without cooling measures and with different thermal management strategies are compared. Without any cooling measures, under a moderate 0.5C rate, at the end of the charging and discharging, the T_{ave} values are at 332K and 325K, respectively, which are under the upper safety limit (333K) of the lithium-ion battery. However, under a more abusive 2C rate, the T_{ave} exceeds the safety limit. Under 2C charge rate (fast charging scenario), T_{ave} reaches 348K, whereas with 2C discharge, T_{ave} rises further to 360K. Compared with the initial temperature, there is a significant increase by 62K. Elevated battery temperatures accelerate its ageing as the rates of side reactions becomes significant. At this high temperature, thermal runaway could occur, leading to a safety hazard.

When different cooling methods are applied, a significant level of temperature control is achieved. This can be observed from Figure 97, the maximum temperature using all cooling methods is observed to be 320K, under a safe battery operation condition. Under 2C discharge, at $\mathrm{v}_{f,\mathrm{in}} = 0.01\mathrm{m/s}$, with EG based CPCM cooling, T_{ave} can be controlled close to the initial

temperature. While with the other three cooling methods, a phase change process can be observed between ~500-900s, which is due to the inherent thermal regulation function of the PCM. The duration that T_{ave} can be maintained at the phase change temperature account for some 70% of the total discharge time with EG based CPCM at $v_{f,\text{in}} = 0.001\text{m/s}$, showing that the PCM plays an important role in managing battery temperature.

6.2.2. Multi charge-discharge cycles

Figure 98 shows the battery temperature variation versus time with an EG based CPCM cooling unit under charge-discharge cycles, at different current rates. The time at which the upper safety limit (333K) occurs inversely proportional to the current rate: the higher the charge/discharge rate, the shorter the duration length.

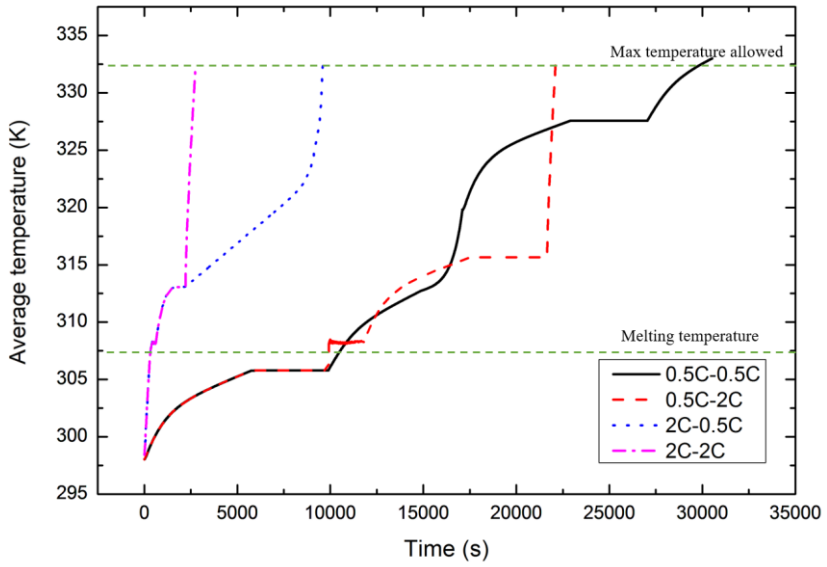

Figure 98 Time evolution of average battery surface temperature with only EG based CPCM cooling

For operations with the 0.5C current rate including charge-discharge cycles of 0.5C-0.5C, 0.5C-2C and 2C-0.5C, the time at which the upper safety limit is reached is observed to be 30700s, 22500s and 10000s, respectively, after the first charge/discharge cycle. Under the 0.5C-0.5C charge-discharge operation, after the first cycle (ending at t =19259s), T_{ave} reaches 320K, which is still under the safe limit of 333K given by the manufacturer datasheet. However, EG based CPCM is not able to control the battery temperate with continuous operation. When the second charge/discharge cycle begins, the starting T_{ave} is 22K higher than the first cycle. T_{ave} reaches 333K at 30700s during the second charge period. Under 0.5C-2C rate, the first plateau occurred in the constant voltage charging period when the current decreased to a very

low level, and the heat generated from the battery is insignificant, hence the CPCM temperature remains constant. In the second plateau, when the battery is at constant current discharging period, the CPCM took effect and the battery heat is stored as latent heat, hence the temperature remained the same for a period. Under an abusive 2C-2C operation, EG/PCM cooling gives an unacceptable performance. At t = 2900s when the first discharge period begins, T_{ave} has already exceeded the safe temperature.

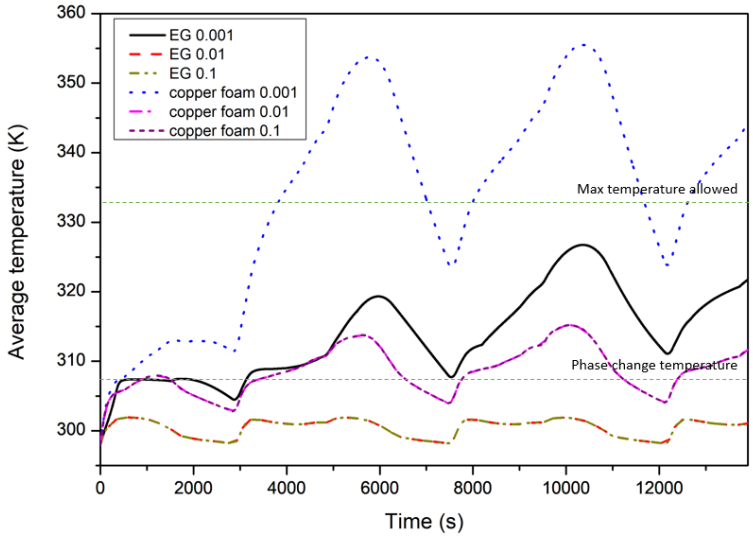

Figure 99 Time evolution of average battery surface temperature at $\nu_{f,\mathrm{in}} = 0.001, 0.01$ and $0.1\mathrm{m/s}$, with EG based CPCM and copper foam-based CPCM cooling, under 2C-2C charge-discharge cycle

To resolve the uncontrolled temperature increase, liquid cooling at $\nu_{f,\mathrm{in}} = 0.001, 0.01$ and $0.1\mathrm{m/s}$ is used in the BTMS, which can boost the heat dissipation from the batteries and CPCM. Figure 99 compares T_{ave} with EG based CPCM and copper foam based CPCM, under three abusive 2C-2C charge-discharge cycles. Comparing with pure CPCM cooling (Figure 98), T_{ave} is significantly reduced due to the benefit of liquid cooling, with maximum temperature observed to be 325K with EG based CPCM cooling. A significant heat transfer enhancement is observed when comparing $\nu_{f,\mathrm{in}} = 0.01m/s$ with $\nu_{f,\mathrm{in}} = 0.001m/s$, with EG based CPCM the maximum temperature is reduced by 23K to 302K, and with copper foam-based CPMC the maximum temperature is observed to be 315K. These are both under the safe limit of 333K. However, further enhancement has not been achieved when the $\nu_{f,\mathrm{in}}$ is increased from 0.01m/s to 0.1m/s. The temperature variations at $\nu_{f,\mathrm{in}} = 0.01\mathrm{m/s}$ and $\nu_{f,\mathrm{in}} = 0.1\mathrm{m/s}$ overlap each other, indicating that an increase in the flow rate can only enhance heat

transfer to a certain level, and hence in the following only the cases at $\nu_{f,\mathrm{in}} = 0.001$ and $0.01\mathrm{m/s}$ will be discussed.

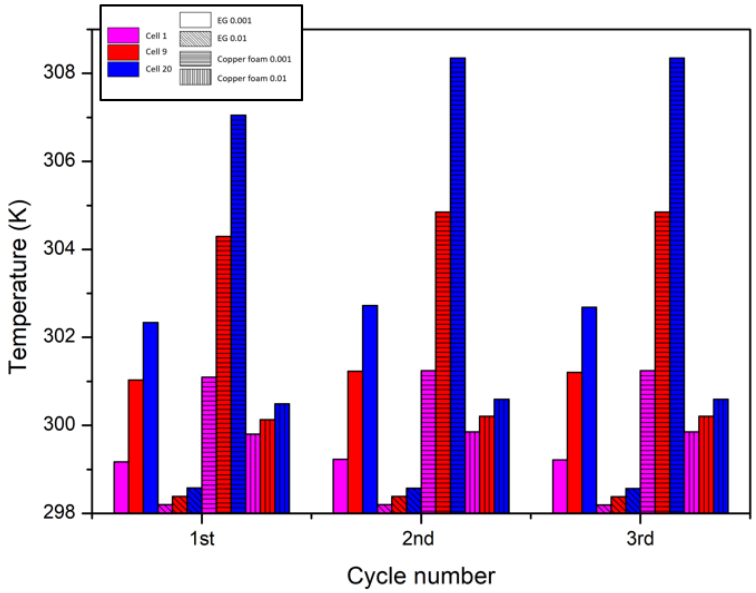

(a) 0.5C-0.5C

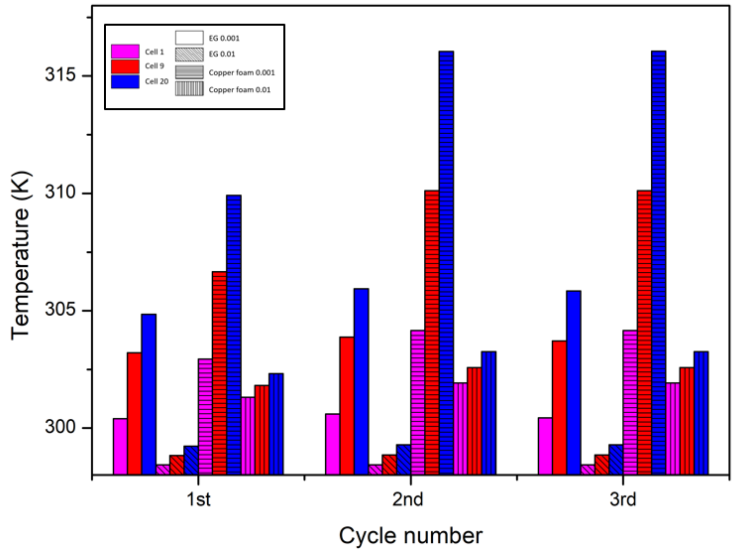

(b) 0.5C-2C

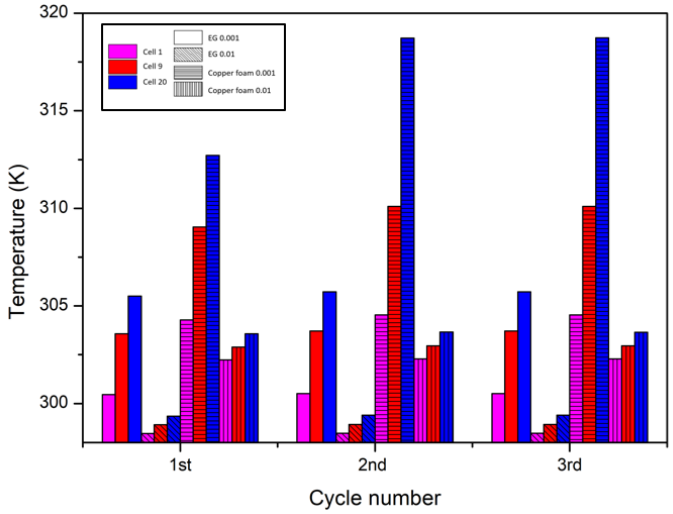

(c) 2C-0.5C

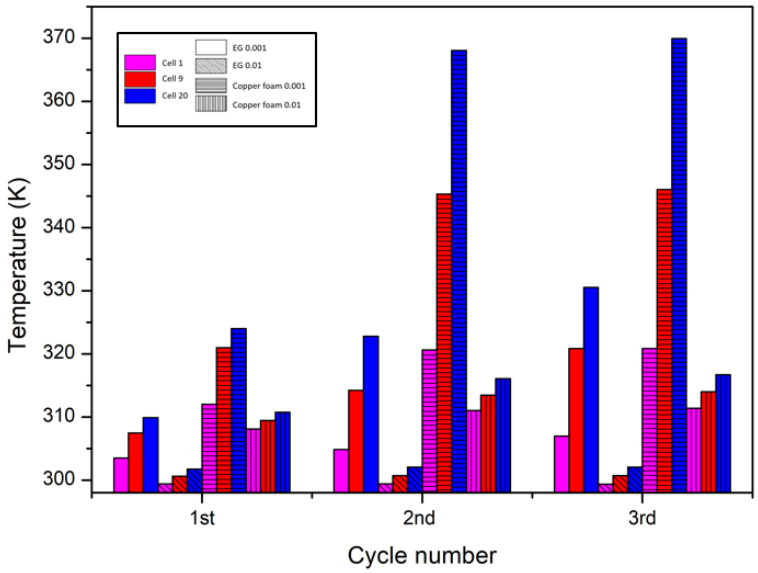

(d) 2C-2C

Figure 100 average cell temperature of cell (1), cell (9) and cell (20) during each cycle, at $\nu_{f,\text{in}} = 0.001$ and $0.01 m/s$ and with EG based CPCM and copper foam-based CPCM cooling, under (a) 0.5C-0.5C, (b) 0.5C-2C, (c) 2C-0.5C and (d) 2C-2C charge-discharge cycle

Figure 100 illustrates T_{ave} at different cycles under different operation conditions (positions of the are cells shown in Figure 47). The current rate has a significant impact on T_{ave}, as can be observed from Figure 100. The maximum cell temperature is 308K under 0.5C-0.5C cycle, ~317K under 0.5C-2C and 2C-0.5C cycles and a much higher value of 370K under 2C-2C cycle. It can also be concluded that EG based CPCM generally has a better cooling ability than

copper foam-based CPCM. This can be observed from Figure 100 (a), in the third cycle at $v_{f,\text{in}} = 0.001\ m/s$, with EG based CPCM cooling, T_{ave} of cell (20) is observed to be 6K less than the case with copper foam based CPCM cooling. Less temperature difference within the battery pack is apparent with EG based CPCM cooling. Under 0.5C-2C cycle (Figure 100 (b)), the maximum temperature difference (between cell 20 and cell 1) with copper foam-based CPCM cooling at $v_{f,\text{in}} = 0.001\ m/s$ is found to be 12K, while that with EG based CPCM cooling the temperature difference is only 6K. The T_{ave} is also seen to increase with cycle number, as shown in Figure 100 (d). With EG based CPCM cooling at $v_{f,\text{in}} = 0.001\ m/s$, the cell (20) temperature is 310K in the first cycle, and 323K in the second cycle. With copper foam-based CPCM cooling, the increment is 44K.

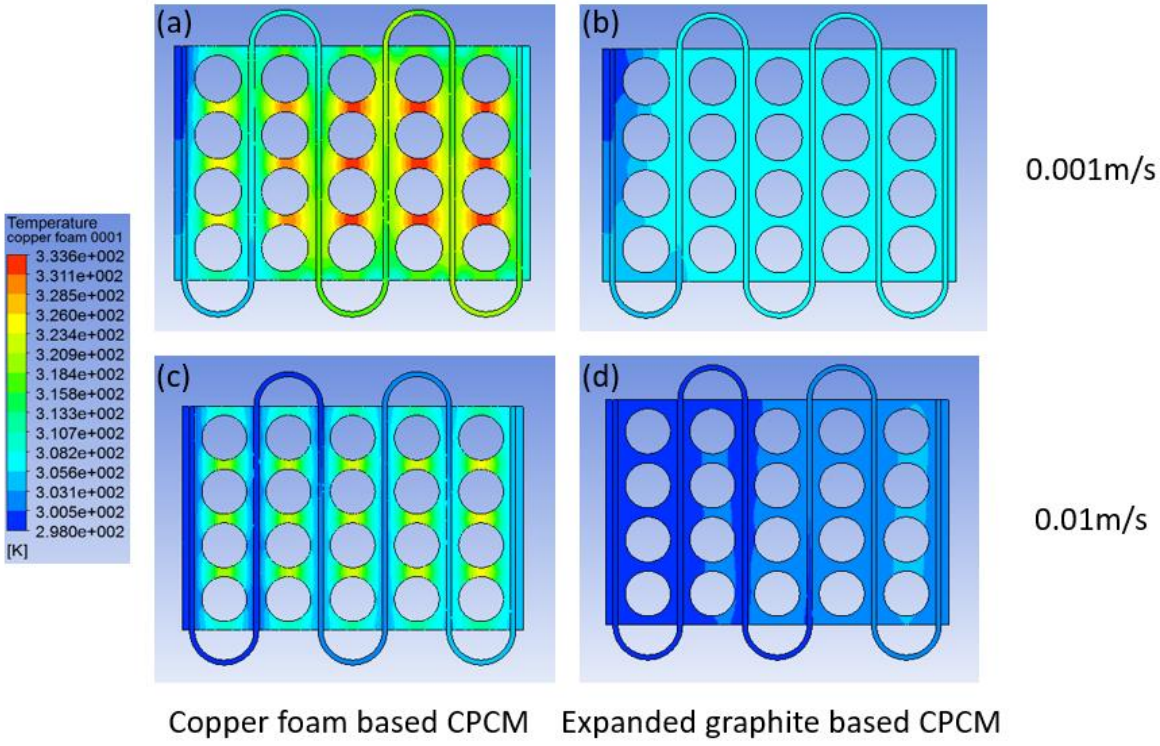

Figure 101 Temperature distribution of the BTMS module under 0.5C-2C cycle at the end of the operation with different cooling methods. (a) $v_{f,\text{in}} = 0.001\ m/s$, copper foam based CPCM (b) $v_{f,\text{in}} = 0.001\ m/s$ EG based CPCM (c) $v_{f,\text{in}} = 0.01 m/s$ copper foam based CPCM (d) $v_{f,\text{in}} = 0.01 m/s$ EG based CPCM

Temperature differences within BMTS module can also be observed. The contour shown in Figure 101 clearly shows the non-uniformity of the temperatures with different cooling methods. Significant temperature gradients can result in mismatched capacities within single

cells, and the battery pack cannot release all stored energy. With copper foam-based CPCM cooling and at $v_{f,\text{in}} = 0.001\ m/s$ (Figure 101 (a)), after the 3 charge/discharge cycles, the temperature of the battery (1), which is close to the inlet of the fluid, rises by 19K, where the battery (20) which is close to the outlet of the fluid, rises by 24K, forming a 5K difference in the temperature. The significant temperature difference also forms on the single cell as 19K of temperature gradient can be observed between the two sides of the battery (20). With an increased $v_{f,\text{in}}$ (Figure 101 (c)), lower temperature difference of 4K is observed within both the battery pack and the single cell. EG based CPCM provides an excellent temperature uniformity to the battery pack. As it is shown in Figure 101 (b) and Figure 101 (d), the maximum temperature difference within the battery module and single cell are kept of 5K.

Dimensional analysis has been carried out on the numerical results. With an aim to generalize the finding. The results with the following dimensionless parameters:

- Dimensionless time: $\tau = \frac{C_p(T_i - T_m)}{L}\frac{\alpha t}{l^2}$ (54)

where C_p is the specific heat capacity, T_{in} is the initial temperature, T_m is the phase change temperature, L is the latent heat, α is the PCM thermal diffusivity, t is the time elapsed, l is the length through heat conduction.

- Dimensionless temperature: $\theta = \left|\frac{T - T_m}{T_i - T_m}\right|$ (55)
- Nusselt number: $Nu = \frac{\vec{q}}{\Delta T}\frac{l}{k}$ (56)

where $\vec{q}$ is the heat flux, ΔT is the temperature difference between the T_f and T_m , k is the thermal conductivity of HTF.

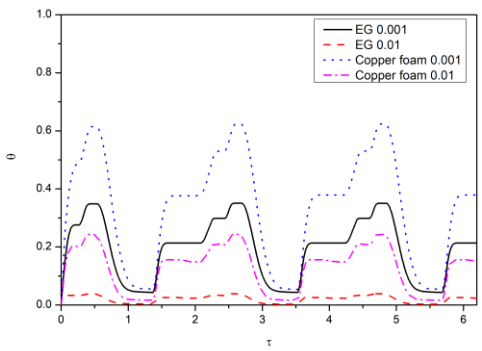

(a) 0.5C-0.5C

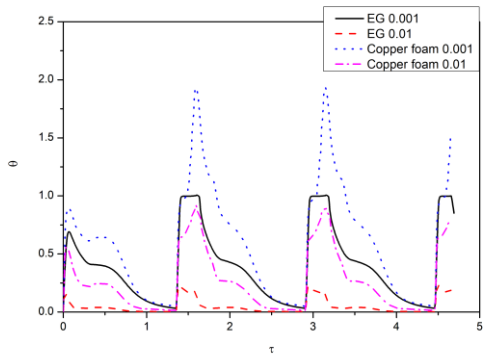

(b) 0.5C-2C

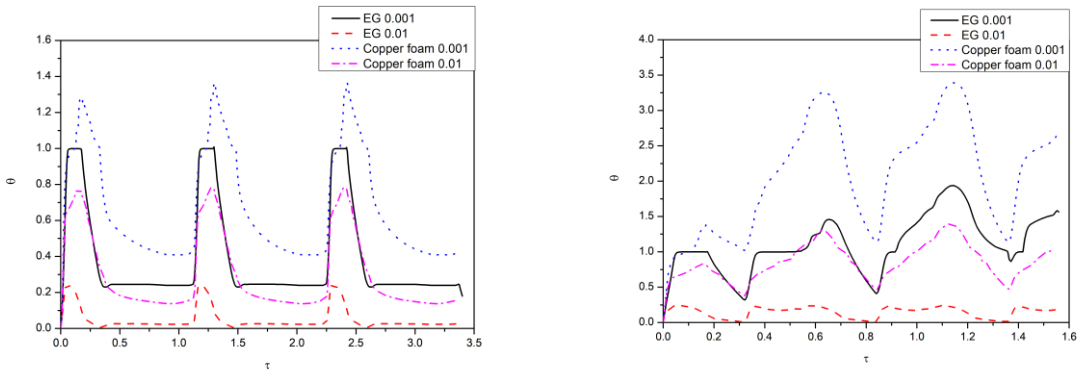

(c) 2C-0.5C (d) 2C-2C

Figure 102 Dimensionless HTF temperature θ at $\nu_{f,\mathrm{in}} = 0.001$ and $0.01\mathrm{m/s}$, with EG based CPCM and copper foam based CPCM, under (a) 0.5C-0.5C, (b) 0.5C-2C, (c) 2C-0.5C and (d) 2C-2C charge-discharge cycle

Dimensionless HTF temperature θ against dimensionless time τ is shown in Figure 102. One can see from Figure 102(a), θ in all cases are maintained under 1, which shows that the CPCMs are in a solid state. This is due to a relatively low heat generation rate under the low current rate. In Figure 102(b), under 0.5C-2C charge-discharge rate, at $\nu_{f,\mathrm{in}} = 0.01\mathrm{m/s}$ the CPCMs are also in the solid state, which is resulted from the high heat transfer coefficient under a high inlet velocity. At $\nu_{f,\mathrm{in}} = 0.001\mathrm{m/s}$, with EG based CPCM, there is a period within which θ = 1. EG based CPCM exhibits an inherent thermal regulation function, maintaining the HTF temperature at the phase change temperature. While with copper foam-based CPCM, the phase change period does not last for a long time, and the CPCM changes into a liquid phase within a short duration. After each discharge period, i.e. at $\tau = 1.6$ and 3.3, the battery pack is charged under a low current rate, the θ is then able to be cooled down close to 0. The case under 2C-0.5C charge-discharge cycle shows similar results with the case under 0.5C-2C charge-discharge rate. Under abusive 2C-2C charge-discharge rate, at $\nu_{f,\mathrm{in}} = 0.01\mathrm{m/s}$, with EG based CPCM the θ is still kept close to 0. With copper foam based CPCM, during most of the periods the HTF temperature is held under the phase change temperature. However, at $\nu_{f,\mathrm{in}} = 0.001\mathrm{m/s}$, with EG based CPCM after the second charge period, i.e. at $\tau = 0.9$, the HTF temperature is over the CPCM phase change temperature. The heat generated from previous charge-discharge cycle accumulates in the CPCM, and HTF is not efficient enough to cool down the CPCM under relatively low inlet velocity. The case with copper foam-based CPCM is out of control, and the θ reached 3.2 (T_f=330K).

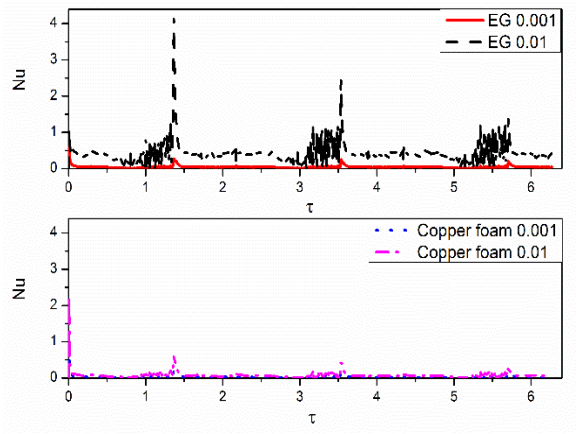

(a) 0.5C-0.5C

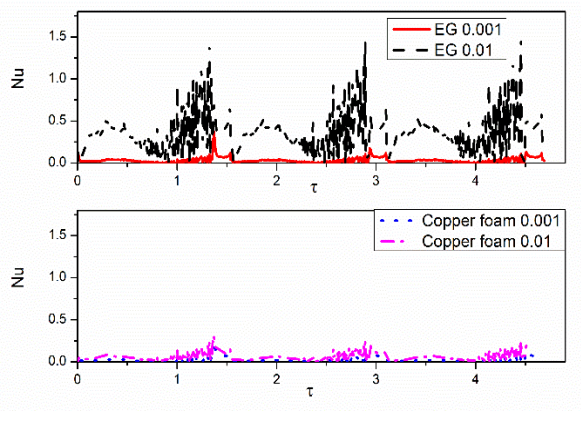

(b) 0.5C-2C

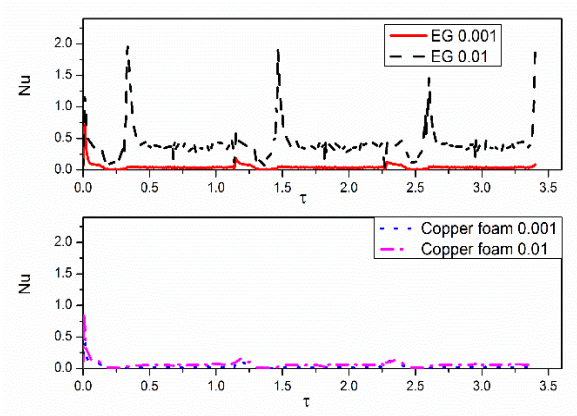

(c) 2C-0.5C

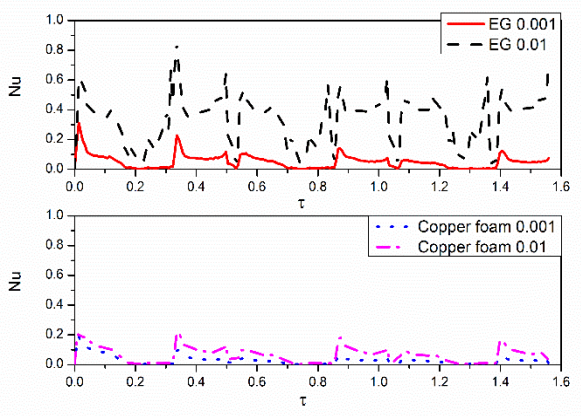

(d) 2C-2C

Figure 103 The Nusselt number of HTF at $v_{f,\mathrm{in}} = 0.001$ and $0.01\mathrm{m/s}$, with EG based CPCM and copper foam based CPCM, under (a) 0.5C-0.5C, (b) 0.5C-2C, (c) 2C-0.5C and (d) 2C-2C charge-discharge cycle

The Nusselt number against the dimensionless time is shown in Figure 103. Since most of the time in all cases, Nu is lower than 1, it can be concluded that conduction heat transfer dominates the heat transfer process. Short periods of convective heat transfer can be observed with EG based CPCM under $v_{f,\mathrm{in}} = 0.01\mathrm{m/s}$, i.e. $\tau = 1.4, 3.6$ and 5.6 under 0.5C-0.5C charge-discharge cycle, $\tau = 1.3, 3$ and 4.5 under 0.5C-2C charge-discharge cycle and $\tau = 0.3, 1.5, 2.6$ and 3.3 under 2C-0.5C charge-discharge cycle. It can also be observed from the results that, in all cases the Nu with EG based CPCM under $v_{f,\mathrm{in}} = 0.01\mathrm{m/s}$ is higher than other cases, and it leads to better temperature control than the other cases, as indicated in Figure 100.

CPCM with high thermal conductivity filled the gaps between the cells and the cooling channels, and efficiently enhancing the heat transfer. If CPCM is not used, the gap between the cooling channels and cells will be air (very low thermal conductivity), and the temperature uniformity will be significantly reduced.

6.3. Summary of chapter 6

In chapter 6.1, the performance of active cooling based BTMS with copper foam-based CPCM was investigated experimentally and numerically. The experimental results showed an excellent match with the simulation results, with the maximum temperature deviation being 0.5K. Both inlet velocity of the HTF and discharge current rate influenced the maximum temperature of the battery pack and the temperature difference within different cells and the same cell.

With CPCM cooling only, the battery pack has a relatively high temperature as the heat accumulated in the CPCM and was not able to dissipate. The temperature difference was not observed due to the uniform heat transfer within the whole module. When liquid cooling was used, it efficiently reduced the temperature. Under 0.5C discharge rate, the maximum battery temperature was 7K higher than without liquid cooling. However, it caused the temperature non-uniformity within the battery module. The temperature difference was at a relatively low level at a low inlet velocity of HTF, and it increased with the increase of inlet velocity and reached the peak before the highest inlet velocity. The temperature difference then dropped at the highest inlet velocity. Under 2C discharge rate, the temperature difference within different cells was 6K at $v_{f,\mathrm{in}} = 0.003$ and $0.001\mathrm{m/s}$, and the difference increased to 8K at $v_{f,\mathrm{in}} = 0.005$ and $0.01\mathrm{m/s}$, then back to 8K at $v_{f,\mathrm{in}} = 0.02\mathrm{m/s}$.

The current rate also had a significant effect on the maximum temperature and temperature difference, and high current rate lead to higher maximum temperature and higher temperature difference. At $v_{f,\mathrm{in}} = 0.02\mathrm{m/s}$, under 0.5C discharge rate both the maximum temperature difference within different cells and the same cell was 1K. While under 2C discharge rate, the maximum temperature difference reached 6K within different cells and 2K with the same cell. In a real application in EV, it is recommend that the hybrid BTMS based on liquid/CPCM cooling should be used. The liquid cooling can control the maximum battery temperature, and CPCM with high thermal conductivity brings temperature uniformity to the cells.

In chapter 6.2, the investigation on the BTMS focused on the comparison between EG based CPCM and copper foam-based CPCM, and the performance of BTMS under multi charge/discharge cycles. The performance of BTMS using CPCM has been explored numerically. The computational results indicate that with CPCM cooling only, battery temperature under low current rate can be controlled under only one charge/discharge operation. It is insufficient for continuous operation, and under high current rate, hence BTMS with liquid cooling was further studied.

The effects of inlet velocity of HTF and material type on the performance of BTMS under different current rates have been examined. With 0.001m/s inlet velocity of liquid cooling and EG based composite cooling, the maximum battery temperature can be controlled below 325K under three abusive 2C-2C charge/discharge cycle. Further temperature reduction of 23K was observed when the inlet velocity was improved to 0.01m/s. It has been concluded that EG based CPCM has better cooling ability than copper foam-based CPCM. With EG based CPCM, both the maximum operating temperature and temperature difference within the battery pack and single cell was well maintained at a lower value and in its optimum range. Under 2C-2C charge/discharge cycle, the differences on battery temperature between copper foam-based composite and EG based composite were observed to be 13K and 35K under 0.01m/s and 0.001m/s inlet velocity of HTF, respectively. At 0.001m/s inlet velocity of HTF, 19K of battery temperature gradient was observed with copper foam-based composite while the temperature was controlled within 5K with EG based CPCM.

Generalization of the results has been attempted through a dimensional analysis with results showing that heat conduction dominates the heat transfer between the CPCM and the HTF. Future commercial BTMS is recommended to use hybrid BTMS which is consisted of both liquid cooling and CPCM cooling. Liquid cooling is powerful to manage the battery temperature, and with the incorporation of the CPCM, part of the generated heat can be stored in CPCM, which can help with reducing the load of water cooling pump hence reduces the cost and volume of BTMS. The CPCM is also advantageous to enhance the heat transfer between the cells and the cooling tube.

For further application of BTMS using CPCM in sub-zero temperature environment, the isothermal property of CPCM could not only absorb heat from battery to reduce battery temperature, but also provide the heat to the battery when battery temperature drops. This is practically meaningful for lithium-ion battery system (e.g. backup power for

telecommunication cell towers, traction battery system of EV, and energy storage system integrated with renewable energy sources, etc.) in cold areas.

Chapter 7 Conclusions and Future Work

This chapter summarizes the main conclusions from this PhD work and recommendations for the future work are given based on the results of this research.

7.1. Summary of main conclusions

In this study, battery thermal management system (BTMS) using both active liquid cooling and passive composite phase change material cooling (CPCM) has been investigated. The three promising CPCMs for battery thermal management, including expanded graphite (EG)/paraffin composite, copper foam/paraffin composite and colloidal graphite/paraffin composite has been studied first.

In the study of **EG/paraffin composite**, it has been observed that EG particles with different particle size have different structures, results in dissimilarities on EG matrix structures. Different structural arrangements of EG had a significant impact on paraffin adsorptions, hence affects the thermal behaviour of EG/paraffin composites. The pores and voids of large EG matrix confined PCM and led to an increased temperature hysteresis. The pore structure of the large EG matrix also helps with improving the thermal stability of the composite after the thermal cycling test. The thermal conductivity of composites with large EG particles increased by 1360% - 1695% because of the high thermal conductivity of the EG matrix. In the case of small EG particles, interfacial thermal resistance dominates the influence on thermal conductivity, which results in less improvement in thermal conductivity. A 90 ~ 340% increment on thermal conductivity was obtained regarding different EG contents. Interfacial thermal resistance also helped with improving the thermal stability of the composite.

Copper foam/paraffin composites with different porosity of copper foam were investigated. The SEM observation revealed that the absorption of paraffin into copper foam was successful. The porosity of the copper foam had a significant effect on the thermal property of the composites, with the increase in copper foam porosity, the latent heat dramatically increased with the dramatic decrease of thermal conductivity. With 18% of porosity difference, the difference in latent heat can be 128kJ/kg and the difference in thermal conductivity reached 20.5W/m·K. The experimental measurement of thermal conductivity validated the copper foam/paraffin composite model, which was used for numerical modelling.

The thermal properties of the **colloidal graphite/paraffin composite** were also studied. Study on latent heat showed that the composites have 20 kJ/kg of decrease with every 10% increase of graphite mass ratio. With 40wt% of colloidal graphite, the thermal conductivity of the composite was 2 W/m·K, which was 10.27 times of the pure paraffin. With the addition of melamine, the end set degradation temperature can be significantly increased. With 15wt% of

melamine, the endset degradation temperature reached 334 °C, which was increased by 126 °C when compared with 0% melamine.

Through the comparison of the different CPCMs, it was found that, with the same latent heat, the EG/paraffin composite has the highest thermal conductivity and reasonable price for industrial applications. The copper foam/paraffin composite can reach very high thermal conductivity with low copper foam porosity, which could dissipate heat efficiently and is necessary for battery operation under high current rate cycling operation.

In the battery characterization, it was concluded that battery heat generation is highly dependent on the current rate, and a higher current rate leads to higher heat generation rate. Under the charging process, the peak heat flux at 2C is 8 times of which at 0.5C. Under the discharge process, the ratio was 9 times. The internal resistance affected the heat generation rate at different state of charge (SoC). The internal resistance is relatively high at high and low SoC. Hence the heat generation rate of the battery reached its peak when the charge/discharge began and increased again when it is close to the end of discharge. The battery performance is highly dependent on the current rate and operating temperature. Low operation temperature causes significant battery polarization and leads to reduce constant current charging time and discharging time. Under 1C charge process, the constant current charge time was 2400s at 60 °C and 1000s at 20°C. It prolongs the charging time and decreases the discharging time and leads to reduced battery performance in terms of the specific energy and specific power. Under high current rate, although the battery polarization was further aggravated, the specific power is increased proportionally to the current rate. It saves much charging time with relatively small energy loss. Under 0.5C discharge current rate, the specific energy and specific power at 20 ^{o}C is 93% and 82% of which at 60 ^{o}C, respectively. The study of current rate on battery charging discovered that although high current rate causes reduced specific energy due to heat generation, it greatly saves the charging time. At 60 ^{o}C, the charge time under 2C current rate is only 63% of which under 0.5C with only 5% of specific energy loss. Both current rate and temperature have a significant effect on round trip efficiency (RTE) of LIB.

In the research of BTMS using the round tube, the experimental results showed an excellent match with the simulation results. Both the inlet velocity of the heat transfer fluid (HTF) and the discharge current rate influenced the maximum temperature of the battery pack and the temperature difference within different cells and the same cell. With CPCM cooling only, the battery pack has a relatively high temperature and no temperature difference within the battery

module. When liquid cooling was used, it efficiently reduced the temperature while it caused the temperature non-uniformity within the battery module. The temperature difference was at a relatively low level at a low inlet velocity of HTF, and it increased with the increase of inlet velocity and reached the peak before the highest inlet velocity. The temperature difference then dropped at the highest inlet velocity.

In the research of BTMS using the tabular tube, the investigation on the BTMS focused on the comparison between EG based CPCM and copper foam-based CPCM, and the performance of BTMS under multi charge/discharge cycles. The computational results indicate that with CPCM cooling only, battery temperature under low current rate can be controlled under only one charge/discharge operation. It is insufficient for continuous operation, and under high current rate, hence BTMS with liquid cooling was further studied. It has been concluded that EG based CPCM has better cooling ability than copper foam-based CPCM. With EG based CPCM, both the maximum operating temperature and temperature difference within the battery pack and single cell was well maintained at a lower value and in its optimum range. Generalization of the results has been attempted through a dimensional analysis with results shown that heat conduction dominates the heat transfer between the CPCM and the HTF.

Future commercial BTMS is recommended to use hybrid BTMS which is consisted of both liquid cooling and CPCM cooling. Liquid cooling is powerful to manage the battery temperature, and with the incorporation of the CPCM, part of the generated heat can be stored in CPCM, which can help with reducing the load of water cooling pump hence reduces the cost and volume of BTMS. The CPCM is also advantageous to enhance the heat transfer between the cells and the cooling tube. In a real application, it is recommended that the hybrid BTMS based on both liquid cooling and CPCM cooling should be used. The hybrid system can not only control the battery maximum temperature, but also provide temperature uniformity.

7.2. Recommendations for future work

(1) Composite phase change material with “solid-solid” phase change

Further development on the BTMS will focus on novel phase change material with “solid-solid” phase change. As mentioned in section 2.5.5, the polymer is a promising supporting material which confines the phase change material and prevents the leakage during phase change. Ongoing research is aiming to develop the CPCM without any leakage problem. Hence it can be used as the outer covering for LIBs. As shown in Figure 104, the initial test showed that after 100 times of thermal cycling, no change on the physical shape could be observed,

meaning the material only had “solid-solid” phase change. The polymer-paraffin composite can not only thermally manage the battery temperature, the elasticity of it could also provide protection. The research will include both the thermal property and mechanical property of the material. High energy density pouch cells will be tested along with the novel CPCM.

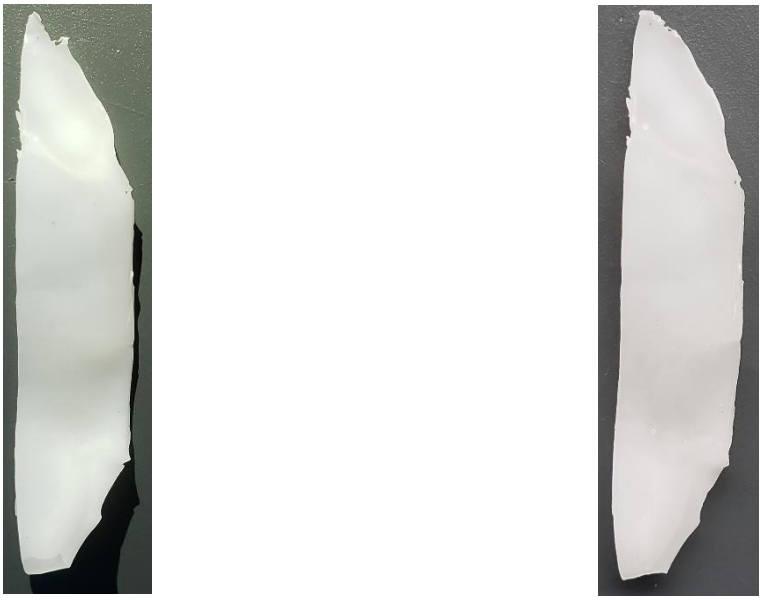

(a) (b)

Figure 104 Developed polymer-phase change material composite samples (still in the study) (a) Sample before cycling (b) Sample after 100 times of cycling

(2) Electric vehicle thermal management system

When applied in EV, the BTMS using CPCM will not work independently. As discussed in section 2.4.3, the BTMS is a part of vehicle thermal management. In some EV models, one heating/cooling unit serves the function of thermally managing vehicle cabin and the battery pack simultaneously. Hence a further development of the BTMS should be integrated with the vehicle thermal management system. Currently, the cooling method in the electric vehicle is the HVAC system, and the heating method is heat pump or PTC heating. The methods consume a significant amount of electric energy from the traction battery and reduce the driving range. A report from American Automobile Association [222] revealed that, under Urban Dynamometer Driving Schedule, at an ambient temperature of -6.7℃, BWM i3s (2018 model) will have 60% of range loss if the vehicle thermal management system is on. The range loss is 56% for Chevy volt (2019 model), 38% for Nissan leaf (2018 model), 46% for Tesla Model S 75D (2017 model), and 47% for Volkswagen Golf-e (2017 model). With the thermal energy storage onboard, the loss driving range resulted from the power drain from the HVAC, heat

pump or PCT heating will regain, which maximizes the vehicle driving range. Figure 105 showed the design of the electric vehicle thermal management system from the PCT patent [223]. The battery pack 102 is surrounded by CPCM and has heat exchange behaviour through heat transfer fluid with the thermal energy storage 108. Thermal energy storage108 provides heating or cooling to the battery pack 102 and to the vehicle cabin through cabin vent 122. The objective of this work will be building the prototype for vehicle thermal management based on the published patent and validating the proposed system.

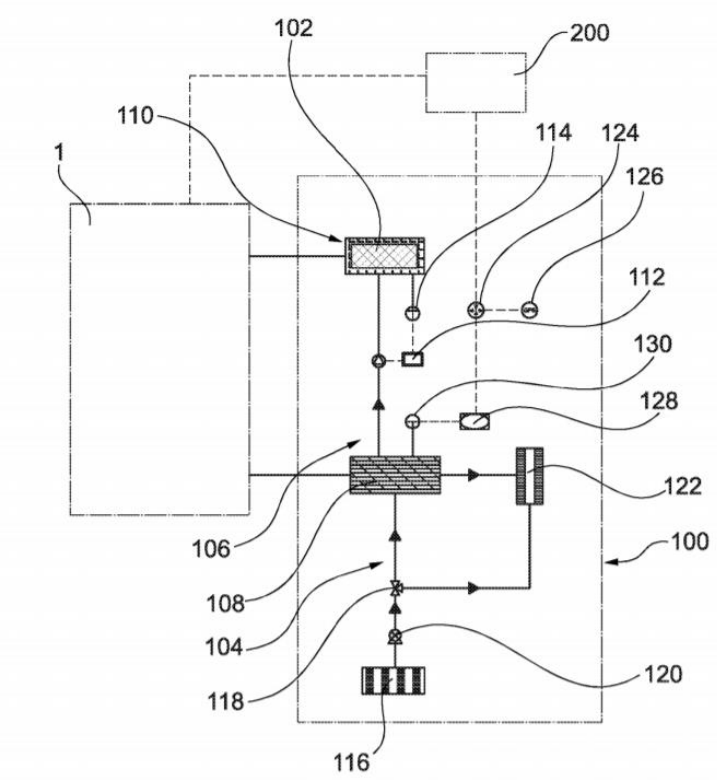

Figure 105 Electric vehicle thermal management system based on phase change material [223]

Appendix Publications and Patents

JOURNAL PAPER:

[1] **Zhao Y**, Jin L, Zou B, Qiao G, Zhang T, Cong L, et al. Expanded graphite – Paraffin composite phase change materials: Effect of particle size on the composite structure and properties. Appl Therm Eng 2020;171:115015. doi:https://doi.org/10.1016/j.applthermaleng.2020.115015.

[2] **Zhao Y**, Li Q, Zou B, Zhang T, Jin L, Qiao G, et al. Performance of a liquid cooling-based battery thermal management system with a composite phase change material. Int J Energy Res 2020;44:4727–42. doi:10.1002/er.5254.

[3] Grosu Y, **Zhao Y**, Giacomello A, Meloni S, Dauvergne J-L, Nikulin A, et al. Hierarchical macro-nanoporous metals for leakage-freeygrosu@cicenergigune.com high-thermal conductivity shape-stabilized phase change materials. Appl Energy 2020;269. doi:10.1016/j.apenergy.2020.115088.

[4] Nie B, She X, Yu Q, Zou B, **Zhao Y**, Li Y, et al. Experimental study of charging a compact PCM energy storage device for transport application with dynamic exergy analysis. Energy Convers Manag 2019;196:536–44. doi:https://doi.org/10.1016/j.enconman.2019.06.032.

[5] Li C, Li Q, Cong L, jiang F, **Zhao Y**, Liu C, et al. MgO based composite phase change materials for thermal energy storage: The effects of MgO particle density and size on microstructural characteristics as well as thermophysical and mechanical properties. Appl Energy 2019;250:81–91. doi:https://doi.org/10.1016/j.apenergy.2019.04.094.

CONFERENCE PAPER:

[1] **Zhao Y**, Zou B, Li C, Ding Y. Active cooling based battery thermal management using composite phase change materials. Energy Procedia 2019;158:4933–40. doi:https://doi.org/10.1016/j.egypro.2019.01.697.

[2] Li C, Li Q, **Zhao Y**, Cong L, Jiang Z, Li Y, et al. Composite phase change materials for thermal energy storage: From molecular modelling based formulation to innovative manufacture. Energy Procedia 2019;158:4510–6. doi:https://doi.org/10.1016/j.egypro.2019.01.760.

[3] Li Q, Li C, Qiao G, **Zhao Y**, Huang Y, Peng X, et al. Effects of MgO particle size and density on microstructure development of MgO based composite phase change materials. Energy Procedia 2019;158:4517–22. doi:https://doi.org/10.1016/j.egypro.2019.01.759.

PATENT:

[1] Ding Y, Hui C, **Zhao Y**, Nie B. Vehicle Charging. WO2019162680A1, 2019.

[2] Jin L, Qiao G, **Zhao Y**, Lan Y, Ding Y. A kind of thermal management device and system for battery pack. CN110277604A, 2019.

[3] Jin L, **Zhao Y**, Qiao G, Xie P, Zou B, Lan Y, et al. Composite binary phase change material and application thereof in battery thermal management system. CN111082185A, 2019.

[4] Ding Y, **Zhao Y**, Ahmad A. Heat energy supply and management system of logistics transport vehicle. CN111873750A, 2020.

[5] Ding Y, **Zhao Y**, Ahmad A. Heat energy generation and storage integrated indoor temperature control cold and hot supply system. CN111854234A, 2020.

Reference

[1] Kane M. Global EV Sales For 2019 Now In: Tesla Model 3 Totally Dominated. Insideevs 2019. https://insideevs.com/news/396177/global-ev-sales-december-2019/ (accessed July 23, 2020).

[2] Janek J, Zeier WG. A solid future for battery development. Nat Energy 2016;1:16141. https://doi.org/10.1038/nenergy.2016.141.

[3] How long it takes to fully charge an electric car？. POD-POINT 2020. https://pod-point.com/guides/driver/how-long-to-charge-an-electric-car (accessed May 25, 2020).

[4] Moloughney T. How NIO Changed My Mind On EV Battery Swapping. Insideevs 2020. https://insideevs.com/news/392660/nio-battery-swap-loved-by-customers/ (accessed August 25, 2020).

[5] Tesla Reignites Hours After Earlier Fire Extinguished In Los Gatos 2018. https://sanfrancisco.cbslocal.com/2018/12/18/officials-investigate-mysterious-tesla-fire-los-gatos/ (accessed July 31, 2020).

[6] Aurbach D, McCloskey BD, Nazar LF, Bruce PG. Advances in understanding mechanisms underpinning lithium–air batteries. Nat Energy 2016;1:16128. https://doi.org/10.1038/nenergy.2016.128.

[7] Pang Q, Liang X, Kwok CY, Nazar LF. Advances in lithium–sulfur batteries based on multifunctional cathodes and electrolytes. Nat Energy 2016;1:16132. https://doi.org/10.1038/nenergy.2016.132.

[8] Li W, Zhao Q, Ni Y, Ma R. Tesla Battery Preview Special Report (in Chinese). 2020.

[9] Brown Z. Solid-State Batteries: The Technology of the 2030s but the Research Challenge of the 2020s. 2020.

[10] WHITTINGHAM MS. Electrical Energy Storage and Intercalation Chemistry. Science (80-) 1976;192:1126 LP – 1127. https://doi.org/10.1126/science.192.4244.1126.

[11] Binghamton professor recognized for energy research. Suny RF n.d. https://www.rfsuny.org/rf-news/binghamton-energy/binghamton---energy.html (accessed July 15, 2020).

[12] Oh DY, Choi YE, Kim DH, Lee Y-G, Kim B-S, Park J, et al. All-solid-state lithium-ion

batteries with TiS2 nanosheets and sulphide solid electrolytes. J Mater Chem A 2016;4:10329–35. https://doi.org/10.1039/C6TA01628F.

[13] Trevey JE, Stoldt CR, Lee S-H. High Power Nanocomposite TiS2 Cathodes for All-Solid-State Lithium Batteries. J Electrochem Soc 2011;158:A1282. https://doi.org/10.1149/2.017112jes.

[14] Manthiram A. A reflection on lithium-ion battery cathode chemistry. Nat Commun 2020;11:1550. https://doi.org/10.1038/s41467-020-15355-0.

[15] Mizushima K, Jones PC, Wiseman PJ, Goodenough JB. LixCoO2 (0<x<-1): A new cathode material for batteries of high energy density. Mater Res Bull 1980;15:783–9. https://doi.org/https://doi.org/10.1016/0025-5408(80)90012-4.

[16] Van der Ven A. Lithium Diffusion in Layered Li[sub x]CoO[sub 2]. Electrochem Solid-State Lett 1999;3:301. https://doi.org/10.1149/1.1391130.

[17] Van der Ven A, Ceder G. Lithium diffusion mechanisms in layered intercalation compounds. J Power Sources 2001;97–98:529–31. https://doi.org/https://doi.org/10.1016/S0378-7753(01)00638-3.

[18] Lithium Cobalt Oxide – LiCoO2. Chemtube3D 2020. https://www.chemtube3d.com/lib_lco-2/ (accessed July 15, 2020).

[19] Lancashire RJ. Crystal Field Stabilization Energy. Chem Libr 2019. https://chem.libretexts.org/Bookshelves/Inorganic_Chemistry/Modules_and_Websites_(Inorganic_Chemistry)/Crystal_Field_Theory/Crystal_Field_Stabilization_Energy#:~:text=Definition%3A Crystal Field Stabilization Energy,configuration in the isotropic field. (accessed July 20, 2020).

[20] Wang X-L, An K, Cai L, Feng Z, Nagler SE, Daniel C, et al. Visualizing the chemistry and structure dynamics in lithium-ion batteries by in-situ neutron diffraction. Sci Rep 2012;2:747. https://doi.org/10.1038/srep00747.

[21] Li T, Yuan X-Z, Zhang L, Song D, Shi K, Bock C. Degradation Mechanisms and Mitigation Strategies of Nickel-Rich NMC-Based Lithium-Ion Batteries. Electrochem Energy Rev 2020;3:43–80. https://doi.org/10.1007/s41918-019-00053-3.

[22] Thackeray MM, Johnson CS, Amine K, Kim J. Lithium metal oxide electrodes for

lithium cells and batteries. US20020136954A1, 2001.

[23] Lu Z, Dahn JR. Cathode compositions for lithium-ion batteries. CA2602008C, 2001.

[24] Nitta N, Wu F, Lee JT, Yushin G. Li-ion battery materials: present and future. Mater Today 2015;18:252–64. https://doi.org/https://doi.org/10.1016/j.mattod.2014.10.040.

[25] Chakraborty A, Kunnikuruvan S, Kumar S, Markovsky B, Aurbach D, Dixit M, et al. Layered Cathode Materials for Lithium-Ion Batteries: Review of Computational Studies on LiNi1–x–yCoxMnyO2 and LiNi1–x–yCoxAlyO2. Chem Mater 2020;32:915–52. https://doi.org/10.1021/acs.chemmater.9b04066.

[26] Thackeray MM, David WIF, Bruce PG, Goodenough JB. Lithium insertion into manganese spinels. Mater Res Bull 1983;18:461–72. https://doi.org/https://doi.org/10.1016/0025-5408(83)90138-1.

[27] Lithium Manganese Oxide – LiMn2O4. Chemtube3D n.d. https://www.chemtube3d.com/lib_lmo-2/ (accessed July 16, 2020).

[28] Padhi AK. Phospho-olivines as Positive-Electrode Materials for Rechargeable Lithium Batteries. J Electrochem Soc 1997;144:1188. https://doi.org/10.1149/1.1837571.

[29] Lithium Iron Phosphate-LiFePO4. Chemtube3D n.d. https://www.chemtube3d.com/lib_lfp-2/ (accessed July 16, 2020).

[30] Deschanvres A, Raveau B, Sekkal Z. Mise en evidence et etude cristallographique d'une nouvelle solution solide de type spinelle Li1+ xTi2− xO4 0⩽ x⩽ 0, 333. Mater Res Bull 1971;6:699–704.

[31] Ferg E. Spinel Anodes for Lithium-Ion Batteries. J Electrochem Soc 1994;141:L147. https://doi.org/10.1149/1.2059324.

[32] Vijayakumar M, Kerisit S, Rosso KM, Burton SD, Sears JA, Yang Z, et al. Lithium diffusion in Li4Ti5O12 at high temperatures. J Power Sources 2011;196:2211–20. https://doi.org/https://doi.org/10.1016/j.jpowsour.2010.09.060.

[33] Lithium titanate-Li4Ti5O12. Chemtube3D 2020. https://www.chemtube3d.com/lib_lithium-titanate-2/ (accessed July 21, 2020).

[34] Liu Z. The History of the Lithium-Ion Battery. ThermoFisher Sci 2019. https://www.thermofisher.com/blog/microscopy/the-history-of-the-lithium-ion-battery/

(accessed June 30, 2020).

[35] Asahi-kasei.com. Profile of Akira Yoshino, Dr.Eng., and Overview of His Invention of the Lithium-ion Battery n.d. https://www.asahi-kasei.com//asahikasei-brands/interview/yoshino/profile/pdf/lithium-ion_battery.pdf (accessed June 30, 2020).

[36] Liu Q, Su X, Lei D, Qin Y, Wen J, Guo F, et al. Approaching the capacity limit of lithium cobalt oxide in lithium ion batteries via lanthanum and aluminium doping. Nat Energy 2018;3:936–43. https://doi.org/10.1038/s41560-018-0180-6.

[37] IRENA. Electricity Storage and Renewables: Costs and Markets to 2030. Int Renew Energy Agency 2017.

[38] Battery University. BU-205: Types of Lithium-ion n.d. https://batteryuniversity.com/learn/article/types_of_lithium_ion (accessed July 1, 2020).

[39] Lightingglobal. Lithium-ion Batteries Part II: Safety. 2019.

[40] Belharouak I, Sun Y-K, Lu W, Amine K. On the safety of the Li4Ti5O12/ LiMn2O4 lithium-ion battery system. J Electrochem Soc 2007;154:A1083.

[41] Wang W, Qiu W, Ding Q. Nickel Cobalt Manganese based cathode material for Li-ion batteries technology production and application. Beijing: Chemical industry press; 2015.

[42] J. Hawkins A. Electric car battery with 600 miles of range? This startup claims to have done it. The Verge 2019. https://www.theverge.com/2019/4/4/18293989/innolith-ev-battery-breakthrough-lithium-ion#:~:text=(Watt-hours per kilogram is,that to 330 Wh%2Fkg. (accessed July 23, 2020).

[43] Global and China Ternary Cathode Materials (NCA, NCM) and Battery Industry Report, 2017-2023. ResearchAndMarkets 2018. https://www.prnewswire.com/news-releases/global-and-china-ternary-cathode-materials-nca-ncm-and-battery-industry-report-2017-2023-300680728.html (accessed July 23, 2020).

[44] Arcus C. Exciting Developments In NMC 811 Lithium Battery Technology. Cleantechnica 2018. https://cleantechnica.com/2018/03/04/exciting-developments-nmc-811-lithium-battery-technology/ (accessed July 23, 2020).

[45] Wang W, Ruishan M. Cost of power battery: How to disassemble the cost of power

battery gracefully?(In Chinese). 2019.

[46] Inseok Seo, Steve W. Martin. New Developments in Solid Electrolytes for Thin-Film Lithium Batteries. INTECH Open Access Publisher; 2012.

[47] Vidyu C. How To Select The Right Battery For Your Application? Part 3: Common Secondary Battery Chemistries 2020. https://www.dfrsolutions.com/blog/how-to-select-the-right-battery-for-your-application-part-3-common-secondary-battery-chemistries (accessed March 5, 2020).

[48] Lahiri A, Shah N, Dales C. How to Build a Safer, More Energy-Dense Lithium-ion Battery 2017. https://spectrum.ieee.org/semiconductors/design/how-to-build-a-safer-more-energydense-lithiumion-battery (accessed March 5, 2020).

[49] Lipo Batteries 2012. http://chasewatermbc.blogspot.com/2012/04/lipo-batteries.html (accessed March 5, 2020).

[50] Ciez RE, Whitacre JF. Comparison between cylindrical and prismatic lithium-ion cell costs using a process based cost model. J Power Sources 2017;340:273–81. https://doi.org/https://doi.org/10.1016/j.jpowsour.2016.11.054.

[51] Yoshio Nishi. Natl Acad Eng 2014. https://www.nae.edu/105800/Yoshio-Nishi (accessed July 10, 2020).

[52] EVANNEX. Tesla's Secret Weapon: Intense Focus On Batteries. Insideevs 2019. https://insideevs.com/news/341883/teslas-secret-weapon-intense-focus-on-batteries/ (accessed June 10, 2020).

[53] GSMARENA. iPhone XS teardown reveals L-shaped battery and more watertight seals 2018. https://www.gsmarena.com/iphone_xs_teardown_reveals_lshaped_battery_and_more_watertight_seals-news-33363.php (accessed June 10, 2020).

[54] Flaherty N. Large pouch cell battery tech at heart of GM EV strategy. Eenewspower 2020. https://www.eenewspower.com/news/large-pouch-cell-battery-tech-heart-gm-ev-strategy (accessed June 10, 2020).

[55] Specification of LG INR21700-M50. BatteryspaceCom 2019. https://www.batteryspace.com/prod-specs/11514.pdf (accessed February 26, 2019).

[56] Specificaiton of Samsung INR21700-48G. QueenbatteryCom 2019. queenbattery.com.cn/index.php?controller=attachment&id_attachment=53 (accessed February 26, 2019).

[57] Sun C-F, Hu J, Wang P, Cheng X-Y, Lee SB, Wang Y. Li3PO4 Matrix Enables a Long Cycle Life and High Energy Efficiency Bismuth-Based Battery. Nano Lett 2016;16:5875–82. https://doi.org/10.1021/acs.nanolett.6b02720.

[58] Yang Y, Zheng G, Misra S, Nelson J, Toney MF, Cui Y. High-Capacity Micrometer-Sized Li2S Particles as Cathode Materials for Advanced Rechargeable Lithium-Ion Batteries. J Am Chem Soc 2012;134:15387–94. https://doi.org/10.1021/ja3052206.

[59] Mikhaylik Y V, Kovalev I, Schock R, Kumaresan K, Xu J, Affinito J. High Energy Rechargeable Li-S Cells for EV Application: Status, Remaining Problems and Solutions. ECS Trans 2010;25:23–34. https://doi.org/10.1149/1.3414001.

[60] Jäger K-D, Isabella O, Smets AHM, van Swaaij RA, Zeman M. Solar Energy: Fundamentals, Technology and Systems. UIT Cambridge; 2016.

[61] Fu LJ, Liu H, Li C, Wu YP, Rahm E, Holze R, et al. Surface modifications of electrode materials for lithium ion batteries. Solid State Sci 2006;8:113–28. https://doi.org/https://doi.org/10.1016/j.solidstatesciences.2005.10.019.

[62] Fong R, von Sacken U, Dahn JR. Studies of Lithium Intercalation into Carbons Using Nonaqueous Electrochemical Cells. J Electrochem Soc 1990;137:2009–13. https://doi.org/10.1149/1.2086855.

[63] Smith AJ, Burns JC, Xiong D, Dahn JR. Interpreting High Precision Coulometry Results on Li-ion Cells. J Electrochem Soc 2011;158:A1136–42. https://doi.org/10.1149/1.3625232.

[64] Yao Y, McDowell MT, Ryu I, Wu H, Liu N, Hu L, et al. Interconnected Silicon Hollow Nanospheres for Lithium-Ion Battery Anodes with Long Cycle Life. Nano Lett 2011;11:2949–54. https://doi.org/10.1021/nl201470j.

[65] Jiang J, Ruan H, Sun B, Zhang W, Gao W, Wang LY, et al. A reduced low-temperature electro-thermal coupled model for lithium-ion batteries. Appl Energy 2016;177:804–16. https://doi.org/https://doi.org/10.1016/j.apenergy.2016.05.153.

[66] Ratnakumar B V, Smart MC, Whitcanack LD, Ewell RC. The impedance characteristics of Mars Exploration Rover Li-ion batteries. J Power Sources 2006;159:1428–39. https://doi.org/https://doi.org/10.1016/j.jpowsour.2005.11.085.

[67] Uddin K, Picarelli A, Lyness C, Taylor N, Marco J. An Acausal Li-Ion Battery Pack Model for Automotive Applications. Energies 2014;7:5675–700. https://doi.org/10.3390/en7095675.

[68] Schweiger H-G, Obeidi O, Komesker O, Raschke A, Schiemann M, Zehner C, et al. Comparison of several methods for determining the internal resistance of lithium ion cells. Sensors (Basel) 2010;10:5604–25. https://doi.org/10.3390/s100605604.

[69] Waag W, Käbitz S, Sauer DU. Experimental investigation of the lithium-ion battery impedance characteristic at various conditions and aging states and its influence on the application. Appl Energy 2013;102:885–97. https://doi.org/https://doi.org/10.1016/j.apenergy.2012.09.030.

[70] Ji Y, Zhang Y, Wang C-Y. Li-Ion Cell Operation at Low Temperatures. J Electrochem Soc 2013;160:A636–49. https://doi.org/10.1149/2.047304jes.

[71] Li SE, Wang B, Peng H, Hu X. An electrochemistry-based impedance model for lithium-ion batteries. J Power Sources 2014;258:9–18. https://doi.org/https://doi.org/10.1016/j.jpowsour.2014.02.045.

[72] Barai A, Uddin K, Widanage WD, McGordon A, Jennings P. A study of the influence of measurement timescale on internal resistance characterisation methodologies for lithium-ion cells. Sci Rep 2018;8:21. https://doi.org/10.1038/s41598-017-18424-5.

[73] Wu M-S, Chiang P-CJ, Lin J-C. Electrochemical Investigations on Advanced Lithium-Ion Batteries by Three-Electrode Measurements. J Electrochem Soc 2005;152:A47–52. https://doi.org/10.1149/1.1825385.

[74] Yang F, Qiao Y, Gao B, Duan P, Zhu Y. Investigation on Li-ion battery charging polarization characteristics and influence factors. Ionics (Kiel) 2016;22:1603–10. https://doi.org/10.1007/s11581-016-1694-1.

[75] Li J, Murphy E, Winnick J, Kohl PA. The effects of pulse charging on cycling characteristics of commercial lithium-ion batteries. J Power Sources 2001;102:302–9. https://doi.org/https://doi.org/10.1016/S0378-7753(01)00820-5.

[76] Li SE, Wang B, Peng H, Hu X. An electrochemistry-based impedance model for lithium-ion batteries. J Power Sources 2014;258:9–18. https://doi.org/https://doi.org/10.1016/j.jpowsour.2014.02.045.

[77] Lin H -p., Chua D, Salomon M, Shiao H-C, Hendrickson M, Plichta E, et al. Low-Temperature Behavior of Li-Ion Cells. Electrochem Solid-State Lett 2001;4:A71–3. https://doi.org/10.1149/1.1368736.

[78] Jiang Y, Zhang C, Zhang W, Shi W, Liu Q. Modeling charge polarization voltage for large lithium-ion batteries in electric vehicles. J Ind Eng Manag Vol 6, No 2 (2013)DO - 103926/Jiem895 2013.

[79] Cho H-M, Choi W-S, Go J-Y, Bae S-E, Shin H-C. A study on time-dependent low temperature power performance of a lithium-ion battery. J Power Sources 2012;198:273–80. https://doi.org/https://doi.org/10.1016/j.jpowsour.2011.09.111.

[80] Meister P, Jia H, Li J, Kloepsch R, Winter M, Placke T. Best Practice: Performance and Cost Evaluation of Lithium Ion Battery Active Materials with Special Emphasis on Energy Efficiency. Chem Mater 2016;28:7203–17. https://doi.org/10.1021/acs.chemmater.6b02895.

[81] Laoire C, Mukerjee S, Plichta EJ, Hendrickson MA, Abraham KM. Rechargeable Lithium/TEGDME- LiPF6/O2 Battery. J Electrochem Soc 2011;158:A302–8. https://doi.org/10.1149/1.3531981.

[82] Abraham KM, Jiang Z. A Polymer Electrolyte-Based Rechargeable Lithium/Oxygen Battery. J Electrochem Soc 1996;143:1–5. https://doi.org/10.1149/1.1836378.

[83] Doyle M. Modeling of Galvanostatic Charge and Discharge of the Lithium/Polymer/Insertion Cell. J Electrochem Soc 1993;140:1526. https://doi.org/10.1149/1.2221597.

[84] Bernardi D. A General Energy Balance for Battery Systems. J Electrochem Soc 1985;132:5. https://doi.org/10.1149/1.2113792.

[85] Bandhauer TM, Garimella S, Fuller TF. A Critical Review of Thermal Issues in Lithium-Ion Batteries. J Electrochem Soc 2011;158:R1. https://doi.org/10.1149/1.3515880.

[86] Bandhauer TM, Garimella S, Fuller TF. Temperature-dependent electrochemical heat

generation in a commercial lithium-ion battery. J Power Sources 2014;247:618–28. https://doi.org/10.1016/j.jpowsour.2013.08.015.

[87] Jalkanen K, Aho T, Vuorilehto K. Entropy change effects on the thermal behavior of a LiFePO4/graphite lithium-ion cell at different states of charge. J Power Sources 2013;243:354–60. https://doi.org/https://doi.org/10.1016/j.jpowsour.2013.05.199.

[88] Kumagai N, Koishikawa Y, Komaba S, Koshiba N. Thermodynamics and Kinetics of Lithium Intercalation into Nb2 O 5 Electrodes for a 2 V Rechargeable Lithium Battery. J Electrochem Soc 1999;146:3203–10. https://doi.org/10.1149/1.1392455.

[89] Smith K, Wang CY. Power and thermal characterization of a lithium-ion battery pack for hybrid-electric vehicles. J Power Sources 2006;160:662–73. https://doi.org/10.1016/j.jpowsour.2006.01.038.

[90] Abada S, Marlair G, Lecocq A, Petit M, Sauvant-Moynot V, Huet F. Safety focused modeling of lithium-ion batteries: A review. J Power Sources 2016;306:178–92. https://doi.org/10.1016/j.jpowsour.2015.11.100.

[91] Ramadass P, Haran B, White R, Popov BN. Capacity fade of Sony 18650 cells cycled at elevated temperatures: Part II. Capacity fade analysis. J Power Sources 2002;112:614–20. https://doi.org/10.1016/S0378-7753(02)00473-1.

[92] Kuper C, Hoh M, Houchin-Miller G, Fuhr J. Thermal Management of Hybrid Vehicle Battery Systems. EVS24 Int Batter Hybrid Fuel Cell Electr Veh Symp Stavanger, Norway, 13-16 May 2009 2009:1–10.

[93] Vetter J, Novák P, Wagner MR, Veit C, Möller KC, Besenhard JO, et al. Ageing mechanisms in lithium-ion batteries. J Power Sources 2005;147:269–81. https://doi.org/10.1016/j.jpowsour.2005.01.006.

[94] Barré A, Deguilhem B, Grolleau S, Gérard M, Suard F, Riu D. A review on lithium-ion battery ageing mechanisms and estimations for automotive applications. J Power Sources 2013;241:680–9. https://doi.org/10.1016/j.jpowsour.2013.05.040 Review.

[95] Waldmann T, Wilka M, Kasper M, Fleischhammer M, Wohlfahrt-Mehrens M. Temperature dependent ageing mechanisms in Lithium-ion batteries - A Post-Mortem study. J Power Sources 2014;262:129–35. https://doi.org/10.1016/j.jpowsour.2014.03.112.

[96] Xu B, Oudalov A, Ulbig A, Andersson G, Kirschen D. Modeling of Lithium-Ion Battery Degradation for Cell Life Assessment. IEEE Trans Smart Grid 2016;PP:1. https://doi.org/10.1109/TSG.2016.2578950.

[97] Rao Z, Wang S, Zhang G. Simulation and experiment of thermal energy management with phase change material for ageing LiFePO4 power battery. Energy Convers Manag 2011;52:3408–14. https://doi.org/10.1016/j.enconman.2011.07.009.

[98] Yang N, Zhang X, Shang B, Li G. Unbalanced discharging and aging due to temperature differences among the cells in a lithium-ion battery pack with parallel combination. J Power Sources 2016;306:733–41. https://doi.org/10.1016/j.jpowsour.2015.12.079.

[99] Gogoana R, Pinson MB, Bazant MZ, Sarma SE. Internal resistance matching for parallel-connected lithium-ion cells and impacts on battery pack cycle life. J Power Sources 2014;252:8–13. https://doi.org/10.1016/j.jpowsour.2013.11.101.

[100] Mpoweruk.com. Battery Life and How To Improve It n.d. http://www.mpoweruk.com/life.htm (accessed March 8, 2017).

[101] Batteries HOF, Library DE, Companies TM. Handbook of batteries. 2004. https://doi.org/10.1016/0378-7753(86)80059-3.

[102] Zhang SS, Xu K, Jow TR. Charge and discharge characteristics of a commercial LiCoO2-based 18650 Li-ion battery. J Power Sources 2006;160:1403–9. https://doi.org/https://doi.org/10.1016/j.jpowsour.2006.03.037.

[103] Bugga R, Smart M, Whitacre J, West W. Lithium Ion Batteries for Space Applications. 2007 IEEE Aerosp Conf 2007:1–7. https://doi.org/10.1109/AERO.2007.352728.

[104] Jaguemont J, Boulon L, Dubé Y. A comprehensive review of lithium-ion batteries used in hybrid and electric vehicles at cold temperatures. Appl Energy 2016;164:99–114. https://doi.org/10.1016/j.apenergy.2015.11.034.

[105] Whitacre J, Yazami R, Hamwi A, Smart MC, Bennett W, Surya Prakash GK, et al. Low operational temperature Li-CFxbatteries using cathodes containing sub-fluorinated graphitic materials. J Power Sources 2006;160:577–84. https://doi.org/10.1016/j.jpowsour.2006.01.045.

[106] Smart MC, Whitacre JF, Ratnakumar B V., Amine K. Electrochemical performance and

kinetics of Li1+x(Co1/3Ni1/3Mn1/3)1-xO2cathodes and graphite anodes in low-temperature electrolytes. J Power Sources 2007;168:501–8. https://doi.org/10.1016/j.jpowsour.2006.10.106.

[107] Plichta EJ, Hendrickson M, Thompson R, Au G, Behl WK, Smart MC, et al. Development of low temperature Li-ion electrolytes for NASA and DoD applications. J Power Sources 2001;94:160–2. https://doi.org/10.1016/S0378-7753(00)00578-4.

[108] Smart MC, Ratnakumar BV, Behar a., Whitcanack LD, Yu J-S, Alamgir M. Gel polymer electrolyte lithium-ion cells with improved low temperature performance. J Power Sources 2007;165:535–43. https://doi.org/10.1016/j.jpowsour.2006.10.038.

[109] Shiao HC, Chua D, Lin HP, Slane S, Salomon M. Low temperature electrolytes for Li-ion PVDF cells. J Power Sources 2000;87:167–73. https://doi.org/10.1016/S0378-7753(99)00470-X.

[110] Ryou MH, Han GB, Lee YM, Lee JN, Lee DJ, Yoon YO, et al. Effect of fluoroethylene carbonate on high temperature capacity retention of LiMn2O4/graphite Li-ion cells. Electrochim Acta 2010;55:2073–7. https://doi.org/10.1016/j.electacta.2009.11.036.

[111] Huang C-K, Sakamoto JS, Wolfenstine J, Surampudi S. The Limits of Low-Temperature Performance of Li-Ion Cells. J Electrochem Soc 2000;147:2893. https://doi.org/10.1149/1.1393622.

[112] Zhang SS, Xu K, Jow TR. A new approach toward improved low temperature performance of Li-ion battery. Electrochem Commun 2002;4:928–32. https://doi.org/10.1016/S1388-2481(02)00490-3.

[113] Zhang SS, Xu K, Jow TR. Low temperature performance of graphite electrode in Li-ion cells. Electrochim Acta 2002;48:241–6. https://doi.org/10.1016/S0013-4686(02)00620-5.

[114] Biensan P, Simon B, Pérès J., de Guibert A, Broussely M, Bodet J., et al. On safety of lithium-ion cells. J Power Sources 1999;81–82:906–12. https://doi.org/10.1016/S0378-7753(99)00135-4.

[115] Lu L, Han X, Li J, Hua J, Ouyang M. A review on the key issues for lithium-ion battery management in electric vehicles. J Power Sources 2013;226:272–88. https://doi.org/10.1016/j.jpowsour.2012.10.060.

[116] Barclay S. Dana battery cooling technology featured on all-new Chevrolet Volt. Automot Ind AI 2011;191.

[117] Pan Y. NIO reaclled 4803 ES8 due to battery fire hazard (in Chinese). Guancha 2019. https://www.guancha.cn/qiche/2019_06_27_507278.shtml (accessed July 29, 2020).

[118] JTSB. Aircraft serious incident investigation report 2014.

[119] Song T, Li Y, Song J, Zhang Z. Airworthiness considerations of supply chain management from Boeing 787 Dreamliner battery issue. Procedia Eng., vol. 80, 2014, p. 628–37. https://doi.org/10.1016/j.proeng.2014.09.118.

[120] After waiting for 14 days, the result of the investigation of the Lixiang ONE fire incident is here. Sina Auto 2020. https://auto.sina.com.cn/newcar/x/2020-05-21/detail-iircuyvi4319705.shtml (accessed July 30, 2020).

[121] Hong D. All fires in electric vehicles in S. Korea this year involved Hyundai's Kona Electric. HANKYOREH 2019. http://www.hani.co.kr/arti/english_edition/e_business/912588.html (accessed July 30, 2020).

[122] Lopez L. Life, death, and spontaneous combustion — here's why the debate about Tesla fires just got more fierce. Bus Insid 2019. https://www.businessinsider.com/why-tesla-cars-catch-on-fire-2019-4?r=US&IR=T (accessed July 31, 2020).

[123] Ten Fire Incidents of electric Vehicles in 2017 (in Chinese). EvQd 2017. http://ev.qd-dcw.com/ (accessed July 30, 2020).

[124] Sun Y. Tesla fatal accident ralated with battery (in Chinese). Cbea n.d. http://www.cbea.com/ (accessed July 30, 2020).

[125] The first spontaneous combustion accident of electric vehicle in 2018: Tesla spontaneous combustion (in Chinese). Chejiahao 2018. https://chejiahao.autohome.com.cn/Authors/12266689 (accessed July 30, 2020).

[126] Bruce C. Smouldering BMW i8 dumped in water by firefighters 2019. https://uk.motor1.com/news/315605/bmw-i8-fire-dropped-in-water/ (accessed July 31, 2020).

[127] Sabbah R, Kizilel R, Selman JR, Al-Hallaj S. Active (air-cooled) vs. passive (phase

change material) thermal management of high power lithium-ion packs: Limitation of temperature rise and uniformity of temperature distribution. J Power Sources 2008;182:630–8. https://doi.org/https://doi.org/10.1016/j.jpowsour.2008.03.082.

[128] Xu J, Nie Y, Liu S. Interpretation of liquid cooling system in pure electric vehicle. Automob & Parts Technol 2017:79–81.

[129] Tennessen, Thomas Peter Weintraub, Jeffrey C. Weston AH. Extruded and Ribbed Thermal Interface for use with a Battery Cooling System, 2011.

[130] Lim DK, Kim SH, Kim D, Choi JH. TEMPERATURE CONTROL APPARATUS AND METHOD OF BATTERY SYSTEM FOR VEHICLE, 2013.

[131] Zheng W, Lu Z. Power battery pack and vehicle power battery system. CN201781007U, 2010.

[132] GM Global Technology Operations LLC. Batteries with phase change materials. 20120171523A1, 2010.

[133] Midtronics Inc. Battery maintenance device with thermal buffer. 9419311B2, 2010.

[134] Technology. ALLCELL 2020. https://www.allcelltech.com/#section-about2 (accessed May 27, 2020).

[135] Al-Hallaj S, Selman J. A Novel Thermal Management System for Electric Vehicle Batteries Using Phase-Change Material. J Electrochem Soc 2000;147:3231–6. https://doi.org/10.1149/1.1393888.

[136] Hémery C-V, Pra F, Robin J-F, Marty P. Experimental performances of a battery thermal management system using a phase change material. J Power Sources 2014;270:349–58. https://doi.org/10.1016/j.jpowsour.2014.07.147.

[137] Greco A, Jiang X, Cao D. An investigation of lithium-ion battery thermal management using paraffin/porous-graphite-matrix composite. J Power Sources 2015;278:50–68. https://doi.org/10.1016/j.jpowsour.2014.12.027.

[138] Li WQ, Qu ZG, He YL, Tao YB. Experimental study of a passive thermal management system for high-powered lithium ion batteries using porous metal foam saturated with phase change materials. J Power Sources 2014;255:9–15. https://doi.org/10.1016/j.jpowsour.2014.01.006.

[139] Ramandi MY, Dincer I, Naterer GF. Heat transfer and thermal management of electric vehicle batteries with phase change materials. Heat Mass Transf 2011;47:777–88. https://doi.org/10.1007/s00231-011-0766-z.

[140] Duan X, Naterer GF. Heat transfer in phase change materials for thermal management of electric vehicle battery modules. Int J Heat Mass Transf 2010;53:5176–82. https://doi.org/10.1016/j.ijheatmasstransfer.2010.07.044.

[141] Azizi Y, Sadrameli SM. Thermal management of a LiFePO4 battery pack at high temperature environment using a composite of phase change materials and aluminum wire mesh plates. Energy Convers Manag 2016;128:294–302. https://doi.org/10.1016/j.enconman.2016.09.081.

[142] Frusteri F, Leonardi V, Vasta S, Restuccia G. Thermal conductivity measurement of a PCM based storage system containing carbon fibers. Appl Therm Eng 2005;25:1623–33. https://doi.org/10.1016/j.applthermaleng.2004.10.007.

[143] Mills A, Farid M, Selman JR, Al-Hallaj S. Thermal conductivity enhancement of phase change materials using a graphite matrix. Appl Therm Eng 2006;26:1652–61. https://doi.org/10.1016/j.applthermaleng.2005.11.022.

[144] Wang Z, Zhang Z, Jia L, Yang L. Paraffin and paraffin/aluminum foam composite phase change material heat storage experimental study based on thermal management of Li-ion battery. Appl Therm Eng 2015;78:428–36. https://doi.org/10.1016/j.applthermaleng.2015.01.009.

[145] Babapoor A, Azizi M, Karimi G. Thermal management of a Li-ion battery using carbon fiber-PCM composites. Appl Therm Eng 2015;82:281–90. https://doi.org/10.1016/j.applthermaleng.2015.02.068.

[146] Ling Z, Zhang Z, Shi G, Fang X, Wang L, Gao X, et al. Review on thermal management systems using phase change materials for electronic components, Li-ion batteries and photovoltaic modules. Renew Sustain Energy Rev 2014;31:427–38. https://doi.org/10.1016/j.rser.2013.12.017.

[147] Ramakrishnan S, Wang X, Sanjayan J. Effects of various carbon additives on the thermal storage performance of form-stable PCM integrated cementitious composites. Appl Therm Eng 2019;148:491–501.

https://doi.org/https://doi.org/10.1016/j.applthermaleng.2018.11.025.

[148] Sarı A, Bicer A, Al-Sulaiman FA, Karaipekli A, Tyagi V V. Diatomite/CNTs/PEG composite PCMs with shape-stabilized and improved thermal conductivity: Preparation and thermal energy storage properties. Energy Build 2018;164:166–75. https://doi.org/https://doi.org/10.1016/j.enbuild.2018.01.009.

[149] Sarı A, Al-Ahmed A, Bicer A, Al-Sulaiman FA, Hekimoğlu G. Investigation of thermal properties and enhanced energy storage/release performance of silica fume/myristic acid composite doped with carbon nanotubes. Renew Energy 2019;140:779–88. https://doi.org/https://doi.org/10.1016/j.renene.2019.03.102.

[150] Chirtoc M, Horny N, Tavman I, Turgut A, Kökey I, Omastová M. Preparation and photothermal characterization of nanocomposites based on high density polyethylene filled with expanded and unexpanded graphite: Particle size and shape effects. Int J Therm Sci 2012;62:50–5. https://doi.org/https://doi.org/10.1016/j.ijthermalsci.2012.02.015.

[151] Jiang G, Huang J, Fu Y, Cao M, Liu M. Thermal optimization of composite phase change material/expanded graphite for Li-ion battery thermal management. Appl Therm Eng 2016;108:1119–25. https://doi.org/https://doi.org/10.1016/j.applthermaleng.2016.07.197.

[152] Karaipekli A, Sari A, Kaygusuz K. Thermal conductivity improvement of stearic acid using expanded graphite and carbon fiber for energy storage applications. Renew Energy 2007;32:2201–10. https://doi.org/10.1016/j.renene.2006.11.011.

[153] Sarı A, Karaipekli A. Preparation, thermal properties and thermal reliability of palmitic acid/expanded graphite composite as form-stable PCM for thermal energy storage. Sol Energy Mater Sol Cells 2009;93:571–6. https://doi.org/https://doi.org/10.1016/j.solmat.2008.11.057.

[154] Sari A, Karaipekli A. Thermal conductivity and latent heat thermal energy storage characteristics of paraffin/expanded graphite composite as phase change material. Appl Therm Eng 2007;27:1271–7. https://doi.org/10.1016/j.applthermaleng.2006.11.004.

[155] Zhang P, Hu Y, Song L, Ni J, Xing W, Wang J. Effect of expanded graphite on properties of high-density polyethylene/paraffin composite with intumescent flame retardant as a

shape-stabilized phase change material. Sol Energy Mater Sol Cells 2010;94:360–5. https://doi.org/10.1016/j.solmat.2009.10.014.

[156] Wu W, Wu W, Wang S. Form-stable and thermally induced flexible composite phase change material for thermal energy storage and thermal management applications. Appl Energy 2019;236:10–21. https://doi.org/https://doi.org/10.1016/j.apenergy.2018.11.071.

[157] Xiao C, Zhang G, Li Z, Yang X. Custom design of solid–solid phase change material with ultra-high thermal stability for battery thermal management. J Mater Chem A 2020;8:14624–33. https://doi.org/10.1039/D0TA05247G.

[158] Liu C, Xu Z, Song Y, Lv P, Zhao J, Liu C, et al. A novel shape-stabilization strategy for phase change thermal energy storage. J Mater Chem A 2019;7:8194–203. https://doi.org/10.1039/C9TA01496A.

[159] Hussain A, Tso CY, Chao CYH. Experimental investigation of a passive thermal management system for high-powered lithium ion batteries using nickel foam-paraffin composite. Energy 2016;115:209–18. https://doi.org/https://doi.org/10.1016/j.energy.2016.09.008.

[160] Hussain A, Abidi IH, Tso CY, Chan KC, Luo Z, Chao CYH. Thermal management of lithium ion batteries using graphene coated nickel foam saturated with phase change materials. Int J Therm Sci 2018;124:23–35. https://doi.org/https://doi.org/10.1016/j.ijthermalsci.2017.09.019.

[161] Qu ZG, Li WQ, Tao WQ. Numerical model of the passive thermal management system for high-power lithium ion battery by using porous metal foam saturated with phase change material. Int J Hydrogen Energy 2014;39:3904–13. https://doi.org/https://doi.org/10.1016/j.ijhydene.2013.12.136.

[162] Zhang Z, Cheng J, He X. Numerical simulation of flow and heat transfer in composite PCM on the basis of two different models of open-cell metal foam skeletons. Int J Heat Mass Transf 2017;112:959–71. https://doi.org/https://doi.org/10.1016/j.ijheatmasstransfer.2017.05.012.

[163] Alipanah M, Li X. Numerical studies of lithium-ion battery thermal management systems using phase change materials and metal foams. Int J Heat Mass Transf

2016;102:1159–68.
https://doi.org/https://doi.org/10.1016/j.ijheatmasstransfer.2016.07.010.

[164] Pan M, Lai W. Cutting copper fiber/paraffin composite phase change material discharging experimental study based on heat dissipation capability of Li-ion battery. Renew Energy 2017;114:408–22. https://doi.org/https://doi.org/10.1016/j.renene.2017.07.004.

[165] Khateeb SA, Farid MM, Selman JR, Al-Hallaj S. Design and simulation of a lithium-ion battery with a phase change material thermal management system for an electric scooter. J Power Sources 2004;128:292–307. https://doi.org/10.1016/j.jpowsour.2003.09.070.

[166] Ling Z, Wen X, Zhang Z, Fang X, Gao X. Thermal management performance of phase change materials with different thermal conductivities for Li-ion battery packs operated at low temperatures. Energy 2018;144:977–83. https://doi.org/https://doi.org/10.1016/j.energy.2017.12.098.

[167] Alzoubi MF, Khateeb S, Al-Hallaj S. Modeling of compression curves of phase change graphite composites using Maxwell and Kelvin models. J Compos Mater 2015;50:1123–35. https://doi.org/10.1177/0021998315588624.

[168] Luo X, Guo Q, Li X, Tao Z, Lei S, Liu J, et al. Experimental investigation on a novel phase change material composites coupled with graphite film used for thermal management of lithium-ion batteries. Renew Energy 2020;145:2046–55. https://doi.org/https://doi.org/10.1016/j.renene.2019.07.112.

[169] Wu W, Yang X, Zhang G, Ke X, Wang Z, Situ W, et al. An experimental study of thermal management system using copper mesh-enhanced composite phase change materials for power battery pack. Energy 2016;113:909–16. https://doi.org/https://doi.org/10.1016/j.energy.2016.07.119.

[170] Zou D, Ma X, Liu X, Zheng P, Hu Y. Thermal performance enhancement of composite phase change materials (PCM) using graphene and carbon nanotubes as additives for the potential application in lithium-ion power battery. Int J Heat Mass Transf 2018;120:33–41. https://doi.org/https://doi.org/10.1016/j.ijheatmasstransfer.2017.12.024.

[171] Mortazavi B, Yang H, Mohebbi F, Cuniberti G, Rabczuk T. Graphene or h-BN paraffin

composite structures for the thermal management of Li-ion batteries: A multiscale investigation. Appl Energy 2017;202:323–34. https://doi.org/https://doi.org/10.1016/j.apenergy.2017.05.175.

[172] Bahiraei F, Fartaj A, Nazri G-A. Experimental and numerical investigation on the performance of carbon-based nanoenhanced phase change materials for thermal management applications. Energy Convers Manag 2017;153:115–28. https://doi.org/https://doi.org/10.1016/j.enconman.2017.09.065.

[173] Temel UN. Passive thermal management of a simulated battery pack at different climate conditions. Appl Therm Eng 2019;158:113796. https://doi.org/https://doi.org/10.1016/j.applthermaleng.2019.113796.

[174] Javani N, Dincer I, Naterer GF. New latent heat storage system with nanoparticles for thermal management of electric vehicles. J Power Sources 2014;268:718–27. https://doi.org/10.1016/j.jpowsour.2014.06.107.

[175] Grujicic M, Zhao CL, Dusel EC. The effect of thermal contact resistance on heat management in the electronic packaging. Appl Surf Sci 2005;246:290–302. https://doi.org/https://doi.org/10.1016/j.apsusc.2004.11.030.

[176] Wang Y-F, Wu J-T. Performance improvement of thermal management system of lithium-ion battery module on purely electric AUVs. Appl Therm Eng 2019;146:74–84. https://doi.org/https://doi.org/10.1016/j.applthermaleng.2018.09.108.

[177] Lv Y, Yang X, Li X, Zhang G, Wang Z, Yang C. Experimental study on a novel battery thermal management technology based on low density polyethylene-enhanced composite phase change materials coupled with low fins. Appl Energy 2016;178:376–82. https://doi.org/https://doi.org/10.1016/j.apenergy.2016.06.058.

[178] Lv Y, Situ W, Yang X, Zhang G, Wang Z. A novel nanosilica-enhanced phase change material with anti-leakage and anti-volume-changes properties for battery thermal management. Energy Convers Manag 2018;163:250–9. https://doi.org/https://doi.org/10.1016/j.enconman.2018.02.061.

[179] Lei C, Wu K, Wu L, Liu W, Du R, Chen F, et al. Phase change material with anisotropically high thermal conductivity and excellent shape stability due to its robust cellulose/BNNSs skeleton. J Mater Chem A 2019;7:19364–73.

https://doi.org/10.1039/C9TA05067A.

[180] Shi Y, Hu M, Xing Y, Li Y. Temperature-dependent thermal and mechanical properties of flexible functional PDMS/paraffin composites. Mater Des 2020;185:108219. https://doi.org/https://doi.org/10.1016/j.matdes.2019.108219.

[181] Zhang Q, Feng J. Difunctional olefin block copolymer/paraffin form-stable phase change materials with simultaneous shape memory property. Sol Energy Mater Sol Cells 2013;117:259–66. https://doi.org/https://doi.org/10.1016/j.solmat.2013.06.020.

[182] Li W-W, Cheng W-L, Xie B, Liu N, Zhang L-S. Thermal sensitive flexible phase change materials with high thermal conductivity for thermal energy storage. Energy Convers Manag 2017;149:1–12. https://doi.org/https://doi.org/10.1016/j.enconman.2017.07.019.

[183] Huang Y-H, Cheng W-L, Zhao R. Thermal management of Li-ion battery pack with the application of flexible form-stable composite phase change materials. Energy Convers Manag 2019;182:9–20. https://doi.org/https://doi.org/10.1016/j.enconman.2018.12.064.

[184] He J, Yang X, Zhang G. A phase change material with enhanced thermal conductivity and secondary heat dissipation capability by introducing a binary thermal conductive skeleton for battery thermal management. Appl Therm Eng 2019;148:984–91. https://doi.org/https://doi.org/10.1016/j.applthermaleng.2018.11.100.

[185] Lv Y, Yang X, Zhang G, Li X. Experimental research on the effective heating strategies for a phase change material based power battery module. Int J Heat Mass Transf 2019;128:392–400. https://doi.org/https://doi.org/10.1016/j.ijheatmasstransfer.2018.07.037.

[186] Huang Q, Li X, Zhang G, Zhang J, He F, Li Y. Experimental investigation of the thermal performance of heat pipe assisted phase change material for battery thermal management system. Appl Therm Eng 2018;141:1092–100. https://doi.org/https://doi.org/10.1016/j.applthermaleng.2018.06.048.

[187] Wang X, Xie Y, Day R, Wu H, Hu Z, Zhu J, et al. Performance analysis of a novel thermal management system with composite phase change material for a lithium-ion battery pack. Energy 2018;156:154–68.

https://doi.org/10.1016/J.ENERGY.2018.05.104.

[188] Shi S, Xie Y, Li M, Yuan Y, Yu J, Wu H, et al. Non-steady experimental investigation on an integrated thermal management system for power battery with phase change materials. Energy Convers Manag 2017;138:84–96. https://doi.org/https://doi.org/10.1016/j.enconman.2017.01.069.

[189] Ling Z, Wang F, Fang X, Gao X, Zhang Z. A hybrid thermal management system for lithium ion batteries combining phase change materials with forced-air cooling. Appl Energy 2015;148:403–9. https://doi.org/https://doi.org/10.1016/j.apenergy.2015.03.080.

[190] Qin P, Liao M, Zhang D, Liu Y, Sun J, Wang Q. Experimental and numerical study on a novel hybrid battery thermal management system integrated forced-air convection and phase change material. Energy Convers Manag 2019;195:1371–81. https://doi.org/https://doi.org/10.1016/j.enconman.2019.05.084.

[191] Huang H, Wang H, Gu J, Wu Y. High-dimensional model representation-based global sensitivity analysis and the design of a novel thermal management system for lithium-ion batteries. Energy Convers Manag 2019;190:54–72. https://doi.org/https://doi.org/10.1016/j.enconman.2019.04.013.

[192] Jiang G, Huang J, Liu M, Cao M. Experiment and simulation of thermal management for a tube-shell Li-ion battery pack with composite phase change material. Appl Therm Eng 2017;120:1–9. https://doi.org/10.1016/j.applthermaleng.2017.03.107.

[193] Wu W, Yang X, Zhang G, Chen K, Wang S. Experimental investigation on the thermal performance of heat pipe-assisted phase change material based battery thermal management system. Energy Convers Manag 2017;138:486–92. https://doi.org/https://doi.org/10.1016/j.enconman.2017.02.022.

[194] Liu R, Chen J, Xun J, Jiao K, Du Q. Numerical investigation of thermal behaviors in lithium-ion battery stack discharge. Appl Energy 2014;132:288–97. https://doi.org/10.1016/j.apenergy.2014.07.024.

[195] Zheng Y, Shi Y, Huang Y. Optimisation with adiabatic interlayers for liquid-dominated cooling system on fast charging battery packs. Appl Therm Eng 2019;147:636–46. https://doi.org/https://doi.org/10.1016/j.applthermaleng.2018.10.090.

[196] An Z, Chen X, Zhao L, Gao Z. Numerical investigation on integrated thermal management for a lithium-ion battery module with a composite phase change material and liquid cooling. Appl Therm Eng 2019;163:114345. https://doi.org/https://doi.org/10.1016/j.applthermaleng.2019.114345.

[197] Wang LW, Tamainot-Telto Z, Metcalf SJ, Critoph RE, Wang RZ. Anisotropic thermal conductivity and permeability of compacted expanded natural graphite. Appl Therm Eng 2010;30:1805–11. https://doi.org/https://doi.org/10.1016/j.applthermaleng.2010.04.014.

[198] mettler toledo. Heat Capacity 2019. https://www.mt.com/gb/en/home/perm-lp/product-organizations/ana/TA-Cp_specific_heat_capacity.html (accessed December 19, 2019).

[199] Sobolčiak P, Abdelrazeq H, Ouederni M, Karkri M, Al-Maadeed MA, Krupa I. The stabilizing effect of expanded graphite on the artificial aging of shape stabilized phase change materials. Polym Test 2015;46:65–71. https://doi.org/https://doi.org/10.1016/j.polymertesting.2015.06.017.

[200] Spinner NS, Hinnant KM, Mazurick R, Brandon A, Rose-Pehrsson SL, Tuttle SG. Novel 18650 lithium-ion battery surrogate cell design with anisotropic thermophysical properties for studying failure events. J Power Sources 2016;312:1–11. https://doi.org/https://doi.org/10.1016/j.jpowsour.2016.01.107.

[201] Hatchard TD, MacNeil DD, Basu A, Dahn JR. Thermal model of cylindrical and prismatic lithium-ion cells. J Electrochem Soc 2001;148:A755–61.

[202] PNGV Battery Test Manual, revision 3 2001. https://avt.inl.gov/sites/default/files/pdf/battery/pngv_manual_rev3b.pdf (accessed November 26, 2018).

[203] Schuster E, Ziebert C, Melcher A, Rohde M, Seifert HJ. Thermal behavior and electrochemical heat generation in a commercial 40 Ah lithium ion pouch cell. J Power Sources 2015;286:580–9. https://doi.org/https://doi.org/10.1016/j.jpowsour.2015.03.170.

[204] Wang P, Wang X, Huang Y, Li C, Peng Z, Ding Y. Thermal energy charging behaviour of a heat exchange device with a zigzag plate configuration containing multi-phase-change-materials (m-PCMs). Appl Energy 2015;142:328–36.

https://doi.org/10.1016/j.apenergy.2014.12.050.

[205] Zhao B, Li C, Jin Y, Yang C, Leng G, Cao H, et al. Heat transfer performance of thermal energy storage components containing composite phase change materials. IET Renew Power Gener 2016;10:1515–22.

[206] Liu Z, Yao Y, Wu H. Numerical modeling for solid–liquid phase change phenomena in porous media: Shell-and-tube type latent heat thermal energy storage. Appl Energy 2013;112:1222–32.

[207] Zhao CY, Lu W, Tian Y. Heat transfer enhancement for thermal energy storage using metal foams embedded within phase change materials (PCMs). Sol Energy 2010;84:1402–12. https://doi.org/10.1016/j.solener.2010.04.022.

[208] Esapour M, Hamzehnezhad A, Darzi AAR, Jourabian M. Melting and solidification of PCM embedded in porous metal foam in horizontal multi-tube heat storage system. Energy Convers Manag 2018;171:398–410.

[209] Zhao Y, Jin L, Zou B, Qiao G, Zhang T, Cong L, et al. Expanded graphite – Paraffin composite phase change materials: Effect of particle size on the composite structure and properties. Appl Therm Eng 2020;171:115015. https://doi.org/https://doi.org/10.1016/j.applthermaleng.2020.115015.

[210] Sobolciak P, Mrlík M, AlMaadeed MA, Krupa I. Calorimetric and dynamic mechanical behavior of phase change materials based on paraffin wax supported by expanded graphite. Thermochim Acta 2015;617:111–9. https://doi.org/https://doi.org/10.1016/j.tca.2015.08.026.

[211] Li Y, Yan H, Wang Q, Wang H, Huang Y. Structure and thermal properties of decanoic acid/expanded graphite composite phase change materials. J Therm Anal Calorim 2017;128:1313–26. https://doi.org/10.1007/s10973-016-6068-4.

[212] Zhang D, Zhou J, Wu K, Li Z. Granular phase changing composites for thermal energy storage. Sol Energy 2005;78:471–80. https://doi.org/https://doi.org/10.1016/j.solener.2004.04.022.

[213] Xia L, Zhang P, Wang RZ. Preparation and thermal characterization of expanded graphite/paraffin composite phase change material. Carbon N Y 2010;48:2538–48. https://doi.org/https://doi.org/10.1016/j.carbon.2010.03.030.

[214] Xiao X, Zhang P, Li M. Preparation and thermal characterization of paraffin/metal foam composite phase change material. Appl Energy 2013;112:1357–66. https://doi.org/https://doi.org/10.1016/j.apenergy.2013.04.050.

[215] Vovchenko LL, Matzui LY, Kulichenko AA. Thermal characterization of expanded graphite and its composites. Inorg Mater 2007;43:597–601. https://doi.org/10.1134/S0020168507060088.

[216] Wang J, Carson JK, North MF, Cleland DJ. A new approach to modelling the effective thermal conductivity of heterogeneous materials. Int J Heat Mass Transf 2006;49:3075–83. https://doi.org/https://doi.org/10.1016/j.ijheatmasstransfer.2006.02.007.

[217] Grosu Y, Zhao Y, Giacomello A, Meloni S, Dauvergne J-L, Nikulin A, et al. Hierarchical macro-nanoporous metals for leakage-free high-thermal conductivity shape-stabilized phase change materials. Appl Energy 2020;269:115088. https://doi.org/https://doi.org/10.1016/j.apenergy.2020.115088.

[218] Wang S. Entropy and heat generation of lithium cells/batteries. Chinese Phys B 2016;25:10509.

[219] ARTASHYAN A. NEW FAST CHARGE TECHNOLOGY: 80% OF BATTERY POWER IN 1 MINUTE. Gizchina 2019. https://www.gizchina.com/2019/12/02/new-fast-charge-technology-80-of-battery-power-in-1-minute/ (accessed August 21, 2020).

[220] Luc. What determines the charge speed? Fastned 2020. https://support.fastned.nl/hc/en-gb/articles/205694717-What-determines-the-charge-speed- (accessed August 21, 2020).

[221] Zhao Y, Li Q, Zou B, Zhang T, Jin L, Qiao G, et al. Performance of a liquid cooling-based battery thermal management system with a composite phase change material. Int J Energy Res 2020;44:4727–42. https://doi.org/10.1002/er.5254.

[222] American Automobile Association. AAA ELECTRIC VEHICLE RANGE TESTING 2019. http://www.aaa.com/AAA/common/AAR/files/AAA-Electric-Vehicle-Range-Testing-Report.pdf (accessed April 2, 2019).

[223] Ding Y, Hui C, Zhao Y, Nie B. Vehicle Charging. WO2019162680A1, 2019.